

2017-12

Biogas slurry derived mesoporous carbon/metal oxides composites for supercapacitors application

Enock, Talam

NM-AIST

<https://doi.org/10.58694/20.500.12479/225>

Provided with love from The Nelson Mandela African Institution of Science and Technology

**BIOGAS SLURRY DERIVED MESOPOROUS CARBON/METAL
OXIDES COMPOSITES FOR SUPERCAPACITORS APPLICATION**

Talam Kibona Enock

**A Dissertation Submitted in Partial Fulfillment of the Requirements for the Degree of
Doctor of Philosophy in Sustainable Energy Science and Engineering of the Nelson
Mandela African Institution of Science and Technology**

Arusha, Tanzania

December, 2017

ABSTRACT

With the increasing utilities of intermittent renewable energies, hybrid electric vehicles and portable electronic devices, supercapacitors have been identified as one of the solution for energy storage since they can deliver high power. The main drawback of the supercapacitors is low energy densities which can be increased either by synthesizing nanostructured porous materials or improving the voltage window of the electrolyte. In this study the mesoporous carbons were synthesized from biogas slurry by varying the carbonization temperature (450, 550, and 650 °C); activation temperature (600, 700, and 800 °C); activation time from 30 to 120 min; and KOH activation agent to carbon mass ratio (1:1, 2:1, and 3:1). The mesoporous carbon samples synthesized were characterized by XRD, SEM, EDX, TEM, XPS, nitrogen sorption at 77 K, and the relevant electrochemical performances were investigated using cyclic voltammetry and electrochemical impedance spectroscopy. All samples exhibited type IV isotherms demonstrating the existence of mesopores. The specific surface area increased from 148 for unactivated carbon to 514 m² g⁻¹ for samples activated at 700 °C with the mass ratio of 3:1. The total volume increased from 0.12 to 0.38 cm³ g⁻¹ while the $S_{\text{micro}}/S_{\text{meso}}$ decreased with increasing activation time and KOH/carbon mass ratio. The carbon materials activated at 700 °C, 3:1 KOH to carbon mass ratio for 120 min exhibited high specific capacitance of 289 F g⁻¹ at a scan rate of 5 mV s⁻¹. When mesoporous carbon /MnO₂ composites were synthesized through co-precipitation route; the BET surface area decreased from 514 to 110 m² g⁻¹ while total pore volume decreased from 0.52 to 0.17 cm³ g⁻¹ for samples loaded with 40 mL of 5×10⁻⁴ and 5×10⁻² M KMnO₄, respectively and 0.2 g of mesoporous carbon. The electrode fabricated from the MnO₂/ mesoporous carbon composites exhibited high specific capacitance of 709 F g⁻¹ at scan rate of 5 mV s⁻¹ in three electrodes cell system. XRD studies of the NiCo₂O₄/ mesoporous carbon composites revealed that the spinel structure of the NiCo₂O₄ was maintained in the composites. The nitrogen uptake increased with increasing annealing temperature to 300 °C then decreased at 400 °C. The NiCo₂O₄/ mesoporous carbon composites exhibited high specific capacitance of 835 F g⁻¹ at scan rate of 5 mV s⁻¹ for sample annealed at 350 °C. The cyclic stabilities of the electrodes were above 90% after 50000 cycles. Electrochemical impedance spectroscopy studies demonstrate that synthesized materials have high conductivities. This study shows that high performance electrodes can be designed from biogas slurry derived porous carbon and its MnO₂ and NiCo₂O₄ composites.

DECLARATION

I, **TALAM KIBONA ENOCK** do hereby declare to the Senate of Nelson Mandela African Institution of Science and Technology that this dissertation is my own original work and that it has neither been submitted nor being concurrently submitted for degree award in any other institution.

Talam Kibona Enock



Name and signature of candidate

17/12/2017

Date

The above declaration is confirmed

Dr. Cecil K. King'onde



Name and signature of supervisor 1

17/12/2017

Date

Prof. Alexander Pogrebnoi



Name and signature of supervisor 2

20/12/2017

Date

Dr. Yusufu Abeid Chande Jande

22/12/2017

Name and signature of supervisor 3

Date

COPYRIGHT

This dissertation is copyright material protected under the Berne Convention, the Copyright Act of 1999 and other international and national enactments, in that behalf, on intellectual property. It must not be reproduced by any means, in full or in part, except for short extracts in fair dealing; for researcher private study, critical scholarly review or discourse with an acknowledgement, without a written permission of the Deputy Vice Chancellor for Academic, Research and Innovation, on behalf of both the author and the Nelson Mandela African Institution of Science and Technology.

CERTIFICATION

The undersigned certify that they have read and found that the dissertation conform to the standard and format acceptable for examination, therefore do hereby recommends for examination of dissertation entitled “**Biogas Slurry Derived Mesoporous Carbon/Metal Oxides Composites for Supercapacitor Application**” in partial fulfilment of the requirements for the degree of PhD Sustainable Energy Science and Engineering at Nelson Mandela African Institution of Science and Technology.

Dr. Cecil K. King'ondur



17/12/2017

Name and signature of supervisor

Date

Prof. Alexander Pogrebnoi



20/12/2017

Name and signature of supervisor

Date

Dr. Yusufu Abeid Chande Jande



22/12/2017

Name and signature of supervisor

Date

ACKNOWLEDGEMENT

First and foremost, I thank my Almighty God the creator for giving me strength in doing this research. Second, my Principal supervisor Dr. Cecil Kithongo King'ondeu deserves deepest appreciation for his constant encouragement, guidance, patience, sharp insights as well as technical advice throughout the research. I also express my heartfelt thanks to Prof. Alexander Pogrebnoi for co-supervising this research. His guidance, critics, and directives in writing scientific papers together with this thesis are unforgettable. I would also like to thank my third supervisor Dr. Yusufu Chande Jande for his invaluable guidance and moral support.

Special thanks to Prof. Tatiana Pogrebnyaya for her encouragement during ups and downs of my research progress. She sometimes played motherly roles that print indelible memory in my carrier. I am also thankful to Prof. Karol Njau, Prof. Alfred Muzuka and Prof. Eugene Park for playing their administration roles that facilitated the completion of the research.

Dr. Revocatus Machunda, Dr. Godlisten Shao, and Dr. Askwar Hilonga deserve a special mention as their contributions towards attaining the objectives of this research are unsurpassed. I also appreciate Ms Joyce Elisadiki a PhD candidate for her moral support. I acknowledge the technical support provided by Mr. David Mtweve the NM-AIST laboratory technician.

I extend my sincere appreciations to Mkwawa University College of Education (MUCE) for granting study leave and Tanzania Commission of Science and Technology (COSTECH) for sponsoring my PhD studies. Without COSTECH financial support, this study could be impossible to accomplish. The Nelson Mandela Institution of Science and Technology (NM-AIST) is also acknowledged for offering me a chance to study and allowing me to use their laboratories. I'm also grateful to Hanyang University (South Korea) for SEM, TEM, BET, and XRD characterization of my samples. The Columbia University and The Brookhaven National Laboratory under U.S Department of Energy (DOE) Office is acknowledged for allowing the operation of PDF through beam line 28-ID-2 of the National Synchrotron Light Source II.

Lastly but no least, I would thank my family for everlasting support during my PhD studies. My father Milson Kibona and my mother Laitina Ndembo Mbugi have cared for me a lot through all stages of my school to this level. Their contributions are irreplaceable in my life. My wife

Valentine Faustine Msoffe for boundless love, encouragement, and moral support as well as for taking care of our three sons during my absence. My Sons Lutufyo and Lusubilo and Lughano who missed fatherly care during my studies, has been source of motivation in doing my research.

DEDICATION

I dedicate this work to my lovely wife Valentine Faustine Msoffe, my sons Lutufyo Lusubilo and Lughano, My Parents Milson Kibona and Laitina Ndembo Mbugi.

TABLE OF CONTENTS

ABSTRACT	i
COPYRIGHT	iii
CERTIFICATION	iv
DEDICATION	vii
TABLE OF CONTENTS	viii
LIST OF TABLES	xiii
LIST OF FIGURES	xv
LIST OF APPENDICES	xxi
LIST OF ABBREVIATIONS AND SYMBOLS	xxii
CHAPTER ONE	1
General Introduction	1
1.0 Introduction	1
1.1 Background information	1
1.2 Statement of research problem	4
1.3 Objectives.....	5
1.4 Research questions.....	5
1.5 Significance of the research.....	5
CHAPTER TWO	6
Status of Biomass Derived Carbon for Supercapacitor Electrode Applications	6

2.1	Introduction	6
2.2	Materials for supercapacitor electrodes	9
2.2.1	Activated Carbons.....	10
2.2.2	Carbon aerogel derived from biomasses	22
2.2.3	Metal oxides and carbon composites	23
2.2.4	Activated carbon/ conducting polymers.....	25
2.2.5	Activated carbon/ carbon nanotubes composites.....	25
2.3	Conclusion.....	26
CHAPTER THREE		28
Biogas Slurry Derived Mesoporous Carbon for Supercapacitor Applications.....		28
3.1	Introduction	29
3.2	Materials and Methods.....	30
3.2.1	Materials.....	30
3.2.2	Synthesis of activated carbon from biogas slurry.....	30
3.2.3	Characterization of the synthesized carbon materials.....	31
3.2.4	Electrochemical measurements	32
3.3	Results and discussion.....	33
3.3.1	Effect of carbonization time on the carbon yield.....	33
3.3.2	Morphological, structural, and textural properties of synthesized materials	34
3.3.3	Surface chemistry studies of the synthesized samples.....	43

3.3.4	Electrochemical characterization of the electrodes	45
3.4	Conclusion.....	53
CHAPTER FOUR.....		54
Effect of Biogas Slurry Carbonization Temperature on Specific Capacitance		54
4.1	Introduction	54
4.2	Materials and Methods.....	56
4.2.1	Carbonization and activation process of biogas slurry precursor.....	56
4.2.2	Physical characterisation synthesized porous carbons.....	57
4.2.3	Electrode fabrication.....	57
4.2.4	Electrochemical measurements	57
4.3	Results and discussion.....	58
4.3.1	Elemental analysis of raw and porous carbon materials	58
4.3.2	Physical characterization synthesized materials.....	58
4.3.3	Electrochemical performances of electrodes.....	64
4.4	Conclusion.....	69
Electrochemical Performance and Pair Distribution Function Analysis of Mesoporous Biogas Slurry Derived Carbon Materials Synthesized using Combined KOH and ZnCl₂ Activation		71
5.1	Introduction	71
5.2	Materials and Methods.....	73

5.2.1	Synthesis of porous carbon.....	73
5.2.2	Surface morphology and textural characterization	73
5.2.3	Total scattering measurements and PDF analysis	73
5.2.4	Fabrication of working electrode.....	75
5.2.5	Electrochemical Measurements	75
5.3	Results and discussion.....	75
5.3.1	Physical characterization of carbon materials	75
5.3.2	Pair distribution function analysis (PDF) of the synthesized materials	83
5.3.3	Electrochemical performance of the synthesized porous materials.....	89
5.4	Conclusion.....	92
CHAPTER SIX		93
Mesoporous Carbon/MnO₂ Composites for Synergistic Capacitance		93
6.1	Introduction	93
6.2	Materials and Methods.....	95
6.2.1	Materials.....	95
6.2.2	Synthesis of MnO ₂ /mesoporous carbon composite	95
6.2.3	Physical characterization of the composites.....	96
6.2.4	Fabrication of working electrodes and electrochemical measurements.....	97
6.3	Results and discussion.....	97
6.3.1	Physical characterization of the synthesized composites.....	97

6.3.2	Electrochemical performances of the synthesized MnO ₂ -BC based electrodes....	106
6.4	Conclusion.....	115
CHAPTER SEVEN.....		116
Synthesis of NiCo₂O₄/Mesoporous Carbon Composites for Supercapacitors Application		116
7.1	Introduction	116
7.2	Materials and Methods.....	118
7.2.1	Synthesis of the composites	118
7.2.2	Characterizations	118
7.2.3	Electrochemical measurements of electrodes.....	119
7.3	Results and discussion.....	119
7.3.1	Physical characterizations of NiCo ₂ O ₄ /mesoporous carbon composites	119
7.3.2	Electrochemical performances of the composites	128
7.4	Conclusion.....	132
CHAPTER EIGHT		133
General Discussion Conclusion and Recommendations		133
8.1	General discussion	133
8.2	Conclusions	136
8.3	Recommendations and research outlook.....	138
REFERENCES.....		139
APPENDICES.....		165

LIST OF TABLES

Table 1: Performance comparison of different electrochemical storage systems (Miller and Burke, 2008).....	7
Table 2: The capacitance, energy density, and surface area of porous carbon derived from different plant wastes.....	13
Table 3: The capacitance and surface area of porous carbon derived from different animal wastes.....	15
Table 4: The preparation method and properties of porous carbon derived from coconut shells.	18
Table 5: Specific capacitances and surface area of porous carbon synthesized through molten salt carbonization of different biomass.	21
Table 6: The capacitance, energy density, and stability of different composites.	24
Table 7: The effect of carbonization time on the yield of carbon at carbonization temperature of 650 °C.....	34
Table 8: XRD microcrystallite characterization of the electrode materials.	39
Table 9: Pore size, pore volume, and surface areas of synthesized carbon samples.	41
Table 10: Equivalent circuit parameters of BC-X-Y-Z obtained from Nyquist plot analysis.....	51
Table 11: Elemental compositions of the samples as measured by CHNOs ratio analyzer.....	58
Table 12: Textural properties of mesoporous carbon samples.	61
Table 13: Pore texture and surface area of the BC mesoporous carbon samples.	82
Table 14: Pearson product-moment correlation coefficients calculated from the experimental PDFs of the different samples.	85
Table 15: The resulting weight percent and coherence length for the phases fit in the models described.	89

Table 16: Pore texture and surface area of synthesized samples.....99

Table 17: Comparison of specific capacitance obtained from different MnO₂/carbon composites.
..... 109

Table 18: Pore texture and surface area of NiCo₂O₄/mesoporous carbon composites. 121

Table 19: d-spacings of different planes for the synthesized composites. 127

LIST OF FIGURES

Figure 1: Rangone plot for various energy storage and conversion devices (Kötz and Carlen, 2000).....	2
Figure 2: Schematic expression of a supercapacitor cell (Reproduced with the permission from the Author (Obreja, 2008).....	9
Figure 3: Variation of reported capacitance, pore size, and BET surface area of activated carbon materials derived from different plant precursors.	14
Figure 4: Morphologies of porous carbon derived from water hyacinth through different routes.	19
Figure 5: FE-SEM micrographs at 2 μm (a) B-650, (b) BC-1-700-30, (c) BC-2-700-30, and (d) BC-3-700-30.....	35
Figure 6: FE-SEM micrographs of samples at different magnifications (a) BC-650 at 500 nm, (b) BC-3-700-30 at 500 nm, (c) BC-650 at 10 μm , and (d) BC-3-700-30 at 10 μm	35
Figure 7: XRD Patterns of BC-650, BC-1-700-30, BC-2-700-30, BC-3-700-30, and BC-3-650-60.	37
Figure 8: XRD pattern for BC-3-700-30 from 5 to 80, 2 θ	38
Figure 9: TEM images for (a) BC-1-700-30, (b) BC-3-700-60, (c) BC-3-700-30, and (d) HRTEM for BC-3-700-30.	40
Figure 10: (a) Nitrogen adsorption – desorption isotherms for BC-650, BC-1-700-30, BC-2-700-30, BC-3-700-30, and BC-3-700-60 samples, (b) Pore size distribution calculated from the desorption isotherm using BJH method and (c) Pore distribution at 2 to 5 nm range.....	43
Figure 11: XPS spectra and deconvolution of peaks for BC-3-700-30 (a) Survey spectra, (b) C1s, (c) N1s, and (D) O1s.....	44

Figure 12: Cyclic voltammograms of BC based electrodes in 6 M KOH electrolyte (a) BC-650, (b) BC-3-700-30, (c) BC-2-800-30 and (d) BC-2-800-120.	46
Figure 13: Effect of (a) KOH to carbon ratio, (b) Activation time, (c) Activation temperature on specific capacitance Vs scan rate, and (d) Cyclic stability of BC mesoporous carbon (Capacitance retention).	47
Figure 14: Correlation between micropore and mesopore content, crystallite size, and specific capacitance of synthesized electrodes.	49
Figure 15: (a) Nyquist plots of electrodes based on BC-3-700-30, BC-3-700-60, and BC-3-700-120, (b) Comparison of Nyquist plots using arbitrary real impedance, (c) Fitted Nyquist plots and (d) Specific capacitance versus frequency.	50
Figure 16: Bode plots (a) Z with respect to frequency (b) $Z'/-Z''$ with respect to frequency BC-3-700-30, (c) $Z'/-Z''$ with respect to frequency BC-3-700-60, and (d) $Z'/-Z''$ with respect to frequency BC-3-700-120.	52
Figure 17: Schematic illustration for synthesis of mesoporous carbon under different carbonization temperature condition.	56
Figure 18: Nitrogen adsorption and desorption isotherms (77.3 K) of biogas slurry derived carbon at different carbonization temperature.	60
Figure 19: Pore size distribution of biogas slurry derived carbons by BJH (a) adsorption isotherms (b) desorption isotherms.	60
Figure 20: (a) SEM image of BC450 (b) SEM image of BC550 (c) SEM image of BC650 and (d) TEM image of BC550 carbon samples.	62
Figure 21: The high magnification FESEM images of (a) BC450, (b) BC550 and (c) BC650 carbon samples.	63
Figure 22: XRD patterns of unactivated and activated BC samples (a) unactivated (b) activated.	64

Figure 23: (a, b, and c) Cyclic voltammetry of BC450, BC550 and BC650 activated carbon in 6 M KOH (d) Specific capacitance for BC450, BC550, and BC650 as a function of scan rate.	65
Figure 24: (a-c) Cyclic voltammetry of BC450, BC550 and BC650 activated carbon in 1 M Na ₂ SO ₄ and (d) Specific capacitance for BC450, BC550, and BC650 as a function of scan rate.	66
Figure 25: CV curves for porous carbon based electrodes at scan rate of 150 mV s ⁻¹ (a) 6 M KOH and (b) 1 M Na ₂ SO ₄ electrolytes.....	67
Figure 26: (a) Specific capacitance for BC550 in 6 M KOH and 1 M Na ₂ SO ₄ electrolytes, (b) Nyquist plots for BC450, BC550, and BC650 in 6 M KOH electrolyte, (c) Bode plots for BC450, BC550, and BC650 in 6 M KOH electrolyte and (d) Nyquist plots for BC450, BC550, and BC650 in 1M Na ₂ SO ₄ electrolyte.....	69
Figure 27: SEM micrographs of samples (a) BC-0-0, (b) BC-0-4, (c) BC-4-0, (d) BC-2-2, (e) BC-1-3 and (f) BC-3-1.....	77
Figure 28: High magnification SEM micrography (a) BC-1-3, and (b) BC-3-1.....	78
Figure 29: EDX spectrum of BC-1-3 sample.	79
Figure 30: (a) Nitrogen adsorption and desorption isotherms of all samples, (b) Nitrogen adsorption and desorption isotherms of BC-4-0, (c) Nitrogen adsorption and desorption isotherms of BC-3-1 and (d) Pore size distribution calculated using BJH method.....	80
Figure 31: Surface area values (BET micro and meso) for synthesized porous materials.....	82
Figure 32: (a) Reduced total scattering structure functions, $F(Q)$, for the untreated and treated samples. (b) The resulting PDFs after Fourier transformation of the respective structure function in A.	84

Figure 33: PDFs simulated from refinement of the willemite structure (red) to the measured PDFs (blue), over a range of 1.0 - 40.0 Å. Differences are plotted below in green. ...86

Figure 34: (a) Measured PDFs for BC-4-0, BC-0-0, and BC-0-4 are compared to a PDF measured for amorphous silica, as well as simulated PDFs for both graphite and a single layer of graphene. (b) The PDF measured for BC-0-4 compared to the residual after subtracting willemite from BC-2-2.....87

Figure 35: (a) PDFs simulated from three-phase refinement of graphite + quartz + willemite (red) to the measured PDFs (blue), over a range of 1.0-40.0 Å. Differences are plotted below in green. (b) Simulated PDFs (red) from refinement of graphite + quartz over a range of 1.0-8.0 Å.88

Figure 36: Cyclic voltammograms of the synthesized electrodes (a) B-0-0, (b) B-4-0, (c) B-0-4, (d) B-2-2, (e) B-1-3 and (f) B-3-1.90

Figure 37: (a) Specific capacitance of synthesized porous carbon and (b) Nyquist plots of synthesized electrodes.....92

Figure 38: Schematic diagram for the synthesis of manganese oxide/mesoporous carbon composites materials.....96

Figure 39: (a) Nitrogen adsorption and desorption isotherms and (b) Pore distributions of MnO₂/BC mesoporous carbon composites.98

Figure 40: FESEM images of (a) 1MnO₂-0.2BC, (b) 3MnO₂-0.2BC and (c) 4MnO₂-0.2BC. ... 100

Figure 41: FE-SEM images of (a) 1MnO₂-0.2BC, (b) 3MnO₂-0.2BC and (c) 4MnO₂-0.2BC at high magnification. 100

Figure 42: EDX spectra of (a) 1MnO₂-0. (b) 3MnO₂-0.2BC (c) 4MnO₂-0.2BC. 101

Figure 43: TEM images of (a) 1MnO₂-0.2BC (b) 3MnO₂-0.2BC, and (c,d) 4MnO₂-0.2BC..... 102

Figure 44: HRTEM images at high magnifications (a, b) 1MnO₂-0.2BC (c, d) 3MnO₂-0.2BC, and (e, f) 4MnO₂-0.2BC..... 103

Figure 45: XRD patterns of synthesized MnO ₂ /mesoporous carbon composites.....	104
Figure 46: Raman spectrum of 1MnO ₂ -0.2BC and 4MnO ₂ -0.2BC.....	106
Figure 47: Cyclic voltammograms (a) 1MnO ₂ -0.2BC, (b) 2MnO ₂ -0.2BC, (c) 3MnO ₂ -0.2BC, and (d) 4MnO ₂ -0.2BC.	107
Figure 48: (a) Specific capacitances of MnO ₂ /BC composites for different MnO ₂ loading, (b) Correlation between surface area and specific capacitance (c) Specific capacitances of MnO ₂ /BC composites for different mass of BC, (d) Cyclic stabilities of MnO ₂ /BC composites electrodes measured at 20 mV s ⁻¹	110
Figure 49: Specific capacitance against (a) total pore volume at 5 mV s ⁻¹ (b) total pore volume at 50 mV s ⁻¹ (c) average pore size (d) mesopore content (% V _{meso}).	112
Figure 50: (a) Nyquist plots of MnO ₂ /BC composites, (b) Bode plots of MnO ₂ /BC composites electrodes of Real Z vs frequency, (c) Bode plots of MnO ₂ /BC composites electrodes of phase angle vs frequency and (d) Specific capacitance vs frequency.	114
Figure 51: (a) Nitrogen adsorption and desorption isotherms of NiCo ₂ O ₄ /Mesoporous carbon composites (b) BJH pore size distribution of the composites as calculated from desorption branch.	120
Figure 52: Micrographs of composites at 20k magnification of (a) BC-NiCo-100, (b) BC-NiCo- 250, (c) BC-NiCo-350 and, (d) BC-NiCo-400.....	122
Figure 53: Micrographs of composites at 100k magnification of (a) BC-NiCo-100, (b) BC-NiCo- 250, (c) BC-NiCo-350 and, (d) BC-NiCo-400.....	123
Figure 54: EDX Spectra of (a) BC-NiCo-100, (b) BC-NiCo-250, (c) BC-NiCo-350 and (d) BC- NiCo-400.....	124
Figure 55: TEM images of (a) BC-NiCo-100, (b) BC-NiCo-250, (c) BC-NiCo-350 and, (d) BC- NiCo-400.....	125

Figure 56: HRTEM images of (a) BC-NiCo-100, (b) BC-NiCo-250, (c) BC-NiCo-350 and, (d) BC-NiCo-400.125

Figure 57: X- ray diffraction pattern of the Manganese oxide/ mesoporous carbon composites.126

Figure 58: Raman spectra of BC-NCo-250 and BC-NCo-350..... 128

Figure 59: Cyclic voltammograms of the NiCo₂O₄/ mesoporous carbon composites..... 129

Figure 60: (a) Specific capacitance of BC-NCo-T electrodes at different scan rates, (b) Correlation of specific capacitances, $S_{\text{meso}}/S_{\text{micro}}$ and $V_{\text{meso}}/V_{\text{micro}}$ for BC-NCo-T electrodes, (c) Nyquist plots of different BC-NCo-T electrodes and (d) Cyclic stabilities of BC-NCo-T electrodes. 131

LIST OF APPENDICES

Appendix 1: EDX spectrum for BC-3-700-30.....	165
Appendix 2: Cyclic voltammograms of biogas slurry derived carbons in three-electrode system in 6 M KOH at sweep rates of 5, 10, 30, 50, 100 and 150 mV s ⁻¹ (A) BC-1-700-30 (B) BC-2-700-30, and (C) BC-3-700-30.	166
Appendix 3: Cyclic voltammograms of biogas slurry derived carbons in three-electrode system in 6 M KOH at sweep rates of 5, 10, 30, 50, 100 and 150 mV s ⁻¹ (A) BC-3-700-30 (B) BC-3-700-60, and (C) BC-3-700-120.	167
Appendix 4: Cyclic voltammograms of biogas slurry derived carbons in three-electrode system in 6 M KOH at sweep rates of 5, 10, 30, 50, 100 and 150 mV s ⁻¹ (A) BC-3-600-60 (B) BC-3-700-60, and (C) BC-3-800-60.	168

LIST OF ABBREVIATIONS AND SYMBOLS

BC	Biogas slurry derived carbon
MnO ₂ -BC	Manganese dioxide composite/biogas slurry derived mesoporous carbon
BC-NCo-T	Biogas slurry derived mesoporous carbon /nickel cobaltite composite annealed at temperature T
$B(\theta)$	Full width at half maximum
C	Specific capacitance (F/g)
CTAB	hexadecyltrimethyl ammonium bromide
CV	Cyclic voltammetry
BET	Brunauer- Emmet - Teller method
BJH	Barret –Joyner- Halender method
EDLC	Electric double layer capacitance
EDS	Energy dispersive spectroscopy
EIS	Electrochemical impedance spectroscopy
FESEM	Field emission scanning electron microscope
HRTEM	High resolution transmission electron microscope
L_a	Stack width
L_c	Stack height
OCP	Open circuit potential
PDF	Pair distribution function
PVDF	Polyvinlydene difluoride
RaPDF	Rapid acquisition PDF
ν	Scan rate
XPS	X-ray photoelectron spectroscopy
XRD	X-ray Diffraction
Z'	Real impedance
Z''	Imaginary impedance

CHAPTER ONE

General Introduction

1.0 Introduction

This chapter details the general introduction of the study. It mainly focuses on the background information of the study, problem statement, and the objectives of this study.

1.1 Background information

The realisation of sustainable society is tied to the increased attention on renewable energy sources such as wind, biomass, tides, and solar. The focus on renewable energy sources has been caused by climate change concerns and the potential depletion of fossils worldwide (Martinot *et al.*, 2007). However, with exception of hydropower, most renewable energy sources are intermittent in nature thus the electricity produced need storage mechanisms (Chandra, 2012). Furthermore, the increasing use of electric and hybrid vehicles as well as portable electronics globally has heightened research interest on energy storage strategies.

Typically, energy storage process involves converting one form of energy to another form which is retained for use when needed. In this regard, different methods has been utilized in storing energy ranging from mechanical, thermal, electromagnetic to electrochemical energy storage (Liu *et al.*, 2010a). For thermal storage, the location where the heat is to be used determines where to generate heat. Though the mechanical storage mechanism is the simplest way of storing bulk electricity through hydro storage, they are affected by weak gravity and so can only be efficient in mountainous terrain (Dunn *et al.*, 2011). Batteries and supercapacitors play an important role in storing energy for electric vehicles (EV), hybrid electric vehicles (HEVs) and portable electronic devices. Due to intermittent nature of renewable energies, electromagnetic and electrochemical storage mechanisms are preferred as they have high matching performances and stabilizes the grid (Döşoğlu and Arsoy, 2016).

Currently, secondary batteries are the most used electrochemical storage system yet their low power density, low cyclability, and short life limit their applications. Their low power density is due to their slow reaction kinetics. Though batteries have much higher energy density, they store

energy chemically, thus they undergo physical and chemical change between charging and discharging states. On the other hand, supercapacitors have high power density (10^3 - 10^4 Wkg^{-1}) and cycling stability ($> 10^6$ cycles) and this makes them promising electrochemical energy storage systems (Burke, 2000; Halper and Ellenbogen, 2006; Zhang and Zhao, 2009). However, their use is limited by low energy density, relatively high effective series resistance, and high cost. Supercapacitors have low energy density of 3-5 Whkg^{-1} compared to 30-40 Whkg^{-1} for Lead acid battery and 10-250 Whkg^{-1} for Lithium ion battery. Therefore, the challenges in supercapacitors research and development have been low energy density and high cost.

Batteries, supercapacitors, and conventional capacitors have their own advantages and disadvantages compared to other technology. The differences may arise either from charge and discharge time, energy density, life cycle, specific power, and charging/discharging efficiency among other factors. The appropriate method for identifying good electrochemical energy storage systems is the use of Rangone plot shown in Fig. 1. The figure clearly shows that the gap between conventional capacitor and batteries can be filled well by supercapacitors.

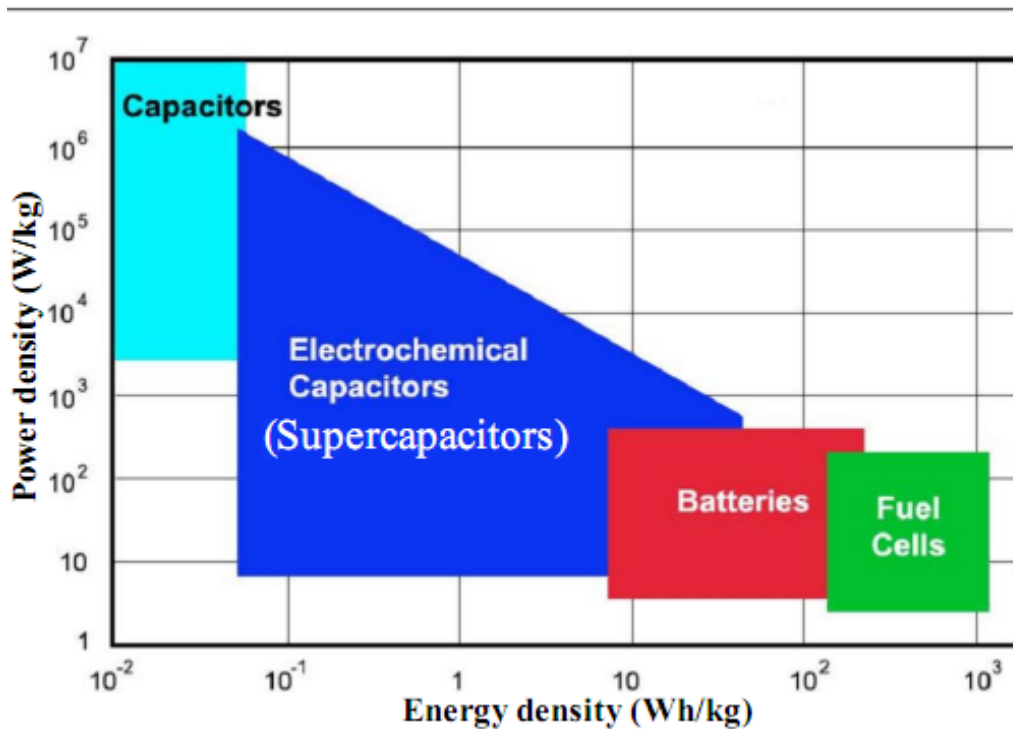


Figure 1: Rangone plot for various energy storage and conversion devices (Kötz and Carlen, 2000).

Considering the low energy density of supercapacitors, researchers apply two strategies in order to increase it. One is to improve the microstructures of the electrode so as to increase the capacitance of the electrode. Second strategy is to increase the voltage window by studying different electrolytes. The voltage window can be increased by good choice of electrolyte while the specific capacitance of the supercapacitor can be improved by synthesizing nanoporous materials or using composite electrode materials. Carbon based materials are among the most used supercapacitor electrode materials due to their abundance, low cost, ease of processing, non-toxicity, tunable pore size for proper transport of electrolyte, and large specific surface area for physical interaction (Xia *et al.*, 2008; Zhang and Zhao, 2009; Wang *et al.*, 2012b). The major limitation of some carbon materials such as graphene and carbon nanotubes is the high cost of processing and hence their limited availability. Therefore, search for alternative carbon precursors for supercapacitor electrodes is imperative.

Biomass based organic materials which are abundant have been used as source of carbon for supercapacitor electrodes. Several materials like coffee beans, pine needles, rice straw (He *et al.*, 2013b), corn stalk (Chen *et al.*, 2013), sorghum pitch (Senthilkumar *et al.*, 2011), water hyacinth (Kurniawan *et al.*, 2015), human hair (Qian *et al.*, 2014), coconut shells and egg yolk (Li *et al.*, 2015) have been employed to synthesize nanostructured carbon materials. The goal with the aforementioned biomass materials was to increase the surface area and other textures so that the biomass derived carbon fit the application as supercapacitor electrode materials. Though most carbon exhibit high conductivity, they also exhibit low capacitance thus resulting to low energy density. One way of increasing energy density would be compositing the biomass derived carbon with high capacitance metal oxides or polymers.

It is no wonder therefore that carbon-metal oxide nanocomposites have been pursued as supercapacitor electrodes. The use of composite is attractive because of the synergistic effects of high power density (coming from carbon) and high energy density (coming from pseudo-capacitive metal oxides) (Jiang *et al.*, 2012).

Additionally, the production of biogas has been increasing both in developing and developed countries. Globally, the biogas production increased from $13.2 \times 10^9 \text{ m}^3$ in the year 2000 to $59.0 \times 10^9 \text{ m}^3$ in 2013 an increase of 3.5 times (Venkata, 2016). The three leading countries in biogas

production as per 2013 records are China ($15.2 \times 10^9 \text{ m}^3$), German ($13.3 \times 10^9 \text{ m}^3$), and USA ($12.3 \times 10^9 \text{ m}^3$). In Africa biogas production has been increasing with Tanzania, Kenya, Rwanda Ethiopia, Uganda, and Cameroon reported to have installed 1,665 formal biogas as per 2010 data (Austin and Morris, 2012). The biogas slurry from the biogas plant has traditionally been used as organic fertilizer; however by taking advantages of cow digestion and bacteria hydrolysis, research on investigating the potential of biogas slurry as supercapacitor electrode materials are indispensable.

The focus of the present study was to improve the capacitance while preserving the high power density and cycling stability in supercapacitors by synthesizing mesoporous carbon derived from biogas slurry and compositing them with metal oxides (nickel cobaltite oxide- (NiCo_2O_4) and manganese dioxide.

1.2 Statement of research problem

Though carbon materials derived different biomass has been used as electrode materials for supercapacitors due to their high electrical conductivity, they possess low capacitance which leads to low energy density of the supercapacitor. In addition, the focus is utilizing carbon nanomaterials that have been derived from biomass sources (e.g coconuts shells, water hyacinth, wastes) that pose little or no environmental, public health, and food security issues. On other hand, metal oxides exhibits high capacitance but low conductivities therefore necessarily putting the need to combine mesoporous carbon derived from biomass with metal oxide for the purpose of improving the electrochemical properties of supercapacitors. For biomass with high cellulose content, there is need for hydrothermal treatment (HT) prior to carbonizing (HT is used to deconstruct cellulose network) in order to get high surface area carbon nanomaterials. HT is not only time consuming but also costly in terms of reactors and energy expended. For biogas slurry carbon precursor the deconstruction of cellulose polymeric network is partially done by bacteria prior to chemical modification.

In order to utilize this advantage, this study therefore, developed biogas slurry-derived mesoporous carbon/metal oxides composites and investigated the electrochemical behaviour for supercapacitor electrode applications.

1.3 Objectives

The main objective of the study was to investigate the applicability of biogas slurry derived porous carbon/ metal oxide composites in supercapacitor electrodes. The main objective was achieved by pursuing the following specific objectives:

- (i) To synthesize and characterize mesoporous carbon materials from biogas slurry for supercapacitor electrodes application
- (ii) To synthesize and characterize selected metal oxides (MnO_2 and NiCo_2O_4) /mesoporous carbon composites for supercapacitor electrodes application.
- (iii) To determine the electrochemical performance of the metal oxides/carbon composite electrodes.

1.4 Research questions

- (i) Which synthetic method yields the desired porous carbon from biogas slurry? Or which synthesis parameters will give the desired porous carbon from biogas slurry?
- (ii) What are the physical characteristics of synthesized mesoporous carbon/metal oxides composites?
- (iii) What is the performance of the synthesized metal oxides/carbon composite electrodes in terms of specific capacitance, cyclic stability, and electrochemical impedance?

1.5 Significance of the research

The study was intended to create knowledge/expertise in use of biogas slurry mesoporous carbon/ metal oxides composites for energy storage. The study also highlights the possibility of synthesizing porous materials from locally available carbon precursors to address the energy storage challenges in photovoltaic (PV), wind farms and PV/wind hybrid systems as well as portable electronics. The use of biogas slurry creates affordable and readily available materials for supercapacitor electrodes hence reducing the overall cost of supercapacitors.

CHAPTER TWO

Status of Biomass Derived Carbon for Supercapacitor Electrode Applications¹

Abstract

Environmental concerns and energy security uncertainties associated with fossil fuels have driven the world to shift to renewable energy sources. However, most renewable energy sources with exception of hydropower are intermittent in nature and thus need storage systems. Amongst various storage systems, supercapacitors are the promising candidates for energy storage not only in renewable energies but also in hybrid vehicles and portable devices due to their high power density. Supercapacitor electrodes are almost invariably made of carbon derived from biomass. Several reviews have focused on general carbon materials for supercapacitor electrode. This review was focussed on understanding the extent to which different types of biomass have been used as porous carbon materials for supercapacitor electrodes. It also expounds on hydrothermal microwave assisted, ionothermal, and molten salts carbonization as techniques for synthesizing activated carbon from biomass as well as their characteristics and their impacts on electrochemical performance.

2.1 Introduction

As climate change concerns escalate and the depletion of fossil fuels becomes more eminent, renewable energy sources have gained momentum as viable cost-effective and environment friendly energy sources. However, most renewable energy sources are intermittent thus need storage strategies. Currently, secondary batteries are the most used storage systems. Batteries have high energy density but low power density. However, since they store energy chemically, both the electrolyte and electrodes undergo physico-chemical changes during charging and discharging, thus their low cyclability and short lifespan. This limits their application in energy storage. Contrary to batteries, supercapacitors have high power density and cycling stability (Burke, 2000; Halper and Ellenbogen, 2006; Zhang and Zhao, 2009). Nonetheless, their utility in

¹ This chapter is based on an article published in International Journal of Electrochemistry Volume 2017 (2017), Article ID 6453420, 14 pages <https://doi.org/10.1155/2017/6453420>

energy storage is limited by their low energy density, relatively high effective series resistance, and high cost. This review focused on the status of maximum energy density attained and low cost electrode materials made so far for supercapacitor electrodes.

Supercapacitors have energy densities lower than those of lead acid and lithium ion batteries, however, they have higher power density, exhibit long life cycles, high cyclability and low safety concerns compared to secondary batteries (Burke, 2000; Winter and Brodd, 2004; Conway, 2013a). The comparison of batteries, conventional capacitors, and supercapacitors is given in Table 2.1.

Table 1: Performance comparison of different electrochemical storage systems (Miller and Burke, 2008).

Parameter/current performance	Lead Batteries	Acid Supercapacitors	Conventional capacitor
Energy density (W h kg^{-1})	30 - 40	1 - 10	< 0.1
Power density (W kg^{-1})	1000	<10000	< 100000
No. of cycles	1000	> 500000	> 500000
Charging time	1-5 h	0.3 - 30 s	10^{-3} - 10^{-6} s
Discharging time	0.3 - 3 h	0.3 - 30 s	10^{-3} - 10^{-6} s
Charging/Discharging Efficiency (%)	70 - 85	85 - 98	95
Operating temperature ($^{\circ}\text{C}$)	- 20 -100	- 40 - 65	- 20 - 65

Current researches focus on increasing the energy density of supercapacitors. Supercapacitors consist of electrode materials, separators, and electrolytes. The energy density of a supercapacitor can be increased by increasing both specific capacitance (C) and operating voltage (V) window (equation 2.1) while the power density can be increased by increasing operating voltage (V) and reducing the equivalent series resistance (R) (equation 2.2). The voltage window can be increased by a good choice of electrolyte while the specific capacitance of the supercapacitor can be improved by either finding new electrode materials or optimizing the existing materials (Conway, 2013a) in terms of interconnected porosity, electrical conductivity, and surface area among others.

$$E = \frac{1}{2} CV^2 \quad (2.1)$$

$$P_{\max} = \frac{V^2}{4R} \quad (2.2)$$

In principal, supercapacitors store energy based on two capacitive behaviours: Electrical Double Layer (EDL) capacitance and pseudocapacitance. While the former is due to electrostatic interaction, pseudocapacitance is due to faradic phenomenon involving fast and reversible electrochemical reactions. In pseudocapacitance, the redox reactions are between the electrolyte and the electrode materials. The product of redox reactions are therefore electrons which are then transferred through electrode/electrolyte interfaces (Conway, 2013b). The EDL has the advantage that electrochemical kinetics is not limited by polarization resistance and no swelling of the active materials is experienced. The energy is stored in two porous electrodes with current collector on each electrode; the stored energy is released when charges accumulated at the electrode discharge as shown in Fig. 2. The number of charges stored in the electrode is assumed to be proportional to the surface area (A) of the electrode and inversely proportional to the effective thickness d of the EDL as per equation 2.3, where ϵ_r and ϵ_0 represent the dielectric constant and permittivity of free space. The energy stored is proportional to the amount of charge stored. Therefore, materials with high surface area are regarded as good candidates for supercapacitor electrode. However, the simple and direct proportionality does not hold as the assumption that submicropores are not involved in the formation of EDL is not true, thus models in equations 2.4 and 2.5 describe the specific capacitance for micropores and mesopore carbon electrodes, respectively (Huang *et al.*, 2008) in which b is pore radius, a_0 is the effective radius of counter ions and d is the distance of the approaching ions to the surface of the electrode.

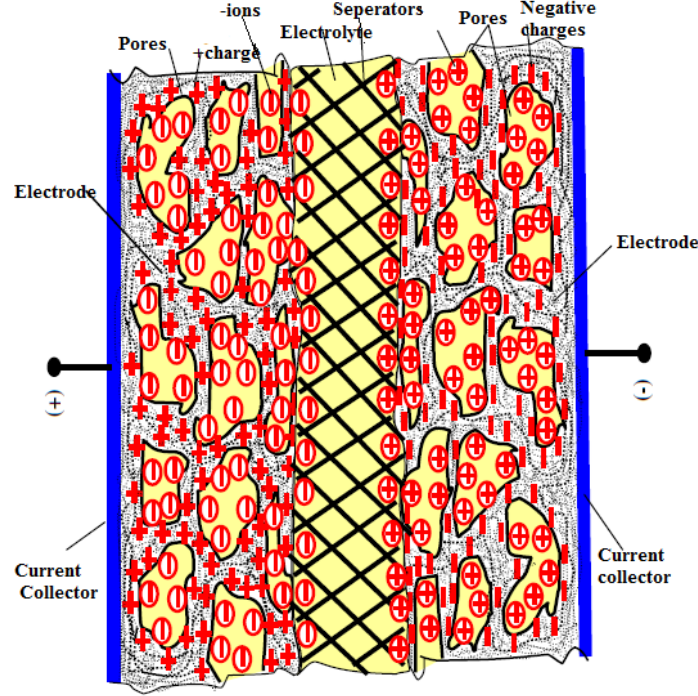


Figure 2: Schematic expression of a supercapacitor cell (Reproduced with the permission from the Author (Obreja, 2008)).

$$C = \frac{\epsilon_r \epsilon_0}{d} A \quad (2.3)$$

$$C = \frac{\epsilon_r \epsilon_0}{b \ln \left[\frac{b}{b-d} \right]} A \quad (2.4)$$

$$C = \frac{\epsilon_r \epsilon_0}{b \ln \left(\frac{b}{a_0} \right)} A \quad (2.5)$$

The improvement of supercapacitor performance (e.g high specific capacitance and high cyclic stability) can be attained through discovery of new electrode materials (with improved microstructures and textures), understanding of ions behaviour in small pores, and designing hybrid system by combining faradic and capacitive electrodes.

2.2 Materials for supercapacitor electrodes

Various materials have been investigated as electrode materials for supercapacitors, for instance, conducting polymers, porous materials, and metal oxides. The focus has been to optimize parameters like pore size and high surface area of electrode materials for a given electrolyte, determine the performance of supercapacitor in terms of power density and energy storage

capability (Simon and Gogotsi, 2008). High surface area is important because the energy in electrochemical storage systems is stored on the surface while the pores size facilitates the storage and transport of charges. Carbon materials are more attractive because they are available in different forms (such as fibers, powders, nanotubes, and nanospheres) and are rich in dimensionality (Zhang and Zhao, 2009).

The microstructure and surface chemistry of carbon can be adjusted easily thus altering the electrochemical performance of the material (Béguin *et al.*, 2014). It has been reported further that carbon materials based electrodes have reasonably high electrical conductivity, high thermal stability, excellent corrosion resistance, tailorable pore distribution, relatively high surface area, low cost, and satisfactory compatibility with a number of materials in making composites (Frackowiak and Beguin, 2001; Zhang and Zhao, 2009).

2.2.1 Activated Carbons

Porous carbon is prepared through various methods depending on the intended application. Commonly used methods are activating the carbon materials either chemically or physically. Activated carbon is synthesized through carbonization of carbon precursor followed by activation at temperature around 600-800 °C in an inert atmosphere. The type of carbon precursor, among other factors, determines the properties of the activated carbons.

Physical activation involves two processes; first, pyrolysis of the carbon precursor at temperatures between 400-1000 °C in an inert atmosphere, second, gasification where the porosity and surface area are developed using oxidizing gases such as carbon dioxide or air and steam between 700-1200 °C (Bouchelta *et al.*, 2008; Sun and Chun Jiang, 2010; Sekirifa *et al.*, 2013). Pyrolysis is intended to remove all volatile materials in the precursor while gasification opens some closed pores by burning away the tar-like pyrolysis product within the pores. Furthermore, the active sites increase as more organics are burned away by oxidizing agent (Sevilla and Mokaya, 2014).

In contrary, chemical activation involves the use potassium hydroxide (Babel and Jurewicz, 2004; Olivares-Marín *et al.*, 2006; Sudaryanto *et al.*, 2006; Bagheri and Abedi, 2009; Wang and Kaskel, 2012), sodium hydroxide (Tseng, 2006, 2007) , phosphoric acid (Laine and Calafat,

1989; Molina-Sabio *et al.*, 1995; Liu *et al.*, 2010b), zinc chloride (Babel and Jurewicz, 2004; Subramanian *et al.*, 2007; Tan *et al.*, 2008), nitric acid, and sulfuric acid among other chemicals (Ademiluyi and David-West, 2012). Phosphoric acid and zinc chloride act as dehydrating agent while potassium hydroxide is an oxidant. In comparison to physical activation method, chemical activation has the following advantages; (1) the pores are well developed and pore size is controllable, (2) materials with high surface area are produced, (3) high carbon yield, (4) involves only one step, and (5) lower pyrolysis temperature (Sevilla and Mokaya, 2014). For energy storage applications such as supercapacitors, the first two advantages dictate the use of chemical activation.

For KOH activation which is mainly applied to supercapacitor electrode materials preparation, the ratio of alkali/carbon varies from 1:1 to 5:1 depending on the concentration of the impregnating solution (Babel and Jurewicz, 2004). The excess KOH is removed by suspending the activated carbon in 0.1 M HCl solution then washed with double distilled water until pH of 7 is achieved. Samples are then oven dried ready to be used for electrochemical testing and other characterizations. Activated carbons sometimes exhibit a high Brunauer-Emmet-Teller (BET) surface area of more than $2500 \text{ m}^2 \text{ g}^{-1}$ and pore volume close to $2 \text{ cm}^3 \text{ g}^{-1}$ (Simon *et al.*, 2013). The majority of pores in the activated carbon are micropores and only small number of mesopores. This is because at higher temperatures, most mesopores break and the pore diameter decreases (Pagketanang *et al.*, 2015).

Due to the availability, low cost, and the ability to become highly porous after carbonization, different biomass feedstocks have been used as precursors for carbon. Understanding the biomass derived porous carbon materials and their properties are of importance in order to match the carbon properties with that of supercapacitors. Porous carbon materials are classified depending on their pore width; those $< 2 \text{ nm}$ pore width are classified as microporous, 2 to 50 nm mesoporous while those with pore width greater than 50 nm classified as macroporous (Liang *et al.*, 2008; Conway, 2013a). For supercapacitors application, both micropores and mesopores play an important role. Micropores are important in storing charges while mesopores store facilitate charge transfer. The reported surface areas and capacitances exhibited by different biomass derived carbon materials are as presented in Table 2.2. Generally, the higher the specific surface area of activated carbon, the higher the active surface area. However, despite high

specific surface areas attained for activated carbons that is around 2500 to 3000 m² g⁻¹, some activated carbons exhibit low specific capacitance as depicted in Table 2.2. This might be due to wide pore size distributions, average pore size, type of the electrolyte used, scan rate, mass or surface area of the electrode. Small pore sizes (below 0.68 nm) limit the electrolyte from accessing the entire active surface area of activated carbon (Largeot *et al.*, 2008). Though it is suggested that the specific capacitance and BET surface area of activated carbon have close correlation, it is not the case for all carbon precursors as shown in Fig. 3. The relationship between surface area and capacitance is not always obvious due to the fact that capacitance is contributed by other factors such as pore size, electrical conductivity, and pore distribution and interconnectivity (Shi, 1996; Largeot *et al.*, 2008).

The increase in the fraction of pore size which cannot be accessed by the organic electrolyte (when the average pore size is below 0.68 nm) is expected to decrease the capacitance (Largeot *et al.*, 2008), however, an anomalous behavior is observed where the capacitance increases with the pores having pore size of less than 1 nm with acetonitrile as the organic electrolyte (Chmiola *et al.*, 2006). Fig. 3 shows that there is no direct correlation between capacitance and the pore size of the electrode materials. Actually, many factors have a huge impact on the capacitance; the materials surface chemistry, method of preparing electrodes, the electrolyte used, and electrode testing method.

Table 2: The capacitance, energy density, and surface area of porous carbon derived from different plant wastes.

Precursor	Activation agent	^a (°C)	^b (m ² g ⁻¹)	Capacitance (F g ⁻¹)	^c Wh kg ⁻¹	Stability	^d (A g ⁻¹)	Electrolyte	Reference
Waste coffee beans	ZnCl ₂	900	1019	368*	20		5	1 M H ₂ SO ₄	(Rufford <i>et al.</i> , 2008)
Sunflower seed shell	KOH	800	1235	144*	4.8		10	30 wt% KOH	(Li <i>et al.</i> , 2011b)
Banana fibers	ZnCl ₂	800	1097	74**		88 (500cycles)	0.5	1 M Na ₂ SO ₄	(Subramanian <i>et al.</i> , 2007)
Sugar cane baggasse	ZnCl ₂	900	1788	300**	10	83%(5000cycles)	0.05-50	1 M H ₂ SO ₄	(Rufford <i>et al.</i> , 2010)
Coffee-shells	ZnCl ₂	900	842	158**	10		1	6 M KOH	(Jisha <i>et al.</i> , 2009)
Neem leaves			1230	400*	55		0.5	1 M H ₂ SO ₄	(Biswal <i>et al.</i> , 2013)
Corn-grains			3420	257**	-			6.M KOH	(Balathanigaimani <i>et al.</i> , 2008)
Sorghum pith	NaOH		35	320**	-		10	1 M H ₂ SO ₄	(Xia <i>et al.</i> , 2012)
Cotton stalk	H ₃ PO ₄	800	1481	114		95.3(500 cycles)	2	1 M Et ₄ NBF ₄	(Chen <i>et al.</i> , 2013)
Coconut kernel	KOH	600	1200	173**	-			1 M H ₂ SO ₄	(Wang <i>et al.</i> , 2012b)
Rice husk	ZnCl ₂		1442	243**	-			6 M KOH	(He <i>et al.</i> , 2013b)
Bamboo	Steam		1025	60*	-	91% (3000)		1 M Et ₄ NBF ₄	(Kim <i>et al.</i> , 2006)
Recycled paper	KOH		416	180**	-	97 (at 2300 cycles)	2	6 M KOH	(Kalpana <i>et al.</i> , 2009)
Coconut shell	Steam	800	1532	228**	38.5	93% (2000 cycles)	5	6 M KOH	(Mi <i>et al.</i> , 2012a)
Pistachio shells	KOH/CO ₂	780	2145	122**	-	77 (200 cycles)		0.5 M H ₂ SO ₄	(Hu <i>et al.</i> , 2007)
Waste tea leaves	KOH		2841	350**	-	92% at 2000 cycles	1	KOH	(Peng <i>et al.</i> , 2013)
Water hyacinth	KOH/microwave assisted		1010	179.6**	-	94% (1000 cycles)		30 wt% KOH	(Kurniawan <i>et al.</i> , 2015)
Water hyacinth	ZnCl ₂		579.94	472**	9.5			1 M H ₂ SO ₄	(Senthilkumar <i>et al.</i> , 2013)
Water hyacinth	KOH	800	1308	273**	7.24	75% (10000 cycles)	1	6 M KOH	(Wu <i>et al.</i> , 2016)
Celtuce leaves	KOH		3400	273**	-	93.1%(1600 cycles)			(Wang <i>et al.</i> , 2012b)
Tobacco Stem	KOH		3326.7	190*	-			1 M LiPF ₆ -EC/DMC/DEC	(Xia <i>et al.</i> , 2012)
Tobacco rods	KOH	800		286.6**	31.3			6 M KOH	(Zhao <i>et al.</i> , 2016)
Hemp back	KOH	800	2287	106*	19		10	M***	(Wang <i>et al.</i> , 2013a)
Argan seed shells	KOH		2100	335**	-	93% (1000 cycles)	1	1 M H ₂ SO ₄	(Elmouwahidi <i>et al.</i> , 2012)
Brussel sprouts	KOH	800	2410	255**	-	99.5 (5000cycles)	0.5	6 M KOH	(Li <i>et al.</i> , 2016)

^a Activation temperature, ^b BET surface area, ^c Energy density, ^d current density, * two cell electrode, ** three cell electrode and M*** (1-butyl-1-methylpyrrolidinium bis- (trifluoromethylsulfonyl)imide)

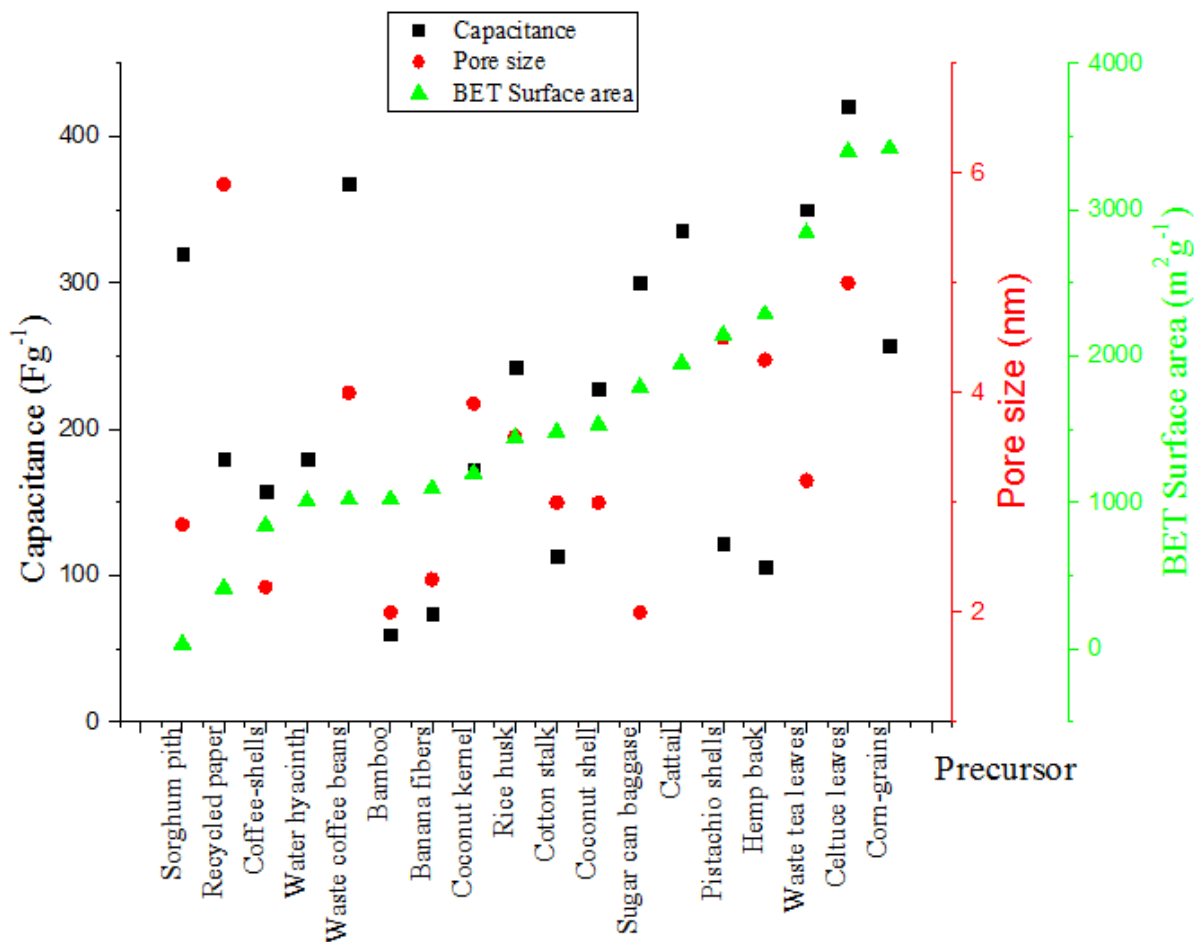


Figure 3: Variation of reported capacitance, pore size, and BET surface area of activated carbon materials derived from different plant precursors.

Apart from plant wastes, animal wastes have been studied as potential carbon precursors for supercapacitors electrode. To date, cow dung (Bhattacharjya and Yu, 2014), animal bones (Huang *et al.*, 2011), chicken egg membranes (Li *et al.*, 2012b) and human hair (Si *et al.*, 2013; Qian *et al.*, 2014) have been reported in the literature. The physical and electrochemical properties of these wastes are presented in Table 2.3.

Table 3: The capacitance and surface area of porous carbon derived from different animal wastes.

Precursor	Activating agent	Activating Temperature (°C)	BET (m ² /g)	Specific Capacitance (F/g)	Current Density (A/g)	Cyclic Stability	Electrolyte	Reference
Cow dung	KOH	800	2000	117*	1	85% (at 1000cycles)	Et ₄ NBF ₄	(Bhattacharjya and Yu, 2014)
Animal bones	HNO ₃	-	2157	130	100	-	-	(Huang <i>et al.</i> , 2011)
Bovine cortical bones		-	1383	134**			2 M KNO ₃	(Goodman <i>et al.</i> , 2013)
Chicken egg membrane	air	300	221	297* 284*	4	96% (at 10000 cycles)	1 M KOH 1 M H ₂ SO ₄	(Li <i>et al.</i> , 2012b)
Human hair	KOH	900	1306	304**	1	98% (at 20000)		(Qian <i>et al.</i> , 2014)
Fish scale			2273	109	10		-	(Chen <i>et al.</i> , 2010b)
Chicken feathers	KOH	800	1839	168**	10	83% (at 5000cycles)	1 M H ₂ SO ₄	(Wang <i>et al.</i> , 2013c)
Egg yolk	KOH	900	2277.79	220.37*	20	97.7 (at 2000 cycles)	6 M KOH	(Li <i>et al.</i> , 2015)

*Two electrode cell, ** Three electrode cell

In order to determine how fast energy can be stored in a unit volume of materials, volumetric capacitance is of importance. Factors affecting the volumetric capacitances were reviewed by Wang and co-workers (Wang *et al.*, 2016c). Surprisingly, a good number of studies overlook these parameters when evaluating the suitability of materials for supercapacitor electrode application. Besides, few authors take into account the volumetric capacitance for characterizing the biomass derived carbon. Xie *et al.*, (2016), composited corn straw and soy protein to obtain a surface area of $1412.9 \text{ m}^2 \text{ g}^{-1}$ with gravimetric and volumetric capacitances of 321.1 F g^{-1} and 213 F cm^{-3} , respectively, at 20 A g^{-1} with 6 M KOH as the electrolyte (Xie *et al.*, 2016). When soybeans was chemically activated after carbonization and tested for supercapacitor electrodes gravimetric and volumetric capacitances of 260 F g^{-1} and 210 F cm^{-3} , respectively, were obtained with $1 \text{ M H}_2\text{SO}_4$ (Ferrero *et al.*, 2015). In the same study, gravimetric and volumetric capacitances of 176 F g^{-1} and 102 F cm^{-3} , respectively, were obtained with $1 \text{ M Li}_2\text{SO}_4$ electrolyte. It was further revealed that volumetric capacitance decreased with activating temperature increase, contrary to the gravimetric capacitance trend. The low volumetric capacitance at high temperature may be caused by low conductivity of biomass derived carbons as the high surface area decreases the density. In another study Eukaryotic organism (*Auricularia*) as precursor afforded porous carbon materials with bulk density of 0.96 g cm^{-3} , surface area of $1103 \text{ m}^2 \text{ g}^{-1}$, volumetric capacitance of 360 F cm^{-3} , and cyclic stability of 99% after 10000 cycles (Long *et al.*, 2015a).

The differences in the reported capacitance are also attributed to the method of testing. It has been reported that the three electrode cell gives higher capacitance results compared to its two electrode counterpart (Stoller and Ruoff, 2010), thus there is need to establish standardized best practice for determining the capacitance of a material. Although the testing method may be the same for different studies, differences in mass loading, electrode thickness, type and amount of binder, and type of current collector have huge impact on the capacitance obtained.

The presence of surface functionalities and heteroatoms such as O and N on carbon also play an important role in the pseudocapacitance behavior of the electrode (Seredych *et al.*, 2008; Zhao *et al.*, 2015). It has been reported that the heteroatom functional groups of biomass derived carbon enhances volumetric capacitance. For example, a high volumetric capacitance of 468 F cm^{-3} , high packing density of 1.1 g cm^{-3} and capacitance retention of 91% after 10000 cycles were

achieved when functionalized porous carbon was synthesized from soybeans (Long *et al.*, 2015b). Oxygen comes from both the activation and biomass itself, while nitrogen can come from the biomass or introduced into the carbon through doping (Cheng and Teng, 2003). It has been reported that the capacitance of O and N containing carbonized chicken egg-shell membrane is 297 Fg^{-1} with cyclic efficiency of 97% after 10000 cycles (Li *et al.*, 2012b), while the activated carbon from the same precursor has specific capacitance of 203 Fg^{-1} despite the fact that the specific surface area was 7 times higher than carbonized chicken egg-shell membrane. It has also been reported that oxygen and nitrogen in activated carbon enhances the specific capacitance differently. While oxygen rich activated carbon exhibits lower capacitance because the electrolyte diffusion into pores is hindered by carboxyl surface, the nitrogen rich one exhibits higher capacitance due to additional faradaic reaction and improved electronic conductivity contributed by nitrogen (Elmouwahidi *et al.*, 2012; Li *et al.*, 2013). Furthermore, it has been shown that the adsorption and transport of electrolyte ions is enhanced by doping activated carbon with heteroatom such as sulfur (Seredych and Bandosz, 2013; Zhang *et al.*, 2014b; Zhao *et al.*, 2015). Heteroatom increases the wettability of the electrode, which in turn increases the capacitance. Thus studies on doping different heteroatoms into the activated carbon are emphasized.

In terms of synthetic methods, microwave assisted heat treatment has been used to synthesize porous carbon for supercapacitor applications. It is a facile, controllable, fast, and energy saving technique. When carbon xerogel was activated chemically using microwave radiation, microspores and mesopores were produced at a time range between 6-30 min (Calvo *et al.*, 2013). Although microwave radiation method produces well modified surface chemistry of activated carbons, it causes significant reduction in micropore volume and size (Nabais *et al.*, 2004; Puligundla *et al.*, 2016).

In addition to microwave, hydrothermal carbonization (HTC) has also been employed to produce porous carbon for supercapacitor electrodes. In this method, a mixture of water and carbon precursor are thermally treated at temperature ranges of 150-300 °C and 300-800 °C for low and high temperature HTC, respectively (Sevilla and Fuertes, 2009; Zhang *et al.*, 2015b). Apart from high solid carbon yield, the method also reduces the oxygen and hydrogen content (Kalderis *et al.*, 2014; Zhang *et al.*, 2015a) and produces materials with very high BET surface area. Jain and

coworkers obtained BET and mesopore areas of up to 2440 and 1121 m² g⁻¹, respectively, after hydrothermal treatment of coconut shells with ZnCl₂ and H₂O₂ at temperature of 275 °C (Jain *et al.*, 2015b). When the same material was chemically activated using ZnCl₂ at 500 °C for 3 h (Azevedo *et al.*, 2007), BET surface area of 1266 m²g⁻¹ was obtained. Elaigwu and Greenway (2015) compared the chemical and structural properties of carbon derived from *prosopis africana* waste plant material prepared by conventional hydrothermal and microwave assisted hydrothermal carbonization. They found that microwave assisted hydrothermal carbonization was faster in decomposing the *prosopis africana* as the degree of structure alteration was achieved within a short time compared to the conventional approach (Elaigwu and Greenway, 2015).

The comparison of the methods is shown in Table 2.4 where CPS represents combined pyrolysis and steam activation, OHCZ represents optimal hydrothermal treatment and chemical activation with ZnCl₂, CZ represents chemical activation with ZnCl₂ and CZP represents chemical activation with ZnCl₂ followed by physical activation. It is worth mentioning that the precursor for all the above-mentioned methods is the same (coconut shell).

Table 4: The preparation method and properties of porous carbon derived from coconut shells.

Preparation method	BET surface area (m ² g ⁻¹)	Capacitance (F g ⁻¹)	Energy Density (W h kg ⁻¹)	Reference
CPS	1559	228	38	(Mi <i>et al.</i> , 2012b)
OHCZ	2440	246	8.5	(Jain <i>et al.</i> , 2015a)
CZ	1266	-	-	(Azevedo <i>et al.</i> , 2007)
CZP	2114	-	-	(Azevedo <i>et al.</i> , 2007)

The porosity of the carbon is also influenced by type of activation, for example, when firewood and pistachio were carbonized and activated using steam and KOH, KOH activated carbon had 9.2 - 15.3% mesopores while steam activated carbon had 33.3 - 49.5% (Wu *et al.*, 2005). On the

other hand, the specific capacitance has been reported to increase with the increase in mesopore content (Gryglewicz *et al.*, 2005).

Electrochemical performance of different biomass derived carbon materials has also shown strong correlation with capacitance, morphology, and the method used to prepare the carbon. For instance, water hyacinth (WH) has been used to prepare porous carbon by different authors, however, their results differ probably due to the methods, morphology and/ or surface area obtained (Senthilkumar *et al.*, 2013; Syarif and Pardede, 2013; Kurniawan *et al.*, 2015).

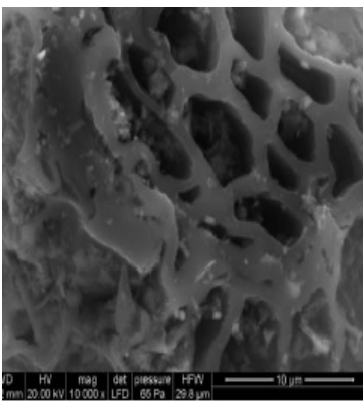
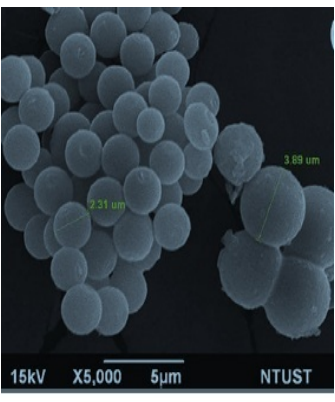
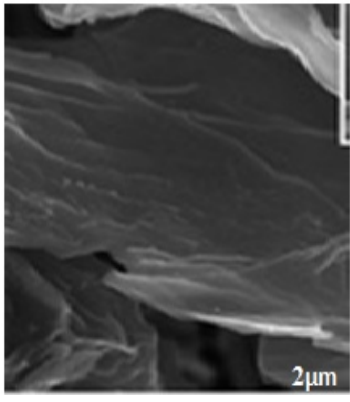
<p>(a)</p>  <p>SEM micrography for water hyacinth derived carbon (Senthilkumar <i>et al.</i>, 2013).</p>	<p>(b)</p>  <p>SEM images of water hyacinth derived carbon activated using $ZnCl_2$ (Kurniawan <i>et al.</i>, 2015).</p>	<p>(c)</p>  <p>SEM images for water hyacinth activated with KOH (Wu <i>et al.</i>, 2016)</p>
--	---	--

Figure 4: Morphologies of porous carbon derived from water hyacinth through different routes.

Senthilkumar and co-workers activated WH derived carbon using $ZnCl_2$ and obtained porous carbon with no particular shape (Fig. 4a), that showed specific capacitance of 472 F g^{-1} in aqueous electrolyte H_2SO_4 (Senthilkumar *et al.*, 2013). Kurniawan and co-workers obtained microsphere morphology (Fig. 4b) after subjecting WH to subcritical water carbonization followed by KOH activation and microwave treatment. The specific capacitance of these

materials was 179.6 F g^{-1} in aqueous electrolyte (Kurniawan *et al.*, 2015). From the same carbon precursor, Syarif and Pardede developed porous carbon through hydrothermal treatment followed by microwave pyrolysis (Syarif and Pardede, 2013). The carbon showed bead chain and waffle structure morphology with open cavities. The capacitance obtained for these materials in aqueous electrolyte (H_2SO_4) was 0.0218 F g^{-1} when no conductive and activating agent was added. The capacitance increased 10 times when graphite was added to the carbon in the ratio of 3:7. Carbon sheets (Fig. 4c) were produced by Wu and co-workers through acid (HCl) treatment and pyrolytic carbonization, followed by KOH activation of water hyacinth biomass (Wu *et al.*, 2016). These carbon sheets afforded specific capacity of 273 F g^{-1} at current density of 1 A g^{-1} .

It was further shown that the capacitance of water hyacinth derived carbon electrode increased from 472 to 912 F g^{-1} when potassium iodide (0.08 M KI) was added to 1 M H_2SO_4 electrolyte signifying the effect of electrolyte (Senthilkumar *et al.*, 2013). The addition of KI in the electrolyte enhanced the capacitance because KI can produce redox pairs ($3\text{I}^-/\text{I}_3^-$, $2\text{I}_3^-/3\text{I}_2$ and others) during electrochemical processes, which in turn could easily access the small micropores and mesopores.

Through hydrothermal treatment, interconnected graphitic carbon nanosheets can also be produced. For example, Wang and co-workers developed nanosheets from hemp back fibers with high specific surface area of $2287 \text{ m}^2 \text{ g}^{-1}$ and 72-92% capacitance retention at current density of 100 A g^{-1} (Wang *et al.*, 2013a). The study also revealed that the materials were stable at different temperatures 20, 60, and $100 \text{ }^\circ\text{C}$.

Ionothermal carbonization is another method of synthesizing porous carbon from biomass where only one step is involved. The method involves treating the carbon precursor with ion liquids (IL) in quasi- solvothermal condition (Ma *et al.*, 2010). The hydrogen bond is formed between (ILs) and solutes which then enhance the solubility of carbohydrates and sugars. The ionic liquids possess high chemical and thermal stability, low melting point, electrical and ionic conductivity, and negligible vapor pressure. This method has been reported to produce carbon with high surface area and large pore volume (Chang *et al.*, 2015). A high surface area ($2160 \text{ m}^2 \text{ g}^{-1}$) and total pore volume of $1.74 \text{ cm}^3 \text{ g}^{-1}$ were obtained when carbon was synthesized from glucose (Pampel *et al.*, 2016). In this study KCl-ZnCl₂ system molar ratio was varied to act as

template/solvent during carbonization, it was further revealed the higher content of KCl increased the pore size and surface area. The gravimetric capacitance obtained was 206 F g⁻¹. Lin *et al.*, (2016) synthesized microporous and mesoporous carbon from fructose through one step ionothermal method using iron chloride (Lin *et al.*, 2016). Surface area of 1200 m² g⁻¹, pore volume of 0.8 cm³ g⁻¹ and specific capacitance of 245 F g⁻¹ at current density of 1 A g⁻¹ were obtained. In the study different masses of fructose were dispersed in 10 mL of 1-butyl-3-methylimidazolium tetrachloroferrate [Bmim][FeCl₄], which was used as template, solvent and catalyst. [Bmim][FeCl₄] has the advantage that it can be reused after recovery. Other biomass derived structured carbon was produced ionothermally from carbohydrates (Xie *et al.*, 2011), sugar baggasse (Zhang *et al.*, 2014c) and bamboo (Guo and Fang, 2014). However, these carbons were not tested for supercapacitor applications.

Table 5: Specific capacitances and surface area of porous carbon synthesized through molten salt carbonization of different biomass.

Precursor	Salt	Carbonization temperature	Surface area (m ² g ⁻¹)	Specific capacitance (F g ⁻¹)	Current density (A g ⁻¹)	Electrolyte	Reference
Firwood	Na ₂ CO ₃ -K ₂ CO ₃	850	818	189	0.5	1 M H ₂ SO ₄	(Wang <i>et al.</i> , 2016a)
Chitosan from Shells of shrimps	ZnCl ₂	600	1582	256	0.5	6 M KOH	(Deng <i>et al.</i> , 2015)
Peanut shells	Na ₂ CO ₃ -K ₂ CO ₃	700		160	1	1 M H ₂ SO ₄	(Yin <i>et al.</i> , 2014)
Bamboo shells	Na ₂ CO ₃ -K ₂ CO ₃	850	843	204	1	1 M H ₂ SO ₄	(Lu <i>et al.</i> , 2016a)
Boiled coffee beans	Na ₂ CO ₃ -K ₂ CO ₃	800	436	161	0.5	1 M MeEt ₃ NBF ₄	(Lu <i>et al.</i> , 2016b)
	CaCl ₂	850	550	93.4	0.4		

Molten salt carbonization (MSC) is another method of synthesizing porous carbon from biomass where the molten salt cracks the large molecules of biomass. In MSC, the salt involved is melted

and then biomass is immersed into the molten salt and carbonized at temperature greater than 400 °C in inert atmosphere. After carbonization, the furnace is cooled to room temperature and the product washed with HCl and distilled water in order to remove salts within the product. It is reported that the size of the particles of the biomass alters the yield (Liu *et al.*, 2014b). Table 2.5 shows different biomass carbonized in different salts and their corresponding gravimetric capacitances and specific surface area. It is difficult to tell the best biomass or salt because the carbonization temperature and electrolyte for electrochemical testing were different.

2.2.2 Carbon aerogel derived from biomasses

Carbon aerogel is another form of carbon used in supercapacitor electrodes whereby the porous carbon is produced through pyrolysis of organic aerogels (Pandolfo and Hollenkamp, 2006). The porosity is a result of a combination of interconnected colloidal particles. The porous carbon materials could be composites, monoliths, powders, microspheres or thin films. The aerogels carbon materials have been reported to exhibit higher surface area than activated carbon (Fischer *et al.*, 1997). Carbon fiber aerogels with surface areas ranging from 1536 to 2436 m² g⁻¹ and pore size range between 1.0 - 4.0 nm, exhibited high specific capacitance of 282 F g⁻¹ (1 A g⁻¹) in 6 M KOH electrolyte (Wang *et al.*, 2013a; Cheng *et al.*, 2016).

A green technology of fabricating sponge-like carbonaceous hydrogels/aerogels from water melon was developed by Wu and coauthors (Wu *et al.*, 2013). The study revealed that watermelon could be polymerized and carbonized to form carbonaceous mesosphere and nanofibres during hydrothermal reaction.

Moreover, cellulose from baggasse has been utilized as the raw materials for carbon aerogel. Two procedures were followed; firstly, cellulose was dissolved in a solvent mixture of NaOH/urea/H₂O and super cooled in -12 °C. Secondly, the gels were regenerated in water at room temperature and then frozen at -80 °C (Hao *et al.*, 2014). The synthesized aerogels exhibited large channels with average diameter in the range of 50 -100 nm. The specific capacitance of the assembled supercapacitor was 142.1 F g⁻¹ at current density of 0.5 A g⁻¹.

In another study, the 3D N-doped carbonaceous aerogels were produced through one pot hydrothermal synthesis using the soft tissue biomass of watermelon as a source of aerogel. The method produced a specific capacitance of 281 F g⁻¹. It has been reported that nitrogen doped

porous carbon possesses higher specific capacitance than the undoped porous carbon because of pseudocapacitive behavior of nitrogen functional groups (Ren *et al.*, 2014).

2.2.3 Metal oxides and carbon composites

The energy density of a carbon material is a function of both capacitance and electrical conductivity exhibited by the electrode. Though activated carbons have low capacitive behavior their high electrical conductivity qualifies them for supercapacitor electrode. On the other hand, transition metal oxides (TMO) have high capacitance but low conductivity. Metal oxide electrodes have poor cyclic stability due to the cracks caused by the strain in the metal oxide during charging and discharging processes (Yang, 2012).

Studies on the application of ruthenium oxide (RuO_2) (Wu *et al.*, 2015), manganese (IV) oxide (MnO_2), cobalt (II, III) oxides (Co_3O_4), nickel oxide (NiO) (Wu *et al.*, 2007), molybdenum trioxide (MoO_3), molybdenum (IV) oxide (MoO_2), and vanadium nitride (VN) as the electrochemical active materials has been conducted (Zhang *et al.*, 2013b). Though RuO_2 has excellent capacitance, its high cost, toxic nature, and low porosity limits its application. Nickel oxide, cobalt oxide, and manganese dioxide are inexpensive thus the huge research interest in improving their electrochemical performance.

Efforts have been made to composite biomass derived carbon and metal oxides so as to capture the strength of the two in increasing the energy density without sacrificing the high power density. An important consideration related to porous carbon/ metal oxide is their performance in terms of capacitance, stability, power and energy densities. Sawdust derived carbon was directly composited with FeCl_3 and TiCl_2 and the composite was oxidized in concentrated nitric acid (Syarif *et al.*, 2011). From this study it was revealed that the metal oxide loading and surface functionalities affect the voltammograms shapes. Moreover, with exception of RuO_2 , the conductivity of other transition metal oxides is poor resulting to low power and energy density. This is because the IR loss is very large at high current density caused by both the charge transfer resistance of the electrode and sheet resistance (Zhi *et al.*, 2013).

Based on its pseudocapacitive behavior, RuO_2 has been found to be an excellent electrode. RuO_2 -carbon composite prepared by Lin *et al.*, exhibited specific surface area of $520 \text{ m}^2 \text{ g}^{-1}$ and

specific capacitance of 256 F g^{-1} at current density 1 A g^{-1} (Lin *et al.*, 1999) . In another study, colloidal method was used to prepare a nanostructured composite of RuO_2 and carbon. The specific capacitance of $\text{RuO}_2/\text{carbon}$ composite electrode (40% RuO_2) was reported to be 407 F g^{-1} as calculated from cyclic voltammetry. When the contribution of double layer capacitance resulting from carbon was subtracted, the specific capacitance of $\text{RuO}_2 \cdot \chi \text{H}_2\text{O}$ was approximately 863 F g^{-1} . The volumetric capacitance of the composite increased as the weight of the RuO_2 increased to 40% wt, then dropped due to increased particle size of the RuO_2 (Kim and Popov, 2002). However, due to the high cost of RuO_2 , its practical application in supercapacitors is limited thus exploitation of alternative metal oxides is very necessary.

The specific area and specific capacitance has been reported to increase when carbon is composited with metal oxide. Specific surface area of NiO–carbon composite increased from $150 \text{ m}^2 \text{ g}^{-1}$ for NiO to $700 \text{ m}^2 \text{ g}^{-1}$ when NiO was composited with carbon, while the specific capacitance increased from 20 to about 100 F g^{-1} (Lota *et al.*, 2010).

Apart from activated carbon being composited with metal oxides, attempts have been made to composite aerogels made from bagasse with Fe_2O_3 . The aerogel/ Fe_2O_3 composite exhibited high specific capacitance of 333.1 F g^{-1} at current density of 1 A g^{-1} with excellent cyclic stability of 96% at 1000 cycles (Wu *et al.*, 2013). The variation of specific capacitance, energy density, and power density of different composites can be seen in Table 2. 6.

Table 6: The capacitance, energy density, and stability of different composites.

Carbon precursor	Composite	Method of preparation	Capacitance (F g^{-1})	Energy density (Wh kg^{-1})	Power density (W kg^{-1})	Stability	Current density (A g^{-1})	Reference
Flax textiles	MnO_2 nanosheet/carbon cloth	In situ	683.73	46.54	45500	94% (1000 cycles)	2	(He and Chen, 2015)
Kenaf Stem	Porous carbon/ MnO_2	-	416	17.3	198-3175	86% (1000 cycles)	16	(Wang <i>et al.</i> , 2014a)
Mollusc shell	Macroporous carbon/ NiCo_2O_4	-	1696	8.47		88% (2000 cycles)	-	(Xiong <i>et al.</i> , 2014)

It has been shown that the composition with lowest metal oxide content displays the highest capacitance. This is attributed to the fact that at high metal oxide content, the fraction of accessible active surface area is low and the resistance is high.

2.2.4 Activated carbon/ conducting polymers

Conducting polymers have also been used as electrode materials for supercapacitors due to their good electrochemistry, simplicity in doping, and easy preparation. However, during the charge-discharge cycles, the sites in polymers responsible for redox are not stable thus resulting to low life cycle of the conducting polymers electrode. Qin and coworkers coated activated carbon with polyaniline (PANI) through polymerization of aniline using cyclic voltammetry. It was revealed that the PANI electrode and PANI-activated carbon composite maintained cyclic stability of 65 and 92%, respectively, at 50 cycles and high specific capacitance of 587 F g^{-1} (Qin *et al.*, 2008).

Lin and Teng (2003) demonstrated that the capacitance of a carbon electrode can be increased by at least 50% if 5 wt. % of polyaniline is deposited on the carbon (Lin and Teng, 2003). It has been further reported that the composite made from natural bamboo and polyaniline attained high energy density 47.5 Wh kg^{-1} , demonstrating that the composites was a good candidate for supercapacitor (Li *et al.*, 2012a).

2.2.5 Activated carbon/ carbon nanotubes composites

The electrochemical performance of activated carbon derived from biomass when composited with carbon nanotube (CNTs) has also been investigated. A coconut shell derived activated carbon was composited with CNTs. The capacitance of the coconut-derived activated carbon alone was 92 F g^{-1} while that of carbon nanotube alone was 25 F g^{-1} . However, when the two were composited, the capacitance of 88 and 50 F g^{-1} at 15 and 50 wt% CNTs content, respectively, were obtained (Taberna *et al.*, 2006). The test was conducted in the non-aqueous electrolyte (NEt_4BF_4 1.5 M in acetonitrile). These results imply that CNT materials are not good for activated carbon composites.

A carbon nanotube/self adhesive carbon grain composite has been studied by Basri and coworkers (Basri and Dolah, 2013). The carbon grains were derived from oil palm empty fruit bunch fibers of different palm species. The specific capacitance obtained for the composite was

55, 77, and 85 F g⁻¹ for composites carbonized at 600, 700, and 800 °C, and BET surface area of 434, 415 and 485 m² g⁻¹, correspondingly. However, both the surface area and specific capacitance decreased when the CNTs was added. Likewise, the equivalent series resistance (ESR) decreased by a factor of about 84, which in turn increased the power density since low ESR increases conductivity. Also specific capacitance fading was reduced significantly.

Porous structure in activated carbon, carbon aerogels, carbon nanotubes and composites favor the accessibility by the electrolyte ions. However, the type of an electrolyte used, which is not the main focus of our review, has significant effect. Aqueous, non-aqueous and organic electrolytes are the commonly used electrolytes in energy storages.

2.3 Conclusion

In this review, different carbon materials produced from various biomasses has been discussed. It has been shown that the capacitance and energy density of biomass based supercapacitor depend on the properties of carbon nanostructure and individual carbon precursor. The influence of the pore structure (size and distribution), surface area, and heteroatoms present on the capacitance has been discussed. From the perspective of this review, the following conclusions were drawn:

- (i) The variation of physical characteristics not only necessitates finding new materials for supercapacitor electrodes but also argues for improvement of already studied materials either through method of preparation or compositing with other materials among other strategies.
- (ii) Though hydrothermal treatment route for preparing carbonaceous material for supercapacitor electrode seems to be more efficient, the high temperatures and pressure involved increase the cost. Therefore, there is a need to search for catalysts to lower reaction temperature.
- (iii) Most biomass derived electrodes have demonstrated high cyclic stability thus promising future commercial use.
- (iv) The gravimetric capacitances attained by majority of the biomass derived carbon materials are not high enough thus there is need to composite carbon with other materials to improve the capacitance and energy density. The synergetic effect between metal oxides and biomass-derived carbon need to be optimized.

- (v) Despite the achievements in synthesis of biomass derived carbon materials for supercapacitors, optimization of the structure of the electrode materials need to be further studied in order to increase both gravimetric and volumetric capacitance.
- (vi) Hydrothermal, ionothermal, and salt carbonization methods have shown good potential in synthesis of porous carbon materials. Besides a combination of methods could be used to further enhance the capacitance, energy and power density.

CHAPTER THREE

Biogas Slurry Derived Mesoporous Carbon for Supercapacitor Applications²

Abstract

This study reports on the transformation of biogas slurry into mesoporous carbon for supercapacitor electrodes. Pore structures have been modified by altering activation time, temperature and KOH/carbon mass ratio. The physical characterisations were done through XRD, FE-SEM, TEM, Nitrogen sorption studies BET and XPS. The electrochemical measurements in 6 M KOH using a three-electrode cell with Ag/AgCl as reference electrode and platinum as counter electrode were performed. The mesoporous carbons were successively developed as evidenced by type IV isotherms obtained in nitrogen sorption studies. BET, micropore and mesopore surface area of 515, 350, and 165 m² g⁻¹, respectively, as well as a narrow pore width distribution of 3 - 4.5 nm were obtained. X-ray photoelectron results confirmed the presence of functional groups of oxygen and nitrogen in the samples which facilitates the pseudocapacitance. The materials activated at 700 °C, 3:1 KOH to carbon mass ratio, for 120 min exhibited high specific capacitance of 289 F g⁻¹ at a scan rate of 5 mV s⁻¹. Shortening activation time to 30 and 60 min reduced specific capacitance to 163 and 182 F g⁻¹, in that order. Additionally, at 3:1 KOH to carbon mass ratio and 60 min activation time, specific capacitances of 170 and 210 F g⁻¹ at 600 and 800 °C, respectively, were obtained. Moreover, specific capacitance increased with the KOH to carbon mass ratio from 148 F g⁻¹ for 1:1 to 163 F g⁻¹ for 3:1 at 700 °C. Electrochemical impedance spectroscopy studies demonstrated that material had high conductivity. Moreover, capacity retention of 96% after 20,000 cycles was attained at scan rate of 30 mV s⁻¹. The study showed that high performance electrodes could be designed from biogas slurry derived porous carbon.

² This chapter is based on article published in Journal of Materials Today Energy 5 (2017) pp. 126-137 DOI: [10.1016/j.mtener.2017.06.006](https://doi.org/10.1016/j.mtener.2017.06.006)

3.1 Introduction

Energy storage systems are deemed to be the best storage solution for the intermittent renewable energy sources. Additionally, the increasing use of portable devices, electric and hybrid vehicles, power distributions, telecommunication and railways infrastructure necessitates for highly efficient electrical energy storage strategies. Due to their high power density, operation over a wide range of temperature, and high cycle life, supercapacitors are potentially promising as energy storage devices than rechargeable batteries. (Simon and Gogotsi, 2013)

Activated carbon materials have been used for supercapacitors electrodes due to their cycle stability, low cost, and easy to produce (Wei and Yushin, 2012). Based on renewability, low cost, and abundance, biomass is regarded as the most competitive carbon source for supercapacitor electrode application than synthetic carbons. The application of biomass as precursor for supercapacitor electrode materials has been reported by different research groups (Ismanto *et al.*, 2010; Senthilkumar *et al.*, 2011; Elmouwahidi *et al.*, 2012; Jiang *et al.*, 2013; Senthilkumar *et al.*, 2013; Divyashree *et al.*, 2016; Wang *et al.*, 2016d; Chaitra *et al.*, 2017; Enock *et al.*, 2017b). These studies have demonstrated that surface chemistry and pore structure of the electrode materials have big impact on the electrochemical performance.

Generally, it is believed that capacitance is proportional to surface area (Frackowiak and Beguin, 2001). However, this is not always the case because sometime carbon materials with low surface area exhibits high capacitance than those with high specific surface area (Barbieri *et al.*, 2005). In order to tailor functional groups, pore structures, and textural properties of porous carbon derived from a given precursor, precise control of parameters such as activation temperature, activating agent, and activation time as well as good choice between either chemical or physical activation is critical. Chemical activation involves utilization of activating agents such as KOH, NaOH, ZnCl₂, and H₃PO₄ to generating porous framework. Depending on the activating agent used, the pores are generated through solid-solid reaction between activating agent and carbon followed by solid-liquid reaction (Wang and Kaskel, 2012). In the case of KOH, the activation starts with dehydration at 400 °C followed by water gas reaction and then carbonate formation. Beyond 700 °C, hydrogen and carbon reduction reaction occurs (Otowa *et al.*, 1993). The metallic potassium produced after reduction is believed to intercalate into the carbon matrix

thereby widening the atomic layers of the carbon thus forming pores. The activating agent–carbon mass ratios and time of activation are not fixed as they depend on the type of precursor.

In developing countries, wind, solar, and biogas have emerged as accessible and reliable renewable energy sources. The latter produces biogas slurry which is used in agriculture as fertilizer (Garg *et al.*, 2005; Arthurson, 2009). The use of biogas slurry as a source of activated carbon for super capacitor electrode materials has not been reported to the best of our knowledge. For biomass with high cellulose content, hydrothermal treatment (HT) at about 300 °C is required prior to carbonization (HT is used to deconstruct cellulose network) in order to get high surface area carbon nanomaterials. The biogas slurry was chosen as the carbon precursor since the deconstruction of cellulose polymeric network is partially done by bacteria prior to chemical modification. In this study we report on the synthesis of activated carbon materials derived from biogas slurry and their performance as supercapacitor electrode materials.

3.2 Materials and Methods

3.2.1 Materials

Biogas slurry was obtained from biogas plant at Nambala Village, Arusha region, Tanzania. The chemicals used including potassium hydroxide, hydrochloric acid were purchased from Sigma Aldrich. Carbon black (TIMICA SUPPER C65), and polyvinylidene difluoride (PVDF) were purchased from MTI Corporation. All chemicals were used without further modification. The distilled water was prepared in our laboratory using BARNSTEAD T11 (Thermo Scientific 2555 KERPER BOULEVARD Model D1 4031).

3.2.2 Synthesis of activated carbon from biogas slurry

The biogas slurry was dried in air for one week then crushed to make small particles of approximately 160 µm. Twenty grams of crushed materials were carbonized in a horizontal tube furnace (CTF 12/65/550) at 650 °C for 1 h at a heating rate of 10 °C min⁻¹ in nitrogen atmosphere. The resulting carbonized samples were weighed and ground to obtain fine particles of approximately 6 µm.

The carbonized products were chemically activated at 600, 700, and 800 °C by KOH using KOH to carbon mass ratio of 1:1, 2:1, and 3:1 under nitrogen atmosphere. The activation time was varied from 30, 60, to 120 min at heating rate of 10 °C min⁻¹. The tube furnace was allowed to cool naturally to room temperature and activated samples were taken out. The samples were washed several times using 1 M HCl in order to remove the excess alkaline compounds (Wang and Kaskel, 2012). The samples were washed with distilled water until neutral pH. The washed samples were then dried in an oven at 100 °C for 12 h. The resulted materials were referred as BC representing the biogas slurry derived carbon and activated carbon was designated as BC-X-Y-Z, where X, Y, and Z represent KOH/carbon mass ratio, activation temperature, and time of activation (in minutes), respectively, while as prepared carbon was designated as BC-650, where 650 refers to carbonization temperature.

3.2.3 Characterization of the synthesized carbon materials

Field emission scanning electron microscope (FE-SEM) Hitachi S-4800 of serial no HI-9133-0002 with accelerating voltage of 15 kV, magnification capability of 100000 and working distance of 14800 µm was used to observe the microscopic surface morphology of the samples. Energy dispersive X-ray (EDX) attached to the SEM was used to study surface composition of the samples. The crystal structure studies of the materials were performed using high resolution transition electron microscope (HR, TEM 2100F-Korea). Before SEM and TEM characterization, the samples were sonicated in isopropanol so as to increase the dispersion. The diffraction patterns of the materials were acquired using X-ray Diffractometer (XRD-6000, Shimadzu) with X-ray acceleration of voltage and current of 40 kV and 100 mA, respectively. The diffraction patterns were obtained in the step scanning of 0.02 (2θ°) in the range of 5-55 (2θ°). The wavelength of the X-ray incident beam (Cu Kα radiation) was 1.5406 Å. The crystallite size was estimated through X-diffraction pattern using Scherer equation (Awitdrus *et al.*, 2010; Dolah *et al.*, 2014)

$$L_{c,a} = \frac{K\lambda}{\beta(\theta)_{c,a} \cos\theta} \quad (3.1)$$

where L_a is the stack width, L_c is the stack height, K is the constant shape factor which is equal to 1.84 and 0.89 for L_a and L_c , respectively (Awitdrus *et al.*, 2010; Nor *et al.*, 2015), λ is the

wavelength of X-ray radiation, θ is the diffraction angle and β is the full width at half maximum of the diffraction peak. The X-ray photoelectron spectroscopy (XPS; UVS-20-A, SPECS, Germany) with excitation source of Al K α radiation and with the kinetic energy of photoelectron from 0 to 1486.6 eV was used to investigate the surface chemistry of the samples.

The surface area and pore, size, volume and distribution of the carbon samples were characterized by Micrometrics Tristar 3020, 2.00 instrument using nitrogen gas sorption at 77.3 K. Before sorption, all samples were degassed at 250 °C for 3 h. The measurement records the isotherm data in terms of the volume adsorption/desorption against the relative pressure. It is from this data that the important parameter values namely BET surface area, mesopore and micropore surface area (S_{meso} , S_{micro}), mesopore and micropore volume (V_{meso} , V_{micro}), pore size and pore size distribution are determined. The BET surface area was calculated using the Brunauer-Emmet-Teller (BET) equation. The pore size distribution were calculated from N₂ desorption using Barret-Joyner-Halender (BJH) methods.

3.2.4 Electrochemical measurements

The electrochemical performance of the prepared activated carbon was evaluated using three-electrode cell configuration. Saturated Ag/AgCl₂ (KCl) electrode was used as reference electrode and platinum was used as counter electrode. The working electrode was prepared by mixing biogas derived activated carbon, conducting carbon (MTI), and polyvinylidene defluoride (PVDF-MTI) in the mass ratio of 80:10:10. The mixture was pressed in two pieces of nickel foam ($1 \times 1 \text{ cm}^2$). All electrodes were made from similar amount of active material and conducting material (mass loading was 5 mg). The tests were performed in 6 M KOH aqueous electrolytes solution under room temperature.

Cyclic voltammetry (CV) tests were performed on AUTOLAB Potentiostat/Galvanostat (PGSTAT204, AUT50663 Metrohm). The CV tests were performed between -1 to 0 V versus a reference electrode at the scan rates of 5, 10, 30, 100, and 150 mV s^{-1} . In order to determine the type of electrosorption (anionic or cationic), open circuit potential (OCP) were determined. In order to obtain stable OCP values, electrodes were immersed in 6 M KOH solution before OCP (Dai *et al.*, 2015). Electrochemical impedance spectroscopy (EIS) analysis (frequency response analysis) was performed between 10 mHz and 100 kHz using FRA32 module attached to

PGSTAT204 in an open circuit. The specific capacitances (C) of different electrodes at different scan rates (mV s^{-1}) in the CV measurements were calculated using Eq. (3.2) (Chen *et al.*, 2010a; Kim *et al.*, 2013)

$$C = \frac{1}{2mv(\Delta V)} \int_{V_1}^{V_2} i(V)dV \quad (3.2)$$

where v (mV s^{-1}) is the scan rate, ΔV (V) is the applied potential window (V_1 to V_2), and m (g) is the weight of the active material, $\int_{V_1}^{V_2} i(V)dV$ is the total voltammetric charge obtained by integration of negative sweep and positive in cyclic voltammograms. The current density was calculated based on the weight of the active material. The specific capacitance of the BC activated carbon electrodes in the EIS measurements was calculated using Eq. (3.3) (Wang *et al.*, 2015a).

$$C = \frac{-1}{(2\pi fZ''m)} \quad (3.3)$$

where m is the mass of active material, f is the lowest frequency and Z'' is the imaginary impedance.

3.3 Results and discussion

3.3.1 Effect of carbonization time on the carbon yield

The carbon obtained from carbonization of biogas slurry at 650 °C at different carbonization time (30, 60, and 120 min) was evaluated using Eq. (3), where m_{b_1} and m_{b_2} are the mass of dry biogas slurry and mass of carbon produced after carbonization, respectively.

$$\%Yield = \frac{m_{b_2}}{m_{b_1}} \times 100 \quad (3.4)$$

It was found that for biogas slurry, increase in carbonization time has no significant impact on the yield of carbon, Table 3.1. These results differs from those for other carbon precursors like

cherry sawdust where the yield decreased with increasing carbonization time (Gheorghe *et al.*, 2009), and water hyacinth where the yield increased with increasing activating time (Kurniawan *et al.*, 2015).

Table 7: The effect of carbonization time on the yield of carbon at carbonization temperature of 650 °C.

Time of Carbonization (min)	m_{b1} (g)	m_{b2} (g)	Yield (%)
30	20	7.9	39.5
60	20	8.3	42.0
120	20	8.0	40.0

3.3.2 Morphological, structural, and textural properties of synthesized materials

FE-SEM micrographs of the samples are shown in Fig. 5. As prepared carbon (BC-650) exhibited irregular pores on the surface (Fig. 5a). The number of pores seems to increase with increasing KOH/carbon mass ratio. The number of pores on the surface of BC-3-700-30 is much more than in BC-650, BC-1-700-30 as shown in Fig. 5a-d. This increase might have been caused by the activating agent (KOH), which burnt more carbon to produce more pores. The porosity of carbonized biogas slurry was preserved after activation at 700 °C as depicted by the high magnification SEM images (Fig. 6c, d).

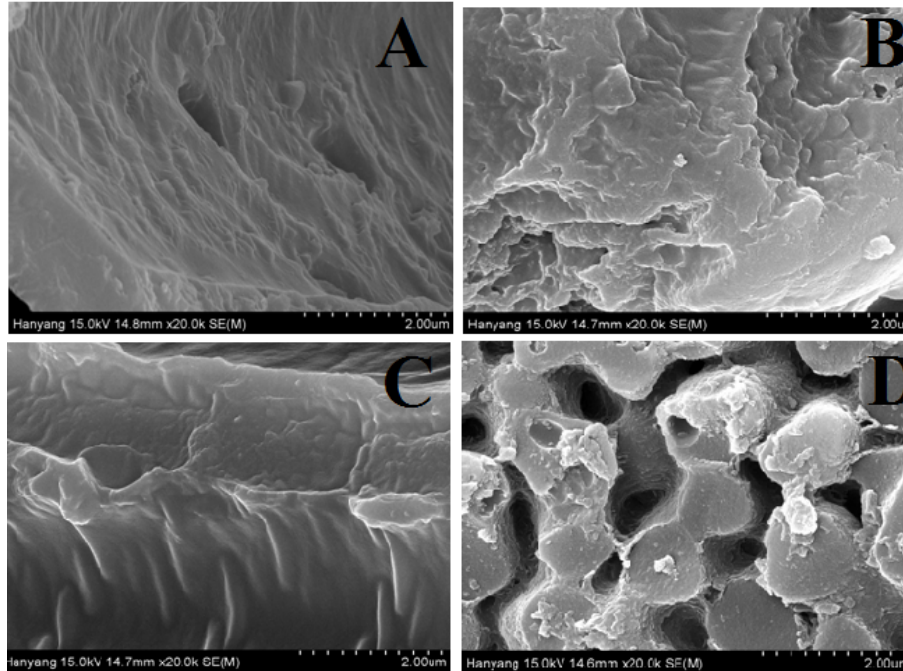


Figure 5: FE-SEM micrographs at 2 μm (a) B-650, (b) BC-1-700-30, (c) BC-2-700-30, and (d) BC-3-700-30.

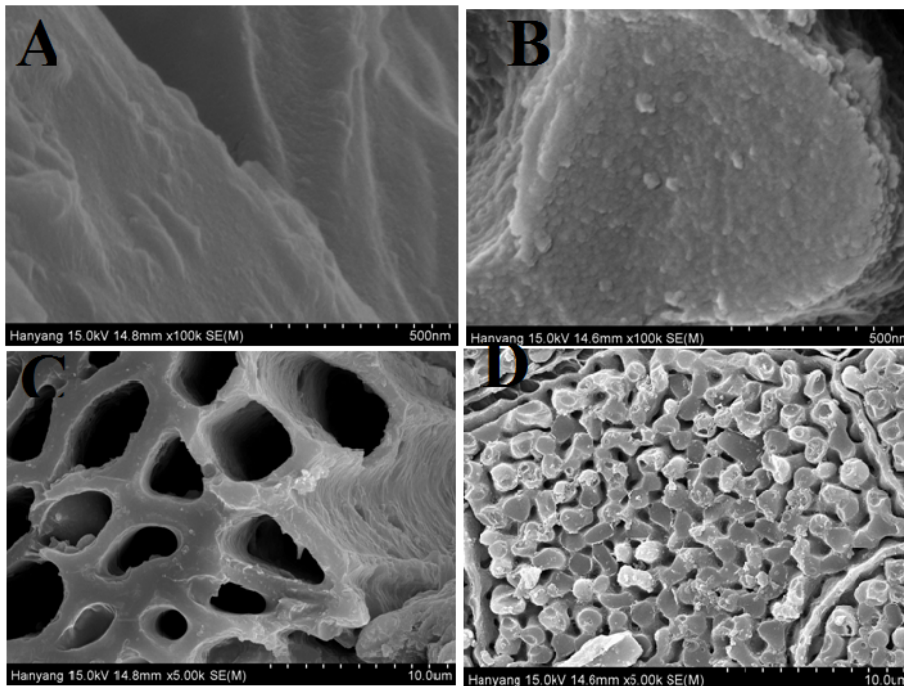


Figure 6: FE-SEM micrographs of samples at different magnifications (a) BC-650 at 500 nm, (b) BC-3-700-30 at 500 nm, (c) BC-650 at 10 μm , and (d) BC-3-700-30 at 10 μm .

At different magnifications, BC-650 sample exhibited smoother surface and less degree of porosity (Fig. 6a, c) compared to BC-3-700-30, which shows rough surface and irregular pores, Fig. 6b, d. The difference may be attributed to the contribution of KOH, which reacted both with the interior and exterior surface of the BC-3-700-30 thus creating more pores on the surface. It is further shown in Fig. 6c that the sample carbonized at 650°C exhibited cylindrical-like pores. On the other hand, the activated carbon consists of interconnected channels, Fig. 5d and 6d. This is promising for double layer capacitors because the interconnected channels are very important for charge transfer in electrochemical double layer capacitors (Elmouwahidi *et al.*, 2012).

The properties of the biogas slurry derived carbon were further studied by X-ray diffraction. The XRD patterns of carbon samples are shown in Fig. 7. Two peaks (002) and (100) were observed at 2θ between 23° and 30° for (002) and around 42° for (100). There were no peaks beyond 55° (Fig. 8) therefore; all the XRD patterns were acquired from 5° to 55°, 2θ . The (002) peak demonstrated the graphitic nature of the BC materials. This has been shown to enhance the electrochemical performance of the materials (Paraknowitsch *et al.*, 2010). Generally, the prepared carbon was mostly amorphous. The carbon materials prepared by carbonizing BC at 650 °C (BC-650) had sharp peaks at 2θ around 30° and 40°. The peaks did not appear in the activated carbons indicating that the impurities were either burned by KOH or removed by HCl. The existence of broad peak at 2θ at about 12° might be due to residual silica or KOH remained in the samples as shown by EDX analysis (Appendix 1). Furthermore, the BC materials showed curly interplanar spacing typical of graphitic carbon materials.

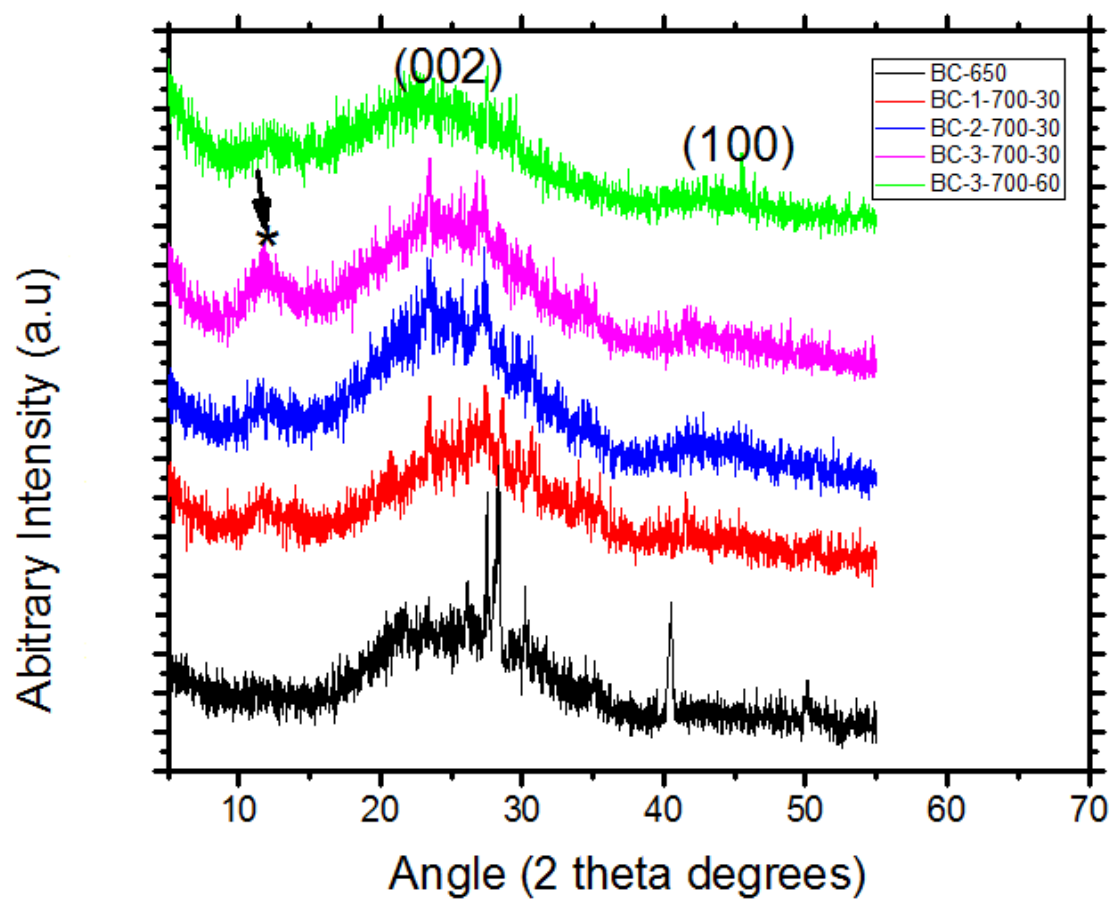


Figure 7: XRD Patterns of BC-650, BC-1-700-30, BC-2-700-30, BC-3-700-30, and BC-3-650-60.

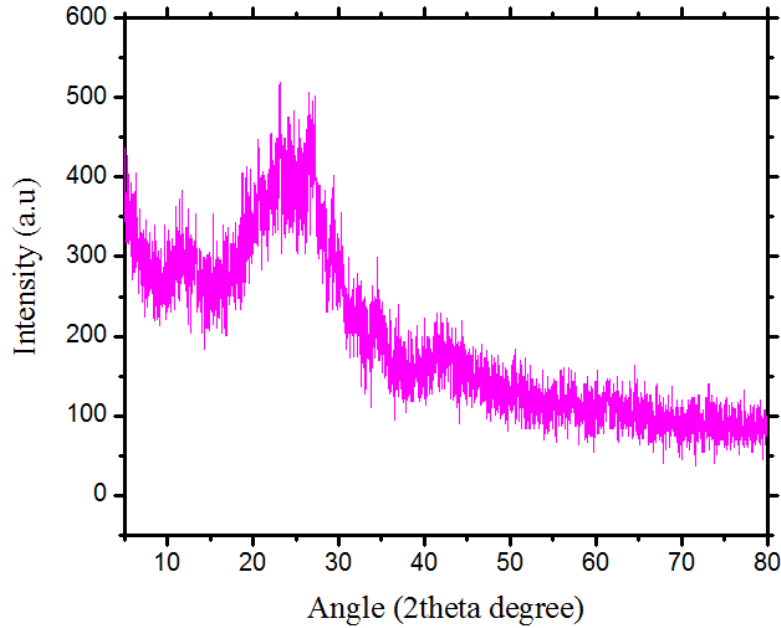


Figure 8: XRD pattern for BC-3-700-30 from 5 to 80, 2θ .

The interplanar spacing, the stacking height (L_c), stacking width (L_a), mean number of the planes (N_p), and the density of the edges and basal planes in the microcrystallites of selected samples are shown in Table 3.2. The interplanar distance d_{002} and d_{100} were evaluated using the Bragg's law ($n\lambda = d \sin \theta$). It was established that there were very small variations in d_{002} and d_{100} implying little or no correlation between interplanar distance and the activating agent. The same trend was also observed when oil palm empty fruits were investigated (Nor *et al.*, 2015).

The values of $N_p \left(\frac{L_c}{d_{002}} \right)$ increased with increasing amount of activating agent but also decreased when activating time was 60 min as evidenced in Table 3.2. The basal planes and relative density of edge $\left(\frac{L_c}{L_a} \right)$ of the activated samples ranged between 0.25 and 0.28, for BC-3-700-30 and BC-1-700-30, respectively. These values are slightly higher than those obtained for oil palm empty fruits bunches (ranged between 1.86 to 0.23) (Nor *et al.*, 2015), however, they are lower than the values obtained for coffee endocarp which ranged from 0.31 to 0.67 (Nabais *et al.*, 2011).

Table 8: XRD microcrystallite characterization of the electrode materials.

Sample	d_{002} (Å)	d_{100} (Å)	L_c (Å)	L_a (Å)	L_c/L_a	L_c/d_{002}
BC-650	3.47	2.22	6.45	512.00	0.013	1.86
BC-1-700-30	3.35	2.18	7.15	25.54	0.28	2.13
BC-2-700-30	3.55	2.17	7.28	28.28	0.26	2.10
BC-3-700-30	3.54	2.05	7.98	31.86	0.25	2.25
BC-3-700-60	3.68	2.07	6.40	23.80	0.27	1.74

Further morphological and structural studies of the samples done by the HR-TEM showed the layered structure of graphitic carbon materials Fig. 3.5a–c. The graphitic nature of our carbon samples was further evidenced by the onion-like lattice fringes with interplanar spacing of 0.34 nm as shown in Fig. 3.5d. The interplanar spacing compared well with the d_{002} spacing of the XRD results shown in Table 3.2. These properties are good for the conductivity of the materials.

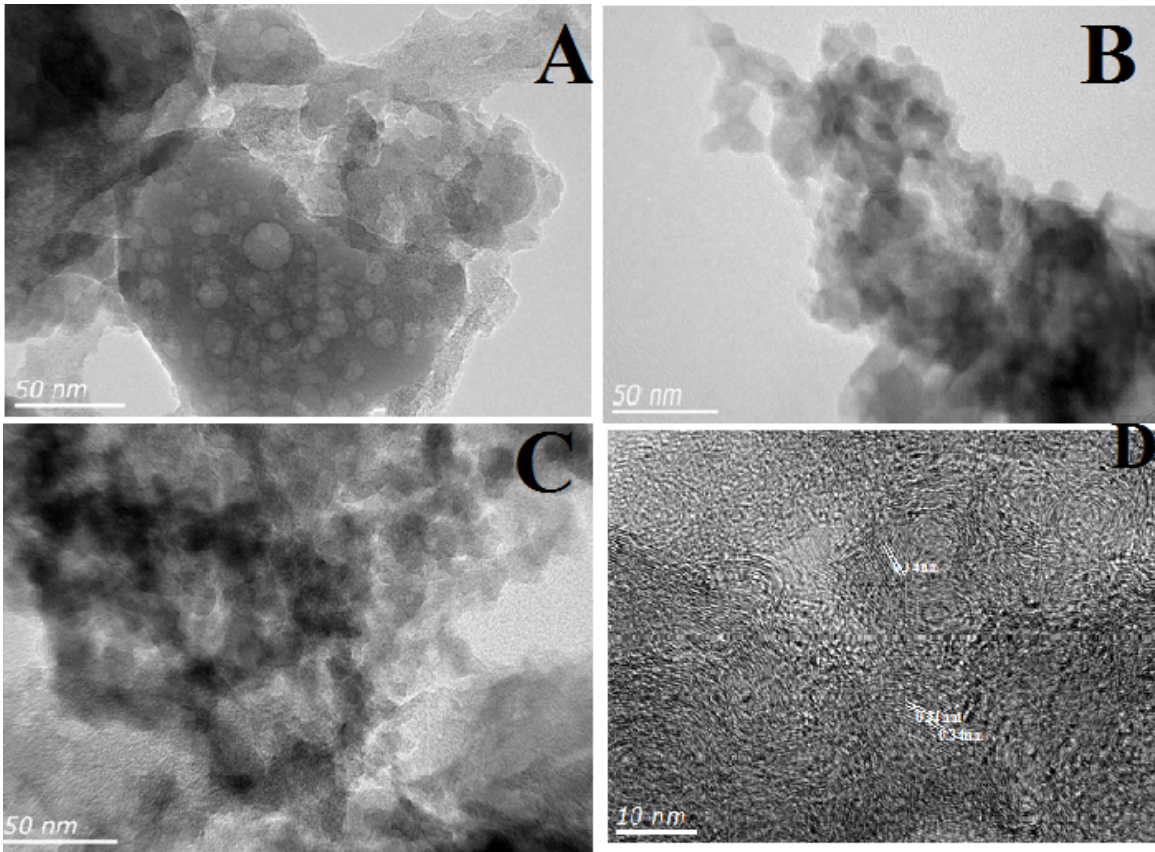


Figure 9: TEM images for (a) BC-1-700-30, (b) BC-3-700-60, (c) BC-3-700-30, and (d) HRTEM for BC-3-700-30.

The BET surface area, S_{micro} , S_{meso} , pore volume, and pore width of BC activated carbon samples are summarized in Table 3.3. The BET surface area of as-prepared carbon (BC-650) was about $148 \text{ m}^2 \text{ g}^{-1}$. After activation, the surface area increased to $158.8 \text{ m}^2 \text{ g}^{-1}$ for BC-1-700-30, $328.4 \text{ m}^2 \text{ g}^{-1}$ for BC-2-700-30, $326.7 \text{ m}^2 \text{ g}^{-1}$ for BC-3-700-30, and $514.6 \text{ m}^2 \text{ g}^{-1}$ for BC-3-700-60. The surface area increased by $178 \text{ m}^2 \text{ g}^{-1}$ when the ratio of KOH to carbon was increased to 3. Activation time on the other hand showed more pronounced effect as the surface area increased by $266 \text{ m}^2 \text{ g}^{-1}$ when activation time was increased from 30 to 60 min while keeping the activation temperature at $700 \text{ }^\circ\text{C}$. The average pore size of all carbon samples was found to be 4.4 - 8.2 nm, which is within the mesoporous range (Table 3.3). Large pore size of the samples may be the reason why the BET surface areas of the samples were moderate. The total pore volume as well as mesopores volume increased with increasing amount of KOH. Similarly, the $V_{\text{micro}}/V_{\text{meso}}$ decreased as the amount of activating agent and activating time increased, meaning

pore widening increased with increasing KOH. The mesopore content as calculated from the ratio of mesopore volume and total pore volume ($V_{\text{meso}}/V_{\text{T}}$) was 63% for BC-3-700-60 compared to 50% for BC-650, 62% for BC-1-700-30, 61% for BC-2-700-30 and 62% for BC-3-700-30. The mesopores content results were comparable to those obtained for coconut shell (75, 72, and 60%) at different activation time (Mi *et al.*, 2012b). Except BC-650, which displayed approximately equal V_{meso} and V_{micro} , the other samples exhibited larger values of V_{meso} than V_{micro} . These results were expected because the nitrogen adsorption and desorption studies presented in Fig. 10 confirmed the existence of mesopores. Similar trend was also observed for oil palm empty tree bunches (Basri *et al.*, 2013). On the other hand, the $S_{\text{micro}}/S_{\text{meso}}$ decreased with the increase in the amount of the activating agent and activation time, signifying the increase of mesopore content as the amount of KOH increased. The micropores are important for charge storage while mesopores are important for ion transport (Simon and Gogotsi, 2008).

Table 9: Pore size, pore volume, and surface areas of synthesized carbon samples.

Carbon sample	¹ S_{BET} (m^2/g)	² S_{micro} (m^2/g)	³ S_{meso} (m^2/g)	$S_{\text{micro}}/S_{\text{meso}}$	⁴ D_{ave} (nm)	⁵ V_{micro} (cm^3/g)	⁶ V_{meso} (cm^3/g)	$\frac{V_{\text{micro}}}{V_{\text{meso}}}$	⁷ V_{T} (cm^3/g)
BC-650	148.5	114.1	23.9	4.77	6.4	0.06	0.06	1	0.12
BC-1-700-30	158.8	118.5	40.3	2.94	8.2	0.08	0.13	0.62	0.21
BC-2-700-30	328.5	232.2	96.3	2.41	4.4	0.09	0.14	0.64	0.23
BC-3-700-30	326.7	229.3	97.4	2.35	4.7	0.09	0.15	0.60	0.24
BC-3-700-60	514.7	350	164.7	2.13	4.7	0.14	0.24	0.58	0.38

1-BET surface area, 2-Micropore surface area, 3-Mesopore surface area, 4-Average pore size 5-Micropore volume, 6-Mesopore volume and 7- Total pore volume.

The nitrogen adsorption and desorption isotherms at 77.3 K for BC-650, BC-1-700-30, BC-2-700-30, BC-3-700-30, and BC-3-700-60 are shown in Fig. 10a. All the isotherm curves exhibited type IV isotherms according to the IUPAC classification. This indicates that mesopores were dominant (Rouquerol *et al.*, 2013). It is evident that the hysteresis loop of the as-prepared carbon (BC-650) was of the H4 type indicating the presence of narrow slit-like pores, while the rest of the samples exhibited H2 type demonstrating the presence of aggregates with uniform channel-like pores. The hysteresis loop of BC-650 (Fig. 10a) is not complete and occurs at low pressure compared to other samples suggesting that there was a capillary condensation of N₂ in mesopores of the activated carbons. The pores formed in BC-1-700-30, BC-2-7000-30, BC-3-700-30, BC-2-700-60, and BC-3-700-60 were uniform while those of BC-650 were not (Fig. 10a). The nitrogen uptake of the sample was centred at relative pressure of $0.4 < \frac{p}{p_0} < 1$ which is indicative of

mesopores. At $\frac{p}{p_0} = 1$ there was a sharp uptake for all samples and was ascribed to the presence of some macropores in the samples (Shao *et al.*, 2016). Fig. 10b shows the pore size distribution as calculated using the BJH method. The plots depict that the pore width of the samples ranged from 2 to 6 nm and interestingly, all samples showed a narrow distribution at 3 - 4.5 nm. As the activation time increased, pores smaller than 2.8 to 3.2 nm size were formed (Fig. 10c). The formation of mesopores in the samples is very beneficial for charge storage and charge transfer in the electrode.

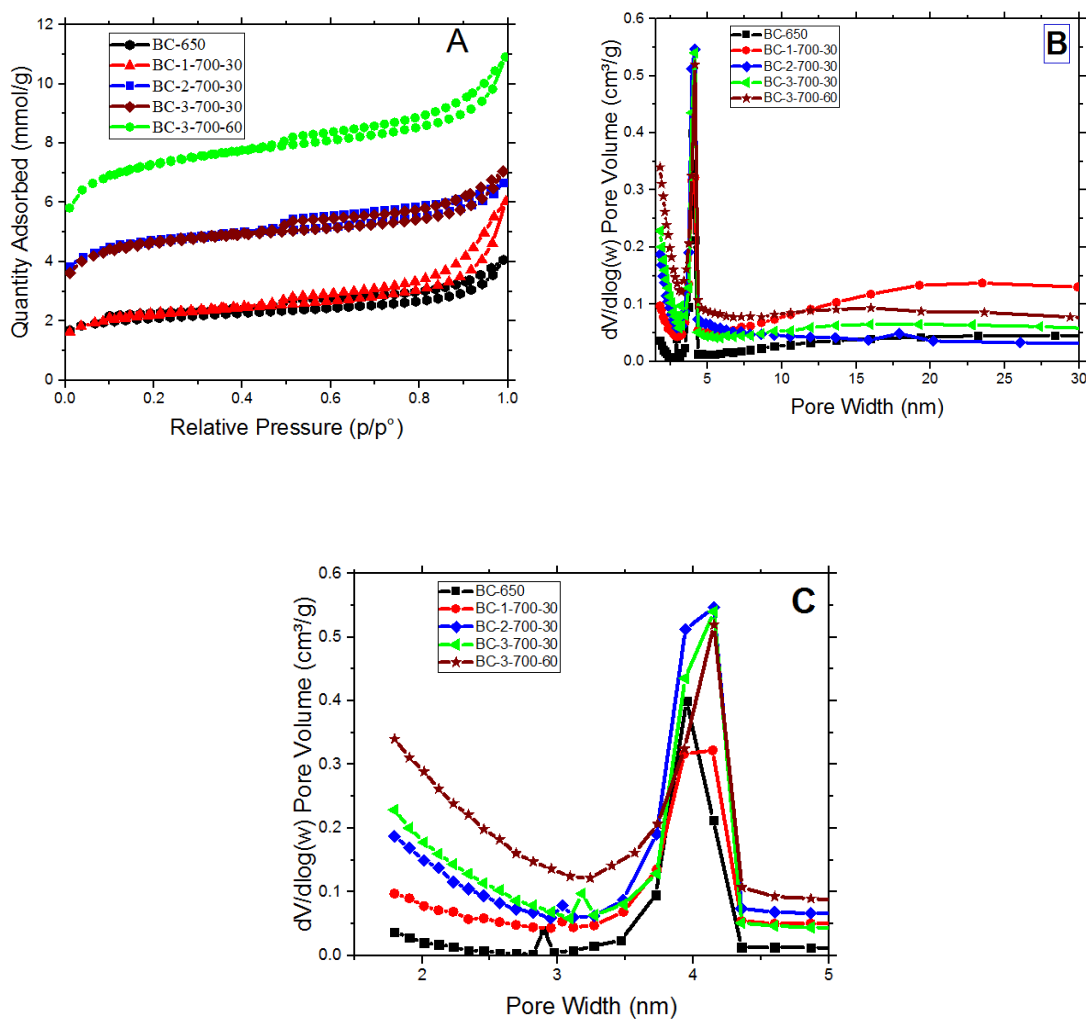


Figure 10: (a) Nitrogen adsorption – desorption isotherms for BC-650, BC-1-700-30, BC-2-700-30, BC-3-700-30, and BC-3-700-60 samples, (b) Pore size distribution calculated from the desorption isotherm using BJH method and (c) Pore distribution at 2 to 5 nm range.

3.3.3 Surface chemistry studies of the synthesized samples.

The surface chemistry of the BC materials was investigated using XPS analysis. Fig. 11a shows the existence of C1s, N1s, and O1s chemical states at 284.2, 399.5, and 532 eV of the XPS spectrum, respectively (Si *et al.*, 2013). C1s has four species (Fig. 11b); C=C (graphitic carbon)

peak at 284.7 eV; C-C peak observed at 285.2 eV, hydroxyl group (C-O) peak at 286.4 eV , and C=O peak at 287.5 eV.

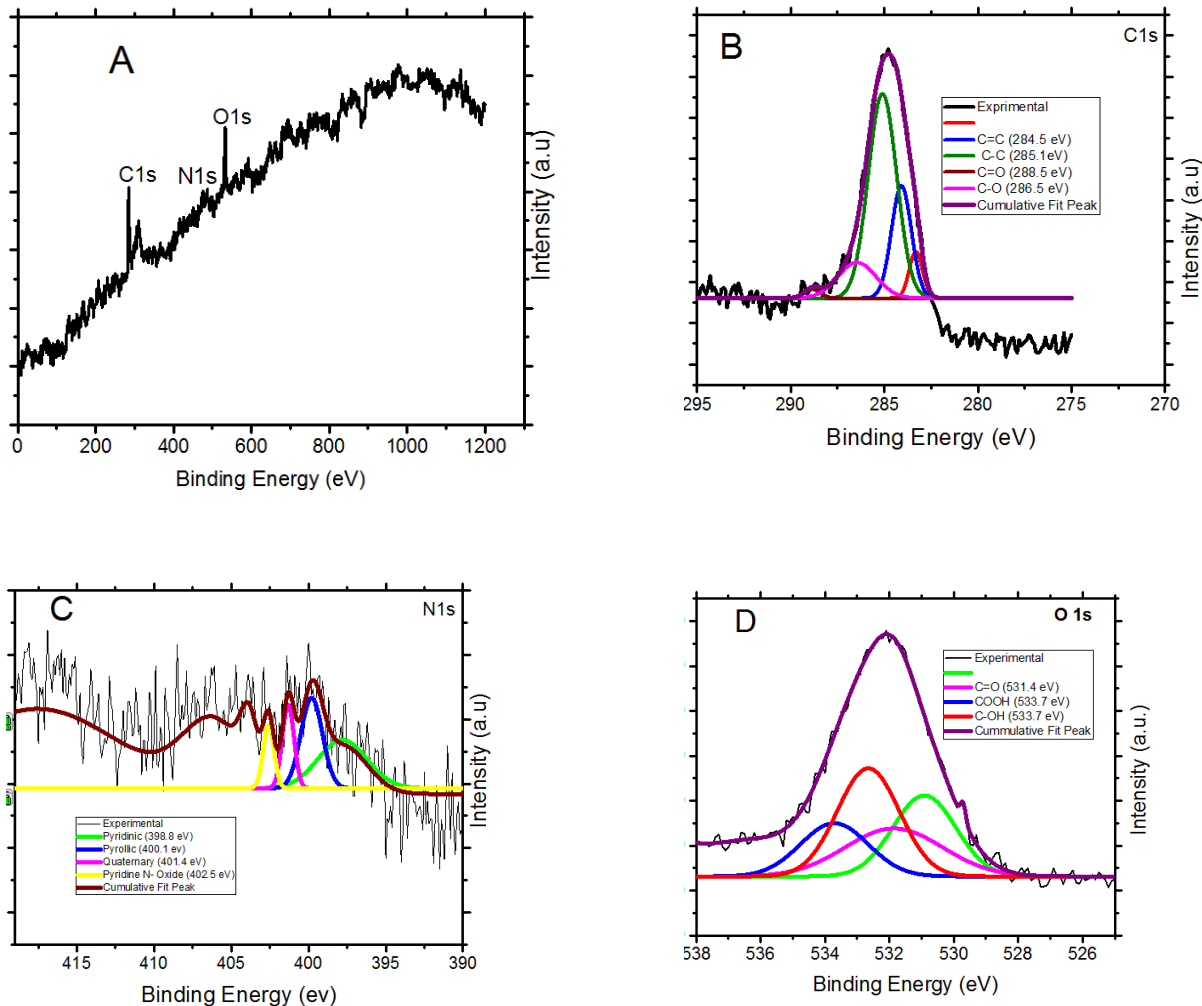


Figure 11: XPS spectra and deconvolution of peaks for BC-3-700-30 (a) Survey spectra, (b) C1s, (c) N1s, and (D) O1s.

In Fig. 11c four species of N1s are shown; pyridinic at 398.6 eV, pyrrolic at 400 eV, quaternary (401.3 eV), and pyridinic N oxide (402.5 eV). The presence of pyridinic and pyrrolic nitrogen has been reported to enhance the pseudocapacitance of the electrode materials in supercapacitors (Hulicova *et al.*, 2005). Fig. 11d shows O1s consistent with phenols (C-OH) groups or ether (C-O-C) groups at binding energy of 532 eV. Generally, the BC materials contained O and N groups

which could facilitate pseudocapacitance and increase wettability of the material (Zhang *et al.*, 2016; Zhou *et al.*, 2016).

3.3.4 Electrochemical characterization of the electrodes

The cyclic voltammetry (CV) measurements in 6 M KOH electrolyte were used to investigate the electrochemical performance of BC materials as supercapacitor electrode. Fig. 12 shows CVs of selected representative samples of the prepared electrodes. Most CV curves displayed a nearly rectangular shape in the voltage window of 1 V from -1 to 0 V. This was due to the remarkable double layer capacitive response of the electrodes. While panel (a) in Fig. 12 shows the CV curve of unactivated carbon; panels (b-d) in Fig. 12 depict the capacitive behaviour of BC materials after being activated at 700 °C for 30 and 60 min, and at 800 °C for 120 min, correspondingly. It is interesting to see that even at high scan rate of 150 mV s⁻¹, the materials exhibited shapes close to rectangular shape indicating that the materials had quick charge transfer and small resistance (Huber *et al.*, 2005).

Additionally, there are some humps appearing on the CV curves, which could probably be ascribed to pseudocapacitance behaviour stemming from the presence of oxygen and nitrogen functional groups on the surface of BC materials as revealed by XPS results. The presence of oxygenated functional groups such as quinone–carbonyl groups on the surface of BC materials promote the faradaic reaction (Calvo *et al.*, 2014). The use of basic electrolyte (6 M KOH) may also have contributed to high conductivity, while its pH might increase the electrolyte/electrode interactions as it is believed that the acidic functional groups react with hydroxyl ions (OH⁻) in the basic aqueous electrolyte (Oh *et al.*, 2014)

The OCP values determined at a scan rate of 5 mV s⁻¹ in the voltage window between -0.9 and 0.1 V were -0.361, -0.362, -0.362, -0.364, and -0.367 V for BC-650, BC-1-700-30, BC-2-700-30, BC-3-700-30, and BC-3-700-60, in that order. The negative sign of the OCP values demonstrate that BC materials were more suitable for cation electrosorption (Hou and Huang, 2013).

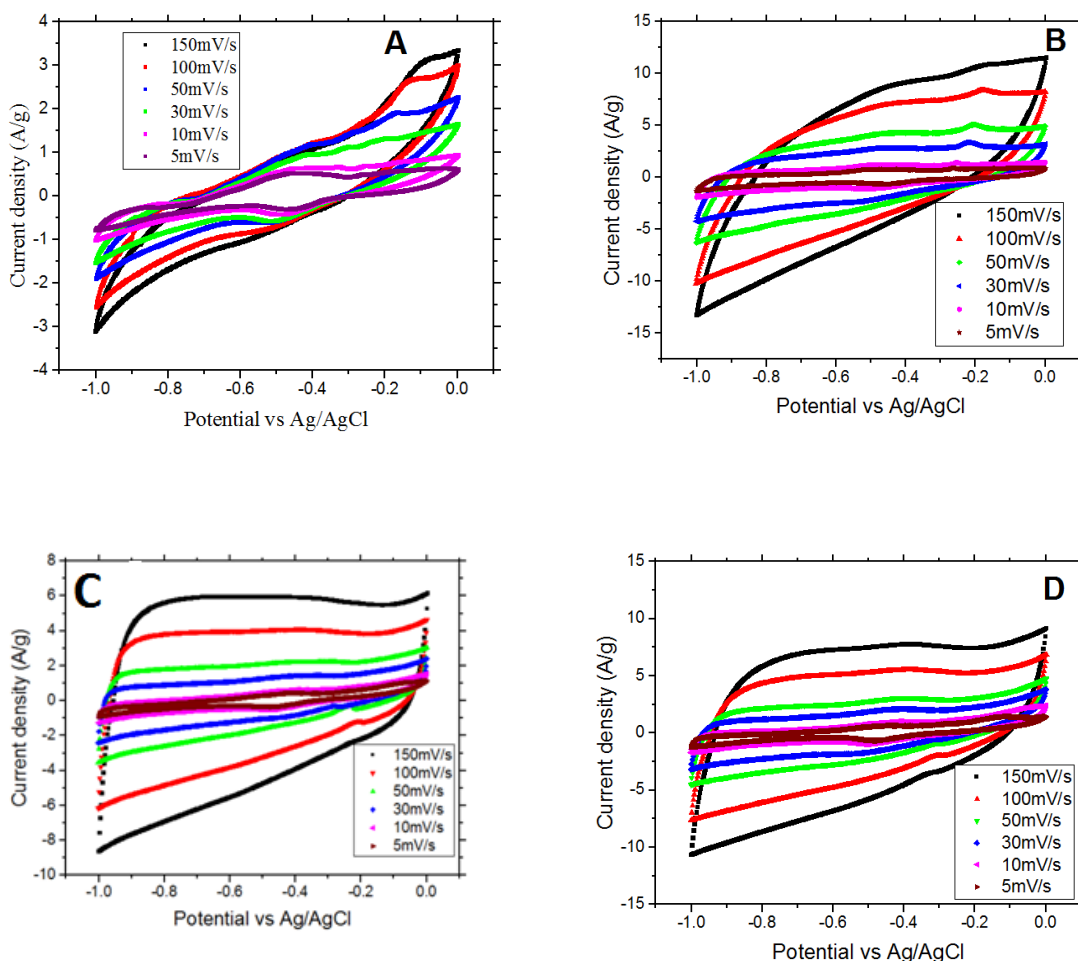


Figure 12: Cyclic voltammograms of BC based electrodes in 6 M KOH electrolyte (a) BC-650, (b) BC-3-700-30, (c) BC-2-800-30 and (d) BC-2-800-120.

Fig. 13a-c shows the effect of KOH/ carbon mass ratio, activation time and activation temperature on the specific capacitances of BC electrodes. The specific capacitances in Fig. 13a-c were calculated from CV curves in Appendices 2 - 4, respectively, at scan rates of 5, 10, 30, 50, 100, and 150 mV s^{-1} . Fig. 13a shows the effect of activation agent ratio on the specific capacitance of the BC materials. It was observed that the specific capacitance increased with KOH/carbon mass ratio. At a scan rate of 5 mV s^{-1} , the specific capacitances were 69, 148, 160, 163 F g^{-1} for BC-650, BC-1-700-30, BC-2-700-30 and BC-3-700-30, respectively. Thus the specific capacitance of the activated samples was about 80-90 F g^{-1} higher compared to the

unactivated but carbonized sample (BC-650). The specific capacitance increase was probably due to the increased BET surface area of activated samples and the mesoporosity increase as shown in Table 3.3 which provides more active sites for ion electrosorption.

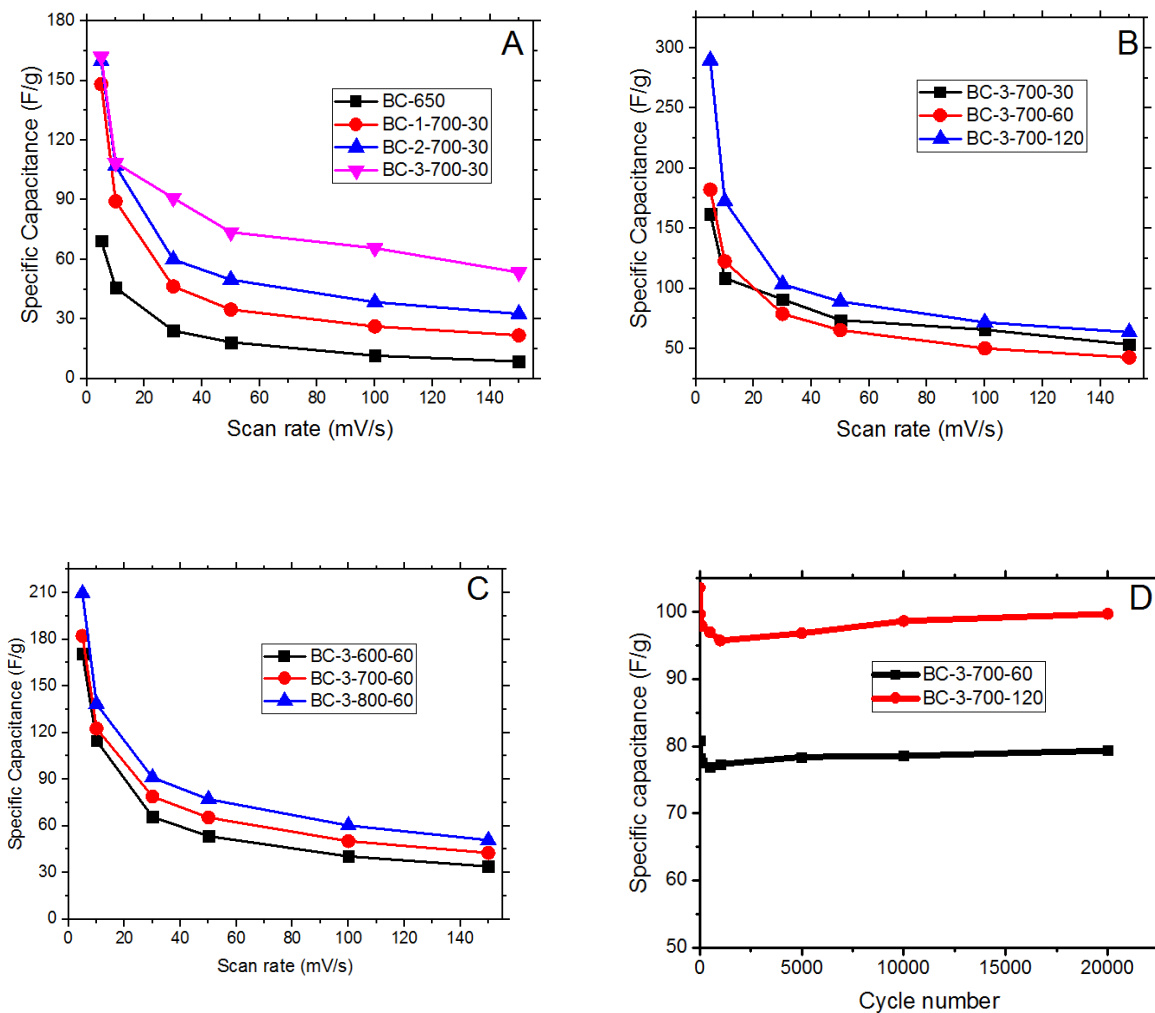


Figure 13: Effect of (a) KOH to carbon ratio, (b) Activation time, (c) Activation temperature on specific capacitance Vs scan rate, and (d) Cyclic stability of BC mesoporous carbon (Capacitance retention).

It is demonstrated in Fig. 13b that BC-3-700-120 electrode exhibited the highest specific capacitance (289 F g^{-1}) followed by BC-3-700-60 (182 F g^{-1}) then BC-3-700-30 (163 F g^{-1}) at scan rate of 5 mV s^{-1} . This suggests that etching of carbon by the KOH increased with activation

time thereby creating more pores and increased surface area. The maximum specific capacitance (C) attained (289 F g^{-1}) is comparable to those obtained with phenolic resin based carbon (282 F g^{-1}) (Du *et al.*, 2009), corn grains (257 F g^{-1}) (Balathanigaimani *et al.*, 2008), banana fibres (66 F g^{-1}) (Subramanian *et al.*, 2007), and coconut shell (228 F g^{-1}) (Mi *et al.*, 2012b) at scan rate of 5 mV s^{-1} . They are comparable also to sugar bagasse and rice straw which exhibited specific capacitance of 340 and 112 F g^{-1} , respectively, at 2 mVs^{-1} (Thambidurai *et al.*, 2014).

Moreover, experiments on corn grains and coconut shells attained the specific capacitance of 250 and 243 F g^{-1} , correspondingly. The slight decay of capacitance of BC-3-700-30 compared to that of BC-3-700-60 at high scan rate implies that the former has better capacitive behaviour than latter. The effect of activation temperature on specific capacitance can be seen in Fig. 13c. The specific capacitance was found to increase with temperature. The BC-3-800-60 electrode afforded the highest specific capacitance of about 210, 138, 91, 77, and 60 F g^{-1} at scan rates of 5, 10, 30, 50, 100, and 150 mV s^{-1} , respectively, while for the BC-3-700-60 the values were 182, 122, 78, 65, 50 and 42 F g^{-1} at the same scan rates. The BC-3-600-60 had a smaller specific capacitance (170 F g^{-1}) than BC-3-700-60 (182 F g^{-1}) and BC-3-800-60 (210 F g^{-1}). This variation of capacitance may be due to the fact that at high activation temperatures, more pores are generated and the materials become more graphitic in nature thereby facilitating charge storage. Additionally, Fig. 13a-c reveals that as the scan rate increased, the specific capacitance decreased because of at higher scan rates the electrolyte ions do not get enough time to penetrate through the pores of the material.

The cyclic stability of the fabricated electrode was also studied in order to evaluate the life cycle of the electrodes. After 20000 cycles at 30 mV s^{-1} , BC-3-700-60 and BC-3-700-120 specific capacitance retention were 98 and 96%, respectively (Fig. 13d). It was observed that the stability of the BC materials dropped within the first 100 cycles as depicted in Fig. 13d and increased as the number of cycle increases meaning BC based electrode get activated after few circles.

The correlation between micropore and mesopore content, crystallite size, and specific capacitance of synthesized electrodes (Fig. 14) shows both the surface area and geometry of microcrystallite behaviour of the electrode were influenced by amount of KOH and time of activation. The same correlation was also observed for oil palm empty fruits (Dolah *et al.*, 2014).

The specific capacitance was observed to increase with decreasing ($S_{\text{micro}}/S_{\text{meso}}$) values implying the contribution of mesopore content in the samples. Furthermore, the specific capacitance was also observed to be dependent on XRD crystallite parameters since it increased with increase in L_a/L_c values (Fig. 14).

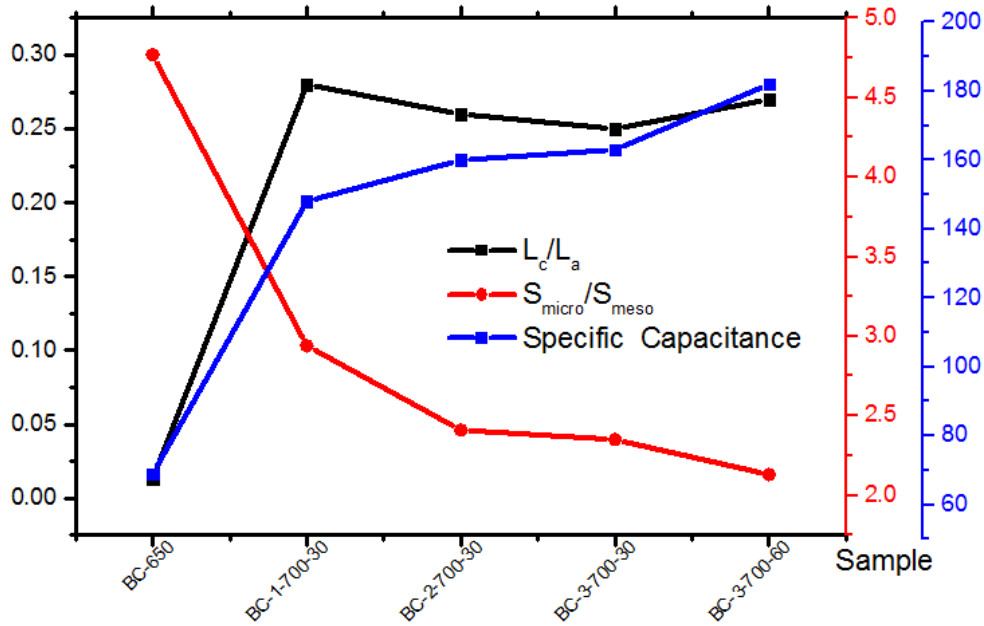


Figure 14: Correlation between micropore and mesopore content, crystallite size, and specific capacitance of synthesized electrodes.

Fig. 15a presents the Nyquist plots for the BC materials based on different activation time at 700 °C. The characterization was performed in KOH electrolyte in the frequency range from 10 mHz to 100 kHz. The BC materials exhibit the vertical slope at low frequency implying good capacitive behaviour of the materials (Li *et al.*, 2012b; Qian *et al.*, 2014). Since from Fig. 15a it was difficult to observe the behaviour of each sample at high frequency, Fig. 15b was plotted using arbitrary real impedance (Z''). It can be seen that the electrodes exhibited semicircles in the high frequency region. The fit and simulation program available in FRA32 module was used to fit the results.

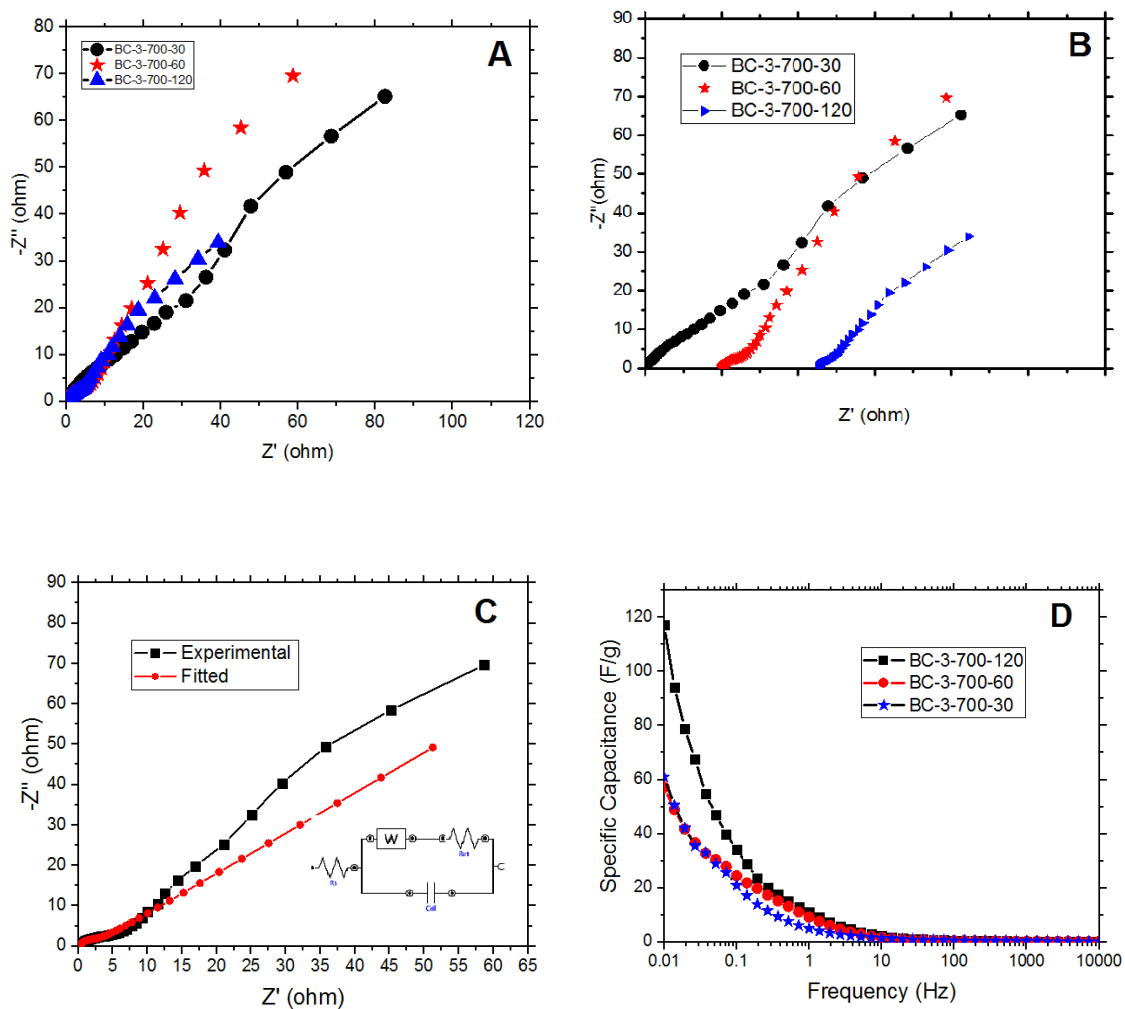


Figure 15: (a) Nyquist plots of electrodes based on BC-3-700-30, BC-3-700-60, and BC-3-700-120, (b) Comparison of Nyquist plots using arbitrary real impedance, (c) Fitted Nyquist plots and (d) Specific capacitance versus frequency.

The Nyquist plots of the fitted and measured data of BC-3-700-60 as representative sample are shown in Fig. 15c. The equivalent circuit with kinetics of diffusion as suggested by Randles (Randles, 1947) was used to identify the impedance parameters (Fig. 15c inset). The sum of ohmic resistances of the electrolyte and internal resistance of the electrode (R_s) was recorded by taking the point at which Nyquist plot start at high frequency region. Warburg impedance (W) which describes the ion diffusion inside the electrode was taken from the straight line in the low

frequency region. The resistance of physisorption of electrolyte ions on pores of the electrode (R_{ct}) was found by measuring the diameter of the semicircle exhibited by the plot.

In Table 3.4, the fitting parameter of the Nyquist plot of the BC materials at different activating time is presented. The materials demonstrated no significant variations of R_s implying that the activation time of BC did not alter the conductivity of the electrode. R_s values are small in the range of 0.23 to 0.28 Ω , which means that the conductivity of the electrolyte was high for both electrodes.

Table 10: Equivalent circuit parameters of BC-X-Y-Z obtained from Nyquist plot analysis.

Sample	R_s (Ω)	R_{ct} (Ω)	$W(Ss^{-1/2})$	C_{dl} (mF)	f_0 (Hz)	τ_0 (s)
BC-3-700-30	0.26	0.96	0.04	1.22	9.5	0.11
BC-3-700-60	0.28	2.17	0.06	1.23	7.5	0.13
BC-3-700-120	0.23	1.09	0.07	1.14	10	0.10

The charge transfer resistance of the electrodes fabricated was shown by the semicircles in Fig. 15a, b indicating that there was good contact between the current collectors and active materials. BC-3-700-60 showed higher R_{ct} (2.17 Ω) as compared to BC-3-700-30 (0.97 Ω), and BC-3-700-120 (1.09 Ω). This might have been due to high adsorption capacity of BC-03-700-60 as evidenced from BET results. This translated to more ions penetrating into the pores of the electrode thereby increasing the contact resistance. The values of R_s are less than 1 Ω signifying the usefulness of the BC materials as supercapacitor electrode. The R_s values are relatively small compared to those obtained in for cornstalk which ranged between 0.32 to 0.69 Ω (Wang *et al.*, 2013b) and egg shell membrane with R_s values between 0.29 and 0.57 Ω (Taer *et al.*, 2014). The variations of specific capacitance with applied frequency as calculated from EIS measurements are shown in Fig. 15d. The capacitances at 0.01 Hz were 61, 57, and 117 for BC-3-700-30, BC-3-700-60, and BC-3-700-120, respectively. It was found that the specific capacitances were lower than those in CV.

The Bode plots for impedance with respect to applied frequency are shown in Fig. 16a. It was revealed that the phase angles were -82° , -75° , and -63° at 0.01 Hz for BC-3-700-30, BC-3-700-60 and BC-3-700-120, respectively. These values are close to an ideal capacitor with phase angle of -90° implying remarkable capacitive behavior of the BC electrodes and are comparable to 67° obtained by Krishnamoorthy and co-workers (Krishnamoorthy *et al.*, 2014). At high frequencies the phase angles are nearly zero implying that current and potential are in phase.

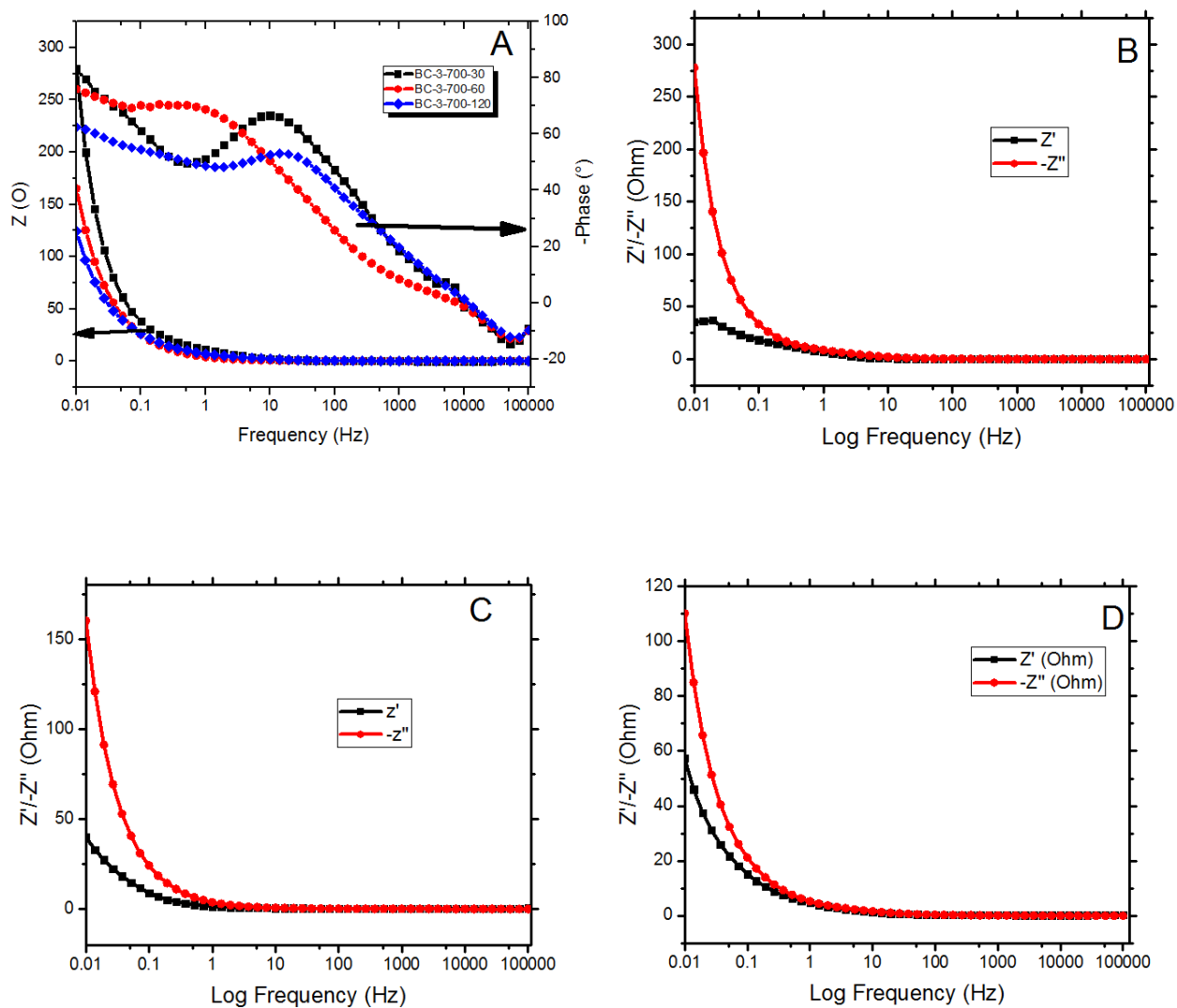


Figure 16: Bode plots (a) Z with respect to frequency (b) $Z'/-Z''$ with respect to frequency BC-3-700-30, (c) $Z'/-Z''$ with respect to frequency BC-3-700-60, and (d) $Z'/-Z''$ with respect to frequency BC-3-700-120.

Fig. 16b-d shows the Bode plots for imaginary and real impedances of sample BC-3-700-30, BC-3-700-60, and BC-3-700-120, respectively. The response frequencies (f_0) for samples as calculated from the intercepts of Z' and Z'' shows the electrodes had high power delivery and the variations between the electrodes are negligible. Furthermore the relaxation times of the selected samples ($\tau_0 = \frac{1}{f_0}$) are less than 1 (see Table 4) signifying the high power delivery of the electrodes. The calculated τ_0 seems to be smaller than those reported for carbon- carbon electrode which had relaxation time of 10 s and for ginkgo shells which had the τ_0 between 0.52 and 1.37s (Taberna *et al.*, 2003). The small frequency and time responses of the BC electrodes ascribes to higher conductivity of the synthesized electrodes.

3.4 Conclusion

Mesoporous carbon materials were successfully synthesized by activating biogas slurry with KOH. BET, micropore and mesopore surface area of 515, 350, and 165 m² g⁻¹, respectively, were obtained. The micropore and mesopore volume ratio ($V_{\text{micro}}/V_{\text{meso}}$) decreased as the KOH amount increased. The mesopore content of about 63% was obtained. The carbon structure obtained favours electrical double layer formation and facilitate the diffusion and transport of ions. The effects of KOH/carbon ratio, activation temperature and time on specific capacitance were investigated. The specific capacitances of 163, 182, and 289 F g⁻¹ at activating time of 30, 60, and 120 min, respectively, were obtained at 700 °C. Based on activating temperature, specific capacitances of 170, 182, and 210 F g⁻¹ at 600, 700 and 800 °C, correspondingly, were obtained at activating time of 60 min. EIS recorded the low values for R_s , R_{ct} and τ_0 of 0.23 Ω, 1.09 Ω and 0.10 s, respectively demonstrating that material had high conductivity. Furthermore, high capacity retention of 96% after 20000 cycles was attained at scan rate of 30 mV s⁻¹. This study therefore demonstrates that high performance electrodes can be designed from biogas slurry derived porous carbon.

CHAPTER FOUR

Effect of Biogas Slurry Carbonization Temperature on Specific Capacitance³

Abstract

The purpose of this study was to investigate the effect of carbonization temperature on specific capacitance. The mesoporous carbon materials were synthesized through carbonization of biogas slurry at 450, 550, and 650 °C followed by activation using KOH at 700 °C for 1 h. The physical characterization done by nitrogen adsorption and desorption, scanning electron microscope, transmission electron microscope, and X-ray diffraction show that carbonization temperature has significant influence on the textural and structural properties of the biogas slurry derived carbon. BET specific surface area of 567, 521, and 499 m² g⁻¹ were obtained for samples carbonized at 450, 550, and 650 °C, respectively. The electrochemical performance of the samples in 6 M KOH electrolyte exhibited high gravimetric capacitance of 262, 272, and 238 F g⁻¹ for samples carbonized at 450, 550, and 650 °C, correspondingly at scan rate of 5 mV s⁻¹. Moderate carbonization temperature of 550 °C therefore afforded the highest capacitance.

4.1 Introduction

Energy storage through supercapacitors has increased attention due to supercapacitors' high power density, high cyclic capacity, and long charge/discharge life (Burke, 2000). However, the low energy density exhibited by supercapacitors limits its applications. The energy density is largely determined by electrode materials, thus research on improving the performance of electrode and development of new electrode materials is on increase (Malmberg, 2007; Enock *et al.*, 2017b).

The energy storage capacity of an electrode depends on the structural and textural properties of the materials used to fabricate the electrode. These properties do change when the same carbon precursor is treated under different conditions thus altering the electrochemical performance of

³ This chapter is based on an article with reference MATPR4707 accepted for publication in Journal of Materials Today: Proceedings.

the carbon based electrode provided that the tests are done in the same electrolyte. The relationship between the electrochemical performance of the electrode and the carbonization temperature is not very clear as it depends on the nature of the precursors (Daud *et al.*, 2000). For example, Xu and co-workers (Xu *et al.*, 2010) observed that as carbonization temperature of apricot shells increased, the surface area, specific capacitance, and pore volume decreased. The surface area decreased from 2335 m² g⁻¹ at 400 °C to 1342 m² g⁻¹ at 800 °C, and specific capacitance decreased from 348 to 235 F g⁻¹. Phenolic resin based spheres as studied by Du and co-workers (Du *et al.*, 2010) demonstrated the decrease of surface area as well as specific capacitance as carbonization temperature increased. The idea is that at high carbonization temperature, the crystal structure of the carbon is more ordered thus hindering the etching by the activating agent. In another study on the optimization of carbonization temperature, polyacrylonitrile (PAN) fabrics were carbonized at temperatures between 400–900 °C with 100 °C step. It was observed that high surface area, pore size, and specific capacitance were obtained at moderate carbonization temperature of 600 °C (Xu *et al.*, 2007). Though the specific surface area increased when PAN fabrics were carbonized at 800, 850, 900, and 950 °C, its capacitance was enhanced by decreasing the carbonization temperature (Lee *et al.*, 2014). The pore volume and BET surface area as well as specific capacitance was observed to increase with increase in carbonization temperature when metal organic frame work (MOF-5) was carbonized at 700, 800, and 900 °C (Lanlan *et al.*, 2013). However, when the carbonization temperature increased to 950 °C the BET surface area and specific capacitance decreased. The composition of the biomass varies from one feedstock/precursor to another (Shafizadeh, 1982), therefore, it is expected that the pyrolytic behaviour differ as the cellulose, hemicelluloses and lignin content differs. Therefore, understanding the effect of carbonization temperature on pore size and structure, microcrystallinity, surface area and hence the electrochemical performance for a given biomass precursor is of prime interest.

This study focused on understanding the effect of carbonization temperature on the physical properties and electrochemical performances of the supercapacitor electrode. The use of biogas slurry as a precursor was motivated by its abundance and the fact that it is a secondary waste from renewable energy.

4.2 Materials and Methods

4.2.1 Carbonization and activation process of biogas slurry precursor

Cow dung fed biogas slurry was used as carbon precursor. The materials were first dried in air for 14 days, and then carbonized at 450, 550, and 650 °C in the presence of nitrogen gas. The carbonized char was mixed with KOH solution in a weight ratio of 1:4. The mixtures were stirred at 80 °C for 2 h to ensure homogeneity and dried in HUMBOLDT (10AF-1) oven at 120 °C for 3 h. The carbon yield obtained was 44, 40, and 38% at 450, 550 and 650 °C, respectively. The activation was done in a horizontal tube furnace at 700 °C with heating ramp rate of 10 °C min⁻¹ for 1 h in inert atmosphere created by flowing nitrogen gas. The activated carbon materials were washed with 1 M HCl to neutralize and remove residual KOH and then rinsed with distilled water until the pH was around 7. The activated carbon obtained was then dried in oven and labelled as BC450, BC550, and BC650 for carbonization temperature of 450, 550, and 650 °C respectively. The carbonized chars (unactivated) were labelled as B450, B550, and B650. The schematic illustration of synthesis of mesoporous carbon is shown in Fig. 17.

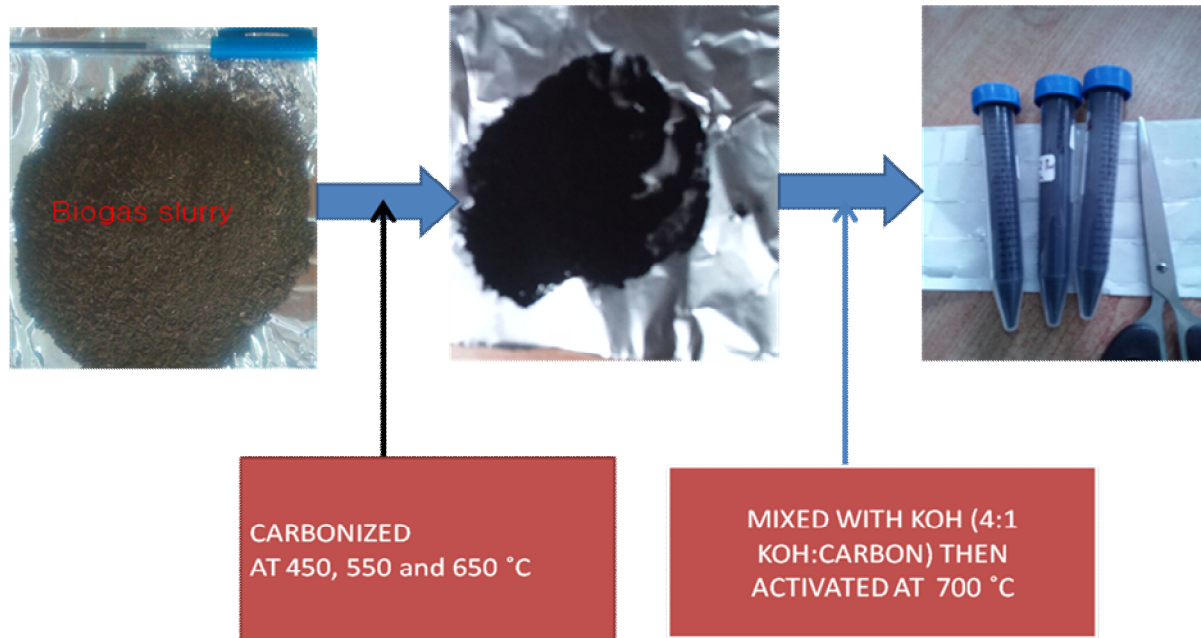


Figure 17: Schematic illustration for synthesis of mesoporous carbon under different carbonization temperature condition.

4.2.2 Physical characterisation synthesized porous carbons

The bulk chemical compositions of the samples were determined through elemental analyzer (Flash 2000 Organic elemental analyzer, Thermo Scientific). The nitrogen adsorption and desorption was performed at 77.3 K in the relative pressure range P/P_0 from approximately 0.0288 to 0.9887 using Micrometrics ASAP2020. The Brunauer–Emmet–Teller (BET) and Barret–Joyner–Hallender (BJH) equations were used to determine the surface area and pore distribution, in that order. The surface morphology of the samples was determined using field emission scanning electron microscope (FE-SEM Hitachi S-4800). X-Ray diffractometer (XRD-6000 Shimadzu) was used to investigate the crystal structures of the samples. High resolution transmission electron microscope (HRTEM) was used to investigate microstructures of the prepared porous carbon.

4.2.3 Electrode fabrication

The mass ratio of 80:10:10 of active material, conducting carbon from MTI Corporation and binder (Polyvinylidene difluoride (PVDF) from MTI Corporation) were mixed to form working electrodes. The mixture was pressed into two pieces of nickel foam ready for use. The mass of each electrode were about 5 mg.

4.2.4 Electrochemical measurements

A potentiostat /galvanostat (PGSTAT204 Metrohm) with nova 1.11 software was used to study the electrochemical performances of the electrode fabricated from biogas slurry derived carbon. In this study, 6 M KOH and 1 M Na_2SO_4 electrolytes were used in a three-electrode cell set up using Ag/AgCl_2 and platinum as reference and counter electrodes, respectively. Cyclic voltammetry was performed at scan rates of 5 to 150 mV s^{-1} in the voltage window of -1.0 to 0.0 V. The FRA32 module attached to PGSTAT204 was used to study the electrochemical impedance spectroscopy (EIS) of the samples in the frequency range of 50 kHz to 50 mHz at open circuit ($V = 0$) and amplitude of 10 mV. The specific capacitances (C) of electrodes in the CV measurements were calculated using Equation 3.2.

4.3 Results and discussion

4.3.1 Elemental analysis of raw and porous carbon materials

The elemental analysis of cow dung biogas slurry indicates that it contains 33% of carbon, 5.55% of hydrogen, 35.9% of oxygen and little amount nitrogen which was below detection limit (BDL) of the equipment used. The analysis shows that biogas slurry has high carbon content that qualify it to be suitable precursor for activated carbon as depicted in Table 4.1. It is further observed that the precursor has less carbon content than its products.

Table 11: Elemental compositions of the samples as measured by CHNOs ratio analyzer.

Sample	% C	% H	% N	% O
Biogas slurry	33.83	5.55	BDL	35.90
B650	47.13	3.99	BDL	21.46
BC450	63.13	1.53	BDL	11.04
BC650	82.73	0.85	BDL	7.03

4.3.2 Physical characterization synthesized materials

Nitrogen adsorption and desorption isotherms at 77.3 K of the samples are shown in Fig. 18. The samples showed type IV isotherms according to IUPAC classification, indicating the presence of mesopores. A H4 type hysteresis loops were observed at relative pressure from 0.5 to 1 suggesting the presence of slit-like pores (Wang *et al.*, 2014b). From 450 to 650 °C carbonization temperature, the nature of mesopores for the samples remained unchanged. At low relative pressure, there was no steep adsorption indicating the absence of significant number of micropores. From Fig. 18, it can be seen that the adsorption capacity of samples decreased with increase in carbonization temperature, similar patterns were also observed when apricot shells were carbonized at different temperatures (Xu *et al.*, 2010). However, the results are contrary to

the pattern obtained by carbonizing oil palm fibres (Ishak *et al.*, 2015) and seaweeds (Raymundo-Piñero *et al.*, 2009) at different temperatures.

The pore distributions as obtained by applying BJH method to the nitrogen adsorption and desorption isotherms are depicted in Fig. 19. As shown by adsorption isotherm (Fig. 19a), there exist micropores (diameter less than 2.0 nm) in all samples. BC450 had substantial number of micropores followed by BC550, and BC650. It is further shown that BC550 had mesoporosity nature compared to BC450 and BC650. Similarly, from the desorption isotherm (Fig 19b), all the samples showed pores distributed between 2 and 4.5 nm exemplifying the mesoporosity nature. The maximum pore volume is found to be located at 4 nm for all samples. On average BC550 sample showed considerable mesopores as compared to BC450 and BC650. The co-existence of micropores and mesopores is beneficial for charge storage and charge transfer. The samples studied exhibited similar patterns of pore distribution characteristics as confirmed by the BJH method (Fig. 19). This pattern of pore distributions in Fig. 19a, b may be due to treating the samples with same carbon to KOH mass ratio during preparation. These results agree well with the results on the adsorption and desorption isotherms in Fig. 18. Furthermore, since the pore size for all three samples are mostly below 5 nm, they can be used for an ion sorption process (Gryglewicz *et al.*, 2005).

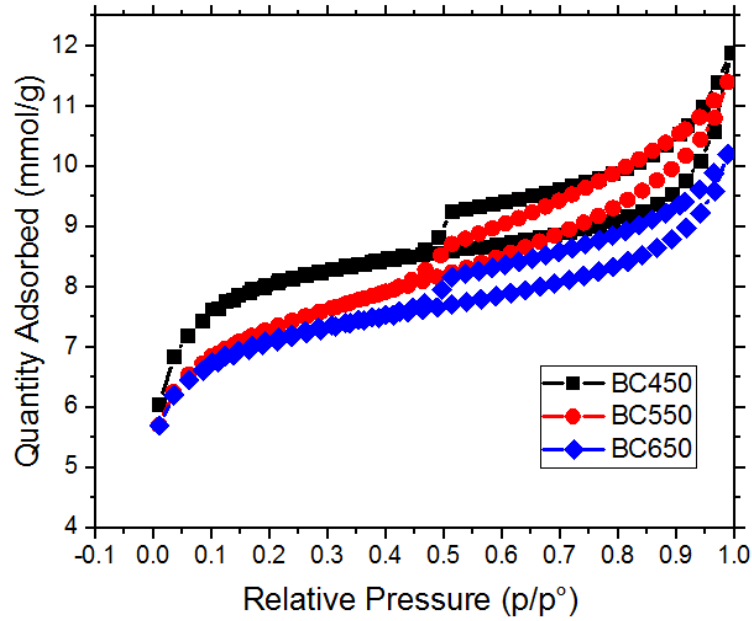


Figure 18: Nitrogen adsorption and desorption isotherms (77.3 K) of biogas slurry derived carbon at different carbonization temperature.

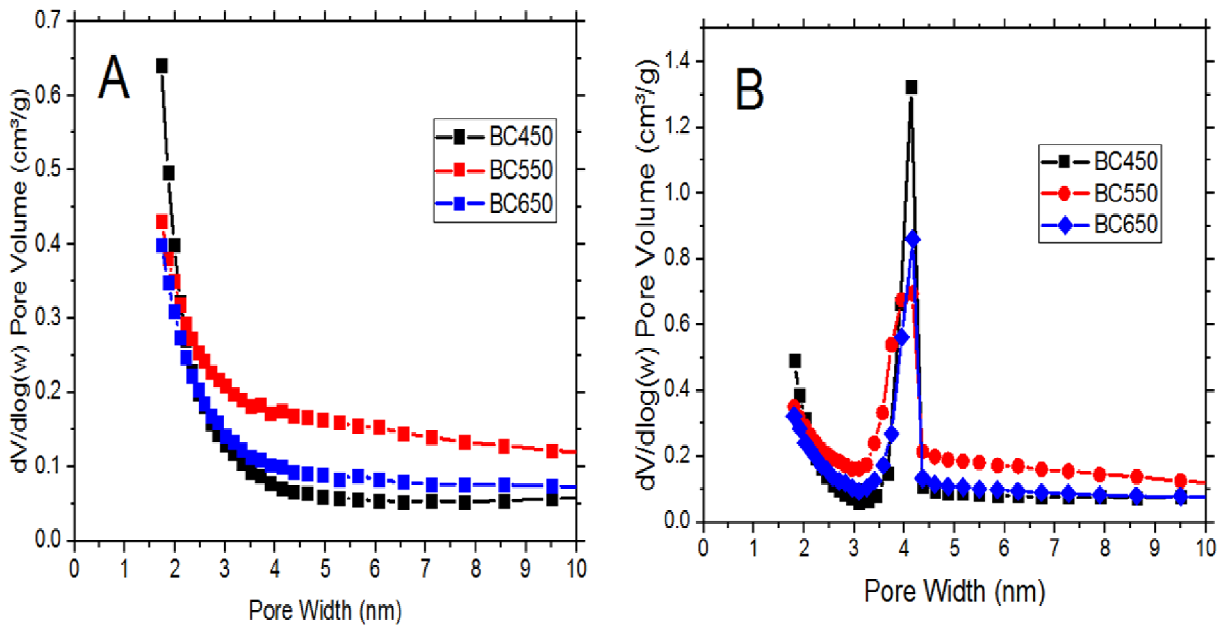


Figure 19: Pore size distribution of biogas slurry derived carbons by BJH (a) adsorption isotherms (b) desorption isotherms.

As shown in Table 4.2, the specific surface area decreased with increase in carbonization temperature. The decrease may be due to the fact that at low carbonization temperatures the biogas slurry is more susceptible to burning off while at higher the structure of BC is more ordered thus hindering the burning off and activation (Abatzoglou and Boivin, 2009; Xu *et al.*, 2010). Pore volume was highest for the BC550 sample compared to BC450 and BC650 samples. At high carbonization temperature (650 °C), the pore volume decreased due to some closure of pores. The pore width decreased with increase in carbonization temperature (from 4.6 to 4.3 nm). The average pore size of all samples was greater than 2 nm indicating that mesoporous carbon materials were successfully synthesized. The presence of mesopores on the surface of the carbon is necessary for the electric double layer capacitance as they enhance the transport of electrolyte ions.

Table 12: Textural properties of mesoporous carbon samples.

Carbon sample	BET surface area ($\text{m}^2 \text{g}^{-1}$)	Pore width (nm)	Pore volume ($\text{cm}^3 \text{g}^{-1}$)
BC450	567	4.6	0.22
BC550	521	4.3	0.24
BC650	499	4.3	0.19

Surface morphologies of the mesoporous carbon were investigated by means of field emission scanning electron microscope (FESEM). The FESEM images of BC450, BC550, and BC650 samples are shown in Fig. 20a-c, respectively. The magnification and scale for Fig. 20a-c were $\times 20 \text{ k}$ and $0.2 \mu\text{m}$, respectively. The images illustrate irregular porous structure. The structure changed slightly as the carbonization temperature increased. At high magnification, both the BC 450 and BC 550 samples show irregular morphology composed of relatively large aggregates of carbon particles, while BC 650 shows monolith morphology, see FESEM images in Fig.21a-c. The monolith morphology was formed probably due to the coalescence of carbon particles at high temperature. These results are congruent with nitrogen sorption results in Fig. 18, which show a decrease in the size of the hysteresis loop with increase in carbonization temperature. The

decrease in the size of the hysteresis loop could be ascribed to the loss of interparticle porosity as carbon particle in the aggregates coalesced at high temperature to form monoliths. The morphology and structure of BC550 sample as was further characterised using high resolution transmission electron microscope (HRTEM). Figure 20d shows that BC550 has significant amount of pores in between carbon particles (interparticle porosity) that is suggested to contribute substantively to the mesoporous nature of the sample demonstrated by nitrogen sorption results (Figs. 18 and 19 and Table 4.1). The porous structure is might be suitable for supercapacitor application.

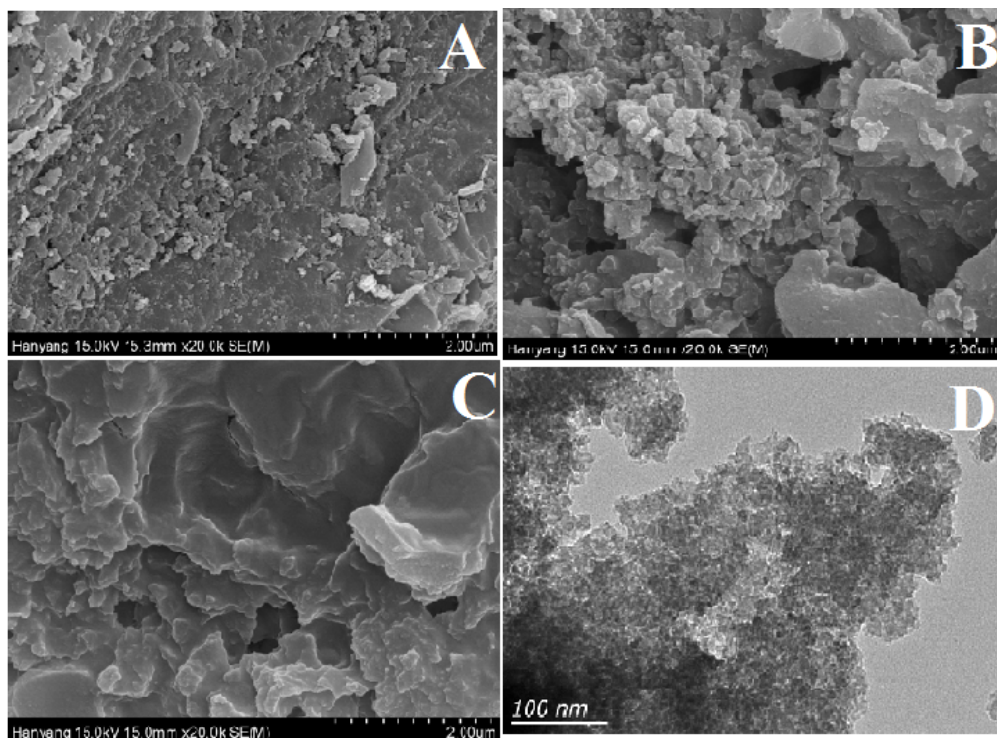


Figure 20: (a) SEM image of BC450 (b) SEM image of BC550 (c) SEM image of BC650 and (d) TEM image of BC550 carbon samples.

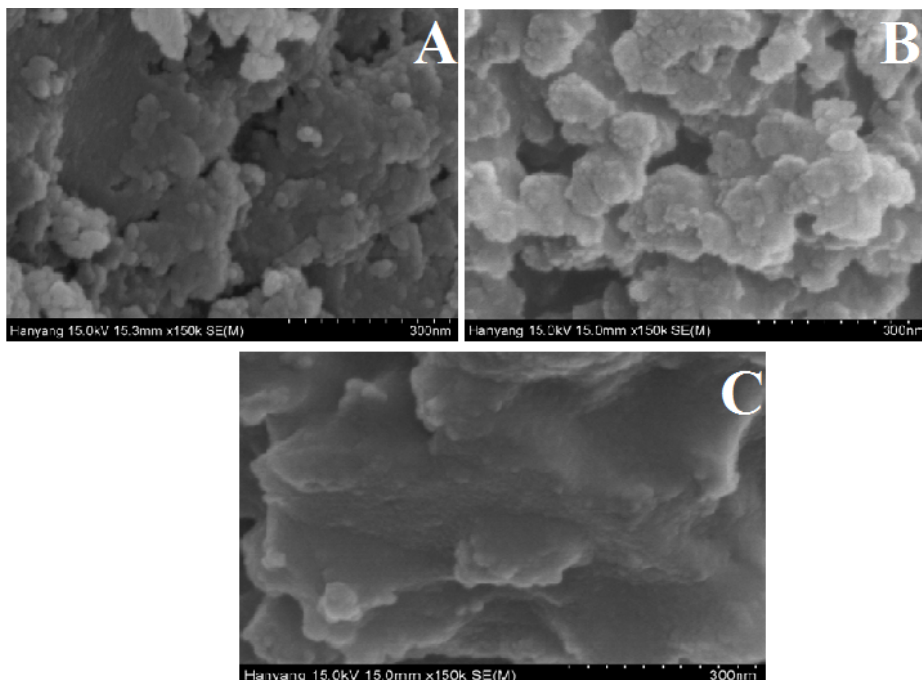


Figure 21: The high magnification FESEM images of (a) BC450, (b) BC550 and (c) BC650 carbon samples.

The X-ray diffraction patterns of the unactivated carbon at different temperatures (B450, B550, and B650) and their counterparts are shown in Fig. 22. In Fig. 22a the unactivated samples exhibit similar patterns for all temperatures. The presence of broad peaks at $2\theta = 26^\circ$ and 43° demonstrates the amorphous structure of the materials. However, Fig. 22a shows presence of sharp peaks which might be due to presence of silica components and other inorganic residues in the samples. Fig. 22b shows the diffractograms for BC450, BC550 and BC650 samples after activation. It is interesting to see the absence of the sharp peaks in activated samples. This implies the removal of the crystalline inorganic residues by both the KOH and HCl during activation and washing, respectively. All samples show nearly graphitic structure which is consistent with the TEM results signifying that they are good candidates for electron transport.

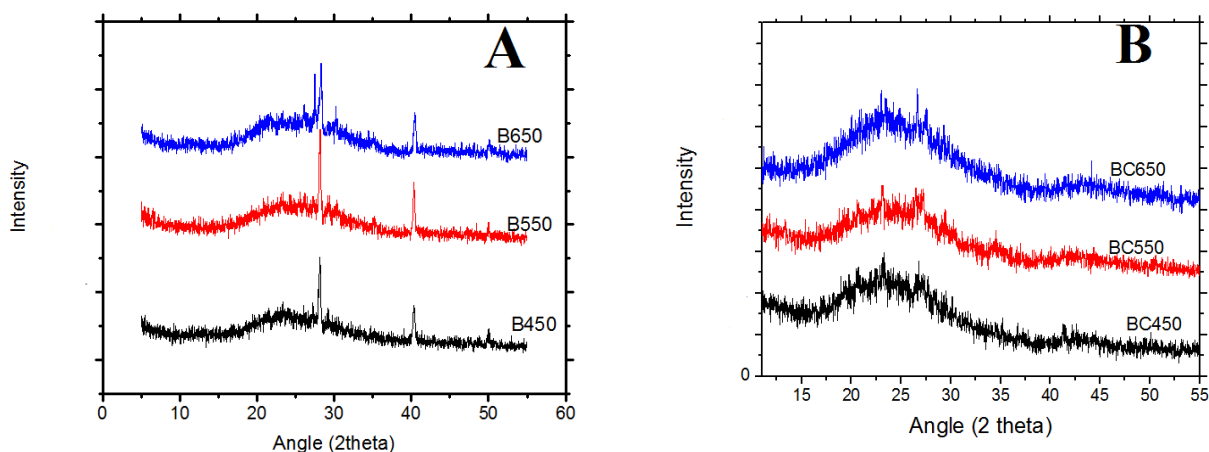


Figure 22: XRD patterns of unactivated and activated BC samples (a) unactivated (b) activated.

4.3.3 Electrochemical performances of electrodes

The electrochemical properties of the porous carbon obtained after carbonization of biogas slurry at different temperatures was studied through cyclic voltammetry (CV) and electrochemical impedance spectroscopy (EIS). Voltammograms of BC450, BC550 and BC650 samples as recorded in 6 M KOH aqueous electrolyte in voltage range of -1.0 to 0.0 V using three cell systems are shown in Fig. 23a-c, respectively. All three samples show nearly rectangular voltammograms even at high scan rates demonstrating good capacitive behaviour of the samples at different carbonization temperatures. Similar results were also reported for KOH activated argan (Elmouwahidi *et al.*, 2012), water hyacinth (Wu *et al.*, 2016), and other biomass.

Additionally, the rectangular behaviour of voltammograms describes the cyclability of the supercapacitors at high current density (Xu *et al.*, 2009). The small humps in the CV curves indicate the pseudocapacitive behaviour of the electrode contributed by the presence of oxygen functional groups. In Fig. 23d, the dependence of specific capacitance (C) on the scan rate is shown. As the scan rate increased, the C decreased meaning that at high scan rate ions get little time to penetrate through the porous electrode. It is further shown that the C of BC550 is higher than that of BC450 and BC650. One can see that in Fig. 23d, at scan rate of 5 mV s^{-1} , BC450 has C of 262 F g^{-1} , BC550 (272 F g^{-1}), and BC650 (238 F g^{-1}).

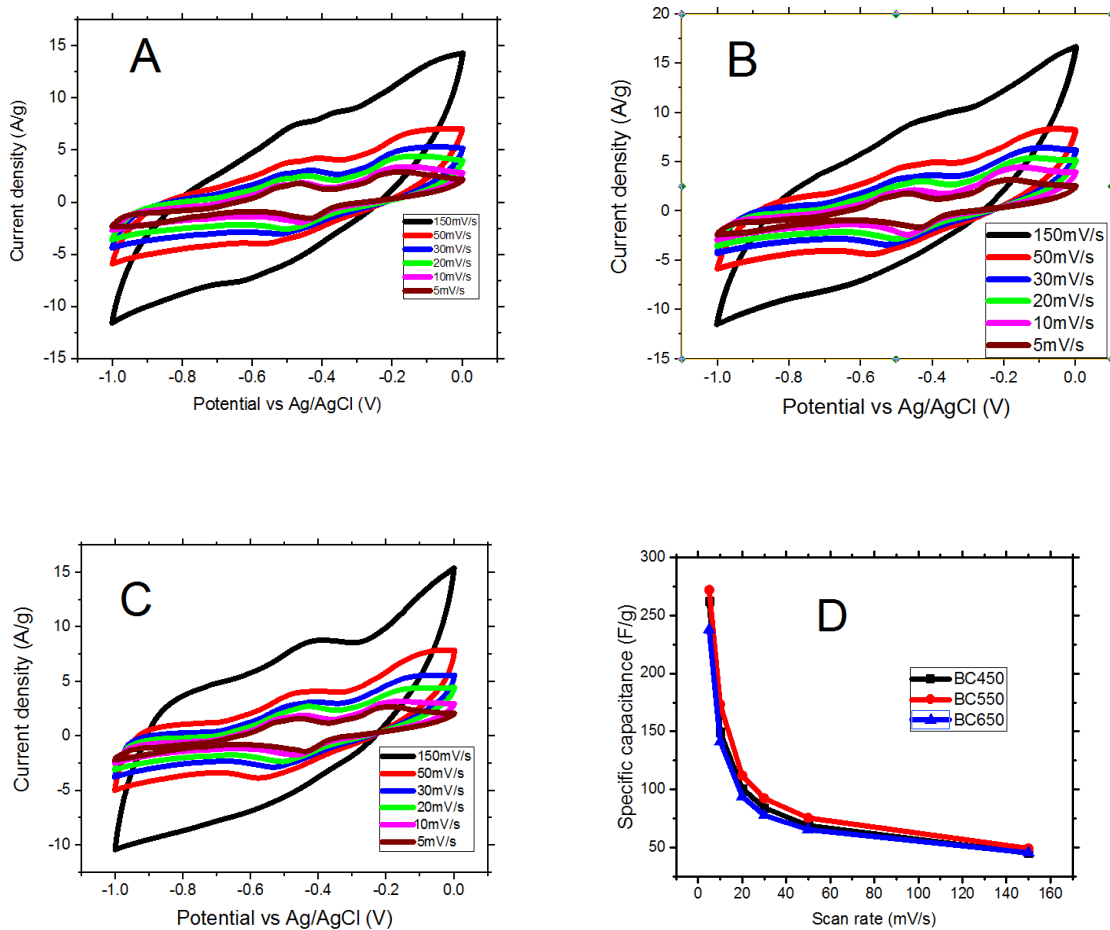


Figure 23: (a, b, and c) Cyclic voltammetry of BC450, BC550 and BC650 activated carbon in 6 M KOH (d) Specific capacitance for BC450, BC550, and BC650 as a function of scan rate.

Though BC450 has higher surface area ($567 \text{ m}^2 \text{ g}^{-1}$) than BC550 ($521 \text{ m}^2 \text{ g}^{-1}$) and BC650 ($499 \text{ m}^2 \text{ g}^{-1}$), its C was lower than that of BC550 implying that slight differences in pores volume of the BC550 ($0.40 \text{ cm}^3 \text{ g}^{-1}$) might have contributed to specific capacitance of the electrodes. As evidenced by pore distribution in Fig. 19b the average pore distribution is broader for BC550 than for other samples and this may also have contributed to specific capacitance. These results are in agreement with other results observed for fibres for oil palm (Ishak *et al.*, 2015) and polyacrylonitrile (Lee *et al.*, 2014), however, the results are contrary to those reported for phenol resin (Du *et al.*, 2010). This demonstrates that the effect of carbonization temperature on the

electrochemical performance of the electrode is not straight forward as it depends on the properties of carbon precursor.

Fig. 24 shows the cyclic voltammograms and specific capacitances of BC450, BC550 and BC650 as obtained in neutral electrolyte (1M Na₂SO₄) in the voltage range of -0.2 to 0.8 V. The CV curves were recorded at scan rate ranges from 5 to 150 mV s⁻¹. The use of Na₂SO₄ was motivated by the fact that it is noncorrosive and environmentally friendly. The supercapacitor behaviour of the BC based electrode is confirmed by presence of rectangular voltammograms shown in Fig. 24a-c for BC450, BC550 and BC650, respectively.

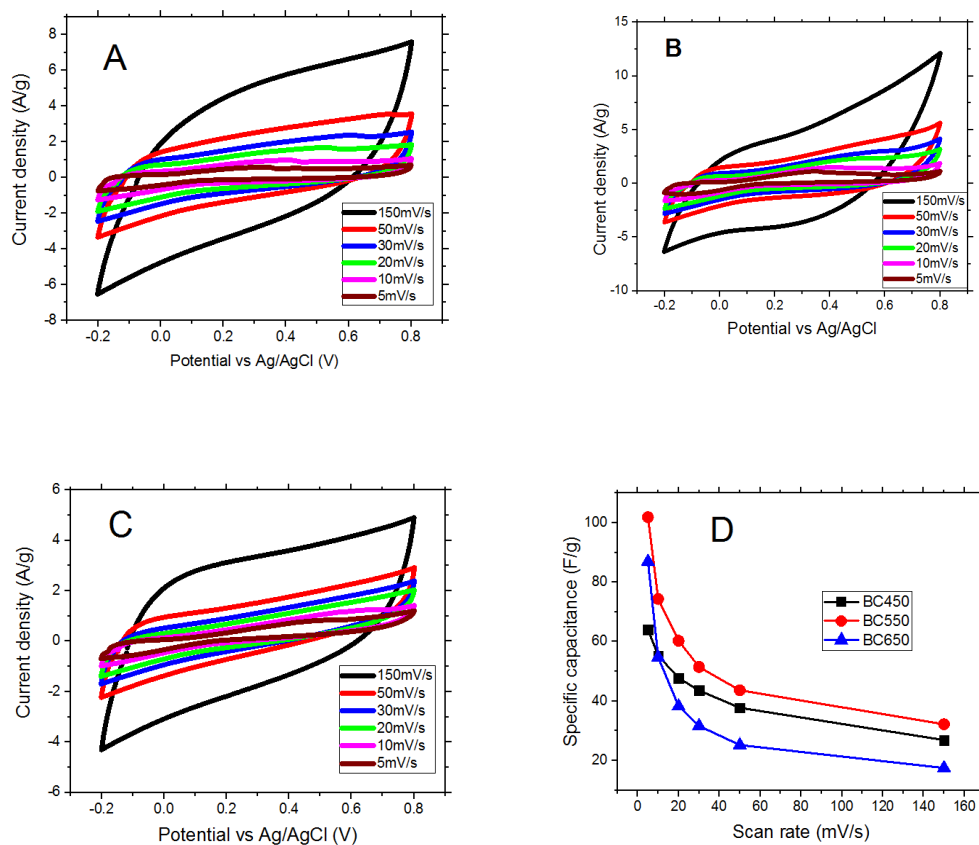


Figure 24: (a-c) Cyclic voltammetry of BC450, BC550 and BC650 activated carbon in 1 M Na₂SO₄ and (d) Specific capacitance for BC450, BC550, and BC650 as a function of scan rate.

Even at high scan rate (150 mV s^{-1}) the CV curves remain unaltered. Interestingly, the BC550 exhibits higher specific capacitance than BC450 and BC650 at the scan rate of 5 mV s^{-1} and at other scan rates. The C of BC550 was found to be around 100 F g^{-1} while BC450 has C of 86 F g^{-1} and BC650 64 F s^{-1} . This trend is akin to that obtained using 6 M KOH electrolyte as can be seen from the graph of specific capacitance versus scan rate for BC550 in 6 M KOH and $1 \text{ M Na}_2\text{SO}_4$ electrolytes in Fig. 26a. The superimposed cyclic voltammograms of BC450, BC 550, and BC 650 at scan rate of 150 mV s^{-1} in both 6 M KOH and $1 \text{ M Na}_2\text{SO}_4$ electrolytes are shown in Fig. 4.9. BC 550 exhibited wide CV curves in both 6 M KOH and $1 \text{ M Na}_2\text{SO}_4$ electrolytes implying good capacitive behaviour as illustrated in Fig. 25a,b.

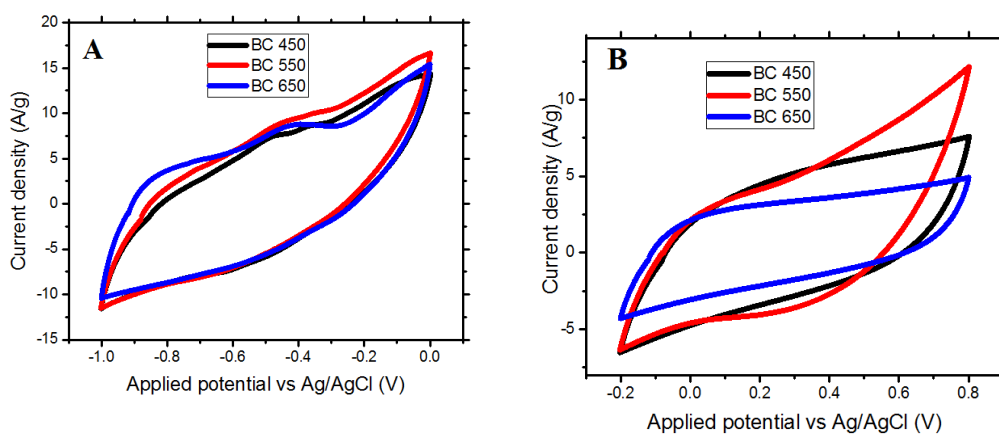


Figure 25: CV curves for porous carbon based electrodes at scan rate of 150 mV s^{-1} (a) 6 M KOH and (b) $1 \text{ M Na}_2\text{SO}_4$ electrolytes.

The electrochemical impedance spectroscopy for three electrodes was recorded in the range between 50 kHz and 50 mHz at 0 V with amplitude of 10 mV . The Nyquist plot presented in Fig. 26b shows that BC materials behave as a resistor at high frequencies and a capacitor at low frequencies. It is further shown that the equivalent series resistance (ESR) does not change much with the increase in carbonization temperature. All the three samples (BC450, BC550, and BC650) exhibited charge transfer due to presence of clear semicircle at the high frequency range (Li *et al.*, 2011a). The radius of the semicircle at high frequency region is small for all samples demonstrating that there is low resistance to mass transport and electrolyte ions diffusion. At low frequency region the slope of BC650 is steeper than those of BC450 and BC550 implying that

the capacitive behaviour of the BC650 is better than that of BC450 and BC550 (Wen *et al.*, 2009; Wang *et al.*, 2011b). These results agree with the CV curves shown in Fig. 22 and 23. Bode plots indicating the dependence of the phase angle and the magnitude of the impedance on frequency are shown in Fig. 26c. It is observed that the response time for all samples is obtained at frequency less than 100 Hz implying that the BC materials are conductive. The ionic and electronic and ionic conduction of the BC electrodes in 1 M Na₂SO₄ electrolytes are shown by the Nyquist plot in Fig. 26d. At high frequency region some small overlap of the semicircles is observed. One can see that the internal resistance of BC550 is lower than that of other samples signifying that the conductivity of the BC550 is higher than that of BC450 and BC650. This can easily be seen by observing the first intercept of the semicircle with the real axis of the plot. The high conductivity may be contributed to high pore volume of the BC550. The existence of Warburg impedance is evidenced at low frequency region with steep slopes of the plots. Presence of Warburg impedance signifies the occurrence of diffusion of ions on the interface of the BC based electrodes and electrolyte.

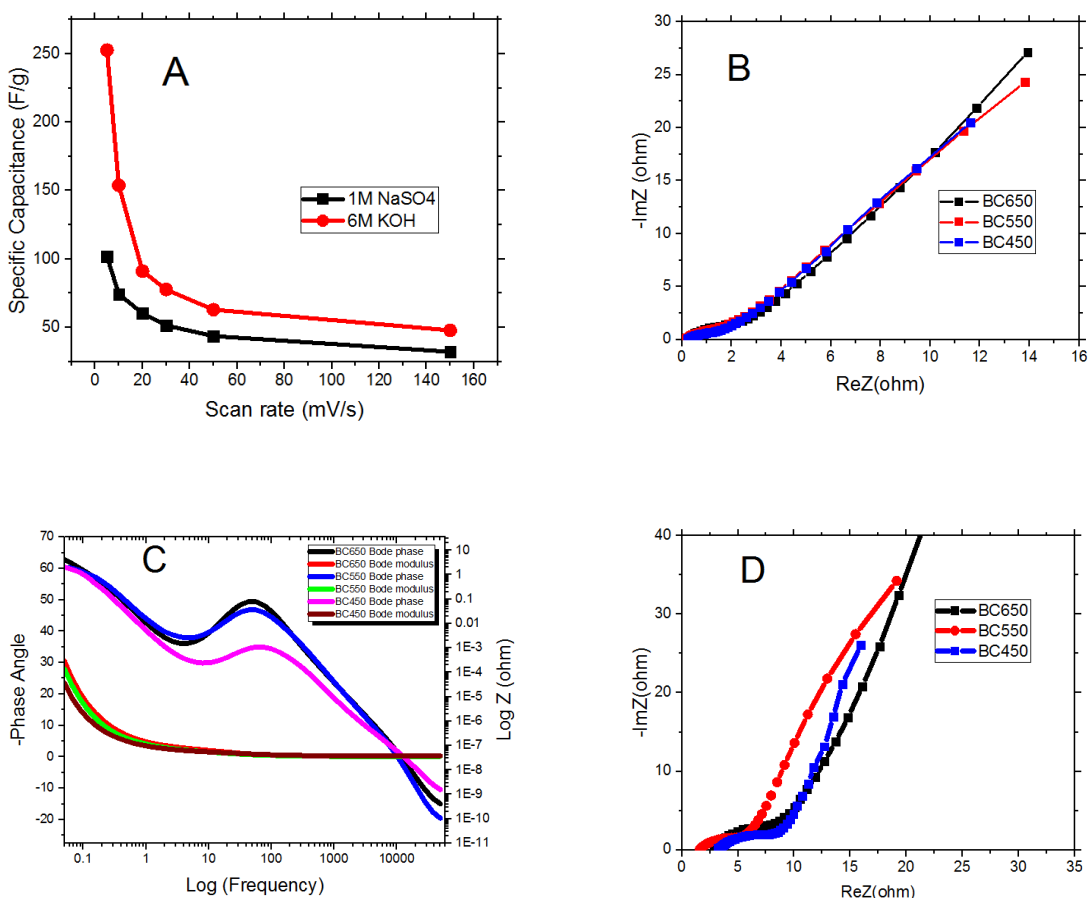


Figure 26: (a) Specific capacitance for BC550 in 6 M KOH and 1 M Na₂SO₄ electrolytes, (b) Nyquist plots for BC450, BC550, and BC650 in 6 M KOH electrolyte, (c) Bode plots for BC450, BC550, and BC650 in 6 M KOH electrolyte and (d) Nyquist plots for BC450, BC550, and BC650 in 1M Na₂SO₄ electrolyte.

4.4 Conclusion

In conclusion, we demonstrate the effect of carbonization temperature on the synthesis of mesoporous carbon from biogas slurry. The mesoporous carbon exhibited a surface area of 567 m² g⁻¹ at low carbonization temperature (450 °C) and 499 m² g⁻¹ at high carbonization temperature (650 °C). Contrary to surface area, which decreased with increasing carbonization temperature, the highest specific capacitance was obtained at moderate carbonization temperature (550 °C) both in 6 M KOH and 1 M Na₂SO₄ electrolytes. These results demonstrate that not only carbonization temperature has huge influence on the electrical performance of the

biogas slurry derived carbon based electrode but also on the pore structure. In the next chapter effect of simultaneously activation of biogas slurry chars with KOH and $ZnCl_2$ is considered.

CHAPTER FIVE

Electrochemical Performance and Pair Distribution Function Analysis of Mesoporous Biogas Slurry Derived Carbon Materials Synthesized using Combined KOH and ZnCl₂ Activation

Abstract

Mesoporous carbon has been synthesized by activating carbonized biogas slurry residues with ZnCl₂ and KOH simultaneously. The carbon to activating agent mass ratio were kept at 1:4 while the ZnCl₂ to KOH mass ratio varied from 4:0, 3:1, 2:2, 1:3, to 0:4. The highest BET specific surface area of 361 m² g⁻¹, micropore surface area of 231 m² g⁻¹, mesopore surface area of 125 m² g⁻¹, and total pore volume of 0.23 cm³ g⁻¹ which amounts to 78% mesopore content, were obtained for the sample with 3:1 ZnCl₂ to KOH mass ratio. Scanning electron microscope (SEM) images were acquired to determine the surface morphology and energy dispersive X-ray (EDX) was used to determine surface composition of the samples. The short, medium, and long-range order of the synthesized materials was studied using pair distribution function (PDF) analysis. PDF showed that in addition to the locally ordered carbon and silica phase components, samples activated using combined ZnCl₂ and KOH also contained crystalline Zn₂SiO₄ phase with the willemite structure. Electrochemical studies in three-electrode cell system revealed maximum specific capacitance of 216 F g⁻¹ exhibited by sample with a ZnCl₂ : KOH mass ratio of 3:1 at a scan rate of 5 mV s⁻¹.

5.1 Introduction

High power delivery of the stored energy devices is deemed to be the best fit for intermittent renewable energy sources, portable electronics, and braking in transport for energy recovery systems. The storage can be achieved through supercapacitors due to their high power density (Conway, 2013a). However, the energy density of supercapacitors is low and needs improvement. Energy storage in supercapacitors is facilitated by the porous nature and surface area of the electrodes, which can be made through chemical activation of carbonaceous materials derived

from biomass (He *et al.*, 2013a; Wang *et al.*, 2013b; Le Van and Thi, 2014; Wang *et al.*, 2015d). Activated carbon can be synthesized by direct carbonization of a biomass precursor, followed by chemical activation using KOH (Li *et al.*, 2010; Yang *et al.*, 2014a; Wang *et al.*, 2016d; Zhou *et al.*, 2016; Enock *et al.*, 2017a), NaOH (Xu *et al.*, 2010), phosphoric acid (Hulicova *et al.*, 2009) and ZnCl₂ (Subramanian *et al.*, 2007; Rufford *et al.*, 2008; Rufford *et al.*, 2010) as activating agents. Potassium hydroxide (KOH) has an advantage of producing activated carbon at low activating temperatures with high surface area and well-defined pore distribution. It also increases the surface oxygen of the porous carbon, which is important for pseudocapacitance and wettability (Ma *et al.*, 2013). ZnCl₂ can be used in molten salt synthesis of activated carbons from biomass (Shang *et al.*, 2015). It has the advantages of dehydrating the biomass, increases the yield of activated carbon, and restricting the formation of tar, thus promoting decomposition during carbonization. When ZnCl₂ is used in molten salt synthesis route, the carbonization temperature decreases, this is because ZnCl₂ favors a flux environment, which allows for solid–phase reactions. Therefore, in order to improve the microstructure of the carbon, combined chemical activations and molten salt synthesis routes are important. An attempt was performed by mixing the formaldehyde/phenol based nanofibre paper with KOH, sodium fluoride (NaF), sodium chloride (NaCl) in the weight ratio of 1 (KOH):1 (NaF):19 (NaCl) (Ma *et al.*, 2017). It was observed that the mixture of KOH, NaF, and NaCl had a significant effect on the specific surface area, which increased from 449 m² g⁻¹ for samples without molten salts to 1007 m² g⁻¹ when molten salts were combined with KOH.

In our previous work mesoporous carbon materials were synthesized by activating biogas slurry with KOH at different KOH to carbon ratios (Enock *et al.*, 2017a). In this study, both KOH and ZnCl₂ were used together in synthesizing active materials from biogas slurry. The effectiveness of using ZnCl₂ and KOH as molten salt and activating agent when used simultaneously in preparing the activated material was investigated. The resulting materials were heterogeneous mixtures of both short and long-range ordered phases. Pair distribution function (PDF) analysis was thus used to simultaneously characterize the order of the materials, using the information from both the Bragg and diffuse scattering components in the X-ray diffraction (XRD) patterns (Egami and Billinge, 2012).

5.2 Materials and Methods

5.2.1 Synthesis of porous carbon

Cow dung fed biogas slurry was used as the biomass source in this study. The activated materials were synthesized as follows. The biogas slurry was dried in air for 14 days then ground in a high-speed rotary cutting mill to form powder. The powder (3 g) was carbonized in a horizontal tube furnace at 550 °C for 1 h. The resulting carbonized char was mixed with ZnCl₂ and KOH then activated at 800 °C for 1 h. The carbonization and activation process was done at a heating rate of 10 °C/min in the presence of white-spot nitrogen gas. The samples produced via this route were referred to as BC-X-Y where X represents the mass of ZnCl₂, and Y represents the mass of KOH, used in the synthesis. For comparison purposes, two samples were prepared by activating carbonized materials with ZnCl₂ and KOH at 800 °C for 1 h separately. These samples were labelled as BC-4-0 and BC-0-4 for ZnCl₂ and KOH activation, respectively. The unactivated sample was designated as BC-0-0. The activated materials were washed with 1 M HCl so as to remove residual inorganics. The samples were further washed with distilled water until the pH of the filtrate was around 7 when measured using pH meter (ORION STAR A214 Thermo Scientific). The washed samples were then dried in an oven at 120 °C for 12 h.

5.2.2 Surface morphology and textural characterization

The morphologies of the sample were investigated using Scanning Electron Microscopy (SEM – PHILIPS XLS 30 with secondary electron detector and acceleration voltage of 20 kV. The samples were coated with platinum before measurements were performed. Energy dispersive X-ray (EDX) microanalysis system attached to the SEM was used to investigate the surface composition of the samples. In order to characterise the pore morphology of the materials, Trista 3020 micrometrics was used to study the nitrogen adsorption and desorption of the materials at 77 K. The BET and BJH methods were used to determine the specific surface area and pore distribution, respectively.

5.2.3 Total scattering measurements and PDF analysis

Synchrotron X-ray total scattering experiments were conducted on beamline 28-ID-2 at the National Synchrotron Light Source II (NSLS-II) at Brookhaven National Laboratory (BNL).

Samples were packed into 1 mm ID kapton capillaries and measured at 100 K using a flowing nitrogen Cryocooler. The rapid acquisition PDF (RaPDF) (Chupas *et al.*, 2003) technique was used with an X-ray energy of 67.563 keV ($\lambda = 0.18351 \text{ \AA}$). A large area 2D PerkinElmer detector (2048×2048 pixels, $200 \times 200 \text{ \mu m}$ pixel size) was mounted orthogonal to the beam path with a sample-to-detector distance of 205.4850 mm. The setup was calibrated by measuring a standard sample of known lattice parameter (Ni). The raw 2D data were azimuthally integrated and converted to 1D intensity versus the magnitude of the scattering momentum transfer Q using FIT2D (Hammersley *et al.*, 1996). The program xPDFsuite (Yang *et al.*, 2014b) was used to correct and normalize the diffraction data, and then Fourier transform them to obtain the experimental PDF, $G(r)$, according to

$$G(r) = \frac{2}{\pi} \int_{Q_{\min}}^{Q_{\max}} Q [S(Q) - 1] \sin QrdQ \quad (5.1)$$

where $S(Q)$ is the properly corrected and normalized powder diffraction intensities measured from Q_{\min} to Q_{\max} , in this case 0.6 and 20.0 \AA^{-1} , respectively. The reduced total scattering structure function is given by $F(Q) = Q[S(Q) - 1]$. The nickel standard measurement was also used to determine the instrument resolution effects on the resulting PDFs. An FCC structure was fit to the PDF using the program PDFgui (Farrow *et al.*, 2007), and the resulting resolution parameters were determined ($Q_{\text{damp}} = 0.0384 \text{ \AA}^{-1}$ and $Q_{\text{broad}} = 0.0165 \text{ \AA}^{-1}$) and fixed in subsequent refinements. For a known structure model, the PDF is simulated by

$$G(r) = 4\pi r \gamma_0(r) [\rho(r) - \rho_0] \quad (5.2)$$

$$\rho(r) = \frac{1}{4\pi r^2 N} \sum_j \sum_{j \neq i} \frac{f_i^* f_j}{\langle f \rangle^2} \delta(r - r_{ij}) \quad (5.3)$$

where ρ_0 is the atomic number density, $\rho(r)$ is the atomic pair density, which is the mean weighted density of neighbour atoms at distance r from an atom at the origin, and $\gamma_0(r)$ is

function which modulates the signal based on the shape and size of the coherently scattering domains in the material (Farrow and Billinge, 2009). The sums run over all atoms in the unit cell with periodic boundary conditions applied. f_i and f_j are the scattering factors for atoms i and j , $\langle f \rangle$ is the average scattering factor, and r_{ij} is the distance between atoms i and j . In this study, this method was applied using PDFgui, where models for separate phases were co-refined by allowing parameters including the scale of the phase, lattice parameters, thermal displacement parameters, a correction term for correlated motion, and the diameter of a finite spherical domain defining $\gamma_0(r)$, (Kodama *et al.*, 2006) to refine.

5.2.4 Fabrication of working electrode

The working electrodes were fabricated by mixing biogas derived activated carbon (4 mg), conducting carbon (0.5 mg), and polyvinylidene fluoride (PVDF) (0.5 mg). The mixtures were pressed onto nickel foam of 1 cm × 1 cm.

5.2.5 Electrochemical Measurements

Electrochemical measurements were performed using computer controlled AUTOLAB PGSTAT204 (Metrohm). Platinum was used as the counter electrode while Silver/Silver Chloride (Ag/AgCl) in a KCl solution was used as reference electrode. All electrochemical measurements were performed at room temperature in 6 M KOH in a three-electrode cell setup. The cyclic voltammetry was performed between a potential range of -1 to 0 V at scan rates of 5, 10, 20, 30, 50, and 150 mV s⁻¹. The electrochemical impedance spectroscopy (EIS) was performed in the frequency range of 1 mHz to 0.1 MHz with an AC amplitude of 10 mV at open circuit voltage. The specific capacitances (C) of different electrodes at different scan rates (mV s⁻¹) in the CV measurements were calculated using Equation 3.2.

5.3 Results and discussion

5.3.1 Physical characterization of carbon materials

Fig. 27 shows the SEM micrographs for the synthesized samples. The unactivated sample exhibits irregular, small particles, Fig. 27a with small pores. BC-0-4 has an irregular pore

structure from the KOH treatment, Fig. 27b. . BC-4-0 sample shows irregular particles Fig. 27c. On the other hand, sample BC-2-2 shows cylinder-like porous structures, Fig. 27d. Fig. 27e shows disintegration of the cylinder-like pore structure when more KOH was used. When the ratio of ZnCl_2 to KOH was changed to 3:1, no obvious change in morphology was observed. Simultaneous use of KOH and ZnCl_2 led to drastic morphology change. It was found that that as the ratio of ZnCl_2 increased, the porous structure broke down (Fig. 27 d, e, and f). From SEM micrographs (Fig. 27b-f), one can see that these samples had open pores on the surface which could facilitate the buffering of ions thus providing short space for the electrolyte ions diffusion (Xing *et al.*, 2016). At high magnification BC-1-3 and BC-3-1(Fig. 28a, b) showed some ZnO nanorods indicating that Zn residues remained in the samples

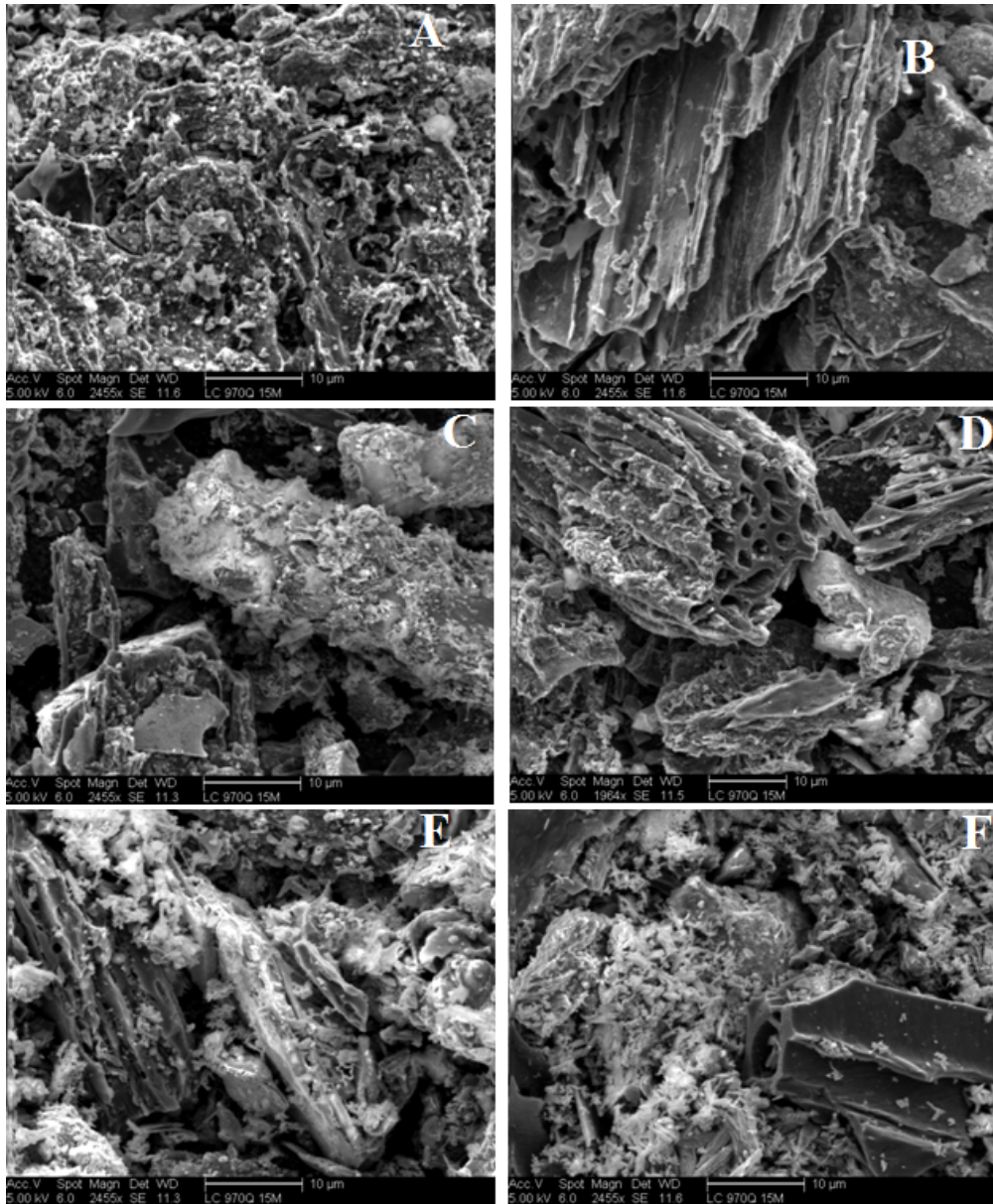


Figure 27: SEM micrographs of samples (a) BC-0-0, (b) BC-0-4, (c) BC-4-0, (d) BC-2-2, (e) BC-1-3 and (f) BC-3-1.

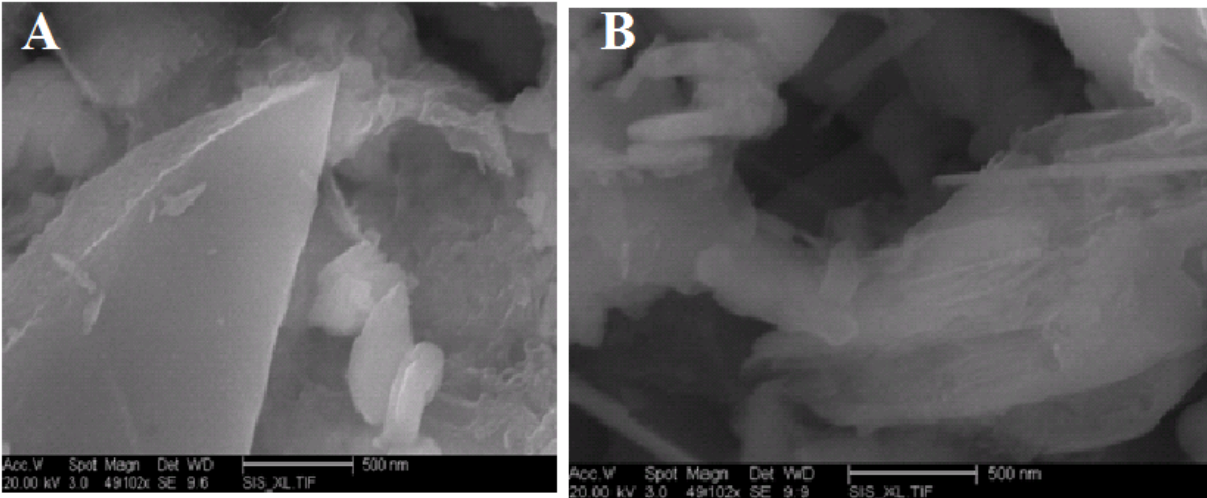


Figure 28: High magnification SEM micrography (a) BC-1-3, and (b) BC-3-1.

The energy dispersive X-rays (EDX) spectrum of BC-1-3 1 samples are shown in Fig. 29. The analysis revealed that sample BC-1-3 contained silica, magnesium, and potassium. The potassium present in the samples may have remained during washing with HCl. The presence of oxygen in the samples facilitates the pseudocapacitance characteristics and wetting behaviour of the electrodes.

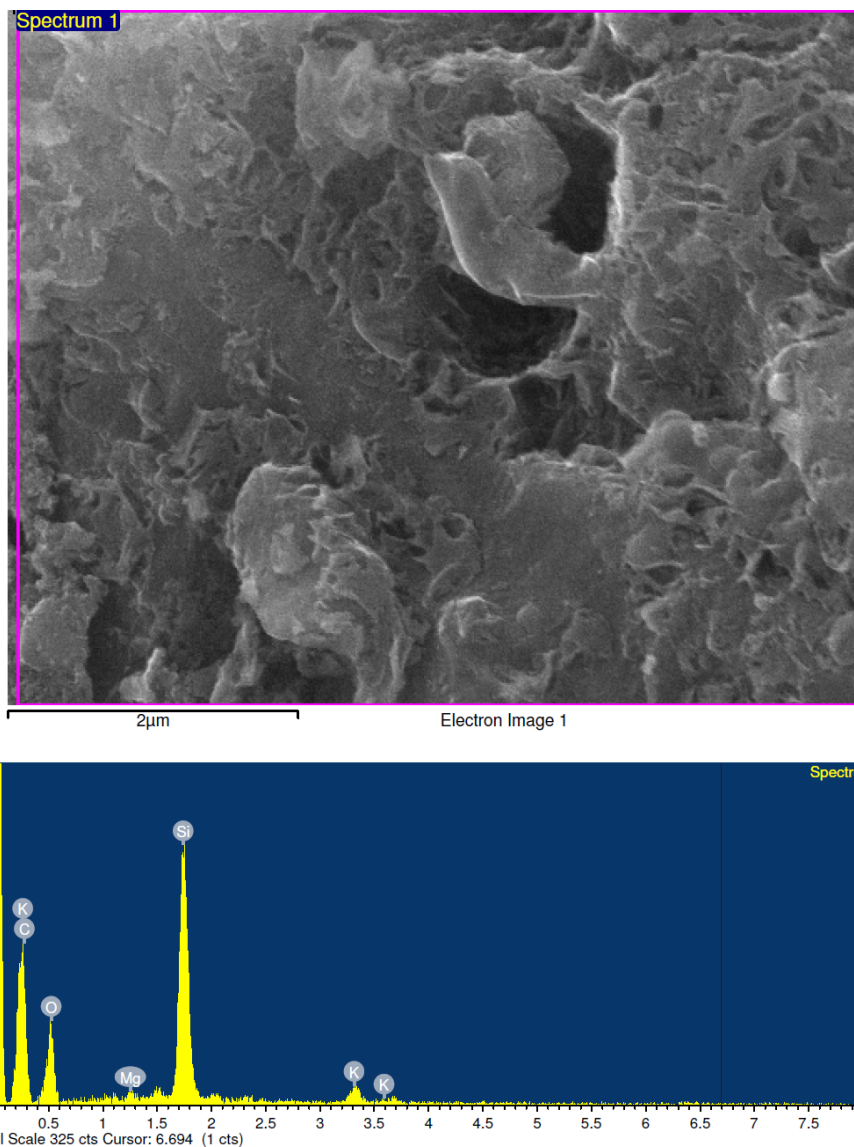


Figure 29: EDX spectrum of BC-1-3 sample.

The effect of activating agents on the pore structure and surface properties of the synthesized porous carbon was investigated using N_2 adsorption and desorption techniques. Fig. 30a shows nitrogen and desorption isotherms of BC-4-0, BC-0-4, BC-3-1, BC-1-3, and BC-2-2 samples. All samples exhibited a type IV isotherm with a well-pronounced H4 type of hysteresis loop, indicating that the mesopores were well developed. The isotherms also demonstrate that there was a complete filling of the mesopores due to the capillary condensation, which starts at $\frac{p}{p_0} = 0.5$ to approximately $\frac{p}{p_0} = 1$. The adsorption/ desorption curves of BC-0-3 and BC-2-2

almost coincide, implying that their adsorption capacities are the same. Fig. 30b and c show nitrogen adsorption and desorption isotherms for BC-4-0 and BC-3-1, respectively. The isotherms for these two samples did not close at low relative pressure (<0.1), indicating that the sorption was not complete.

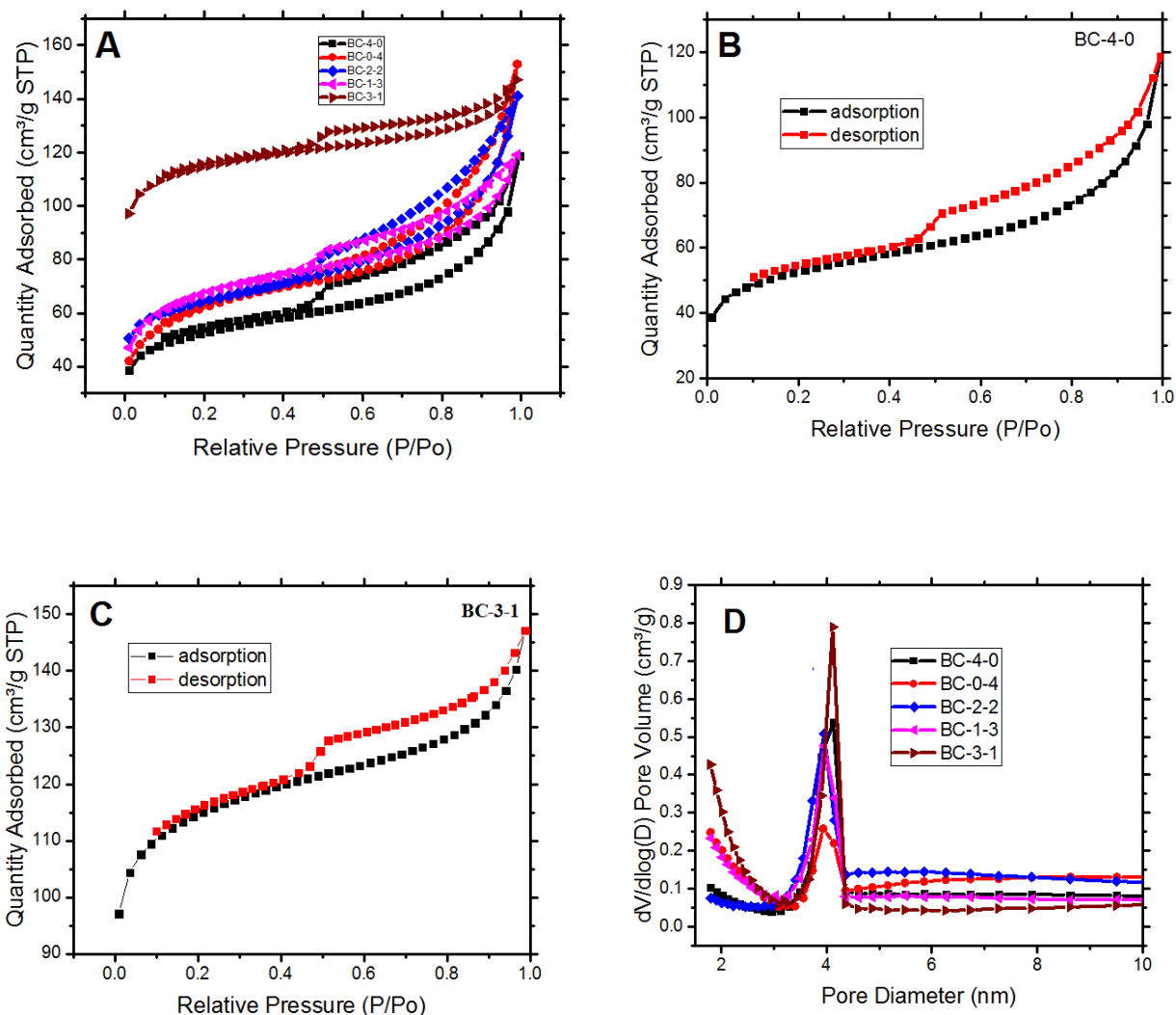


Figure 30: (a) Nitrogen adsorption and desorption isotherms of all samples, (b) Nitrogen adsorption and desorption isotherms of BC-4-0, (c) Nitrogen adsorption and desorption isotherms of BC-3-1 and (d) Pore size distribution calculated using BJH method.

The pore distributions as calculated from the desorption branch are shown in Fig. 30d. All the samples had pores approximately 4 nm in size, which is in the mesopore range. Notably, the highest degree of mesoporosity was obtained when KOH and ZnCl₂ were used simultaneously. The magnitude of the peak at 4 nm was observed in the order of BC-3-1>BC-4-0>BC-2-2>BC-1-3>BC-0-4 implying that KOH has little influence on the pore size. These mesopores are very important in facilitating charge storage as well as charge transfer in supercapacitors. In Fig. 32b, the complete lower limit of the pore size is not shown in the distribution, demonstrating the existence of micropores.

Table 5.1 shows the pore textures of the synthesized porous carbon materials. It can be seen that the ZnCl₂ itself (BC-4-0) had no significant effect on the BET surface area (171 m² g⁻¹). When KOH alone (BC-0-4) was used, 206 m² g⁻¹ surface area was achieved. BC-0-4 and BC-2-2 exhibited approximately the same BET surface area (206 m² g⁻¹). These results are consistent with those presented in Fig. 30a. BC-3-1 exhibited the highest BET surface area (356 m² g⁻¹) signifying the importance of both KOH and ZnCl₂ in activating the materials. The micropore surface area followed the same trend as that of the BET surface area. Fig. 31 depicts the surface area values (BET micro and meso) for synthesized porous materials. Though there is no defined trend of mesopore content as the ZnCl₂ and KOH ratio were altered, BC-0-4 attained 85% of mesopore content, followed by BC-3-1 (78%). The high mesopore content for BC-0-4 may be due to the high volatilisation of the organics by KOH. The average pore sizes for BC-4-0, BC-0-4 and BC-2-2 samples were comparatively equal, meaning that the synthesis routes did not change the sizes of the pores. On the other hand BC-3-1 and BC-1-3 had lower average pore size compared to other three samples.

Table 13: Pore texture and surface area of the BC mesoporous carbon samples.

Sample	$^1S_{\text{BET}}$ (m^2g^{-1})	$^2S_{\text{micro}}$ (m^2g^{-1})	$^3S_{\text{meso}}$ (m^2g^{-1})	$^4V_{\text{micro}}$ (cm^3g^{-1})	$^5V_{\text{meso}}$ (cm^3g^{-1})	$^6V_{\text{T}}$ (cm^3g^{-1})	% V_{meso}	$^7D_{\text{Average}}$ (nm)
BC-4-0	171	120	51	0.06	0.12	0.18	67	6.1
BC-0-4	206	140	66	0.03	0.18	0.21	85	6.1
BC-2-2	206	137	68	0.07	0.15	0.22	68	6.3
BC-1-3	220	176	44	0.09	0.09	0.18	50	4.4
BC-3-1	356	231	125	0.05	0.18	0.23	78	4.1

1-BET surface area, 2-Micropore surface area, 3-Mesopore surface area, 4-Micropore volume, 5-Mesopore volume, 6- Total pore volume and 7-Average pore size

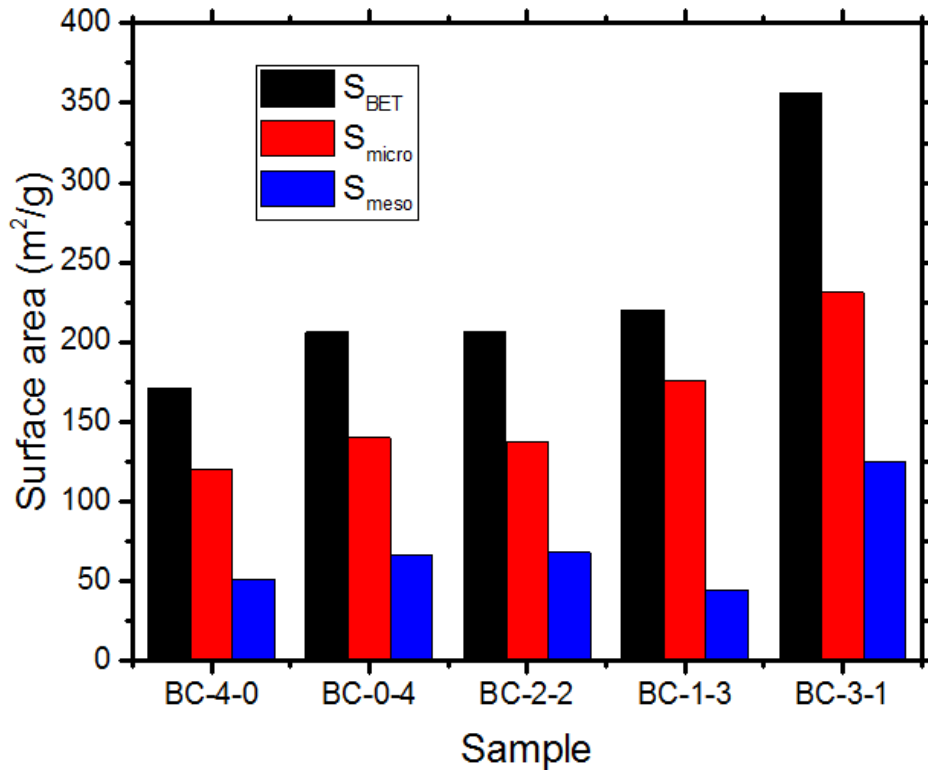


Figure 31: Surface area values (BET micro and meso) for synthesized porous materials.

5.3.2 Pair distribution function analysis (PDF) of the synthesized materials

PDF analysis was used to determine the range of order and phases present in the samples. The reduced total scattering structure functions measured and the resulting PDFs from Fourier transformation are shown in Fig. 32a and b, respectively. It is worth noting that the curves have been individually rescaled for visual comparison, and the scaling constant is given above the curves in the plot. The structure functions in Fig. 32a have been ordered based on apparent relative crystallinity, qualitatively observed by the presence of sharp Bragg peaks in the scattering pattern. The same Bragg reflections were observed in the samples activated using ZnCl_2 and KOH, BC-3-1, BC-2-2, and BC-3-1. In the case of BC-2-2, some additional sharp Bragg peaks were also present indicating the presence of another crystalline phase. More diffuse scattering was present for the untreated sample, BC-0-0, though different and less intense Bragg reflections were still present; indicating the presence of both disordered and ordered phases. The BC-4-0 and BC-0-4 structure functions appear to be the most disordered, though, they too also have minority Bragg scattering components.

The Pearson product-moment correlation coefficient was calculated between the PDFs, over different r -ranges, in order to compare the likeness between curves for the different samples. The resulting values can be seen in Table 5.2. The first number is for a range of 1.0-10.0 Å and the number in parentheses corresponds to a range of 10.0-50.0 Å. Large numbers are bold representing a high degree of similarity between the structures over the given range. The results confirm the expectations from before. The samples activated with both ZnCl_2 and KOH are the most crystalline as indicated by the presence of high amplitude, sharp peaks present out to high distances, and all have highly similar local and long range structures present. On the other hand, the unactivated sample, and the samples activated using only ZnCl_2 or KOH, are all different from the co-activated samples. These three samples have similar local structures, but are remarkably different over long ranges. The long-long range signals in BC-0-0 and BC-4-0 extend to high distances but have an overall smaller peak to trough amplitude indicating that long range ordered structures are present but different than that in the co-activated samples, and at lower concentrations. BC-0-4 appears to be the most disordered sample.

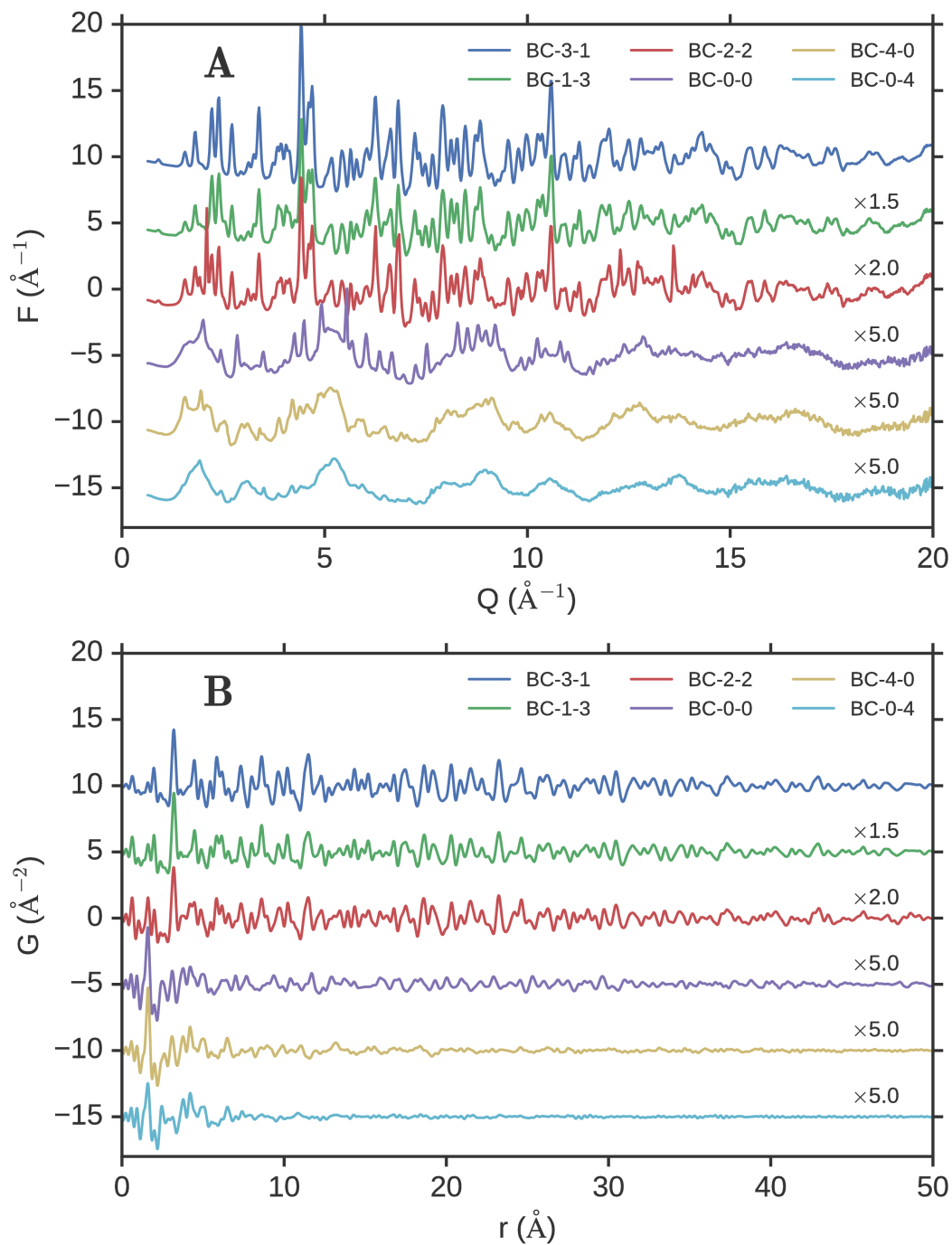


Figure 32: (a) Reduced total scattering structure functions, $F(Q)$, for the untreated and treated samples. (b) The resulting PDFs after Fourier transformation of the respective structure function in A.

Table 14: Pearson product-moment correlation coefficients calculated from the experimental PDFs of the different samples.

Sample	BC-3-1	BC-1-3	BC-2-2	BC-0-0	BC-4-0	BC-0-4
BC-3-1	1.0	0.96(0.97)	0.90(0.93)	0.02(-0.11)	0.12(-0.21)	-0.03(-0.08)
BC-1-3	-	1.0	0.92(0.91)	0.11(-0.06)	0.22(-0.12)	0.03(-0.03)
BC-2-2	-	-	1.0	0.36(-0.12)	0.47(-0.11)	0.29(-0.01)
BC-0-0	-	-	-	1.0	0.92(0.04)	0.90(0.19)
BC-4-0	-	-	-	-	1.0	0.88(0.53)
BC-0-4	-	-	-	-	-	1.0

Based on sample compositions from EDX, the PDFs for the co-activated samples were indexed against a wide range of potential structures, and the crystal structure was determined to be consistent with Zn_2SiO_4 willemite. Single phase fits of the willemite structure of these sample PDFs are shown in Fig. 33. BC-3-1 is very well described by willemite, and it only has some misfit structural features at low- r indicating the presence of some short-range ordered component. The goodness-of-fit for BC-1-3 and BC-2-2 is much worse, and it is clear from the differences that there is likely additional short- and long-range ordered structural components present which are not described by willemite. These results differ from those obtained in microporous carbon derived from wood and activated carbon fibers derived from pitch and activated with KOH (Gallego *et al.*, 2009). The differences might be due the fact that combined activation ($ZnCl_2$ and KOH) leave some residues to the samples. Also the amount of silica might have altered the atomic distances.

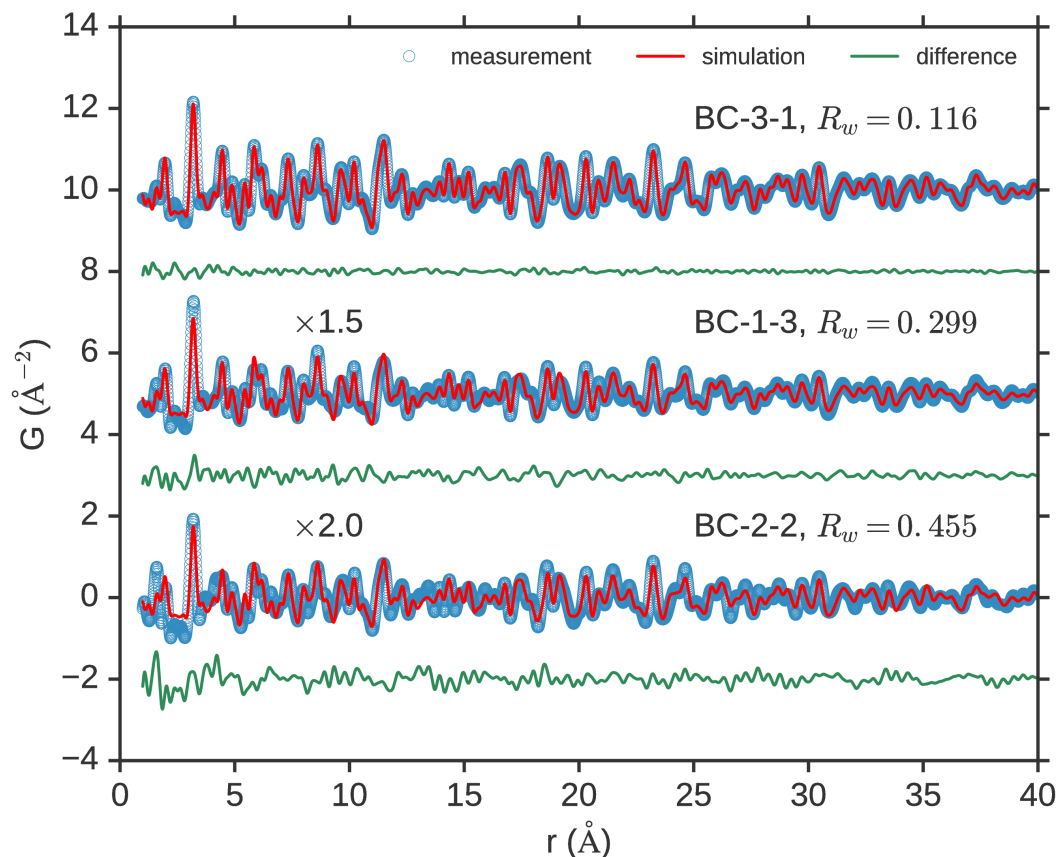


Figure 33: PDFs simulated from refinement of the willemite structure (red) to the measured PDFs (blue), over a range of 1.0 - 40.0 Å. Differences are plotted below in green.

To test this, the more disordered samples were analysed to determine the short-range components present in the active materials. A comparison of these samples is made in Fig. 34. The first and second nearest neighbour distances for graphite and the Si-O distance in silica are labelled, showing that a mixture of these components is present in the samples (Fig. 34a). In Fig. 34b, it is shown that the unfit components in the crystalline samples likely come from the remaining disordered carbonaceous and siliceous components.

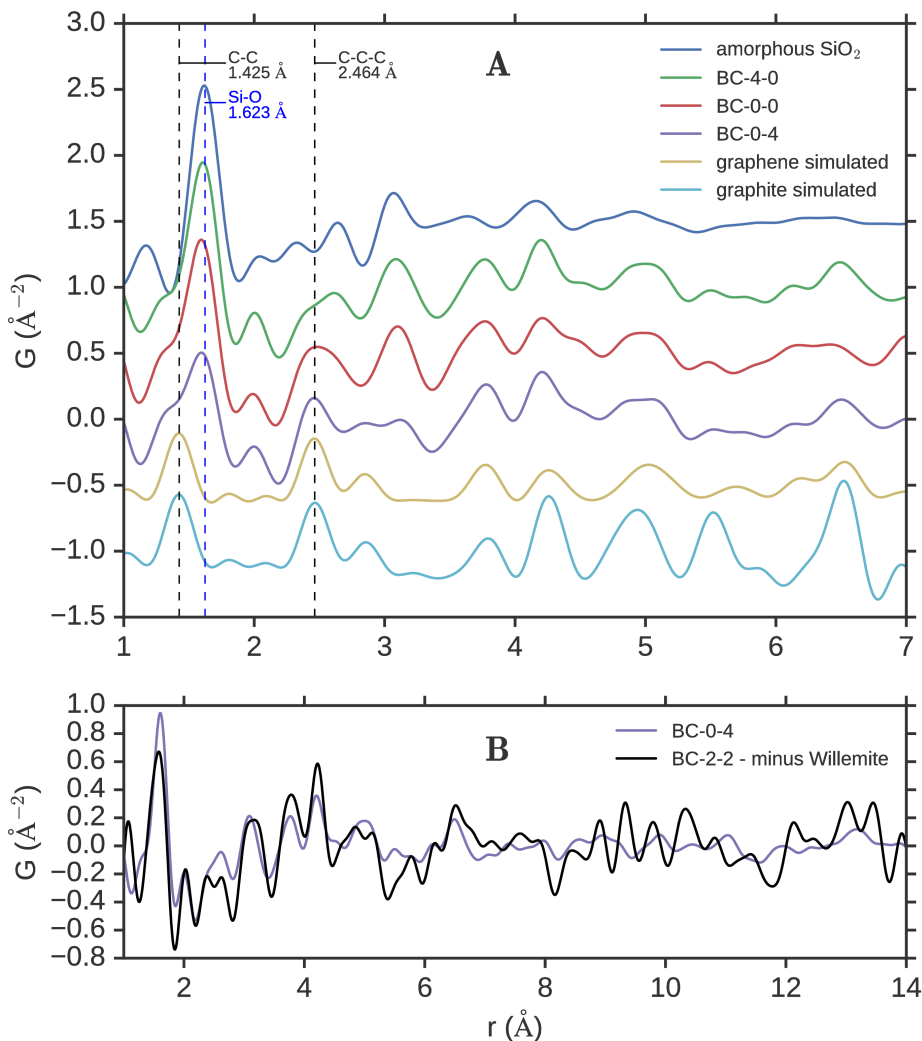


Figure 34: (a) Measured PDFs for BC-4-0, BC-0-0, and BC-0-4 are compared to a PDF measured for amorphous silica, as well as simulated PDFs for both graphite and a single layer of graphene. (b) The PDF measured for BC-0-4 compared to the residual after subtracting willemite from BC-2-2.

All of the disordered samples have a large peak at approximately 1.62\AA , which corresponds to the Si-O neighbour distance in silica. This agrees well with the high level of Si present in the samples observed with EDX. There is also a shoulder on the first peak at approximately 1.4\AA which comes from the active carbon phase in the samples. Upon further examination, it is clear that the local structure shows similarities that are intermediate between the local structure of amorphous silica, and the local structure of graphene. This indicates that the carbon components present are likely highly turbostratically disordered layers of graphite which is better for

supercapacitor applications. Unfortunately, the long range structures in these three samples were not successfully indexed, which is likely due to some longer range ordered phases consisting of silicon dioxide, or in combination with the other alkali and alkaline earth metal impurities present, observed with EDX. However, the focus was on fitting the local structure of these phases to get an estimate of types of local structuring, as well as the relative phase fractions present. The carbon component was fitted with a graphite 2H structure, with P63/mmc symmetry, with ICSD #76767. Turbostratic disorder was modelled by allowing separate thermal displacement values in the plane of the layer and out-of-plane between the layers, such that interlayer correlations were significantly broadened out. The silica component was modelled using α -Quartz low, with P3231 symmetry, ICSD #16331. The multiphase fits including the carbon and silica components are shown for all six samples in Fig. 35. The resulting phase fractions are shown in Table 5.3.

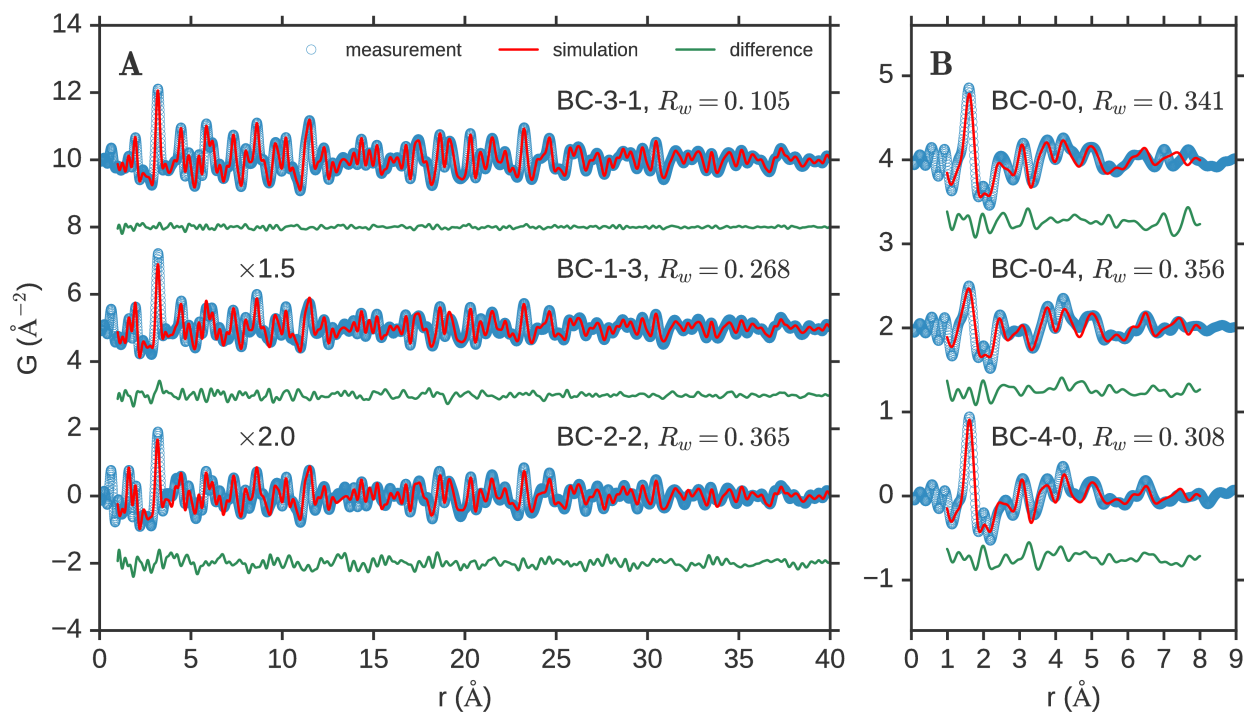


Figure 35: (a) PDFs simulated from three-phase refinement of graphite + quartz + willemite (red) to the measured PDFs (blue), over a range of 1.0-40.0 Å. Differences are plotted below in green. (b) Simulated PDFs (red) from refinement of graphite + quartz over a range of 1.0-8.0 Å.

Table 15: The resulting weight percent and coherence length for the phases fit in the models described.

	BC-0-0	BC-4-0	BC-3-1	BC-2-2	BC-1-3	BC-0-4
Carbon wt%	0.31 ^a	0.22	0.16	0.52	0.44	0.44
$d_c(\text{\AA})$	- ^b	-	10	50	21	-
Quartz wt%	0.69	0.78	0.30	0.33	0.47	0.56
$d_c(\text{\AA})$	6	6	7	8	7	7
Willemite wt%	-	-	0.54	0.15	0.09	-
$d_c(\text{\AA})$	-	-	218	343	186	-
Range (\AA)	1.0-8.0	1.0-8.0	1.0-40.0	1.0-40.0	1.0-40.0	1.0-8.0
R_w	0.341	0.308	0.105	0.365	0.268	0.356

^aAs the models are only rough approximations, phase fractions should only be considered relatively.

^bThe actual coherence lengths for the carbon phase are likely much smaller than the values achieved through the refinement, as phases may try to fit peaks from other structural components or even noise when the signal is very weak.

5.3.3 Electrochemical performance of the synthesized porous materials

Fig. 36 shows the intrinsic electrochemical characteristics of the synthesized porous materials using cyclic voltammograms at scan rates of 5 to 150 mV s^{-1} . It can be seen that the CV curves maintained the rectangular shapes even at high scan rates, indicating good capacitive behaviour of the materials. In Fig. 36a, the unactivated sample (BC-0-0) shows CV curves dramatically distorted from the ideal rectangular shape. This is indicative of poor capacitive behaviour resulting probably from low surface area and micropore and mesopore content.

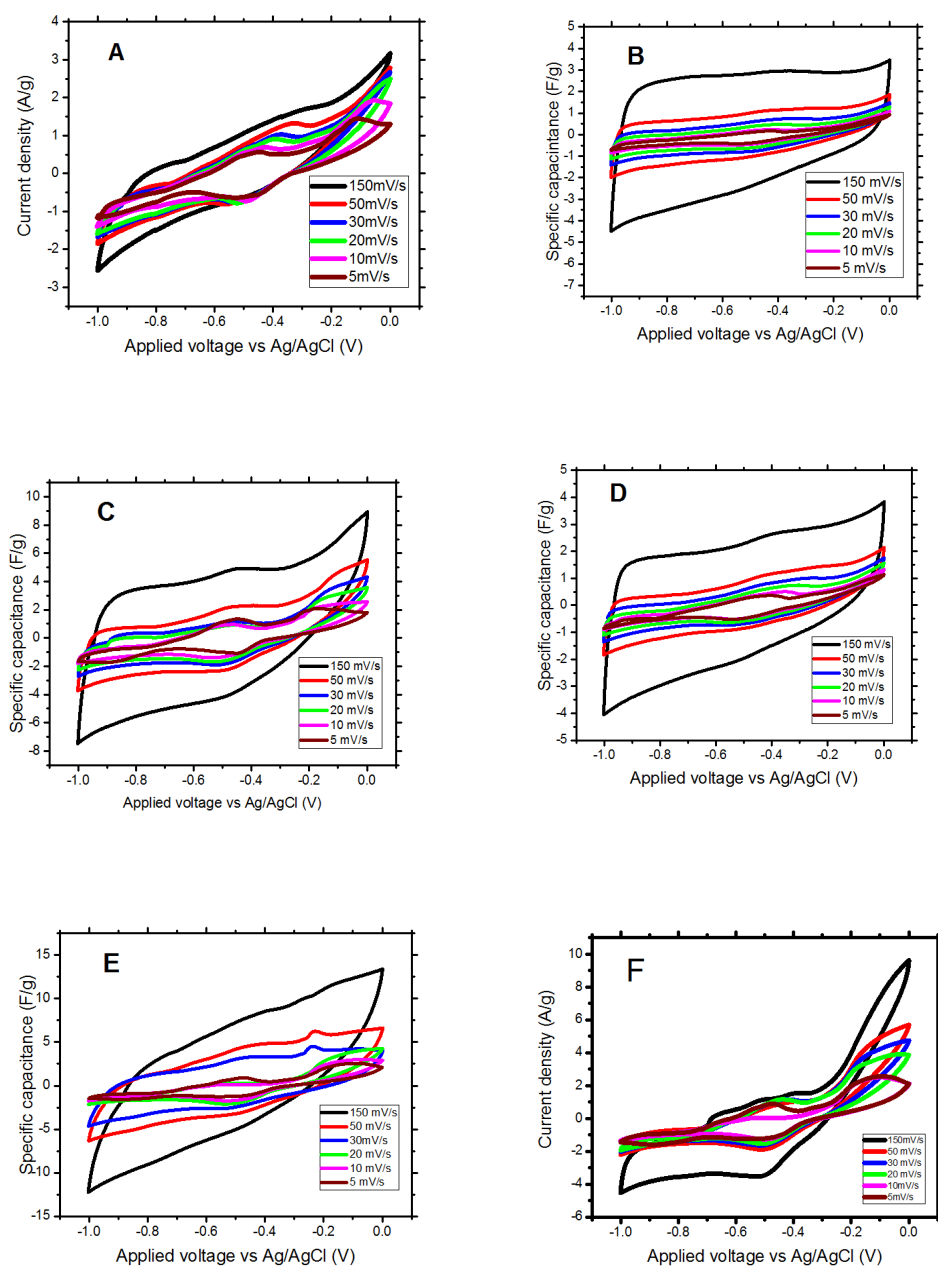


Figure 36: Cyclic voltammograms of the synthesized electrodes (a) B-0-0, (b) B-4-0, (c) B-0-4, (d) B-2-2, (e) B-1-3 and (f) B-3-1.

Fig. 36b-e shows charge and discharge profiles/curves that are nearly rectangular in shape at all the scan rates suggesting remarkable capacitive behaviour. However, as shown in Fig. 36 e-f, for BC-3-1, BC-1-3, samples, there are some humps on the CV curves that might be attributed to the faradaic reactions associated with the redox couples originating from crystalline inorganic phases

in the BC-3-1 and BC-1-3 samples as also confirmed by PDF results. Furthermore, the CV voltammograms of the BC-3-1 sample show marked deviation from the ideal rectangular shape compared to the other samples. This was probably due to the significant amount of residual crystalline ZnO and other crystalline inorganic derivatives of Zn, for instance, Zn_2SiO_4 willemite that greatly reduce the capacitive behaviour. Images of SEM at high magnification showing ZnO nanorods are shown in Fig. 28.

The specific capacitances as calculated from the CV graphs are shown in Fig. 37a. It was observed that there was no obvious trend between the $ZnCl_2$: KOH ratio and the specific capacitance. At scan rate of 5 mVs^{-1} , the unactivated sample exhibited a specific capacitance of 126 F g^{-1} while the capacitance increased to 143, 202, 161, 210 and 216 F g^{-1} for BC-0-4, BC-4-0, BC-2-2, BC-1-3 and BC-3-1, respectively. The obtained specific capacitance is lower than those obtained for phenolic resin based carbon fibers (288 F g^{-1}) (Ma *et al.*, 2017). From Fig. 37a, it is clear that the combining both the KOH and $ZnCl_2$ during activation is more suitable for supercapacitors materials.

Fig. 37b shows the electrochemical impedance spectroscopy (EIS) of the fabricated electrodes. The Nyquist plots demonstrate that all samples had high conductivity since the total ohmic resistances are low (the intercept with real Z high frequencies). The series resistance is lower than $1\ \Omega$ for all samples, implying that the electrodes had high ionic conductivity (see the inset of Fig. 37b). Moreover, BC-3-1 exhibited lower internal resistance than other samples. This might be the reason why BC-3-1 exhibited high specific capacitance. The Warburg diffusion, which is represented by the vertical nature of the graphs at low frequency, shows that BC-0-4 had more capacitive behaviour than the other electrodes.

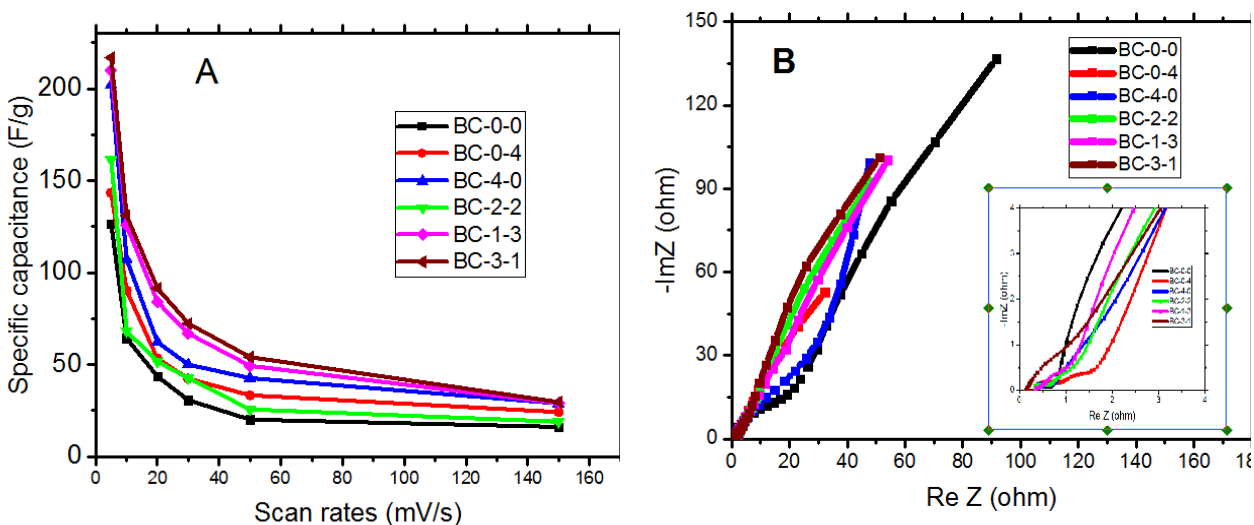


Figure 37: (a) Specific capacitance of synthesized porous carbon and (b) Nyquist plots of synthesized electrodes.

5.4 Conclusion

ZnCl₂ as a molten salt and KOH as an activating agent have been used to synthesize mesoporous carbon from biogas slurry. The ratio between ZnCl₂ and KOH was varied from 0:4, 1:3, 2:2, 3:1 and 4:0. The samples were activated at 700 °C for 1 h under nitrogen flow. Nitrogen sorption studies revealed that mesoporous carbon materials were successfully synthesized. The BC-3-1 showed the highest uptake of nitrogen as well as the highest specific surface area (356 m² g⁻¹). The short and long range structure of the samples as studied using pair distribution function (PDF) showed significant amount of siliceous components in the form of crystalline willemite in samples activated with both ZnCl₂ and KOH, and amorphous or medium range ordered silica. The electrochemical studies in three-electrode cell system revealed high specific capacitance of 216 F g⁻¹ exhibited by the sample with ZnCl₂:KOH mass ratio of 3:1:at scan rate of 5 mV s⁻¹, implying that both ZnCl₂ and KOH had significant impact in development of the materials.

CHAPTER SIX

Mesoporous Carbon/MnO₂ Composites for Synergistic Capacitance

Abstract

This chapter reports on synthesis of mesoporous carbon/MnO₂ composites through co-precipitation route followed by thermal treatment at 250 °C for 6 h. Biogas slurry was used as carbon precursor while Mn₂SO₄ and KMnO₄ were used as MnO₂ precursor. The texture and microstructure of the composites were investigated by nitrogen sorption studies at 77 K and X-ray diffraction, and Raman spectroscopy while the surface morphologies were studied through SEM and TEM. All samples exhibit type IV isotherm with total pore volume, BET, micropore, and mesopore surface area decreasing with increasing MnO₂ content in the composites. The BET surface area decreased from 514 to 110 m² g⁻¹ while total pore volume decreased from 0.52 to 0.17 cm³ g⁻¹ for samples loaded with 40 mL of 5×10⁻⁴ and 5×10⁻²M KMnO₄, respectively. The electrodes fabricated from the MnO₂/mesoporous carbon composites exhibited high specific capacitance of 709 F g⁻¹ at scan rate of 5 mV s⁻¹ in three-electrode cell system. Contrary to BET trend, specific capacitance at scan rate of 5 mV s⁻¹ is observed to increase with increasing MnO₂ content due to faradic reaction. However, at scan rate of 50 mV s⁻¹, the specific capacitance decreased with increasing amount of MnO₂ implying high electric double layer capacitance contribution. There are strong correlations between pore size, mesopore contents and specific capacitance. The microstructure together with the high electrochemical capacitance exhibited by MnO₂/mesoporous carbon composites highlights their great potential in supercapacitor applications.

6.1 Introduction

The growing interest of supercapacitors in renewable energies, transportation, and in portable electronic devices is accelerated by the fact that supercapacitors have high power density, high life cycle. However, their energy density is low thus increasing the need to the search for mechanism to increase the energy density.

Increasing energy density of supercapacitors calls for two strategies: The first is by modifying the structure and texture of the electrode materials which in turn increases the specific

capacitance and second is by increasing the operating voltage window. The first strategy has seen development of electrode materials from different precursors and exploitation of different synthetic recipes. Carbon materials such as biomass derived activated carbon (Xing *et al.*, 2011; Li *et al.*, 2012b; Ong *et al.*, 2012; Lebedeva *et al.*, 2015), graphene (Stoller *et al.*, 2008; Gong *et al.*, 2015; Enock *et al.*, 2017b) and carbon nanotube have been studied for supercapacitor applications. These carbons have a high electrical conductivity but exhibits low capacitance. Transition metal oxides such as ruthenium oxide, manganese oxides, nickel oxides, and nickel cobaltites have been extensively studied for application in supercapacitor electrodes (Subramanian *et al.*, 2006; Wang *et al.*, 2008; Inamdar *et al.*, 2011). Due to abundance, environment friendliness, and low cost of manganese (Mn), several studies have been done using MnO₂ as electrode materials for supercapacitors (Zhang *et al.*, 2013a; Wallar *et al.*, 2016). Furthermore, MnO₂ stores charges through two different mechanisms: the first is by electrolyte cations being adsorbed on the surface and the second is the intercalation of alkali metal cations or protons in the bulk of the materials. Nonetheless, its application is limited by its poor electronic and ionic conductivities ($10^{-5} - 10^{-6} \text{ S cm}^{-1}$), which hinder the rate capabilities for high power performance of supercapacitors. To improve its performance, manganese oxide materials (MnO₂) have been composited with graphene (Li *et al.*, 2011c), conducting polymers (Sivakkumar *et al.*, 2007; Han *et al.*, 2012), carbon nanotubes (CNTs) (Subramanian *et al.*, 2006; Deng *et al.*, 2013; Li *et al.*, 2014a; Li *et al.*, 2014b), and activated carbon (Wang *et al.*, 2015b). Biogas slurry has been transformed into mesoporous carbon using different synthesis routes and optimization of different parameters in previous three chapters (chapter 3, 4, and 5) of this dissertation.

It is well known that for carbon based electrodes the capacitance the specific capacitance is controlled by pore width dependence on ion salvation and the dielectric permittivity increases with increasing pore size (Redondo *et al.*, 2015) Furthermore the correlation between specific capacitance and parameters like pore volume, mesopore volume and others are complex as they depend on nature of carbon precursor and method of synthesis (Fernández *et al.*, 2009; Amaral *et al.*, 2012). To the knowledge of the authors no study has investigated the correlation between specific capacitance with pore size and mesopore content of the MnO₂/carbon composites.

In previous chapters (chapter 3-5) biogas slurry was transformed into mesoporous carbon by varying activation time, temperature and KOH to carbon mass ratio then tested for supercapacitor electrode applications (Enock *et al.*, 2017a). Owing to outstanding interconnected pores, nitrogen content and electrochemical performances of biogas slurry derived carbons, the objective of this study was to synthesize MnO₂/biogas slurry derived mesoporous carbon composites through co-precipitation method and investigate their electrochemical capabilities. Additionally, their textural, microstructure, and crystal structure characterizations were done to understand the key parameters influencing electrochemical performance. In the present chapter it has been revealed that beside the high specific capacitance (709 F g⁻¹) exhibited by MnO₂/BC derived carbon composites, the specific capacitance was also influenced by the pore size of the composites.

6.2 Materials and Methods

6.2.1 Materials

All chemicals used in this study were analytical grade and were used without further modifications. KMnO₄, MnSO₄·H₂O, KOH, and HCl were purchased from Sigma Andrich. Polyvinylene defluoride (PVDF) and conducting carbon were purchased from MTI- Corporation. Distilled water used in this study was prepared using distiller machine WSC004.MH3.4 with serial number F1-P020027.

6.2.2 Synthesis of MnO₂/mesoporous carbon composite

Co-precipitation method was used to incorporate MnO₂ in biogas derived mesoporous carbon. Different masses (0.1, 0.2, and 0.3 g) of biogas slurry derived mesoporous carbon were impregnated into 40 mL of 0.5 M MnSO₄ solution there after magnetically stirred for 3 h. After filtering the powder was put into 40 mL of 5×10⁻², 5×10⁻³, 1×10⁻³ and 5×10⁻⁴ M KMnO₄ (Lei *et al.*, 2008) and stirred for 10 min then the excess KMnO₄ was filtered.. For enhancement of the composite, the mixture was thermally treated at 250 °C in a box furnace (Lindberg Blue M Model BF51731 BC-1 Thermo Scientific) for 6 h. The thermally treated samples were labelled as 1MnO₂-*m*BC, 2MnO₂-*m*BC, 3MnO₂-*m*BC, 4MnO₂-*m*BC where numbers 1, 2, 3, and 4 represents 5×10⁻⁴, 1×10⁻³, 5×10⁻³ and 5×10⁻² M KMnO₄, respectively, and *m* is the mass of

biogas slurry derived carbon. The schematic diagram for synthesis of manganese oxide/mesoporous carbon composites is shown in Fig. 38.

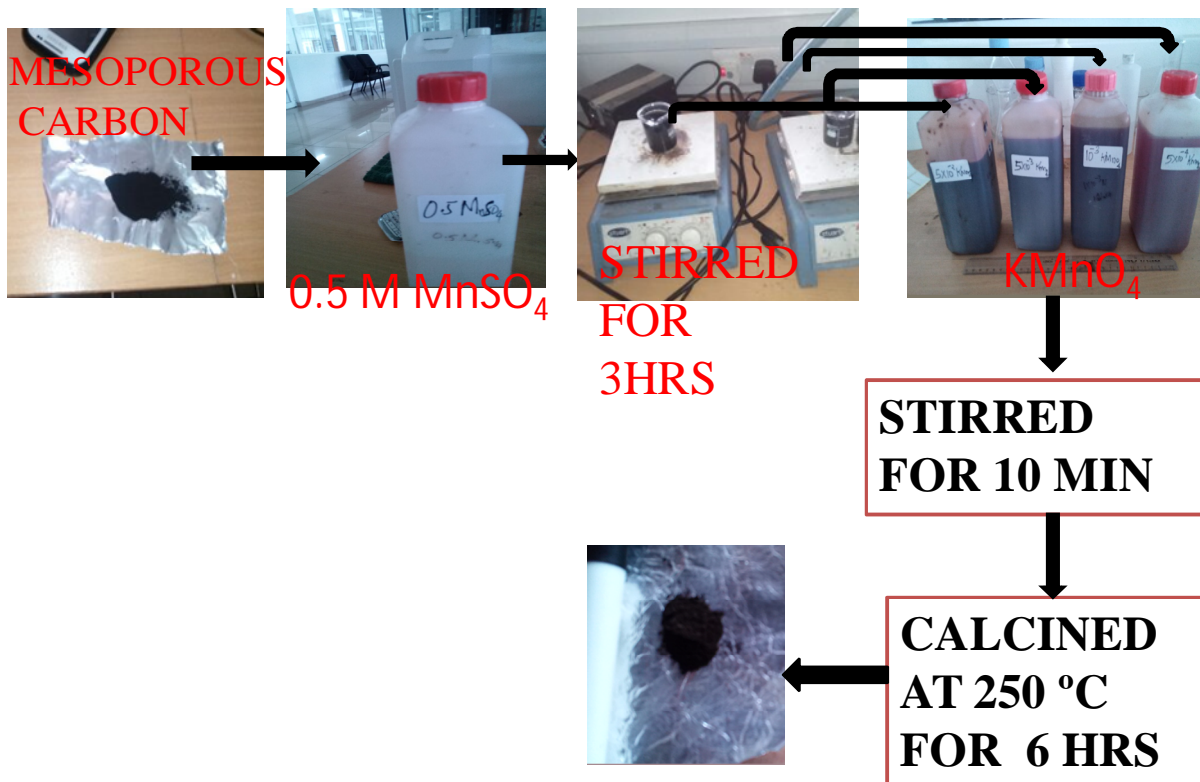


Figure 38: Schematic diagram for the synthesis of manganese oxide/mesoporous carbon composites materials.

6.2.3 Physical characterization of the composites

X-ray Diffractometer (XRD-6000, Shimadzu) with X-ray acceleration of voltage and current of 40 kV and 100 mA, respectively, was used to study the crystallographic structure of the synthesized composites. Raman spectra were recorded using Uniram-193DR, Uni Nanotech, South Korea equipped with laser of wavelength of 582.832 nm. The porosity measurement and Brunauer-Emmet-Teller (BET) surface area were determined by nitrogen adsorption and desorption machine (Micrometrics ASAP 2020) at 77 K. The actual measurements were done

after the samples were degassed at 200 °C for 6 h. Barrett-Joyner-Halenda method was employed to determine the pore distribution using the desorption branch.

6.2.4 Fabrication of working electrodes and electrochemical measurements

The working electrodes were mechanically prepared by mixing active materials (MnO₂/carbon composite) 80%, polyvinylidene difluoride (PVDF) 10% weight and conductive carbon 10 % weight. The resulting mixture was pressed in nickel foam as current collector (1 cm x 1 cm).

All electrochemical measurements were performed in computer controlled PGSTAT204 with NOVA 1.11 software. Platinum wire was used as counter electrode and Ag/AgCl was used as the reference electrode. The measurements were obtained in a three electrode configuration cell in 6 M KOH electrolyte. The cyclic voltammetry were measured at scan rates of 5 to 150 mVs⁻¹. The gravimetric capacitance was calculated from CV curves using equation (3.1).

6.3. Results and discussion

6.3.1 Physical characterization of the synthesized composites

The probing of pore structures of the MnO₂-BC mesoporous carbon composites was done by the nitrogen sorption studies. Fig. 29a shows type IV isotherms with the H4 hysteresis loop indicating the presence of mesoporous structures in all the four samples. The adsorption at low relative pressure show the presence of micropores in the synthesized composites while the increased of adsorption at high relative pressure ($\frac{P}{P_0} \geq 0.5$) points to the presence of capillary condensation. The nitrogen uptake was highest for the 1MnO₂-0.2BC followed by 2MnO₂-0.2BC, 3MnO₂-0.2BC, and 4MnO₂-0.2BC. The decrease may have been caused by the increased MnO₂ content which fills the micro and mesopores of the carbon. The pore size distributions of the composites as calculated from desorption branch are shown in Fig. 29b. 1MnO₂-0.2BC exhibits an intense peak at 4 nm compared to other samples. Furthermore, there was no shift of the peaks to the left or right as indicated in the inset of Fig. 29b, meaning that the pore structure of BC mesoporous carbon was not distorted by inclusion of MnO₂. The pores are uniformly distributed with the main peaks centred at around 4 nm.

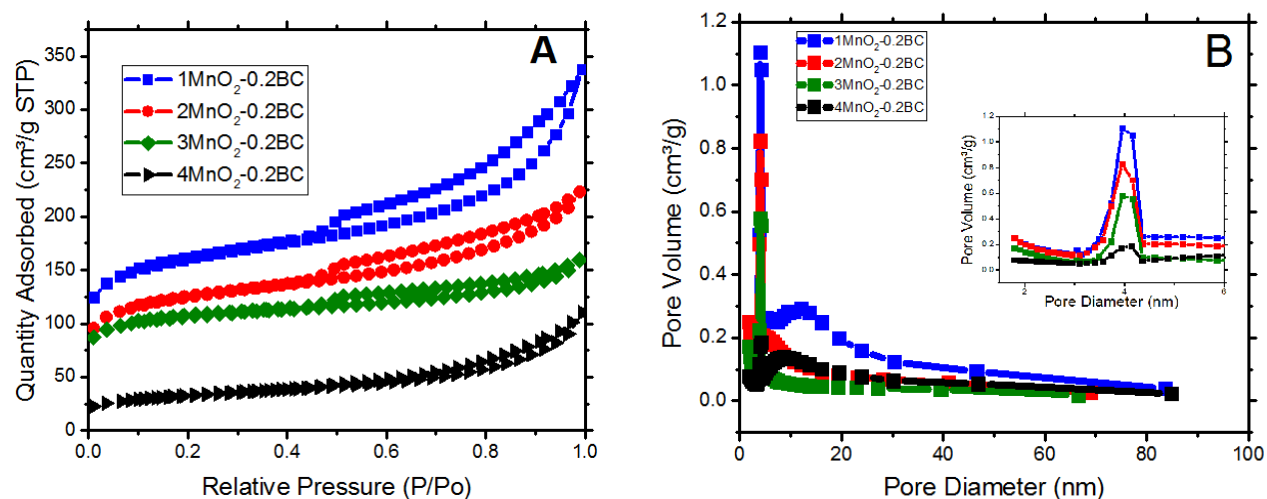


Figure 39: (a) Nitrogen adsorption and desorption isotherms and (b) Pore distributions of MnO_2/BC mesoporous carbon composites.

Table 6.1 shows the textural properties of the synthesized composites. The BET surface area, mesopore surface area (S_{meso}), micropore surface areas (S_{micro}), total pore volume (V_{T}), micropore volume (V_{micro}), and mesopore volume (V_{meso}) was found to decrease with increasing MnO_2 content in the composites. The BET surface area decreased from 514 to 110 $\text{m}^2 \text{g}^{-1}$, S_{micro} from 363 to 55 $\text{m}^2 \text{g}^{-1}$, S_{meso} from 151 to 55 $\text{m}^2 \text{g}^{-1}$, V_{micro} from 0.19 to 0.03 $\text{cm}^3 \text{g}^{-1}$, V_{meso} from 0.33 to 0.14 $\text{cm}^3 \text{g}^{-1}$, and V_{T} from 0.52 to 0.17 $\text{cm}^3 \text{g}^{-1}$. The decrease of these parameters implies that MnO_2 dispersed on the biogas slurry derived mesoporous carbon reduced the surface area and pore volume. It further confirms that MnO_2 was successfully precipitated within the pore structure of the composite rather than as separate powder. The highest values of $S_{\text{meso}}/S_{\text{micro}}$ and $V_{\text{meso}}/V_{\text{micro}}$ obtained were 1 and 4.67, respectively, and these were exhibited by the 4 MnO_2 -0.2BC, which might have been due to improved crystallinity. The average pore size for all samples was greater than 2 nm implying that the mesoporous network in the biogas slurry derived carbon were maintained after inclusion of MnO_2 . It is anticipated that the MnO_2 content will enhance pseudocapacitance behaviour while mesoporous carbon derived from biogas slurry will contribute to double layer capacitance.

Table 16: Pore texture and surface area of synthesized samples.

Sample	$^1S_{\text{BET}}$ (m^2 g^{-1})	$^2S_{\text{micro}}$ (m^2 g^{-1})	$^3S_{\text{meso}}$ (m^2 g^{-1})	$S_{\text{meso}}/S_{\text{micro}}$	$^4V_{\text{micro}}$ (cm^3 g^{-1})	$^5V_{\text{meso}}$ (cm^3 g^{-1})	$V_{\text{meso}}/V_{\text{micro}}$	$^6V_{\text{T}}$ (cm^3 g^{-1})	$^7D_{\text{Ave}}$ (nm)
1MnO ₂ - 0.2BC	514	363	151	0.42	0.19	0.33	1.74	0.52	6.2
2MnO ₂ - 0.2BC	399	311	88	0.28	0.17	0.18	1.06	0.35	5.0
3MnO ₂ - 0.2BC	334	289	45	0.16	0.15	0.10	0.67	0.25	4.7
4MnO ₂ - 0.2BC	110	55	55	1	0.03	0.14	4.67	0.17	7.3

1-BET surface area, 2-Micropore surface area, 3-Mesopore surface area, 4-Micropore volume, 5-Mesopore volume, 6- Total pore volume and 7-Average pore size

The FESEM morphological images of 1MnO₂-0.2BC, 3MnO₂-0.2BC, and 4MnO₂-0.2BC are presented in Fig. 40a-c, respectively. It can be seen that the MnO₂ was successfully dispersed on the surface of BC mesoporous. The presence of MnO₂ in the carbon is proved by existence of disordered particles with spherical shapes, which connect with each other in the images. In the high magnification FESEM image, Fig. 41a-c, it can be seen that the samples consist of microspheres whose building blocks are pseudo-nanorods, Fig. 41c

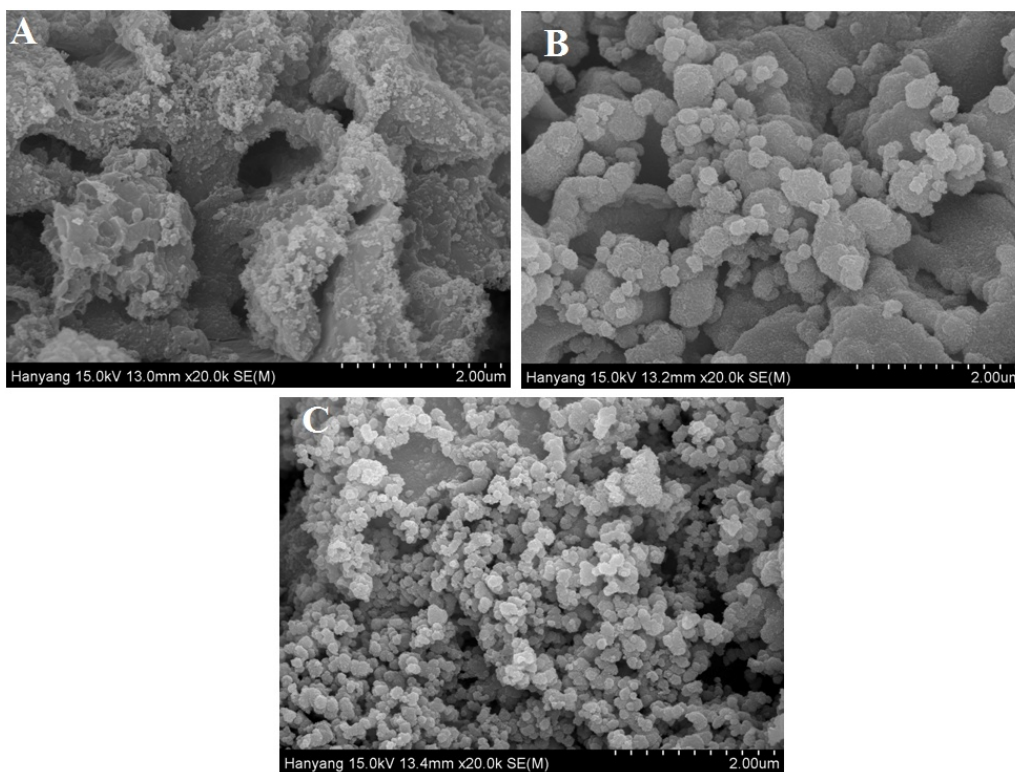


Figure 40: FESEM images of (a) $1\text{MnO}_2\text{-}0.2\text{BC}$, (b) $3\text{MnO}_2\text{-}0.2\text{BC}$ and (c) $4\text{MnO}_2\text{-}0.2\text{BC}$.

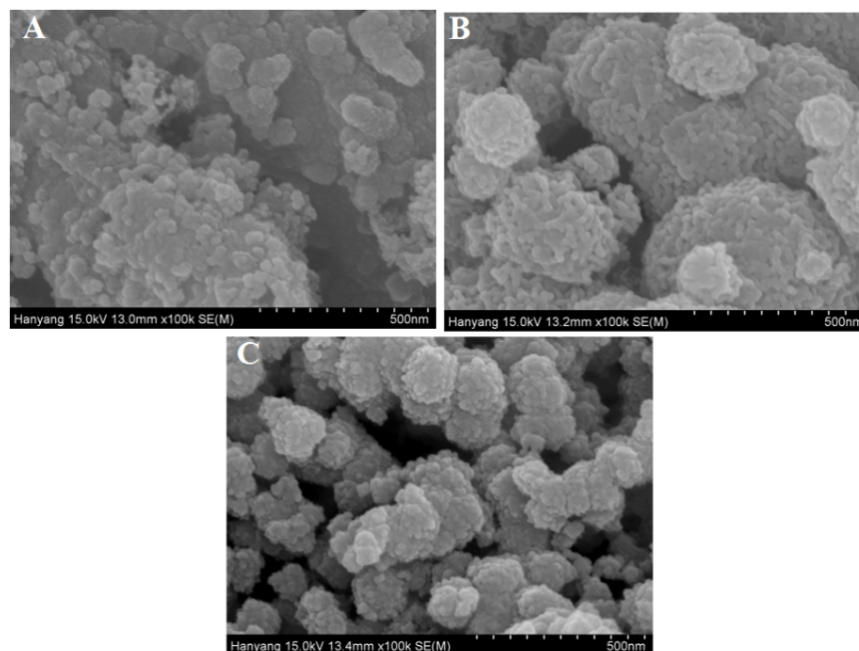


Figure 41: FE-SEM images of (a) $1\text{MnO}_2\text{-}0.2\text{BC}$, (b) $3\text{MnO}_2\text{-}0.2\text{BC}$ and (c) $4\text{MnO}_2\text{-}0.2\text{BC}$ at high magnification.

The energy dispersive X-ray spectrometer (EDX) was used to determine the surface composition of the samples. Fig. 42 shows peaks for the elements present in the samples. Each Figure has table inset, which shows the weight and atomic percentages of each element present in the composite. It can be seen that the weight percentage of Mn was lowest for 1MnO₂-0.2BC (3.61%), Fig. 42a, followed by 3MnO₂-0.2BC (8.78%) in Fig. 42b, and 4MnO₂-0.2BC (55.7%) in Fig. 42c. These results are consistent with the FESEM images in Fig. 40c and 41c where the relatively large MnO₂ pseudo-nanorods could be seen on the surface of 4MnO₂-0.2BC sample. On the other hand, carbon content decreased in the order of 1MnO₂-0.2BC (64.41%) > 3MnO₂-0.2BC (15.80) > 4MnO₂-0.2BC (4.99%). The EDX spectra also confirmed the presence of other elements such as nitrogen, oxygen, and sulphur in the composites. These elements are important in energy storage as they enhance pseudocapacitance behaviour and improve wettability of the electrodes. The high content of Mn and O indicates that the MnO₂ were successfully formed.

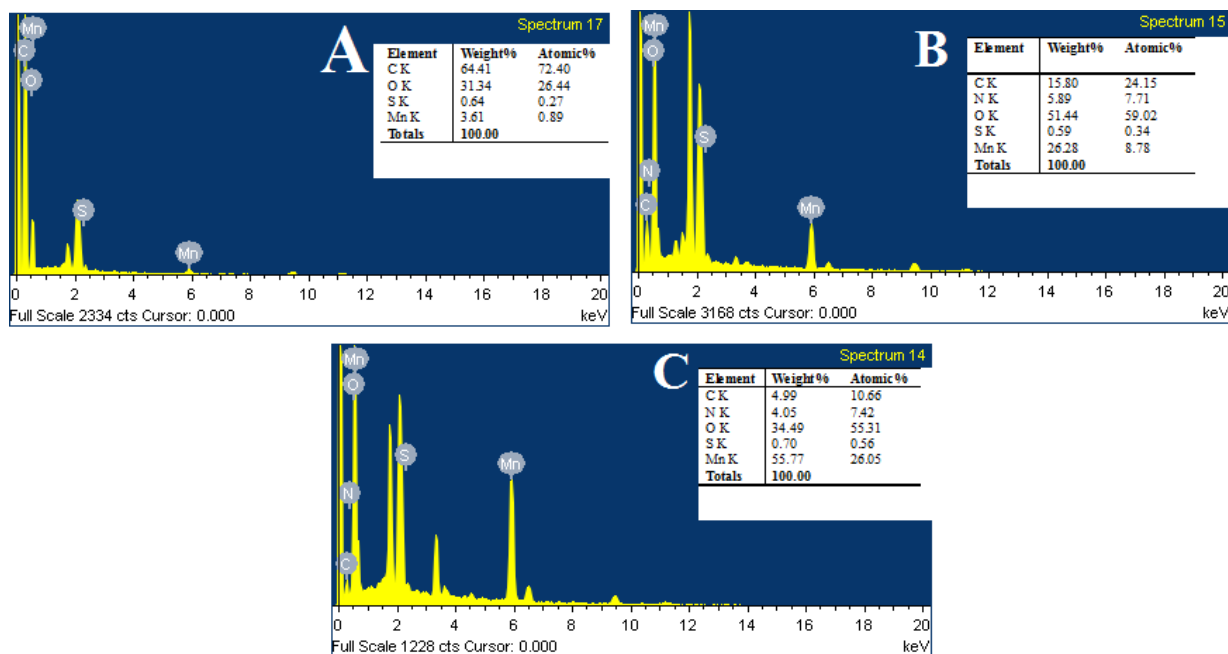


Figure 42: EDX spectra of (a) 1MnO₂-0.2BC (b) 3MnO₂-0.2BC (c) 4MnO₂-0.2BC.

The microstructures of the MnO₂/BC composites were further investigated using TEM at different magnifications. Fig. 43 shows the low magnification TEM images of the composites. In Fig. 43a-c it can be seen that there were co-existence of mesoporous carbon and MnO₂. It is shown further in Fig. 43c that 4MnO₂-0.2BC exposed slightly flower like structure morphology.

The nanoparticles with few nanorods of MnO₂ are shown in Fig.43d. The occurrence of MnO₂ nanorods exemplify that MnO₂ were successfully intercalated in the mesoporous carbon.

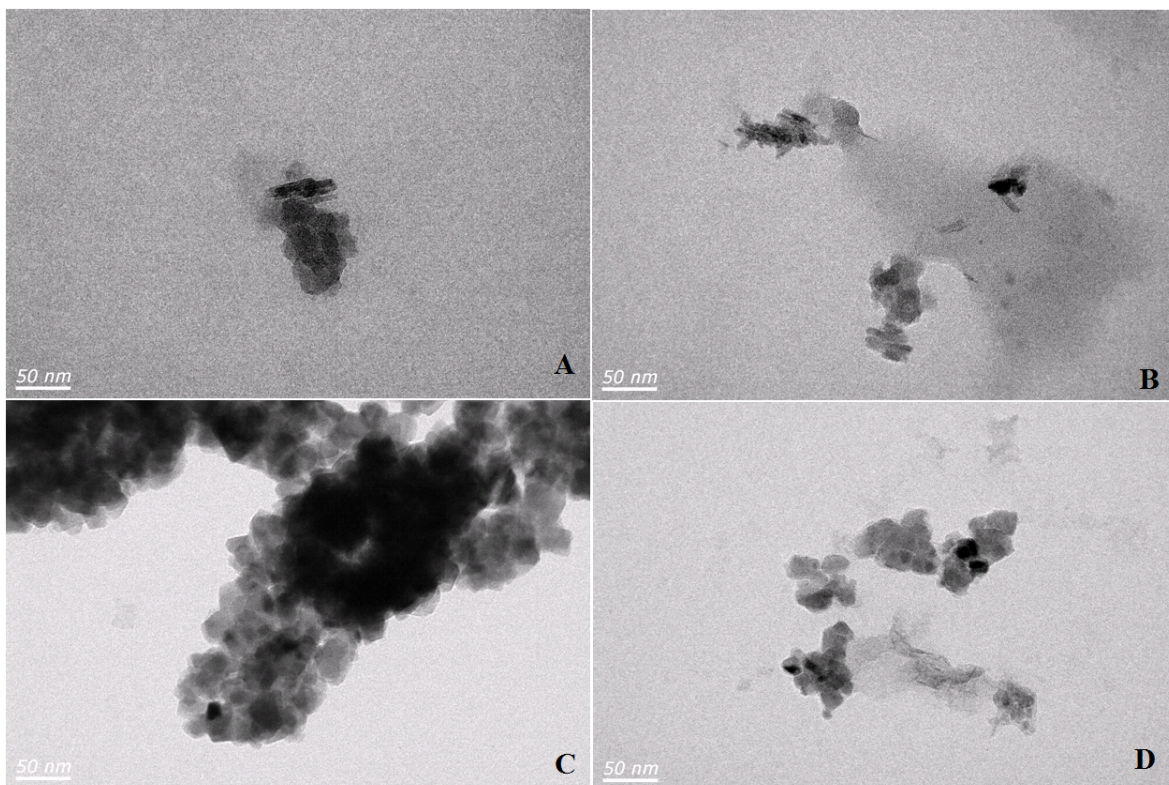


Figure 43: TEM images of (a) 1MnO₂-0.2BC (b) 3MnO₂-0.2BC, and (c,d) 4MnO₂-0.2BC.

Fig. 44 shows the HRTEM images of the composites. It is shown that the MnO₂ were intercalated into the carbon matrix (see Fig. 44a, c and d). In Fig. 44b the interplane spacing of 1MnO₂-0.2BC was determined to be 0.36 nm which corresponds to (002) plane of reflection of MnO₂. The combined carbon and MnO₂ structures were revealed in Figure 6c and d in which the lattice distance were 0.31 nm corresponding to (311) plane of reflection of MnO₂. It can be seen further that different particle was formed as MnO₂ content increased (see Fig. 44d). 4MnO₂-0.2BC revealed the interplanar spacings of 0.29, 0.32, 0.34, and 0.53 The Fast Fourier transform (FFT) pattern (inserts of Fig. 44b and d) verify the single crystal character of MnO₂ nano rods

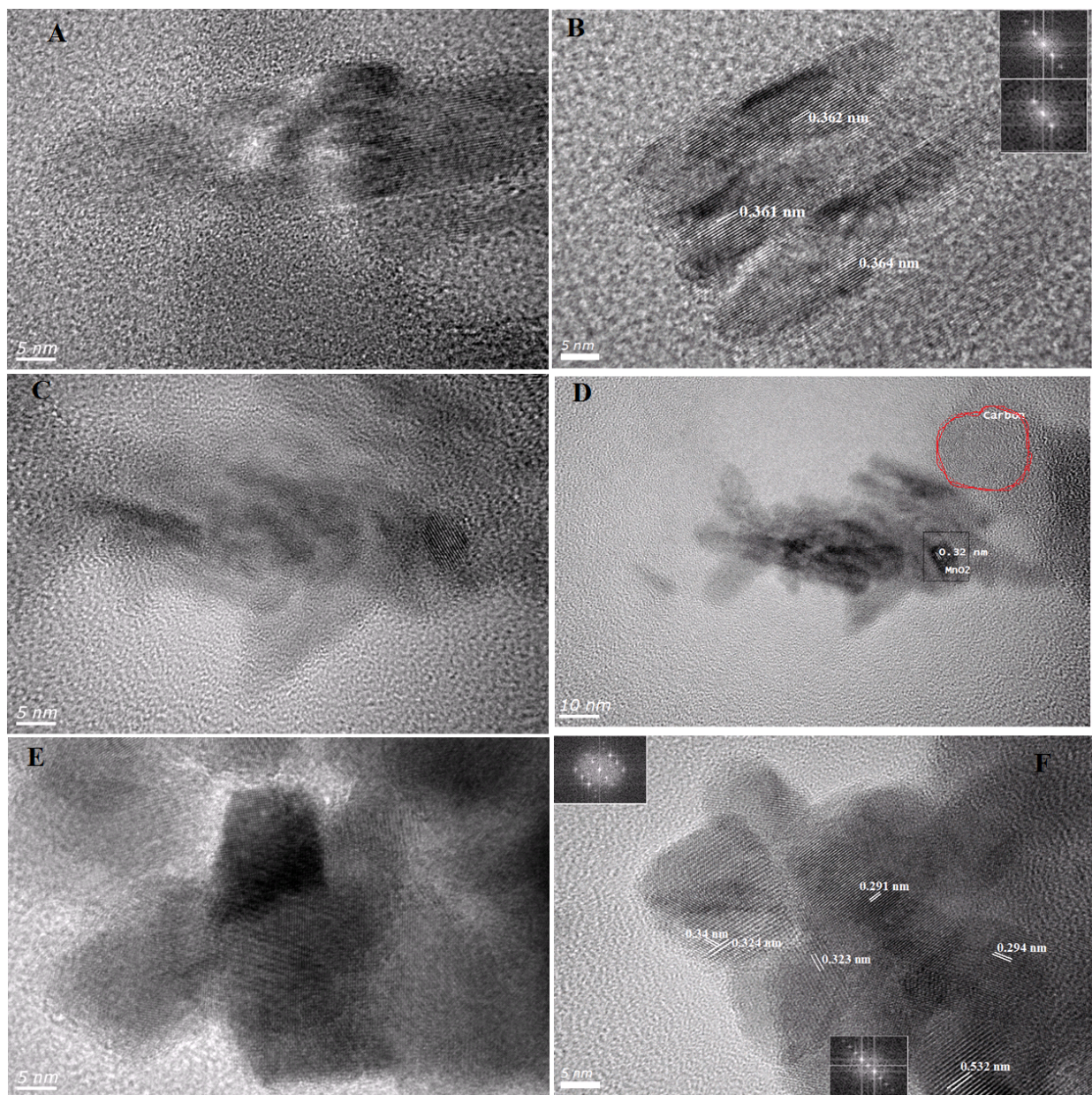


Figure 44: HRTEM images at high magnifications (a, b) 1MnO₂-0.2BC (c, d) 3MnO₂-0.2BC, and (e, f) 4MnO₂-0.2BC.

To further investigate the crystallography behaviour of the composites, X-ray diffraction studies were conducted. It is shown in Fig. 45 that the composites exhibited three main broad peaks at 11.5°, 25°, and 42° (2θ). The intensities of these peaks were observed to be stronger than those for the BC - mesoporous carbon materials in Chapters 3 and 4 of this dissertation indicating that the MnO₂ precipitation promotes graphitization of the carbon matrix (Liu *et al.*, 2014a). The

broad peak at $2\theta = 25^\circ$ is due to contribution of the amorphous biogas slurry derived carbon present in the composites. Despite the poor crystallinity, the presence of broad peaks at $2\theta = 11.5^\circ$, 25° and 42° which are characteristics of amorphous carbon, presence of MnO_2 pseudo-nanorods, Fig. 41c, and EDX results validates the formation of composites.

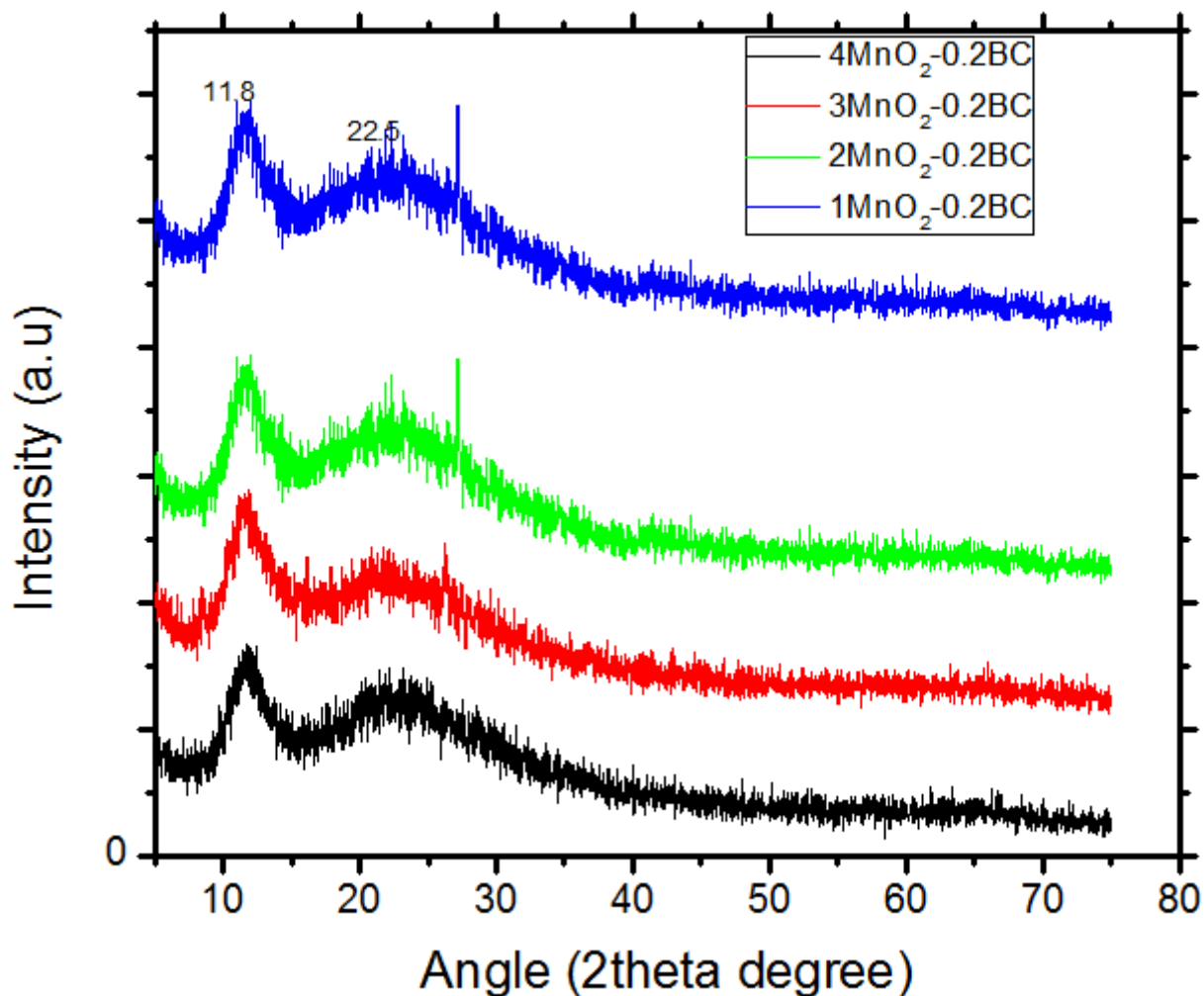


Figure 45: XRD patterns of synthesized MnO_2 /mesoporous carbon composites.

The Raman spectra of the $1\text{MnO}_2\text{-}0.2\text{BC}$ and $4\text{MnO}_2\text{-}0.2\text{BC}$ as representative samples were recorded to confirm the graphitic structure of the synthesized composites. It is shown in Fig. 46 that the $1\text{MnO}_2\text{-}0.2\text{BC}$ exhibited mainly two dominant bands. The peaks at 1361 and 1595 cm^{-1} correspond to D and G bands, respectively. The presence of D (defect) band confirms that the sample was amorphous and there were some structural disorder in the composites while G

(Graphite) band is associated with vibration of sp^2 hybridized carbon in graphite structure (Abbas *et al.*, 2016). The ratio of the intensity of D band to that of G band ($\frac{I_D}{I_G}$) was 0.98. This ratio is proportional to the number of defect sites in the sample and the lower the ratio the higher the graphitization (Liu *et al.*, 2013). The ($\frac{I_D}{I_G}$) value obtained in this study is higher than those obtained when 5% MnO_2 was composited by activated carbon (Liu *et al.*, 2014a). This study attained higher graphitization than that reported by (Wang *et al.*, 2016b) which is a good indicator for supercapacitors. Successful deposition of MnO_2 on the BC materials was furthermore confirmed by the peak shift at 647 cm^{-1} . There were no D and G bands for $4MnO_2-0.2BC$ meaning that as the MnO_2 increased either the C-C bonds were broken to form C-Mn bonds or all the carbon surface were covered by Mn. These results agree well with the EDX results, which show Mn content as high as 55.7% in $4MnO_2-0.2BC$ sample compared to 4.99% in $1MnO_2-0.2BC$ sample.

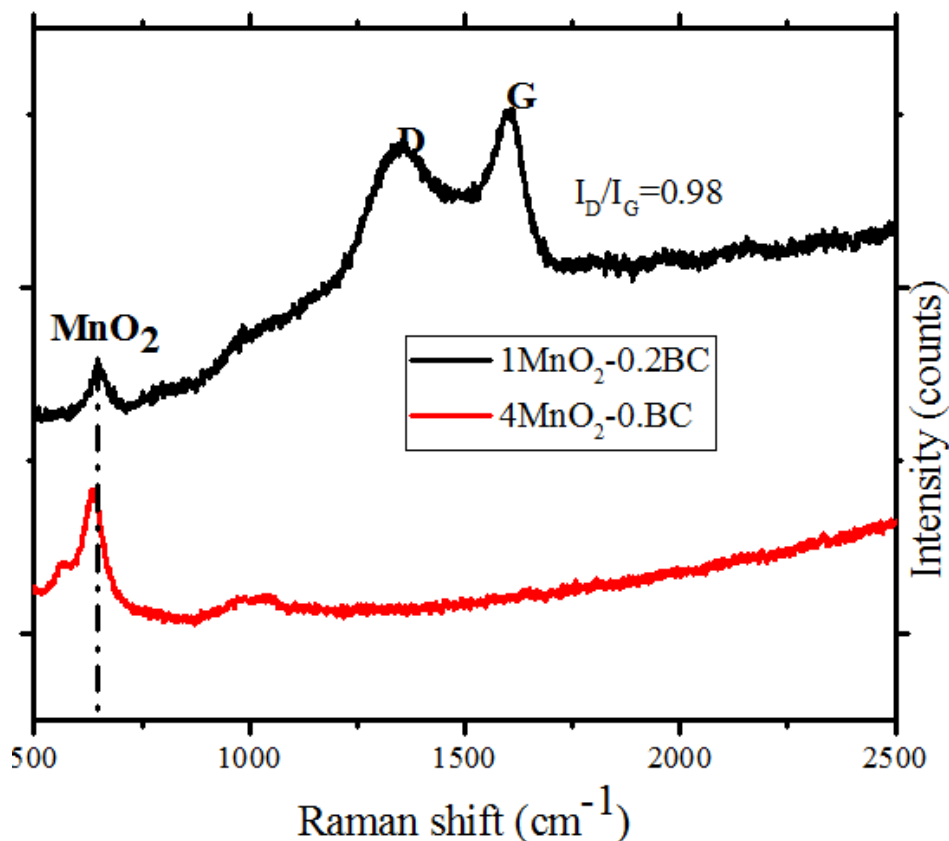


Figure 46: Raman spectrum of 1MnO₂-0.2BC and 4MnO₂-0.2BC.

6.3.2 Electrochemical performances of the synthesized MnO₂-BC based electrodes

The electrochemical performances of the prepared electrodes were evaluated by CV voltammometry and electrochemical impedance spectroscopy (EIS). Fig. 47 shows the cyclic voltammograms of synthesized electrodes at scan rates 5, 10, 20, 30, 50, and 150 mV s⁻¹. Sample 4MnO₂-0.2BC deviates from the ideal double layer capacitor behaviour due to high content of MnO₂ in the composite, Fig. 47d. The presence of redox peaks in the voltammograms is due the faradaic reaction caused by the MnO₂ in alkali electrolyte. It is anticipated that the 6 M KOH electrolyte interaction with BC electrodes occurred according to equation 6.1 with the K⁺ ions optimizing the pseudocapacitance by enhancing the chemisorptions rate.



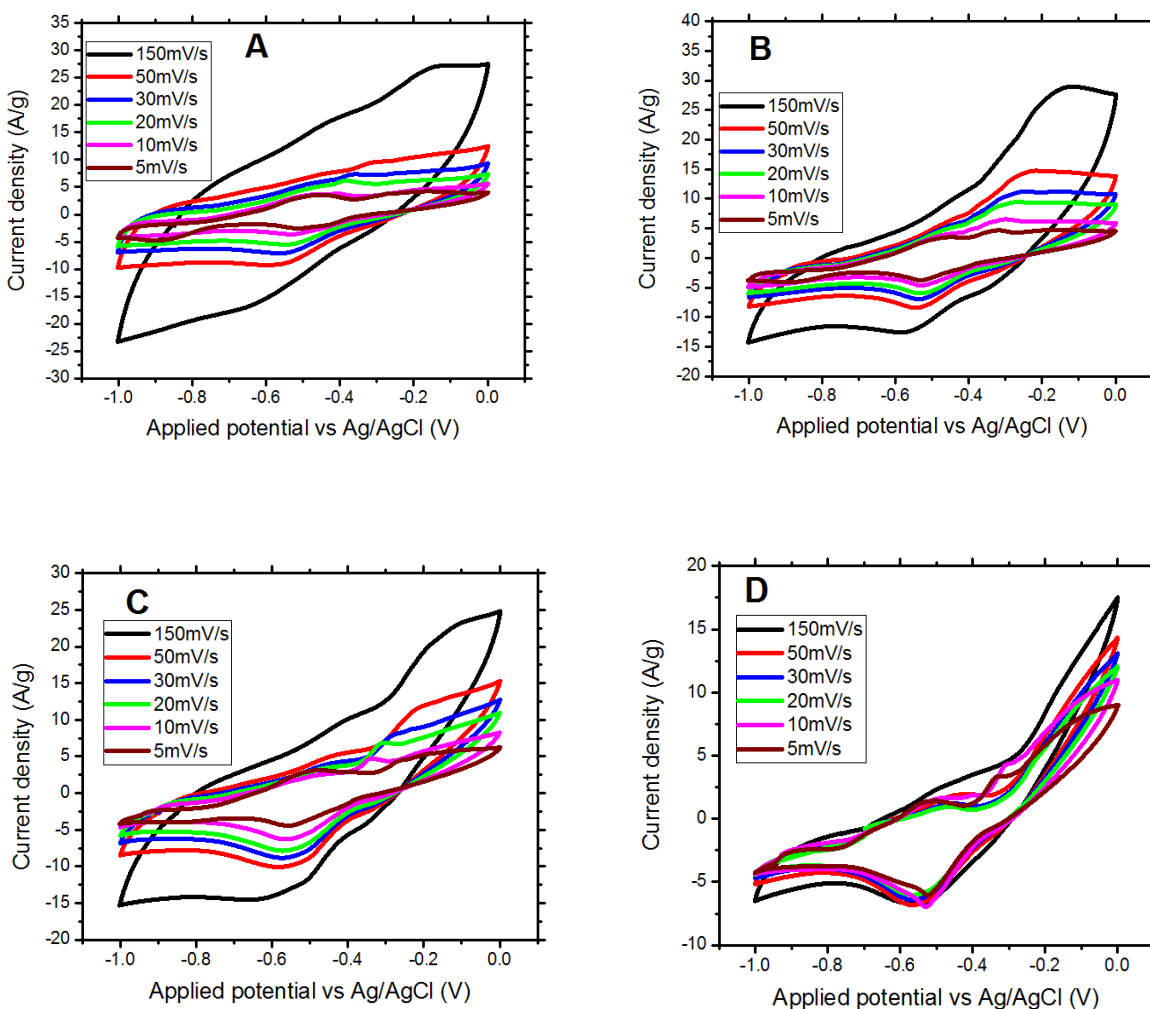


Figure 47: Cyclic voltammograms (a) $1\text{MnO}_2\text{-}0.2\text{BC}$, (b) $2\text{MnO}_2\text{-}0.2\text{BC}$, (c) $3\text{MnO}_2\text{-}0.2\text{BC}$, and (d) $4\text{MnO}_2\text{-}0.2\text{BC}$.

At high scan rates (50 and 150 mV s^{-1}), Fig. 47a-c shows that the pseudocapacitance behaviour of the composites was less pronounced as compared to EDL behaviour. This is because the CV curves acquired quasi-rectangular curves with some weak redox peaks. This might have happened due to the fact at high scan rate there was not enough time for the faradaic reaction to take place and hence less pseudocapacitance. Therefore the contribution of the electric double layer capacitance was much pronounced due to adsorption of ions on surface areas of the composites. At low scan rates $1\text{MnO}_2\text{-}0.2\text{BC}$, $2\text{MnO}_2\text{-}0.2\text{BC}$, $3\text{MnO}_2\text{-}0.2\text{BC}$, and $4\text{MnO}_2\text{-}0.2\text{BC}$

samples show redox peaks. Redox peaks are shifting to negative as the scan rate decreases due to polarization of the electrode.

The specific capacitances of the electrodes synthesized from the composites as calculated from the CV curves are shown in Fig. 48a. At scan rate of 5 mVs^{-1} , $4\text{MnO}_2\text{-0.2BC}$ exhibited the highest specific capacitance of 709 F g^{-1} followed by $3\text{MnO}_2\text{-0.2BC}$ (618 F g^{-1}), $2\text{MnO}_2\text{-0.2BC}$ (548 F g^{-1}), and $1\text{MnO}_2\text{-0.2BC}$ (487 F g^{-1}). In general, the specific capacitance at scan rate of 5 mV s^{-1} increased with MnO_2 content in the composite. This might be due to the strong contribution of pseudocapacitance caused by MnO_2 despite the fact that surface area decreased with MnO_2 content. At scan rates of 50 mV s^{-1} , the trend reversed whereby $4\text{MnO}_2\text{-0.2BC}$ exhibited the lowest specific capacitance (88 F g^{-1}) and $1\text{MnO}_2\text{-0.2BC}$ exhibited the highest specific capacitance (131 F g^{-1}). This was suggested to be due to significant EDLC contribution by the mesoporous carbon materials than pseudocapacitance of MnO_2 content. At low scan rate, 5 mV s^{-1} , specific capacitances of the $\text{MnO}_2\text{-BC}$ composites were independent of the BET surface area but dependent on MnO_2 content. However, at high scan rate (50 mVs^{-1}), the specific capacitances depended on the BET surface area (Fig. 48b) and hence the EDLC contribution by mesoporous carbon materials. These results corroborate cyclic voltammetry results in Figure 6.8a-c, which show absence of redox peaks at high scan rates.

The MnO_2 /biogas slurry composites capacitances compare with other reported MnO_2 /carbon composites as shown in Table 6.2. One can see that the MnO_2 /BC composites exhibited specific capacitance which is in better agreement with those reported by Wang and co-workers when they prepared the composite of MnO_2 and furfuryl alcohol derived mesoporous carbon (Wang *et al.*, 2015b). Otherwise, the MnO_2 /composites exhibited higher specific capacitances than most of the composites shown in Table 6.2 though the electrolytes were not the same.

Fig. 48c shows the specific capacitances when the mass of the mesoporous carbon were varied from 0.1 to 0.3 g at 40 mL of $5 \times 10^{-2} \text{ M KMnO}_4$. The figure clearly shows the increase in the rate capability with increasing mesoporous carbon content in the composite. This indicates that at high carbon mass loading; most of the pores are not filled with MnO_2 thus allowing substantial access by the electrolyte ions to the pores. The specific capacitance at scan rate of 5 mV s^{-1} was highest for $1\text{MnO}_2\text{-0.2BC}$ followed by $1\text{MnO}_2\text{-0.3BC}$, and $1\text{MnO}_2\text{-0.1BC}$ in that order. This

suggests that at this scan rate (5 mV s^{-1}) and carbon to MnO_2 , EDLC (from carbon) and pseudocapacitance (from MnO_2) synergy was at best.

Table 17: Comparison of specific capacitance obtained from different MnO_2 /carbon composites.

Composite	Carbon precursor	¹ C (F g^{-1})	² V (mV s^{-1} or A g^{-1})	³ M (mg)	electrolyte	Reference
Manganese oxide/ mesoporous carbon	biogas slurry	709	5 mV s^{-1}	5	6 M KOH	This work
Manganese oxide/carbon microsphere	resorcinol/formaldehyde	459	1 A g^{-1}	10	6 M KOH	(Liu <i>et al.</i> , 2014a)
Manganese oxide/reduced graphene	Graphite powder	211	2 mV s^{-1}	3	1 M Na_2SO_4	(Li <i>et al.</i> , 2011c)
Manganese oxide/ mesoporous carbon	furfuryl alcohol	700	5 mV s^{-1}	3	0.1 M K_2SO_4	(Wang <i>et al.</i> , 2015b)
Manganese oxide/reduced graphene	Graphite powder	393	-	-	0.5 M Na_2SO_4	(Sawangphruk <i>et al.</i> , 2013)
Manganese oxide/ graphene	Natural graphite	310	2 mV s^{-1}	3	1 M Na_2SO_4	(Yan <i>et al.</i> , 2010)
Manganese oxide/Activated carbon	Commercial activated carbon	332.6	2 mV s^{-1}	3	0.5 M Na_2SO_4	(Wang <i>et al.</i> , 2015c)
Manganese oxide carbon	Kenaf stem	416	1 mV s^{-1}	2.5	1.0 M Na_2SO_4	(Wang <i>et al.</i> , 2014a)
MnO_2 / activated carbon	Hemp stem	340	1 A g^{-1}	0.76	1.0 M Na_2SO_4	(Yang <i>et al.</i> , 2017)

¹Gravimetric capacitance, ²Scan rate or current density, ³Mass of electrode

Cyclic stabilities at scan rate of 20 mV s^{-1} for $1\text{MnO}_2\text{-}0.2\text{BC}$, $2\text{MnO}_2\text{-}0.2\text{BC}$, $4\text{MnO}_2\text{-}0.2\text{BC}$ as representative samples are shown in Fig. 48d. After 50000 cycles, the capacity retentions of 78, 85, and 91% for $4\text{MnO}_2\text{-}0.2\text{BC}$, $2\text{MnO}_2\text{-}0.2\text{BC}$, and $1\text{MnO}_2\text{-}0.2\text{BC}$, respectively were achieved. As the MnO_2 content increased in the composite, the resistance increased thus reducing the conductivity and hence capacitance retention. That is why $4\text{MnO}_2\text{-}0.2\text{BC}$ has lower capacity retention than other samples. After 500 cycles $4\text{MnO}_2\text{-}0.2\text{BC}$, $2\text{MnO}_2\text{-}0.2\text{BC}$, and $1\text{MnO}_2\text{-}0.2\text{BC}$ were reduced by 18.8, 11, and 9.9%, correspondingly, from the initial specific capacitance. For electrodes with higher content of MnO_2 the capacity fading was high.

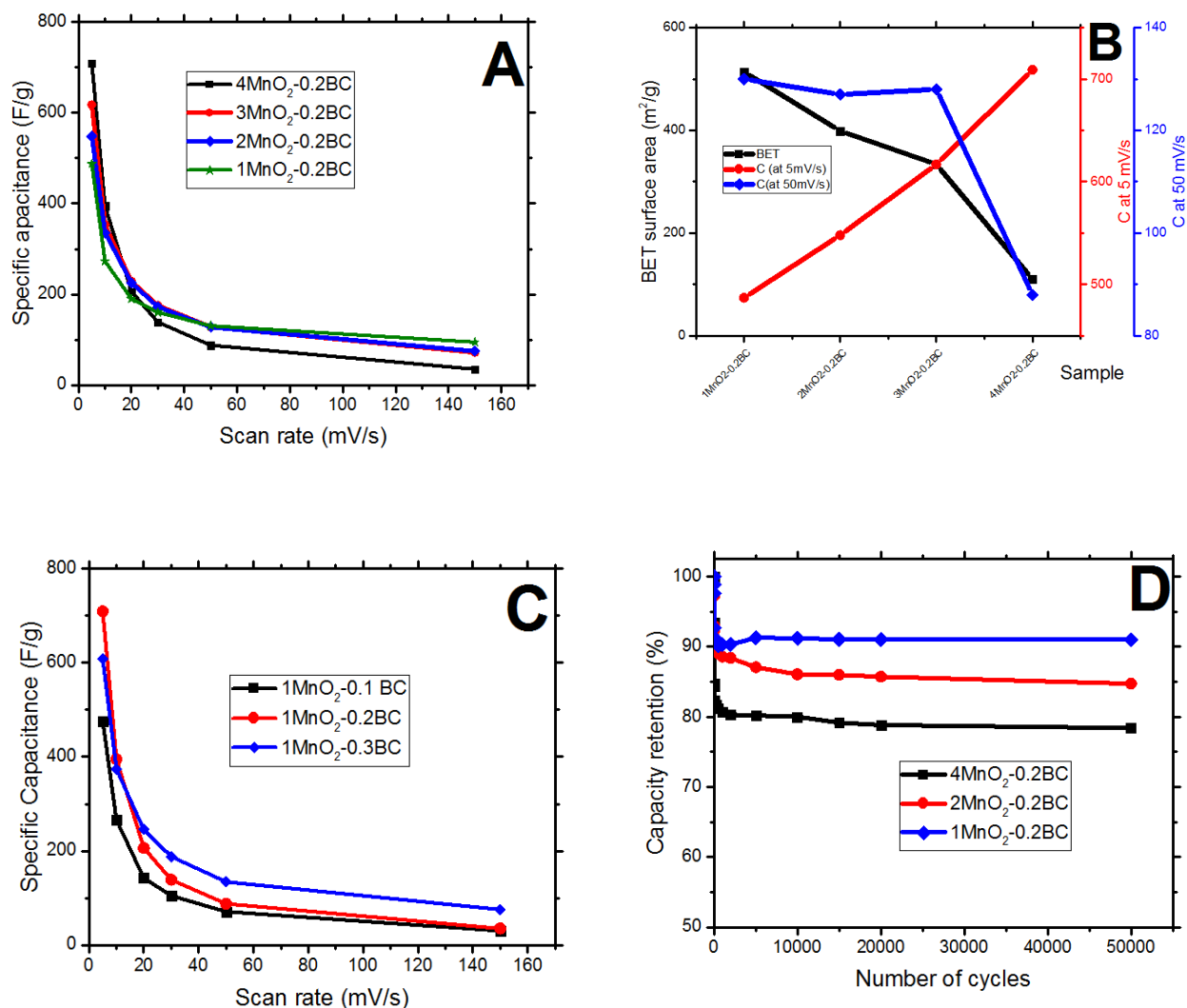


Figure 48: (a) Specific capacitances of MnO₂/BC composites for different MnO₂ loading, (b) Correlation between surface area and specific capacitance (c) Specific capacitances of MnO₂/BC composites for different mass of BC, (d) Cyclic stabilities of MnO₂/BC composites electrodes measured at 20 mV s⁻¹.

Fig. 49a shows the dependence of total pore volume on the specific capacitance at scan rate of 5 mV s⁻¹. It is shown that specific capacitance increased with decreasing total pore volume. The pore volume decreased from 0.52 to 0.17 cm³ g⁻¹ while specific capacitance increased from 487 to 709 F g⁻¹. This explains that at 5 mV s⁻¹, the specific capacitance was mainly contributed by faradaic reaction originating Mn²⁺ and K⁺ ions and thus pseudocapacitance was dominant. On

the other hand, the specific capacitance decreased with decreasing total pore volume at scan rate of 50 mV s^{-1} as depicted in Figure 6.10b. At 50 mV s^{-1} the specific capacitance decreased from 130 to 88 F g^{-1} . It is worth recalling that from Table 6.1, V_{micro} , V_{meso} , and V_{total} were lowest at the highest MnO_2 loading (4 MnO_2 -0.2BC sample). This suggests that at the highest MnO_2 loading, MnO_2 had filled significant fraction of the pores thereby drastically limiting the access of the pores by the electrolyte ions for substantial EDLC to occur. Therefore, at high scan rate (50 mV s^{-1}), both the faradaic reaction (from MnO_2) and electroadsorption of ions into the pores of carbon were severely limited especially at high MnO_2 loading. This in turn reduces both the pseudo capacitance and EDLC. Fig. 49c shows the dependence of specific capacitance on average pore size. The average pore size in Fig. 49c is based on the data presented in Table 6.1. It follows that at scan rates of 20 and 150 mV s^{-1} , the pore size ranging from 4.5 to 7.4 nm had similar effect on capacitance. However, at scan rate below 10 mV s^{-1} the specific capacitance was high for sample with average pore size of 4.7 nm then dropped for sample with pore size of 6.4 nm. A significant increase of specific capacitance was observed for a sample with average pore size of 7.4 nm. To demonstrate the dependence of specific capacitance on mesopore content the graph of specific capacitance vs mesopore contents was plotted (Fig. 49d). It can be seen in the figure that at low scan rate the diffusion of K^+ ions were able to access all the available pores of the electrodes thus facilitating the oxidation/ reduction reaction. More ever it can be seen that at the scan rate lower than 20 mV/s the mass transfer (diffusion) was enhanced for samples with mesopore content greater than 50%. While at the same scan rates ($\leq 20 \text{ mV/s}$) the specific capacitance of samples with mesopore content less than 50% was enhanced by the surface area of the samples.

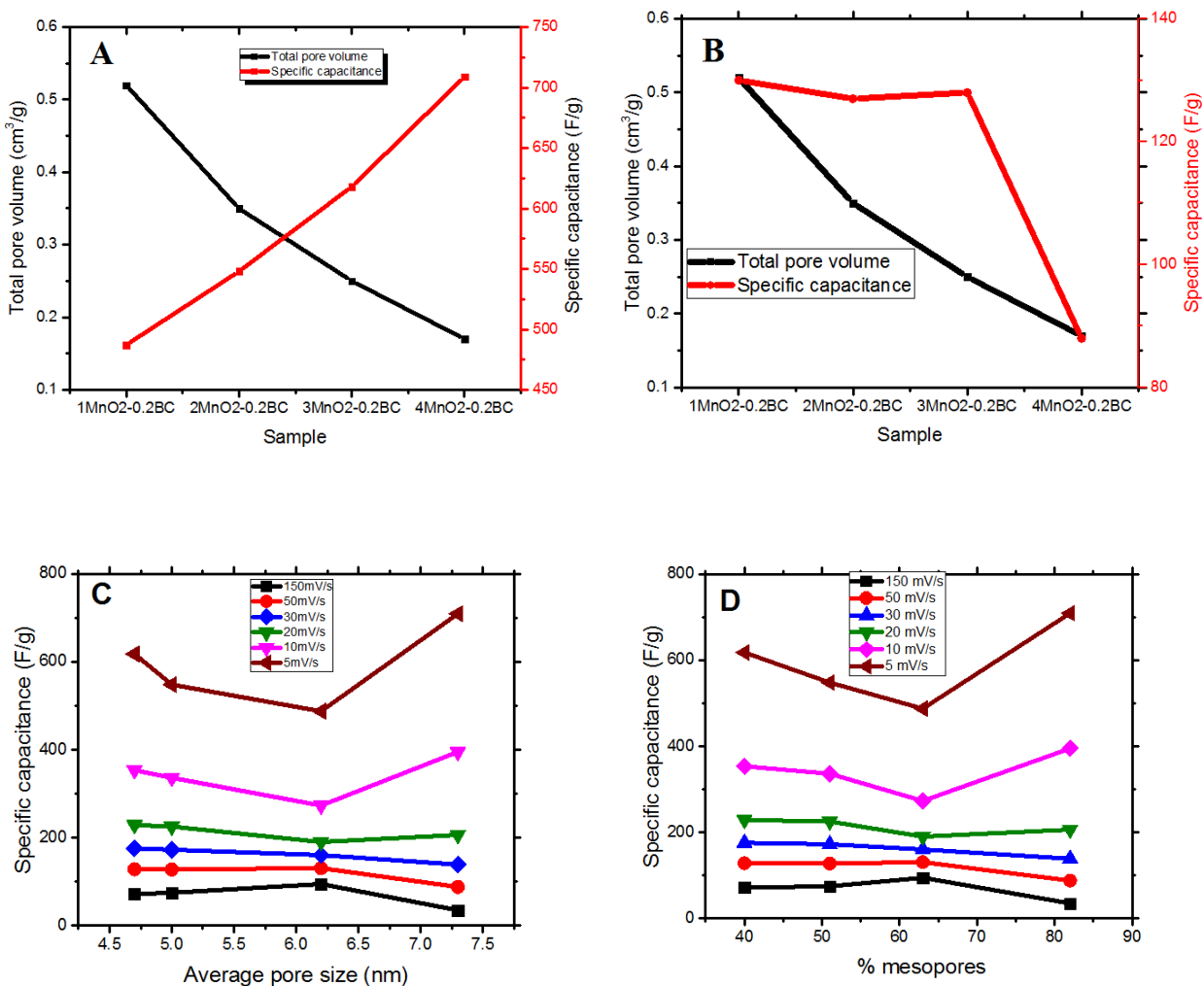


Figure 49: Specific capacitance against (a) total pore volume at 5 mV s^{-1} (b) total pore volume at 50 mV s^{-1} (c) average pore size (d) mesopore content ($\%V_{\text{meso}}$).

For further evaluation of electrochemical properties of the MnO_2/BC composites EIS measurements were performed. Fig. 50a displays the Nyquist plots of the composites. All plots demonstrate the semicircles at the high frequency region (inset of Fig. 50a). The interceptions of each plot with $\text{Re}(Z)$ describe the equivalent resistance (R_s). The plots show that the values of R_s for all samples are less than 1Ω indicating that the synthesized composites had high conductivity. The diameter of the semicircles at high frequency region, which corresponds to the charge transfer resistance almost increased with increasing MnO_2 loading in the composites. The increase might have been caused by the low conductivity of the materials after MnO_2 was

precipitated into biogas slurry derived mesoporous carbon. The 1MnO₂-0.2BC exhibited lowest transfer resistances as shown by the smallest semicircle diameter than all samples. The high conductivity of 1MnO₂-0.2BC may be due to high BET surface area and pore volume as supported by nitrogen sorption studies. The straight line at low frequency region demonstrates the diffusive resistances of the electrolyte ions into the inner parts of the electrodes (Li *et al.*, 2011c). It is further shown that the capacitive behaviour of the composites was in the order of 1MnO₂-0.2BC > 3MnO₂-0.2BC > 4MnO₂-0.2BC > 2MnO₂-0.2BC implying that adsorption and diffusion of electrolyte ions were more pronounced in 1MnO₂-0.2BC than other electrodes.

Fig. 50b shows the bode plots of different electrodes describing real component of impedance as a function of frequency. It can be seen that at high frequency region, the main resistance of the MnO₂/BC composites is electronic combined with ionic resistance of the electrolyte. In the medium frequency range (1-1000 Hz) the ionic transport dominates, which is contributed by the texture of the composites. In this range, 1MnO₂-0.2BC has low resistance than other electrodes because of high surface area and high pore size, volume, and distribution in the range of 4 nm. At frequency between 1 and 10 Hz there is intersection of all plots implying that electronic and ionic resistances are comparable (Lufrano and Staiti, 2010).

In Fig. 50c, it is shown that at high frequency region, the phase angles of all electrodes are less negative. When the frequency was decreased, the phase angle shifted to more negative with 1MnO₂-0.2BC exhibiting a phase shift from 8° to 55°, 2MnO₂-0.2BC has phase shift from 14° to 55°, 3MnO₂-0.2BC shifted from 16° to 40°, and 4MnO₂-0.2BC exhibited phase shift from 17° to 36°. The shift of phase angle as a function of frequency is nonlinear indicating that both capacitive reactance and resistance reactance contributed to the total impedance of the electrodes fabricated from MnO₂-0.2BC composites (Xie and Gao, 2007).

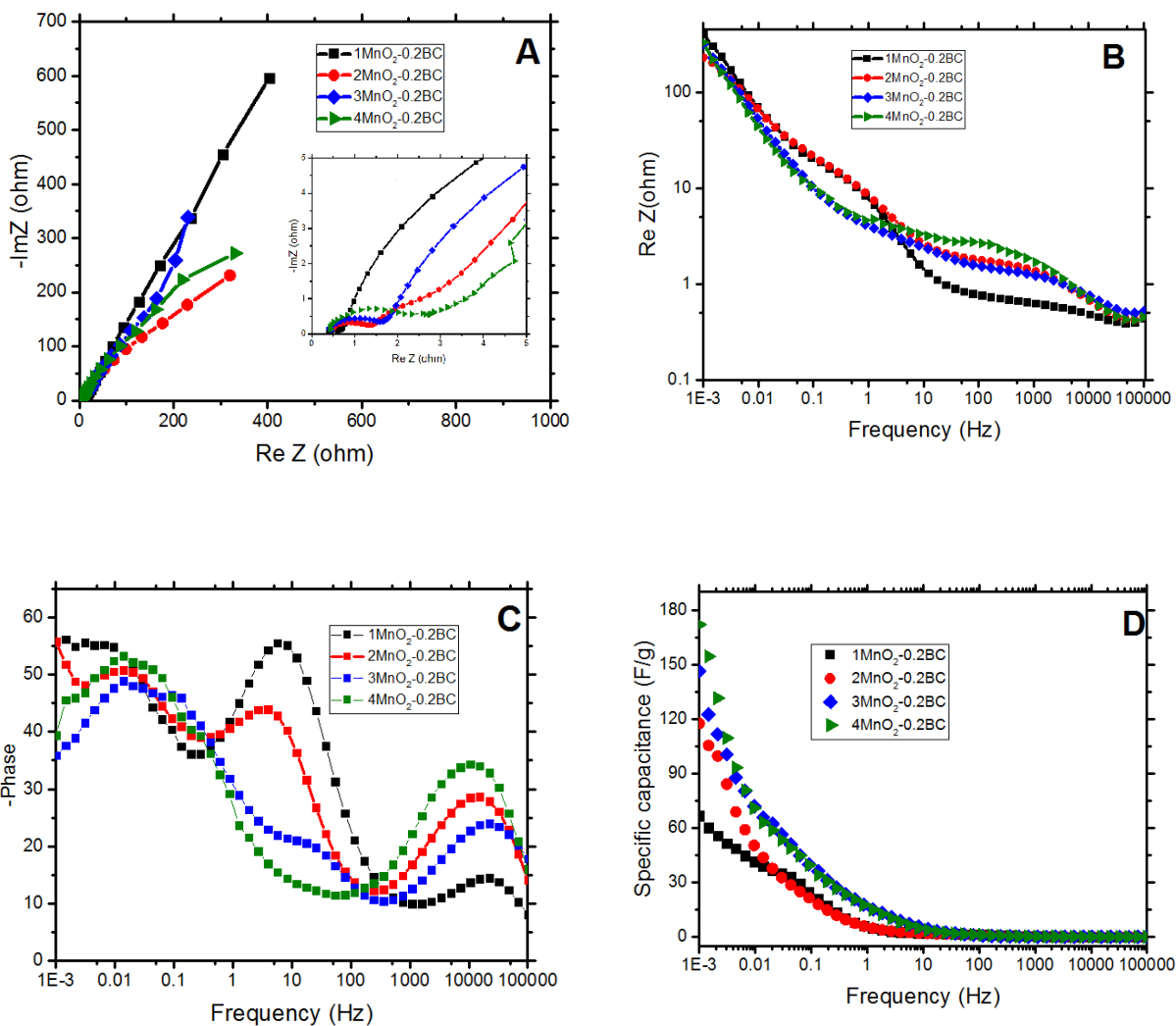


Figure 50: (a) Nyquist plots of MnO₂/BC composites, (b) Bode plots of MnO₂/BC composites electrodes of Real Z vs frequency, (c) Bode plots of MnO₂/BC composites electrodes of phase angle vs frequency and (d) Specific capacitance vs frequency.

Fig. 50d displays the specific capacitance as the function of the frequency of the synthesized electrodes. It can be seen that at low frequency region, the specific capacitance increased as the MnO₂ content increased in the composites. The trend agrees well with that obtained from the specific capacitance calculated from CV curves. At high frequency, the capacitance is very low (approaching zero) because of the influence of electrolyte resistance.

6.4 Conclusion

The MnO₂/biogas slurry derived mesoporous carbon composites were synthesized through co-precipitation method. Nitrogen sorption studies showed that as the MnO₂ loading increased, the BET surface area and total pore volume decreased. In contrast to textural trend, the specific capacitances increased with increasing MnO₂ loading, demonstrating the contribution of pseudocapacitance in the composites at scan rate of 5 mV s⁻¹. The highest specific capacitance of 709 F g⁻¹ was attained by the 4MnO₂-0.2BC and decreased to 487 F g⁻¹ for 1MnO₂-0.2BC at scan rate of 5 mV s⁻¹ while the highest BET specific surface area was exhibited by 1MnO₂-0.2BC (514 m² g⁻¹) and lowest for 4MnO₂-0.2BC at 110 m² g⁻¹. In addition, the fast ion transport in the electrodes was evident from the EIS results in which the ESR was observed to be lower than 1 Ω. Furthermore, the cyclic stability at scan rate of 20 mV s⁻¹ was observed to increase with decreasing MnO₂ loading. After 50000 cycles the capacity retentions of 78, 85, and 91% for 4MnO₂-0.2BC, 2MnO₂-0.2BC, 1MnO₂-0.2BC, respectively were achieved. The high specific capacitances and cyclic stability of the synthesized microstructured MnO₂/BC composites shows that these materials are very promising for supercapacitor electrodes.

CHAPTER SEVEN

Synthesis of NiCo₂O₄/Mesoporous Carbon Composites for Supercapacitors Application

Abstract

In this chapter, nickel cobaltite/ mesoporous carbon composites were synthesizing by reacting CoCl₂, Ni(NO₃)₂ and nitric acid treated biogas slurry mesoporous carbon using urea as hydrolyzing agent and CTAB as surfactant. The presence of Ni, Co, C, and O peaks in the EDAX results confirmed that BC mesoporous carbon/NiCo₂O₄ composites were successfully synthesized. Interestingly at 350 °C the composite surface morphology switched to cross- linked nanoflakes structures interconnected with mesoporous carbon. The X-ray diffraction analysis of the NiCo₂O₄/mesoporous carbon composites revealed that the spinel structure of the NiCo₂O₄ was maintained in the composites by showing diffraction peaks can be indexed and assigned to (111), (002), (220), (311), (400), (422), (511), and (440) reflection planes of the composite. The nitrogen uptake increased with increasing annealing temperature to 300 °C then decreased at 400 °C. The type IV isotherms were exhibited by all the composites. The contribution of mesopores increased with increasing annealing temperature: 32% for BC-NCo-200, 41% for BC-NCo-250, 56% for BC-NCo-300, 66% for BC-NCo-350, and 86% for BC-NCo-400. The NiCo₂O₄/mesoporous carbon composites exhibited high specific capacitance of 835 F g⁻¹ at scan rate of 5 mV s⁻¹ for sample annealed at 350 °C. The cyclic stabilities of the electrodes were above 90% after 50000 cycles indicating that the synthesized composites were suitable candidates for supercapacitors.

7.1 Introduction

In recent years both carbon and metal oxides have been used to synthesize electrodes for supercapacitors application. While carbons have advantages of considerable high electrical conductance they suffer from low capacitance. On the other hand, metal oxides have high capacitance but low electrical conductivity. The effort has been to composite metal oxides with carbon so as to increase both capacitance and electrical conductivity thus increasing the energy density of supercapacitors.

Cobalt based ternary transition metal oxides (TTMOs) has been reported to exhibits nanostructure properties that can be controlled thus enhancing the capacitance (Zhang and Lou, 2013). The theoretical capacitance of cobalt based TTMOs is approximately 3000 F g^{-1} which is mainly contributed by the unique physiochemical properties of the cobaltite (Lota *et al.*, 2011). Different cobaltites have been investigated for supercapacitors applications including NiCo_2O_4 (Wang *et al.*, 2011a; Wu *et al.*, 2014), MgCo_2O_4 (Cui *et al.*, 2016) and ZnCo_2O_4 (Cheng *et al.*, 2015). The weakness of most metal oxides in supercapacitors has been poor electrical conductivity thus researchers are finding methods of improving this drawback.

Nickel cobaltite store energy both in the bulk near the surface and on the surface of the electrode thereby exhibiting promising pseudocapacitance behavior. The low resistance exhibited by nickel cobaltite than those of nickel oxides and cobaltites separately and richer sites contribution from both cobaltite and nickel oxides also contributes to high capacitance (Chen *et al.*, 2014). The redox reaction in nickel cobaltite is enhanced by multiple oxidation states of nickel cobaltite thus storing more charges (Cui *et al.*, 2008). Structure wise, the NiCo_2O_4 has spinel structure in which cobalt cations occupy the tetrahedral interstices while nickel occupy the octahedral interstices (Zhang and Lou, 2013). The abundance of nickel and cobalt in the world as well as their relatively low toxicity has been the driving force for the use of nickel and cobalt in industry including energy storage (Dalvi *et al.*, 2004). In order to further increase the electrical conductivity and rate capability, synthesizing NiCo_2O_4 -carbon composites has been the focus of many researchers.

Wang and co workers (Wang *et al.*, 2012a) composited graphene and nickel cobaltite and obtained the high specific capacitance of 618 F g^{-1} . The role of graphene in the composite was to increase the conductivity of the composite. However, the use of graphene is not advantageous because its cost is very high. In search of low cost materials, nickel cobaltite has been composited with aerogel (Chien *et al.*, 2012), carbon nanotubes (Wang *et al.*, 2012c), carbon nanofibers (Zhang and Lou, 2013), carbon cloth (Zhang *et al.*, 2014a), and activated carbon (Chang *et al.*, 2012). To the best of our knowledge, no report on the nanostructured composites between and mesoporous carbon derived from biogas slurry and nickel colbatite.

In this study composites of NiCo₂O₄ and mesoporous carbon derived biogas slurry were fabricated through chemical synthesis. The crystal structures of the samples were studied using X-ray diffraction and texture of the samples was investigated by nitrogen sorption studies. Three-electrode cell system was used to investigate the electrochemical performances of the synthesized electrodes.

7.2 Materials and Methods

7.2.1 Synthesis of the composites

In this study all reagents were analytical and were used without further modifications. Mesoporous carbon was synthesized as described in section 3.3.2 of this dissertation. Carbon obtained after carbonization at 400 °C for 1 h and activation at 700 °C for 1 h with carbon to KOH mass ratio of 1:3 was used. Biogas slurry derived mesoporous carbon was treated with concentrated nitric acid for 24 h at room temperature in order to introduce the hydrophilic functional groups. 1 g of treated mesoporous carbon was dispersed in 1000 mL of distilled water followed by addition of 10 g hexadecyltrimethylammonium bromide (CTAB) as surfactant, urea as hydrolyzing agent, cobalt chloride hexahydrate and nickel nitrate hexahydrate. The molar ratio of urea: Ni²⁺:Co²⁺ was 45:1:2 (Wang *et al.*, 2012a). The mixture was stirred into a sealed container for 10 h. The product was washed in distilled water and dried in oven at 100 °C for 24 h. The composites were annealed in air at 200, 250, 300, 350, and 400 °C for 3 h in order to increase the crystallinity. The samples were designated BC-NCo-T where BC represents the biogas slurry mesoporous carbon, N stands for nickel, Co represents cobaltite and T stand for annealing temperature.

7.2.2 Characterizations

Field emission scanning electron microscope (Hitachi S-4800 microscope) with accelerating voltage of 15 kV and current of 10 mA was used to obtain the surface morphology of the samples. EDX attached to FESEM was used to study the surface composition of the composites. XRD-6000, Shimadzu X-ray diffractometer was used to record the diffraction patterns of the composites at X-ray acceleration of 40kV/100 mA. The Diffraction pattern was obtained in step scanning of 0.02 (2θ) in the range of 5-75 (2θ). The X-ray photoelectron spectroscopy (XPS;

UVS-20-A, SPECS, Germany) with excitation source of Al K α radiation of 1486.6 eV was used to investigate the surface chemistry of the samples. Renishaw 2000 Raman microscope system was used to obtain the Raman spectra of the samples.

Micrometrics Tristar 3020 2.00 instrument was used to study the surface area and structure of the pores of the composites using N₂ sorption at 77.3 K. Samples were degassed at 200 °C for 3 h. Brunauer-Emmet-Teller (BET) equation was employed to calculate the surface area. Barret-Joyner-Halender (BJH) method was used to calculate pore size distribution (PSD) and pore volume from N₂ desorption.

7.2.3 Electrochemical measurements of electrodes

Electrochemical testing of the composites was performed in a standard three-electrode system. Ag/AgCl was used as reference electrode while platinum was used as counter electrode. The working electrode were prepared by mixing 4 mg of active materials (NiCo₂O₄/biogas slurry derived mesoporous carbon composite), 0.5 mg of conducting carbon from MTI for increasing conductivity, 0.5 mg of poly vinylidenedifluoride from MTI Corporation as a binder. The mixtures were pressed in Nickel foam purchased from Heze Jiaotong (Group) Xinda- China. The measurements were done in aqueous electrolyte of 6 M KOH. Before any measurements were taken the electrodes were soaked in 6 M KOH for 30 min. All electrochemical measurements were performed in PGSTAT204 incorporated with FRA32 module.

7.3 Results and discussion

7.3.1 Physical characterizations of NiCo₂O₄/mesoporous carbon composites

The nitrogen adsorption–desorption isotherms of the nickel cobaltite/carbon composites are illustrated in Fig. 51a. It is seen that all the samples exhibited type IV isotherms indicating that there were significant amount of mesopores. The desorption branch was forced to closure at $0.4 < \frac{P}{P_0} < 5.5$ due to tensile strength effect which signify the existence of large amount of small mesopores with diameter less than 4 nm in the samples. Furthermore, the nitrogen uptake increased with increasing annealing temperature to 300 °C then decreased. The adsorption at

around $\frac{P}{P_0} \approx 1$ was around $250 \text{ cm}^3 \text{ g}^{-1}$ for BC-NCo-400 and BC-NCo-300 then decreased with decreasing calcinations temperature. At $\frac{P}{P_0} < 1$ the nitrogen adsorption of BC-NCo-400 is lower compared to BC-NCo-300, BC-NCo-200 and BC-NCo-250 indicating that BC-NCo-400 had less micropore fillings than other samples but exhibited higher capillary condensation and multilayer sorption at higher pressure than other samples demonstrating the presence of both mesopores and macropores. It is worth to note that at $\frac{P}{P_0} \approx 1$ the nitrogen adsorption of BC-NCo-400 increases rapidly than other samples exemplifying the existence of interparticle voids. The existence of mesoporous nanoparticles facilitates not only the ion transport but also favours the contact between electrolytes and interfacial active species.

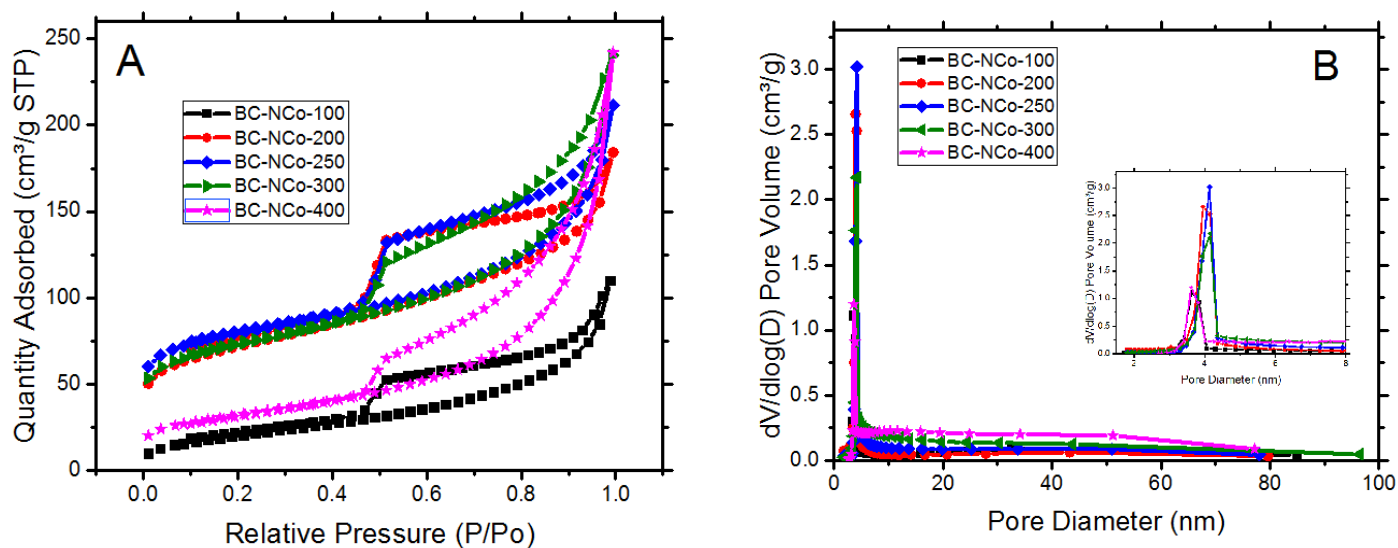


Figure 51: (a) Nitrogen adsorption and desorption isotherms of $\text{NiCo}_2\text{O}_4/\text{Mesoporous carbon}$ composites (b) BJH pore size distribution of the composites as calculated from desorption branch.

Fig. 51b shows the BJH pore distribution of the prepared samples. All samples exhibited monomodal pore size distribution. The pore size peaks are located in the mesopore regions with pore diameter $3 < d < 4.5$ where d represent the pore size. The peak of BC-NCo-400 is shifted to the left

values than the rest suggesting that incorporation of NiCo₂O₄ reduced the pore spaces of the porous carbon (Chien *et al.*, 2012).

The BET, micropores, and mesopores surface areas together with pore volumes and pore sizes of the composites are summarized in Table 7.1. With exception of BC-NCo-100, the contribution of mesopores increased with increasing annealing temperature: 32% for BC-NCo-200, 41% for BC-NCo-250, 56% for BC-NCo-300, 66% for BC-NCo-350, and 86% for BC-NCo-400. Similarly, the mesopore volume content increased with annealing temperature BC-NCo-400 (99%) > BC-NCo-350 (93%) > BC-NCo-300 (86%) > BC-NCo-250 (76%) > BC-NCo-200 (61%). This implies that thermal treatments of the composites significantly enhanced the filling of the micropores with the incorporation of NiCo₂O₄ (Chien *et al.*, 2012). Because of the decreased micropores, the average pore sizes increased from 4.7 nm for BC-3-700-60 as reported in Table 3.3 of chapter 3 of this thesis to 9.6 nm for BC-NCo-400.

Table 18: Pore texture and surface area of NiCo₂O₄/mesoporous carbon composites.

Sample	¹ S _{BET} (m ² g ⁻¹)	² S _{micro} (m ² g ⁻¹)	³ S _{meso} (m ² g ⁻¹)	S _{meso} / S _{micro}	⁴ V _{micro} (cm ³ g ⁻¹)	⁵ V _{meso} (cm ³ g ⁻¹)	V _{meso} / V _{micro}	⁶ V _T (cm ³ g ⁻¹)	⁷ D _{Average} (nm)
BC-NCo-100	75	2	73	36.5	0.003	0.167	55.67	0.17	6.3
BC-NCo-200	240	163	77	0.47	0.11	0.17	1.55	0.28	5.0
BC-NCo-250	258	151	107	0.71	0.08	0.25	3.13	0.33	6.1
BC-NCo-300	241	106	135	1.27	0.05	0.32	6.40	0.37	6.7
BC-NCo-400	112	15	97	6.47	0.007	0.367	52.43	0.37	9.6

1-BET surface area, 2-Micropore surface area, 3-Mesopore surface area, 4-Micropore volume, 5-Mesopore volume, 6- Total pore volume and 7-Average pore size

The surface morphology of the electrode can affect the ion transfer and adsorption. It is therefore important to study the morphology of the synthesized samples. Fig. 52 show the morphology of

NiCo₂O₄/BC mesoporous carbon composites annealed at different temperature. It was seen that at 100 °C the mesoporous carbons were discernible compared to metal oxide. In Fig. 52b the existence of NiCo₂O₄ particles were observed in the sample BC-NiCo-250. Interestingly at 350 °C the composite surface morphology switched to cross- linked nanoflakes structures interconnected with mesoporous carbon (Fig. 52c). These morphologies has been reported to enhance capacitance(Wang *et al.*, 2012c). As temperature increased to 400 °C the growth of big NiCo₂O₄ particles (Fig. 52b) was observed.

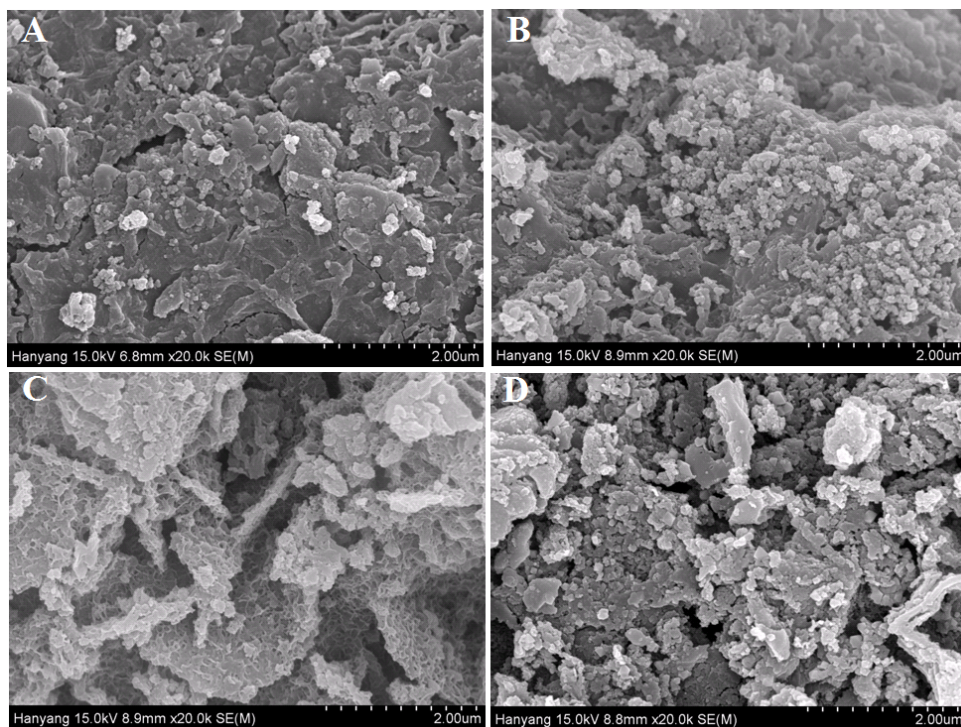


Figure 52: Micrographs of composites at 20k magnification of (a) BC-NiCo-100, (b) BC-NiCo-250, (c) BC-NiCo-350 and, (d) BC-NiCo-400.

At high magnification (Fig. 53) it was observed that at low temperature (100 °C) the particles aggregated slowly to large particles (see Fig. 53a). As the annealing temperature increased to 250 °C the aggregation of the particles to microspheres were enhanced (Fig. 53b) The aggregates might have happened due to Ostwald repining process of the NiCo₂O₄ (Umeshbabu *et al.*, 2014). In Fig. 53c it was observed that at 350 °C the interconnected nanorods of NiCo₂O₄ were developed and grown well on the BC mesoporous carbon. Fig. 53d displayed the nanoparticle in spherical shapes aggregated together. Furthermore it was seen that the particles in Fig. 3b-d are

somehow uniformly distributed which can be beneficial for electrochemical reaction. In both Fig. 52 and 53 it was observed that BC-NiCo-100 showed smooth surface than other samples. The roughness of the surface increased as the annealing temperature increased because of the removal of surfactant (CTAB) and H₂O residue during annealing process. These results propose that the optimal annealing temperature were in the range of 300 °C in which the cross- linked nanoflakes of NiCo₂O₄ interconnected with mesoporous carbon were observed. Furthermore it was shown in Fig. 52 and 53 that the annealing temperature had significant effect on the surface morphologies of the samples.

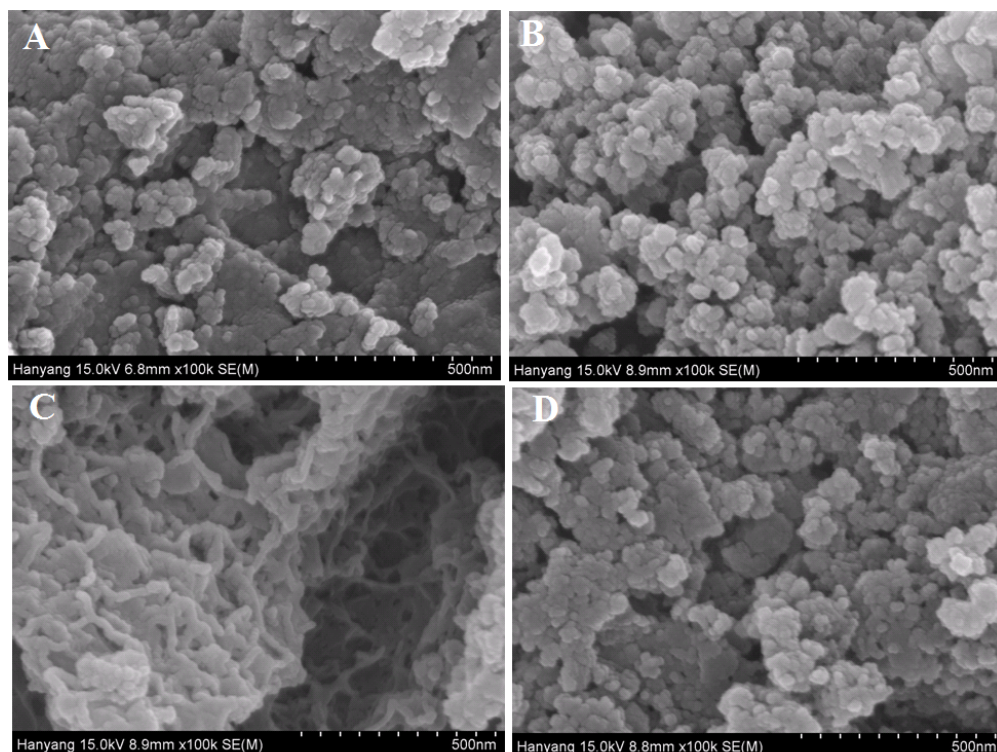


Figure 53: Micrographs of composites at 100k magnification of (a) BC-NiCo-100, (b) BC-NiCo-250, (c) BC-NiCo-350 and, (d) BC-NiCo-400.

Energy dispersive X-ray spectroscopy was used to study the surface elemental composition of the samples. It can be seen that Ni and Co peaks exist in the spectra of BC-NiCo-250 (Fig. 54b), BC-NiCo-350 (Fig. 54c), and BC-NiCo-400 (Fig. 54d). These confirm the formation of the ternary oxides. However, Ni was not detected in BC-NiCo-100 but its content increased to 0.18% for BC-NiCo-250, 1.76% for BC-NiCo-350, and 5.54% for BC-NiCo-400. The carbon peak is

from the BC mesoporous carbon. The presence of Ni, Co, C, and O peaks further confirmed that BC mesoporous carbon/ NiCo_2O_4 composites were successfully synthesized. As reported in chapter six, the spectra also showed peaks of N and S which are important parameters for pseudocapacitance.

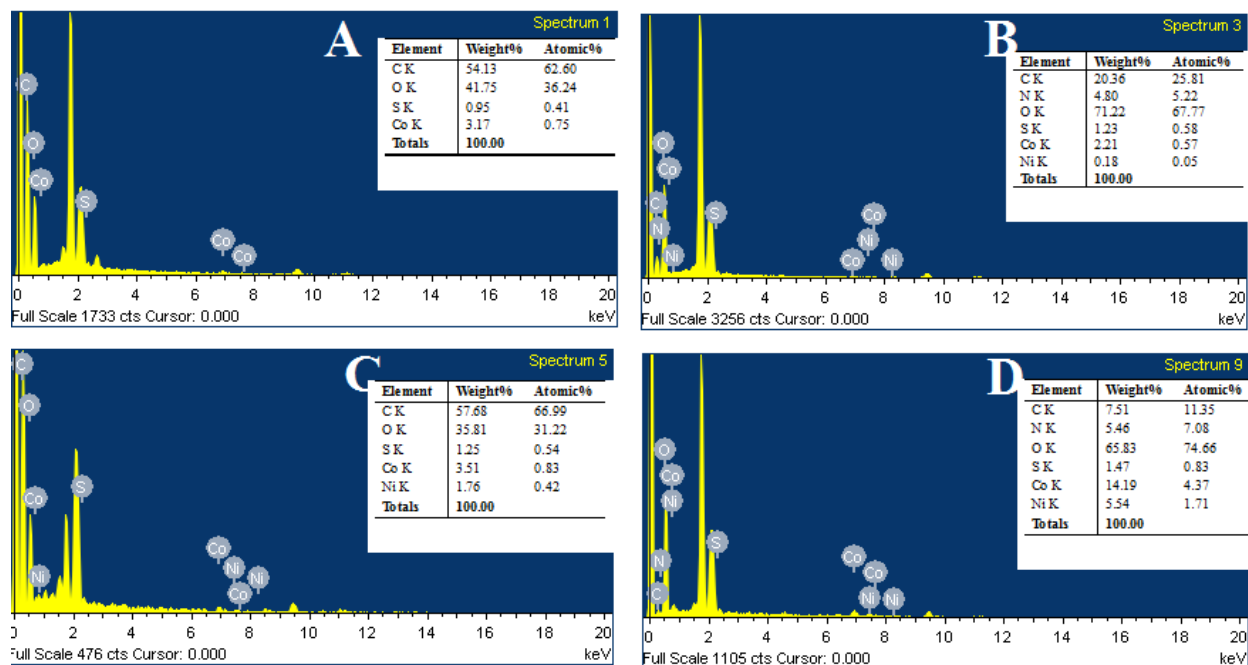


Figure 54: EDX Spectra of (a) BC-NCo-100, (b) BC-NCo-250, (c) BC-NCo-350 and (d) BC-NCo-400.

Fig. 55 shows further the information of microstructures of NiCo_2O_4 / BC carbon composites. In Fig. 55a it can be seen that the mesopores are well distributed. Fig. 55b demonstrates that the BCNiCo-250 sample consisted both carbon and NiCo_2O_4 . It further shows the pores which may have resulted from biogas slurry mesoporous carbon. The insert of Fig. 55b and Fig. 55c-d confirm that the crystalline NiCo_2O_4 were intercalated into the mesoporous carbon. Furthermore the HRTEM images are shown in Fig. 56. It can be seen in Fig. 56a that no clear lattice fringes from the image an indication that at 100 °C the crystallinity of NiCo_2O_4 in the BCNiCo-100 was not revealed. As annealing temperature increased to 250 °C it can be seen that NiCo_2O_4 is pronounced. Fig. 56c-d clearly justify that NiCo_2O_4 was successfully incorporated into the matrix of mesoporous carbon. As shown in Fig. 56c the lattice distance of 0.31 nm which

corresponds (220) diffraction plane of NiCo_2O_4 is demonstrated. Interestingly the lattice fringes of 0.34 nm which can be indexed to diffraction plane (002) of carbon were obtained.

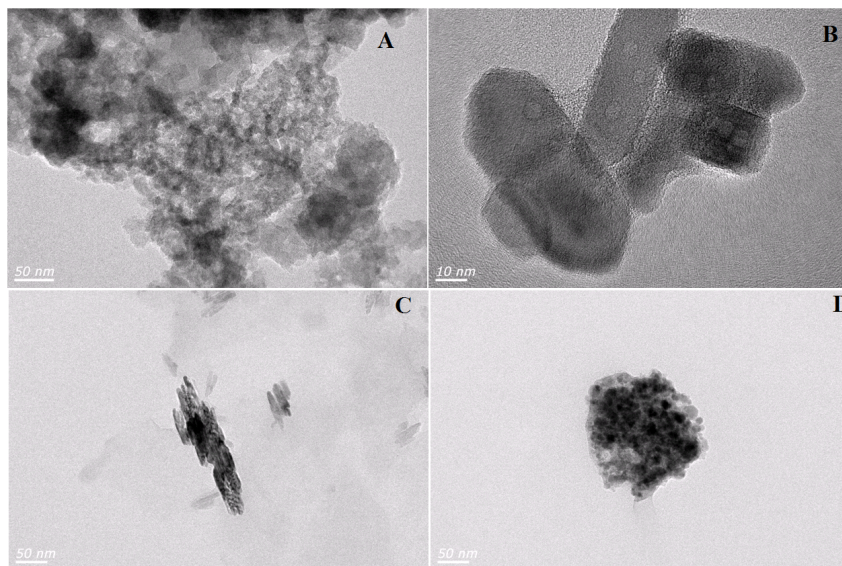


Figure 55: TEM images of (a) BC-NiCo-100, (b) BC-NiCo-250, (c) BC-NiCo-350 and, (d) BC-NiCo-400.

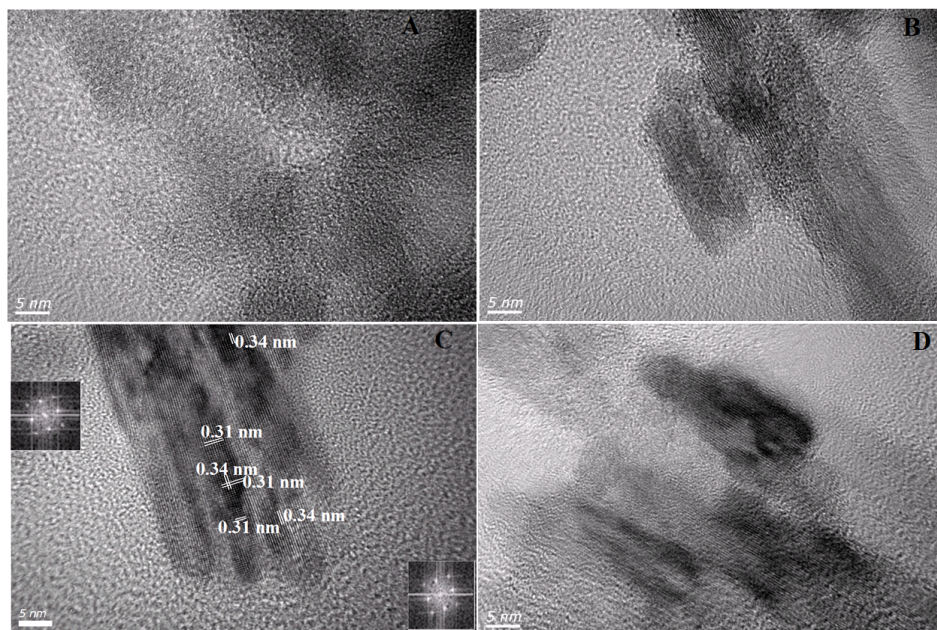


Figure 56: HRTEM images of (a) BC-NiCo-100, (b) BC-NiCo-250, (c) BC-NiCo-350 and, (d) BC-NiCo-400.

Fig. 57 shows the XRD pattern of BC-NCo-T composites. It can be seen that the broad peaks at 23° and 42° 2θ which corresponds to (002) and (100) reflection planes, respectively, decreased as the annealing temperature increased. This indicates that as calcinations temperature increased the carbon was burnt out. The crystallographic structure of BC-NCo-100 and BC-NCo-200 are the same meaning that after thermal treatment to 200°C the phase did not change. With exception of broad peak at 23.5° which arise from BC mesoporous carbon, all diffraction peaks of BC-NCo-400 can be indexed to spinel structure of NiCo_2O_4 (as per Joint Committee of Powder Diffraction Standards [JCPDS] card no 020-0781), $a = 8.111 \text{ \AA}$). The diffraction peaks of BC-NCo-400 can be indexed and assigned to (111), (002), (220), (311), (400), (422), (511), and (440) reflection planes of the composite. As the thermal treatment temperature increased the intensity of peaks corresponding to (111), (220), (311), (400), (422), (511) and (440) increased implying increased crystallinity of the samples. Furthermore, since the miller indices are all odd or even, the NiCo_2O_4 in the composites adopted face centered cubic (FCC) Bravais lattice. Interestingly, all samples demonstrated the existence of interlayer spacing.

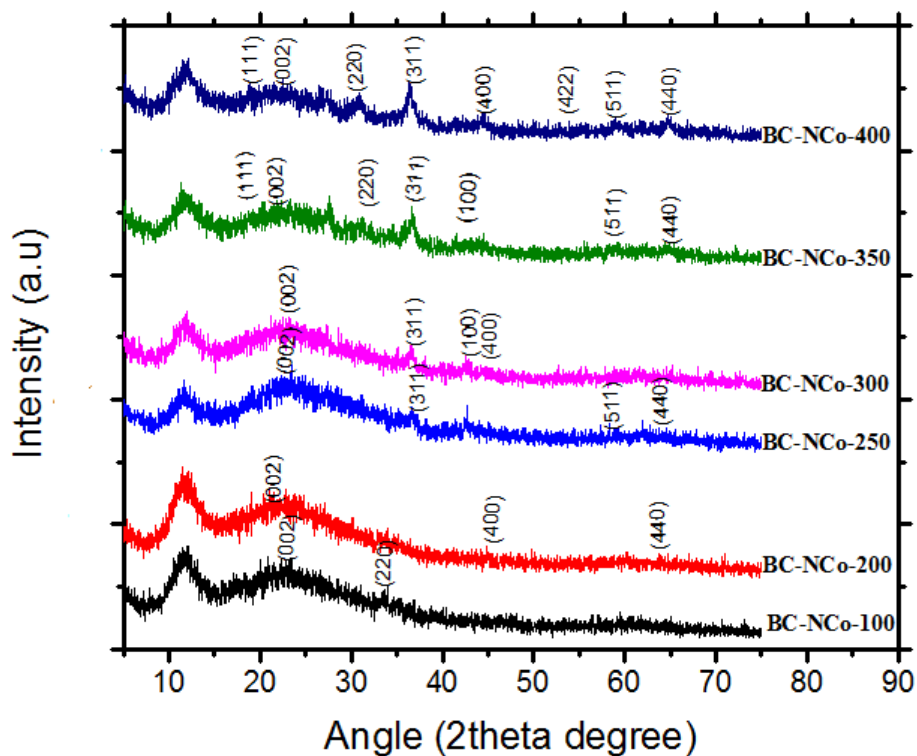


Figure 57: X- ray diffraction pattern of the Manganese oxide/ mesoporous carbon composites.

Table 7.2 shows the d spacing of the composites at different miller indices. It can be seen that the first two samples (BC-NCo-100 and BC-NCo-200) did not exhibit (111) plane. As the annealing temperature was increased, the (111) plane evolved in samples BC-NCo-250 to 350. The d-spacings were about 0.48, 0.47, 0.46, and 0.47 nm for BC-NCo-250, BC-NCo-300, BC-NCo-350 and BC-NCo-400 for (111) reflections/planes, respectively. These values are comparable to the theoretical interplane spacing of spinel NiCo₂O₄ (111) planes (Kuang *et al.*, 2014). Furthermore, the planes (220) and (311) with d-spacing of 0.29 nm and 0.24 nm, respectively, were obtained which correspond to cubic spinel structure of NiCo₂O₄. The d₀₀₂ spacing corresponds to the amorphous carbon present in the composites and was approximately 0.38 nm.

Table 19: d-spacings of different planes for the synthesized composites.

Sample	d ₁₁₁ (nm)	d ₀₀₂ (nm)	d ₂₂₀ (nm)	d ₃₁₁ (nm)	d ₄₀₀ (nm)	d ₅₁₁ (nm)	d ₄₄₀ (nm)
BC-NCo-100		0.39	0.27	0.25	0.21	0.16	0.14
BC-NCo-200		0.39	0.27	0.24	0.21	0.16	0.14
BC-NCo-250	0.48	0.38	0.29	0.24	0.20	0.15	0.15
BC-NCo-300	0.47	0.38	0.29	0.24	0.20	0.15	0.15
BC-NCo-350	0.46	0.38	0.29	0.24	0.20	0.16	0.14
BC-NCo-400	0.47	0.39	0.29	0.24	0.20	0.17	0.14

The vibration characteristics of the NiCo-BC-250 and NiCo-350 as representative samples were further investigated by Raman spectroscopy. As shown in Fig. 58, very weak peaks of D band were exhibited by the selected two samples. The D band peaks were observed at 1353 and 1328 cm⁻¹ by NiCo-BC-250 and NiCo-350 samples, respectively. The G bands which were slightly pronounced than D bands existed at raman shift of 1609 and 1614 cm⁻¹ for NiCo-BC-250 and NiCo-350, correspondingly. The presence of these bands (D and G) indicate that the mesoporous carbon materials were present in the synthesized composites. It was further observed that the ratio between D band peaks and G band peaks ($\frac{I_D}{I_G}$) were 0.94 and 0.93 for NiCo-BC-250 and

NiCo-350, respectively, suggesting that the synthesized composites had low graphitization crystalline structure.

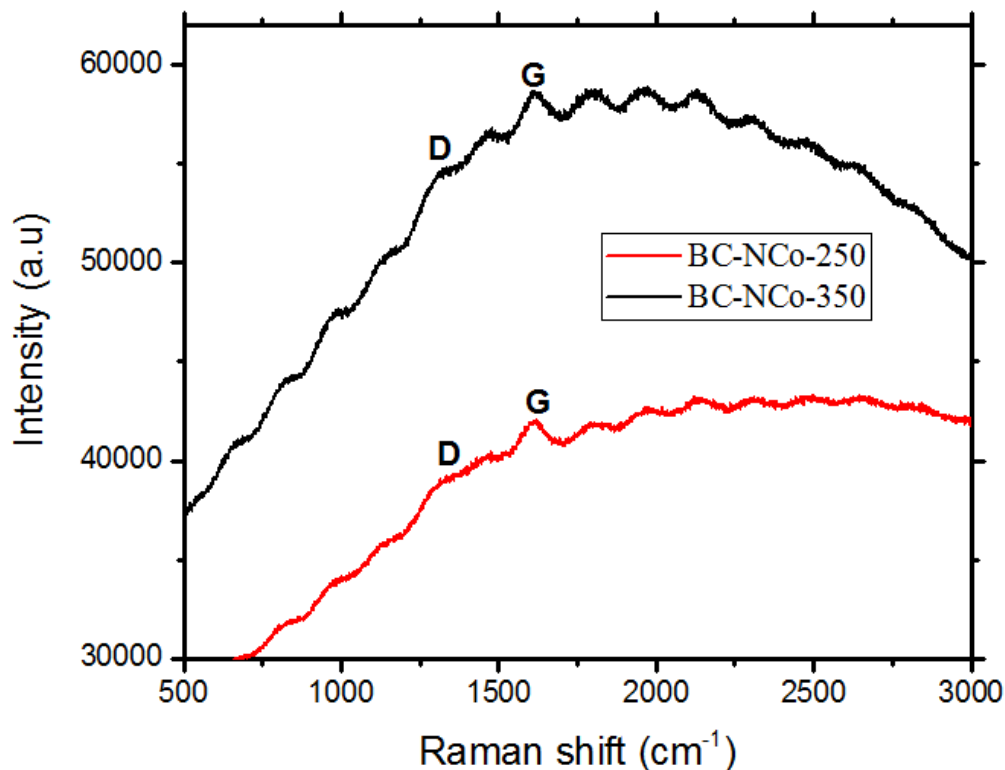


Figure 58: Raman spectra of BC-NCo-250 and BC-NCo-350

7.3.2 Electrochemical performances of the composites

The electrochemical performance of BC-NCo-100, BC-NCo-200, BC-NCo-250, BC-NCo-300, BC-NCo-350, and BC-NCo-400 was investigated in three-electrode cell. Fig. 59 shows the cyclic voltammetry (CV) results of the composites at the scan rates from 5, 10, 20, 30, 50, and 150 mV s^{-1} . Except BC-NCo-400, all other four samples exhibited the quasi rectangular cyclic voltammograms with some humps at potential range from -0.7 to -0.4 V indicating the contribution of both double layer and pseudocapacitance in the electrochemical performances. The pseudocapacitance effect is more pronounced in BC-NCo-400 indicating that it is more crystalline than other samples. The peaks at potential range -0.7 to -0.4 V might have been caused by the contribution of both $\text{Ni}^{2+}/\text{Ni}^{3+}$ and $\text{Co}^{2+}/\text{Co}^{3+}$ redox couples (Shakir, 2014) in the

composites. When scan rate was increased from 5 to 150 mV s⁻¹, all samples showed negative cathodic shift.

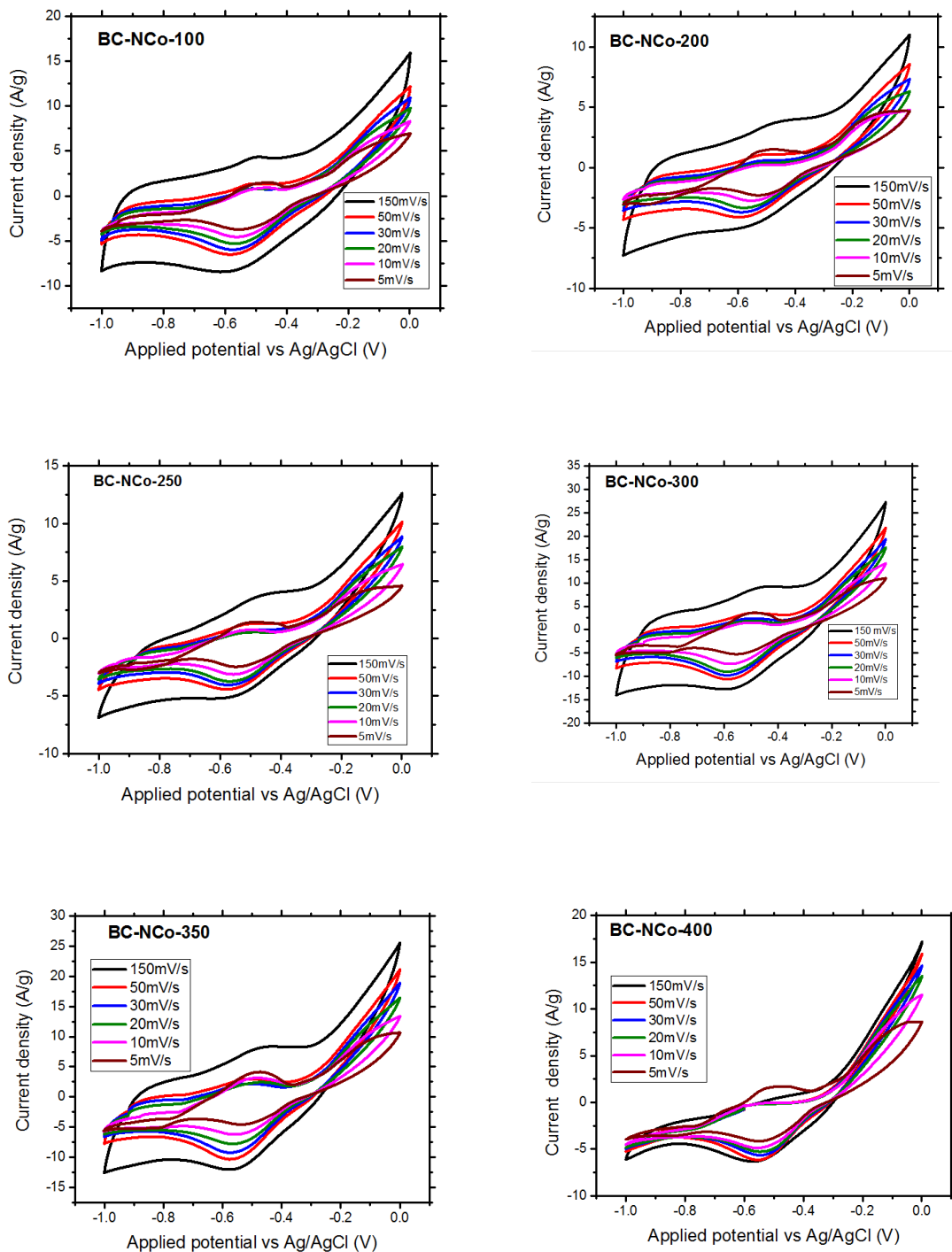


Figure 59: Cyclic voltammograms of the NiCo₂O₄/ mesoporous carbon composites.

The specific capacitances of the synthesized electrodes were calculated using equation 3.2 (chapter 3). Fig. 60a illustrates the specific capacitances of the electrodes at different scan rates. At scan rate of 5 mV s^{-1} , the specific capacitance was 535 F g^{-1} for BC-NCo-100, 412 F g^{-1} for BC-NCo-200, 404 F g^{-1} for BC-NCo-250, 833 F g^{-1} for BC-NCo-300, 835 F g^{-1} for BC-NCo-350, and 632 F g^{-1} for BC-NCo-400. BC-NCo-100 had higher specific capacitance than those of BC-NCo-200 and BC-NCo-250 because at $100 \text{ }^\circ\text{C}$ some moisture content (H_2O) may have remained in the sample thus contributing in the reactions. In contrast, the specific capacitance of BC-NCo-300 and BC-NCo-350 was higher than those of BC-NCo-100, BC-NCo-200, and BC-NCo-250 because as the annealing temperature increased, the hydroxides were converted to oxides, which then enhanced the pseudocapacitance contribution as well as EDLC capacitance. Furthermore the cross-linked nanoflakes surface morphology of BC-NiCo-350 might have contributed to high capacitance. In Fig. 60b, the relationship between the microstructures and specific capacitance is shown. It can be seen that at low annealing temperature ($100\text{-}250 \text{ }^\circ\text{C}$), the specific capacitance followed the trend of $S_{\text{meso}}/S_{\text{micro}}$ and $V_{\text{meso}}/V_{\text{micro}}$ indicating that at these temperatures, EDLC capacitance had significant contribution than pseudocapacitance. When thermal treatment was increased to 300 and $350 \text{ }^\circ\text{C}$ the contributions from EDLC and pseudocapacitance were optimal. When the annealing temperature was further increased to $400 \text{ }^\circ\text{C}$, the crystallinity of the NiCo_2O_4 increased while the carbon in the composites burnt out.

The electrochemical properties of the BC- NiCo_2O_4 electrodes were further analysed by electrochemical impedance spectroscopy (EIS). The Nyquist spectra in Fig. 60c show that all the six samples exhibited double layer capacitance as demonstrated by the straight steep slopes in the low frequency region. At high frequency, clear semicircle arcs were observable as shown by the inset in Fig. 60c. These semicircles are due to charge transfer resistance between the interface of electrode and electrolyte. It was found that BC-NCo-100 exhibited high charge transfer resistance than other samples.

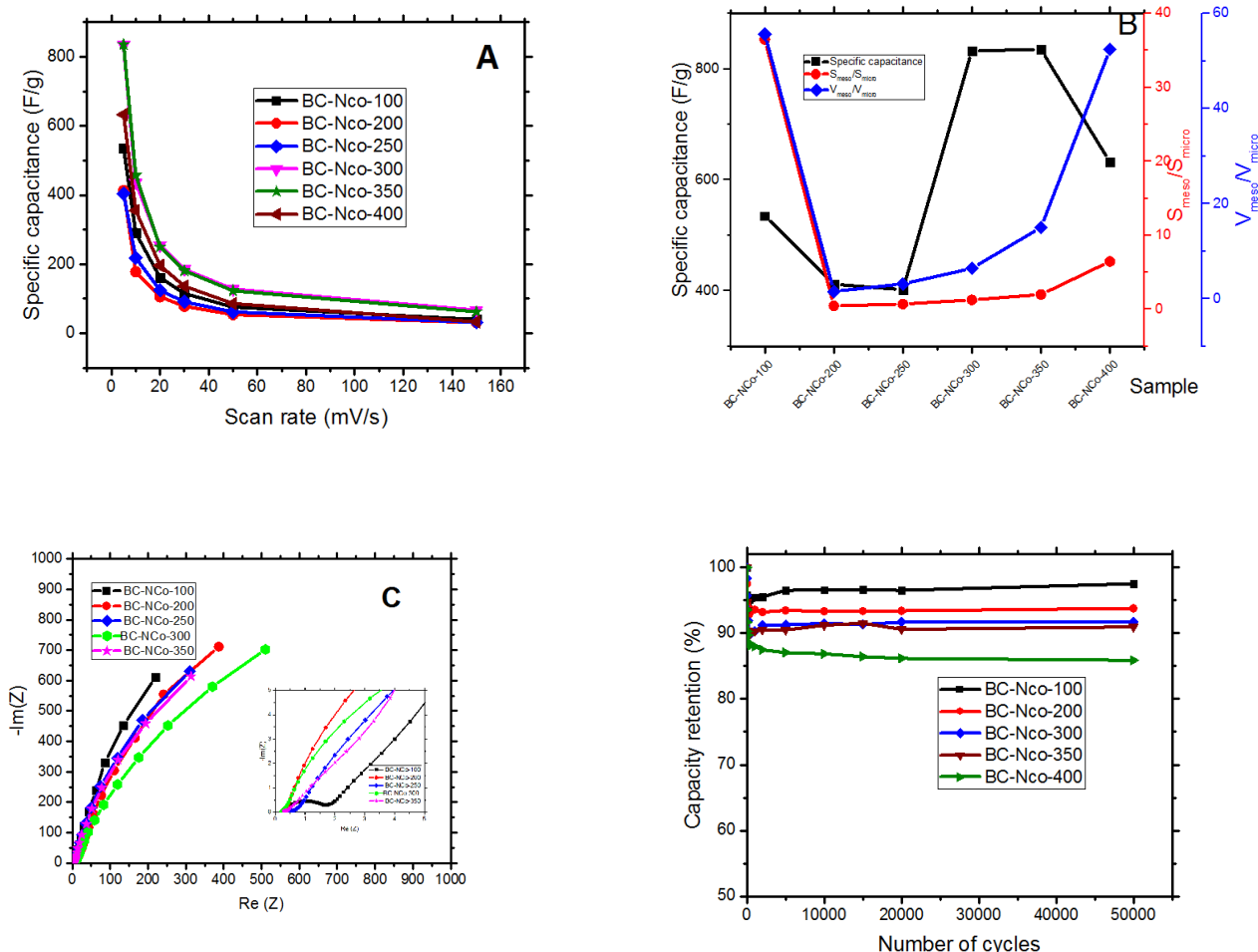


Figure 60: (a) Specific capacitance of BC-NCo-T electrodes at different scan rates, (b) Correlation of specific capacitances, $S_{\text{meso}}/S_{\text{micro}}$ and $V_{\text{meso}}/V_{\text{micro}}$ for BC-NCo-T electrodes, (c) Nyquist plots of different BC-NCo-T electrodes and (d) Cyclic stabilities of BC-NCo-T electrodes.

Cyclic stabilities at scan rate of 20 mV s^{-1} were tested to find out the cycle life of the fabricated electrodes. Fig. 60d shows a decrease in specific capacitance after the initial first 300 cycles for all the samples. The loss of specific capacitance at the first 100 cycles is associated with wettability and polarization issues (Hu *et al.*, 2010). This observation is also reported by (Wang *et al.*, 2012a) who noted that the specific capacitance of graphene-nickel cobaltite nano composites based electrode decreased during the first 100 cycles. However, in the same experiment, the specific capacitance was observed to increase after > 500 cycles implying that

cycling improved the surface wetting of the of the electrode leading to more electroactive surface area hence improved specific capacitance. The capacity retention of the nickel cobaltite/BC mesoporous composites at 50000 cycles decreased as the annealing temperature was increased. NiCo-BC-100 had about 96% capacity retention followed by NiCo-BC-200 (93%), NiCo-BC-300 (91%), and NiCo-BC-350 (90%). The cyclic stability decreased as the crystallinity of the samples increased.

7.4 Conclusion

High performance BC/NiCo₂O₄ composite supercapacitor electrodes have been successfully synthesized. The mesoporous carbon was prepared by carbonization of biogas slurry followed by chemical activation with KOH. The BC/NiCo₂O₄ composites were synthesized by reacting CoCl₂ and Ni(NO₃)₂ and nitric acid treated biogas derived mesoporous carbon using urea as hydrolyzing agent and CTAB as surfactant. The characterization carried out by nitrogen sorption studies and X-ray diffraction confirmed the formation of BC/NiCo₂O₄ composites. The specific capacitance increased when the annealing temperature was increased to 300 and 350 °C as BC-NCo-300 and BC-NCo-350 exhibited specific capacitance of 833 and 835 F g⁻¹, correspondingly. This signifies the contribution of both the EDL and pseudocapacitance of the composite. BC-NCo-200 and BC-NCo-250 composite electrodes yielded inferior specific capacitance of 412 and 404 F g⁻¹, respectively, compared to BC-NCo-100 (535 F g⁻¹). The superiority of BC-NCo-100 could be ascribed to the presence of moisture in the sample, which enhances faradic reaction via OH⁻ moistures. The high electrochemical performances of the samples might be due to well-developed microstructures and crystalline of NiCo₂O₄ in the composites.

CHAPTER EIGHT

General Discussion Conclusion and Recommendations

8.1 General discussion

This study was aimed at synthesizing porous materials for energy storage purposes. The mesoporous carbons were synthesized from biogas slurry and composited with MnO_2 and NiCo_2O_4 . This chapter therefore covers the discussion of the results contained in chapter two to seven. It details the synthesis methods, physical characterization of the synthesized samples, and electrochemical performances of the fabricated electrodes. All this eventually culminates into general conclusion recommendations and research outlook.

The synthesis routes for biogas slurry derived porous carbon and its composites produced mesopores as confirmed by the nitrogen sorption results. In synthesizing mesoporous from biogas slurry, parameters such as activating time, activating temperature, activating agent to carbon mass ratio, and carbonization temperature were varied. For all the samples, type IV isotherms were observed, an indication of existence of mesopores. In chapter five, the synthesis route was changed by incorporating both molten salts (ZnCl_2) and activating agent (KOH) in different ratios and still mesoporous carbon was obtained.

Furthermore, when BC derived mesoporous carbon was composited with MnO_2 in chapter 6, type IV isotherms were observed with H4 hysteresis loops between the adsorption and desorption. The nitrogen uptake decreased when the biogas slurry derived mesoporous carbon was composited with manganese dioxide. The decrease in nitrogen uptake with increasing MnO_2 content confirmed that the carbon matrix was filled with MnO_2 and composites were successfully synthesized.

The goal in chapter seven of this dissertation was to synthesize the BC mesoporous carbon/ NiCo_2O_4 composites. The idea was to utilize fully, the adsorption capacity of the BC carbon and the faradaic capacity of the ternary composites (NiCo_2O_4). It was found that the nitrogen adsorption capacity of composites were lower than those obtained in BC mesoporous carbon.

The textural parameters of the synthesized mesoporous carbon were investigated by varying different parameters. In chapter 3 it was observed that the specific surface area of BC based mesoporous carbon increased with KOH content, activation time as well as activation temperature. When the carbonization temperature was varied in chapter 4, it was observed that lower carbonization temperature had the highest BET surface area. The decrease of BET surface area with increasing carbonization temperature might have been due to the fact that at low carbonization temperatures, the carbonized BC was more susceptible to etching with KOH while at higher carbonization temperature the crystal structure of carbonized BC was more ordered thus hindering the etching with KOH. When the BC carbon was composited with MnO₂ the BET and micropore surface area decreased as MnO₂ loading increased. Similar trend was observed when BC carbon was composited with NiCo₂O₄. The BET surface area decreased from 514 to 110, and 112 m² g⁻¹ for BC-3-700-60, MnO₂-0.2BC, and BC-NCo-400, respectively. The decrease was due to the fact that transition metal oxide (MnO₂) and ternary metal oxide (NiCo₂O₄) filled significant fraction of the pores in carbon materials.

The average pore sizes were observed to vary depending on the method used to synthesize the porous materials. For BC mesoporous carbon the average pore sizes were found to range between 4.4 to 8.2 nm (in chapter 3) When the BC mesoporous carbons were composited with MnO₂ in chapter 6 (Table 6.1), the average pore size ranged between 4.7 to 7.3 nm. NiCo₂O₄/ BC mesoporous carbon composites in chapter 7 (Table 7.1) exhibited the average pore size ranging from 5.0 to 9.6 nm. The average sizes of all the samples were found to be in the mesoporous range. The variations of average pore sizes of the samples might have been caused by three reasons: 1) Thermal treatment of the samples which resulted to burning of more carbon hence pore size increased, 2) Time for thermal treatment which exposed more carbon to high temperature and 3) the NiCo₂O₄ filled the micropores and low size mesopores thus increasing the average pore diameter of the composites. The mesopore surface area and total pore volume had the same trend where by MnO₂/mesoporous carbon composite exhibited the lowest values.

XRD studies were carried to study the crystallographic patterns of the samples. It was observed that as prepared mesoporous carbon in chapter 3 and 4 were mainly amorphous as they exhibited two broad peaks at 25° and 42° (2θ) which corresponds to (002) and (100) reflection planes,

respectively. Furthermore, when the biogas slurry derived mesoporous carbons were composited with MnO₂ (Chapter 6), the results show amorphous phase of carbon.

In chapter 7 the TTMOs (NiCo₂O₄) was composited with biogas slurry derived mesoporous carbon. The crystallinity increased with annealing temperature due to crystal growth. The coexistence of both (002), (220), (311), (400), (511) and (440) planes confirmed the formation of composites of BC amorphous carbon and spinel structured NiCo₂O₄.

The electrochemical studies were conducted to evaluate the performances of fabricated electrodes. The cyclic voltammetry (CV) curves were used to investigate whether the electrodes exhibited electric double layer, pseudocapacitance characteristics or both. The fabricated electrodes were tested in the same electrolyte (6 M KOH) using three cell system. Electrodes fabricated from the biogas slurry derived carbon as represented by BC-3-700-30 sample displayed rectangular CV curves with minor redox hump indicating the double layer capacitance behavior and the pseudocapacitance behaviour caused by the presence of heteroatom functional groups such as nitrogen and oxygen. These functional groups were also confirmed by EDX and XPS results. Electrodes fabricated from nanomaterials synthesized through simultaneously use of ZnCl₂ and KOH also displayed rectangular CV curves and minor humps which may have been caused by residues of ZnO as shown also in the EDX results in chapter 5. The BC/MnO₂ composited electrodes and BC/Nickel cobaltite composites had semi rectangular CV curves with some redox peaks an indication of contribution from both double layer and pseudocapacitance characteristics.

The main purpose of this study was to determine the specific capacitances of the fabricated electrodes from biogas derived mesoporous carbon and composites. By comparing the specific capacitance at scan rate of 5 mV s⁻¹ the values obtained varied depending on the method used to synthesize the porous material or carbon precursor.

BC-3-700-60 exhibited lower specific capacitance (182 F g⁻¹) than BC-3-1 (216 F g⁻¹) due to faradaic contribution of Zn in BC-3-1. There is much improved specific capacitance for 4MnO₂-0.2BC to 709 F g⁻¹ due to not only the faradaic contribution of MnO₂ in the composite but also MnO₂ particle may have formed pores for ion buffering reservoir which in turn improve the ions diffusion rate of K⁺ within the bulk of the synthesized composites. Furthermore, the size of

MnO₂ particles may have reduced the diffusion length over which K⁺ must travel during the charge and discharge processes thus increasing the specific capacitance. The specific capacitance of BC-NCo-350 was around 835 F g⁻¹, the highest of all the fabricated electrodes in this dissertation. It is to be stressed that the high specific capacitance may be contributed by three factors: 1) High electrical conductivity of NiCo₂O₄, 2) The spinel structure habited by NiCo₂O₄ which could promote the redox as both Ni ion in octahedral sites and Co ions in tetrahedral form were involved and 3) there are contributions of BC mesoporous carbon through electric double layer capacitance in which the K⁺ or OH⁻ were adsorbed at the pores of the synthesized materials.

In comparison to other materials, the specific capacitance (289F g⁻¹), 709 F g⁻¹ and 835 F g⁻¹ exhibited by BC based electrode, BC/MnO₂ and BC/NiCo₂O₄ electrodes, respectively were high. The values were higher than other electrodes as elaborated in individual chapters (chapter 3,4,5,6 and 7). Therefore, it is potentially convenient for energy storage purposes.

8.2 Conclusions

The following conclusions could be made based on the results obtained in this study:

- (i) Biogas slurry was successfully transformed into mesoporous carbon for supercapacitor electrodes. Pore structures were modified by varying activation time, temperature, and KOH/carbon mass ratio. The mesoporous carbons were successively developed as evidenced by type IV isotherms obtained in nitrogen sorption studies. The synthesized porous carbon had a well-interconnected pore structure, with enough surface and interconnectivity for the efficient formation of an electric double layer. The mesoporous network preserved after chemical activation process facilitated the rapid transfer and diffusion of the electrolyte ions.
- (ii) The specific capacitances of the fabricated electrodes were observed to increase as activating time increased. The specific capacitance of 163, 182, and 289 F g⁻¹ at activating time of 30, 60, and 120 min, respectively, were obtained at 700 °C. Based on activating temperature, specific capacitances of 170, 182, and 210 F g⁻¹ at 600, 700 and 800 °C, respectively, were obtained at activating time of 60 min.

- (iii) The study on effect of carbonization temperature on specific capacitance demonstrated that carbonization temperature has influence not only on the electrical performance of the biogas slurry derived carbon based electrode but also on the pore structures. The BET specific surface area of 567, 521, and 499 m² g⁻¹ were obtained for samples carbonized at 450, 550, and 650 °C, respectively. The electrochemical performance of the samples in 6 M KOH electrolyte exhibited high gravimetric capacitance of 262, 272, and 238 F g⁻¹ for samples carbonized at 450, 550, and 650 °C, correspondingly, at scan rate of 5 mV s⁻¹. Contrary to surface area, which decreased with increasing carbonization temperature, the highest specific capacitance was obtained at moderate carbonization temperature (550 °C) both in 6 M KOH and 1 M Na₂SO₄ electrolytes.
- (iv) For mesoporous carbon synthesized through combined ZnCl₂ as molten salt and KOH activating agent route: the electrochemical studies in three-electrode cell system revealed the maximum specific capacitance of 216 F g⁻¹ for a sample with ZnCl₂:KOH mass ratio of 3:1 at scan rate of 5 mV s⁻¹. These results imply that both ZnCl₂ and KOH had significant impact in development of the mesoporous carbon.
- (v) For the electrodes fabricated from the microstructured MnO₂/mesoporous carbon composites, the specific capacitance increased with increasing MnO₂ loading. The maximum specific capacitance of 709 F g⁻¹ was attained at scan rate of 5mV s⁻¹ in three cell setting system. The trend was contrary to that of BET in which the specific surface area was observed to increase with decreasing MnO₂ content due. This signifies the importance of faradic reaction on specific capacitance.
- (vi) The design of optimum correlation between specific capacitance with pore size and mesopore content of the MnO₂/carbon composites based electrodes was realized
- (vii) The specific capacitance was enhanced when the annealing temperature was increased to 300 and 350 °C as BC-NCo-300 and BC-NCo-350 exhibited specific capacitance of 833 and 835 F g⁻¹, correspondingly. This signifies the optimal contribution of both the EDL and pseudocapacitance in the composite based electrodes.
- (viii) The cyclic stabilities of the synthesized electrodes were evaluated through capacity retention. It is concluded that the as prepared mesoporous carbon exhibited capacity retention (98%) followed by BC-NCo-T materials (90%) and then MnO₂-BC materials

(78%) at 50,000 cycles. These high electrochemical stabilities qualify the materials for energy storage applications.

- (ix) The electrical performances of the fabricated electrodes were further investigated through EIS. All electrodes exhibited semi-circles in the high frequency region indicating the charge transfer resistance and straight curves in the low frequency region representing the capacitive behavior of the samples. The semi-circles diameters were lowest for BC mesoporous based electrodes followed by NiCo₂O₄/BC composites based electrodes and then MnO₂/BC composites based electrodes.

8.3 Recommendations and research outlook

- (i) In this study specific capacitances were calculated from CV curves, since PGSTAT204 used had low current limit and was unable to perform charge and discharge. Therefore, there is a need to use potentiostat with high current limit, which is able to perform galvanostatic charge and discharge to closely determine the columbic efficiency power density and energy density.
- (ii) Furthermore, the study used 5 mg as the mass of the active materials in the electrodes, the mass loading effect on specific capacitance values need to be performed so as to determine more accurate optimal mass loading. Additionally, studies on the effect of different binders on the specific capacitance need to be pursued.
- (iii) The aqueous electrolytes used in this thesis are mainly 6 M KOH and 1M NaSO₄, because of their safety and environmentally benign, low material cost, not inflammability and high life time however the range of working potential window is limited to approximately 1 V. Since the energy density of supercapacitors is a function of voltage window future study on developing new electrolyte and test the performance of synthesized electrodes in new electrolyte is fairly important for the flexible supercapacitors.
- (iv) It is recommended also to investigate the physical properties and electrochemical characteristics biogas slurry derived mesoporous carbon/MnO₂/NiCo₂O₄ composite materials for supercapacitor application
- (v) Furthermore, the design of supercapacitors prototype with optimized parameters will be done to enable the cost effect analysis of the materials.

REFERENCES

- Abatzoglou, N. and Boivin, S. (2009). A review of biogas purification processes. *Biofuels, Bioprod. Bior.* **3**(1): 42-71.
- Abbas, N., Shao, G.N., Haider, M.S., Imran, S.M., Park, S.S., Jeon, S.-J. and Kim, H.T. (2016). Inexpensive sol-gel synthesis of multiwalled carbon nanotube-TiO₂ hybrids for high performance antibacterial materials. *Materials Science and Engineering: C.* **68**(2016): 780-788.
- Ademiluyi, F. and David-West, E. (2012). Effect of chemical activation on the adsorption of heavy metals using activated carbons from waste materials. *International Scholarly Research Notices:Chemical Engineering.* **2012**(2012).
- Amaral, L.G., Szczurek, A., Fierro, V., Stein, N., Boulanger, C., Pizzi, A. and Celzard, A. (2012). Pore structure and electrochemical performances of tannin-based carbon cryogels. *Biomass and Bioenergy.* **39**(274-282).
- Arthurson, V. (2009). Closing the global energy and nutrient cycles through application of biogas residue to agricultural land—potential benefits and drawback. *Energies.* **2**(2): 226-242.
- Austin, G. and Morris, G. (2012). Biogas production in Africa, Bioenergy for sustainable development in Africa. Springer, pp. 103-115.
- Awitdrus, M.D., Talib, I., Omar, R., Jumali, M.H.H., Taer, E. and Saman, M. (2010). Microcrystallite dimension and total active surface area of carbon electrode from mixtures of pre-carbonized oil palm empty fruit bunches and green petroleum cokes. *Sains Malaysiana.* **39**(1): 83-86.
- Azevedo, D.C., Araujo, J.C.S., Bastos-Neto, M., Torres, A.E.B., Jaguaribe, E.F. and Cavalcante, C.L. (2007). Microporous activated carbon prepared from coconut shells using chemical activation with zinc chloride. *Microporous and Mesoporous Materials.* **100**(1): 361-364.
- Babel, K. and Jurewicz, K. (2004). KOH activated carbon fabrics as supercapacitor material. *Journal of Physics and Chemistry of Solids.* **65**(2): 275-280.
- Bagheri, N. and Abedi, J. (2009). Preparation of high surface area activated carbon from corn by chemical activation using potassium hydroxide. *Chemical Engineering Research and Design.* **87**(8): 1059-1064.

- Balathanigaimani, M.S., Shim, W.G., Lee, M.J., Kim, C., Lee, J.W. and Moon, H. (2008). Highly porous electrodes from novel corn grains-based activated carbons for electrical double layer capacitors. *Electrochemistry Communications*. **10**(6): 868-871.
- Barbieri, O., Hahn, M., Herzog, A. and Kötz, R. (2005). Capacitance limits of high surface area activated carbons for double layer capacitors. *Carbon*. **43**(6): 1303-1310.
- Basri, N. and Dolah, B. (2013). Physical and electrochemical properties of supercapacitor electrodes derived from carbon nanotube and biomass carbon. *International Journal of Electrochemical Science*. **8**(2013): 257-273.
- Basri, N.H., Deraman, M., Kanwal, S., Talib, I., Manjunatha, J., Aziz, A. and Farma, R. (2013). Supercapacitors using binderless composite monolith electrodes from carbon nanotubes and pre-carbonized biomass residues. *Biomass and Bioenergy*. **59**(2013): 370-379.
- Béguin, F., Presser, V., Balducci, A. and Frackowiak, E. (2014). Carbons and electrolytes for advanced supercapacitors. *Advanced Materials*. **26**(14): 2219-2251.
- Bhattacharjya, D. and Yu, J.-S. (2014). Activated carbon made from cow dung as electrode material for electrochemical double layer capacitor. *Journal of Power Sources*. **262**(2014): 224-231.
- Biswal, M., Banerjee, A., Deo, M. and Ogale, S. (2013). From dead leaves to high energy density supercapacitors. *Energy & Environmental Science*. **6**(4): 1249-1259.
- Bouchelta, C., Medjram, M.S., Bertrand, O. and Bellat, J.P. (2008). Preparation and characterization of activated carbon from date stones by physical activation with steam. *Journal of Analytical and Applied Pyrolysis*. **82**(1): 70-77.
- Burke, A. (2000). Ultracapacitors: why, how, and where is the technology. *Journal of Power Sources*. **91**(1): 37-50.
- Calvo, E., Ferrera-Lorenzo, N., Menéndez, J. and Arenillas, A. (2013). Microwave synthesis of micro-mesoporous activated carbon xerogels for high performance supercapacitors. *Microporous and Mesoporous Materials*. **168**(2013): 206-212.
- Calvo, E., Rey-Raap, N., Arenillas, A. and Menendez, J. (2014). The effect of the carbon surface chemistry and electrolyte pH on the energy storage of supercapacitors. *Royal Society of Chemistry Advances*. **4**(61): 32398-32404.
- Chaitra, K., Vinny, R., Sivaraman, P., Reddy, N., Hu, C., Venkatesh, K., Vivek, C., Nagaraju, N. and Kathyayini, N. (2017). KOH activated carbon derived from biomass-banana fibers as

- an efficient negative electrode in high performance asymmetric supercapacitor. *Journal of Energy Chemistry*. **26**(1): 56-62.
- Chandra, A. (2012). Supercapacitors: an alternate technology for energy storage. *Proceedings of the National Academy of Sciences, India Section A: Physical Sciences*. **82**(1): 79-90.
- Chang, S.-K., Zainal, Z., Tan, K.-B., Yusof, N.A., Yusoff, W.M.D.W. and Prabakaran, S. (2012). Nickel–cobalt oxide/activated carbon composite electrodes for electrochemical capacitors. *Current Applied Physics*. **12**(6): 1421-1428.
- Chang, Y., Antonietti, M. and Fellingner, T.P. (2015). Synthesis of Nanostructured Carbon through Ionothermal Carbonization of Common Organic Solvents and Solutions. *Angewandte Chemie International Edition*. **54**(18): 5507-5512.
- Chen, H., Jiang, J., Zhang, L., Qi, T., Xia, D. and Wan, H. (2014). Facilely synthesized porous NiCo₂O₄ flowerlike nanostructure for high-rate supercapacitors. *Journal of Power Sources*. **248**(2014): 28-36.
- Chen, M., Kang, X., Wumaier, T., Dou, J., Gao, B., Han, Y., Xu, G., Liu, Z. and Zhang, L. (2013). Preparation of activated carbon from cotton stalk and its application in supercapacitor. *Journal of Solid State Electrochemistry*. **17**(4): 1005-1012.
- Chen, W., Fan, Z., Gu, L., Bao, X. and Wang, C. (2010a). Enhanced capacitance of manganese oxide via confinement inside carbon nanotubes. *Chemical Communications*. **46**(22): 3905-3907.
- Chen, W., Zhang, H., Huang, Y. and Wang, W. (2010b). A fish scale based hierarchical lamellar porous carbon material obtained using a natural template for high performance electrochemical capacitors. *Journal of Materials Chemistry*. **20**(23): 4773-4775.
- Cheng, J., Lu, Y., Qiu, K., Yan, H., Hou, X., Xu, J., Han, L., Liu, X., Kim, J.-K. and Luo, Y. (2015). Mesoporous ZnCo₂O₄ nanoflakes grown on nickel foam as electrodes for high performance supercapacitors. *Physical Chemistry Chemical Physics*. **17**(26): 17016-17022.
- Cheng, P.-Z. and Teng, H. (2003). Electrochemical responses from surface oxides present on HNO₃-treated carbons. *Carbon*. **41**(11): 2057-2063.
- Cheng, P., Li, T., Yu, H., Zhi, L., Liu, Z.H. and Lei, Z. (2016). Biomass-Derived Carbon Fiber Aerogel as Binder-Free Electrode for High-Rate Supercapacitor. *The Journal of Physical Chemistry C*. **120**(4): 2079-2086.

- Chien, H.C., Cheng, W.Y., Wang, Y.H. and Lu, S.Y. (2012). Ultrahigh specific capacitances for supercapacitors achieved by nickel cobaltite/carbon aerogel composites. *Advanced Functional Materials*. **22**(23): 5038-5043.
- Chmiola, J., Yushin, G., Gogotsi, Y., Portet, C., Simon, P. and Taberna, P.-L. (2006). Anomalous increase in carbon capacitance at pore sizes less than 1 nanometer. *Science*. **313**(5794): 1760-1763.
- Chupas, P.J., Qiu, X., Hanson, J.C., Lee, P.L., Grey, C.P. and Billinge, S.J. (2003). Rapid-acquisition pair distribution function (RA-PDF) analysis. *Journal of Applied Crystallography*. **36**(6): 1342-1347.
- Conway, B.E. (2013a). Electrochemical supercapacitors: scientific fundamentals and technological applications. Springer Science & Business Mediapp. 11-50pp.
- Conway, B.E. (2013b). Electrochemical supercapacitors: scientific fundamentals and technological applications. Springer Science & Business Mediapp.
- Cui, B., Lin, H., Li, J.B., Li, X., Yang, J. and Tao, J. (2008). Core–ring structured NiCo₂O₄ nanoplatelets: synthesis, characterization, and electrocatalytic applications. *Advanced Functional Materials*. **18**(9): 1440-1447.
- Cui, L., Huang, L., Ji, M., Wang, Y., Shi, H., Zuo, Y. and Kang, S. (2016). High-performance MgCo₂O₄ nanocone arrays grown on three-dimensional nickel foams: Preparation and application as binder-free electrode for pseudo-supercapacitor. *Journal of Power Sources*. **333**(2016): 118-124.
- Dai, Z., Peng, C., Chae, J.H., Ng, K.C. and Chen, G.Z. (2015). Cell voltage versus electrode potential range in aqueous supercapacitors. *Scientific reports*. **5**(2015): 9854.
- Dalvi, A.D., Bacon, W.G. and Osborne, R.C. (Ed.) (2004). The past and the future of nickel laterites. In: *Prospectors and Developers Association of Canada 2004 International Convention, Trade Show and Investors Exchange. Toronto: The prospectors and Developers Association of Canada*, pp. 1-27, 2004.
- Daud, W.M.A.W., Ali, W.S.W. and Sulaiman, M.Z. (2000). The effects of carbonization temperature on pore development in palm-shell-based activated carbon. *Carbon*. **38**(14): 1925-1932.
- Deng, L., Hao, Z., Wang, J., Zhu, G., Kang, L., Liu, Z.-H., Yang, Z. and Wang, Z. (2013). Preparation and capacitance of graphene/multiwall carbon nanotubes/MnO₂ hybrid

- material for high-performance asymmetrical electrochemical capacitor. *Electrochimica Acta*. **89**(2013): 191-198.
- Deng, X., Zhao, B., Zhu, L. and Shao, Z. (2015). Molten salt synthesis of nitrogen-doped carbon with hierarchical pore structures for use as high-performance electrodes in supercapacitors. *Carbon*. **93**(48-58).
- Divyashree, A., Manaf, S.A.B.A., Yallappa, S., Chaitra, K., Kathyayini, N. and Hegde, G. (2016). Low cost, high performance supercapacitor electrode using coconut wastes: eco-friendly approach. *Journal of Energy Chemistry*. **25**(5): 880-887.
- Dolah, B., Deraman, M., Othman, M.A.R., Farma, R., Taer, E., Basri, N., Talib, I., Omar, R. and Nor, N. (2014). A method to produce binderless supercapacitor electrode monoliths from biomass carbon and carbon nanotubes. *Materials Research Bulletin*. **60**(2014): 10-19.
- Döşoğlu, M.K. and Arsoy, A.B. (2016). Transient modeling and analysis of a DFIG based wind farm with supercapacitor energy storage. *International Journal of Electrical Power and Energy Systems*. **78**(2016): 414-421.
- Du, X., Wang, C.-Y., Chen, M.-M., Zhao, S. and Wang, J. (2010). Effects of carbonization temperature on microstructure and electrochemical performances of phenolic resin-based carbon spheres. *Journal of Physics and Chemistry of Solids*. **71**(3): 214-218.
- Du, X., Wang, C., Chen, M., Jiao, Y. and Wang, J. (2009). Electrochemical performances of nanoparticle Fe₃O₄/activated carbon supercapacitor using KOH electrolyte solution. *The Journal of Physical Chemistry C*. **113**(6): 2643-2646.
- Dunn, B., Kamath, H. and Tarascon, J.-M. (2011). Electrical energy storage for the grid: a battery of choices. *Science*. **334**(6058): 928-935.
- Egami, T. and Billinge, S.J. (2012). Underneath the Bragg peaks: structural analysis of complex materials. Newnes.p. 34pp.
- Elaigwu, S.E. and Greenway, G.M. (2015). Microwave-assisted and conventional hydrothermal carbonization of lignocellulosic waste material: Comparison of the chemical and structural properties of the hydrochars. *Journal of Analytical and Applied Pyrolysis*. **118**(2016): 1-8.
- Elmouwahidi, A., Zapata-Benabithé, Z., Carrasco-Marín, F. and Moreno-Castilla, C. (2012). Activated carbons from KOH-activation of argan (*Argania spinosa*) seed shells as supercapacitor electrodes. *Bioresource Technology*. **111**(2012): 185-190.

- Enock, T.K., King'onde, C.K., Pogrebnoi, A. and Jande, Y.A.C. (2017a). Biogas-slurry derived mesoporous carbon for supercapacitor applications. *Materials Today Energy*. **5**(2017): 126-137.
- Enock, T.K., King'onde, C.K., Pogrebnoi, A. and Jande, Y.A.C. (2017b). Status of Biomass Derived Carbon Materials for Supercapacitor Application. *International Journal of Electrochemistry*. **2017**(2017): 14.
- Farrow, C., Juhas, P., Liu, J., Bryndin, D., Božin, E., Bloch, J., Proffen, T. and Billinge, S. (2007). PDFfit2 and PDFgui: computer programs for studying nanostructure in crystals. *Journal of Physics: Condensed Matter*. **19**(33): 335219.
- Farrow, C.L. and Billinge, S.J. (2009). Relationship between the atomic pair distribution function and small-angle scattering: implications for modeling of nanoparticles. *Acta Crystallographica Section A: Foundations of Crystallography*. **65**(3): 232-239.
- Fernández, J.A., Tennison, S., Kozynchenko, O., Rubiera, F., Stoeckli, F. and Centeno, T. (2009). Effect of mesoporosity on specific capacitance of carbons. *Carbon*. **47**(6): 1598-1604.
- Ferrero, G., Fuertes, A. and Sevilla, M. (2015). From Soybean residue to advanced supercapacitors. *Scientific reports*. **5**(2015): 1-13.
- Fischer, U., Saliger, R., Bock, V., Petricevic, R. and Fricke, J. (1997). Carbon aerogels as electrode material in supercapacitors. *Journal of Porous Materials*. **4**(4): 281-285.
- Frackowiak, E. and Beguin, F. (2001). Carbon materials for the electrochemical storage of energy in capacitors. *Carbon*. **39**(6): 937-950.
- Gallego, N.C., Contescu, C.I., Morris, J., Egami, T. and Pennycook, S. (2009). IV. I. 16 Atomistic Mechanisms of Metal-Assisted Hydrogen Storage in Nanostructured Carbon.
- Garg, R., Pathak, H., Das, D. and Tomar, R. (2005). Use of flyash and biogas slurry for improving wheat yield and physical properties of soil. *Environmental Monitoring and Assessment*. **107**(1-3): 1-9.
- Gheorghe, C., Marculescu, C., Badea, A., Dinca, C. and Apostol, T. (Ed.) (2009). Effect of pyrolysis conditions on bio-char production from biomass. In: *Proceedings of the 3rd World Scientific and Engineering Academy and Society International Conference on Renewable Energy Sources. University of La Laguna, Tenerife, Canary Islands Spain*, pp. 239-241, 2009.

- Gong, Y., Li, D., Fu, Q. and Pan, C. (2015). Influence of graphene microstructures on electrochemical performance for supercapacitors. *Progress in Natural Science: Materials International*. **25**(5): 379-385.
- Goodman, P.A., Li, H., Gao, Y., Lu, Y., Stenger-Smith, J. and Redepenning, J. (2013). Preparation and characterization of high surface area, high porosity carbon monoliths from pyrolyzed bovine bone and their performance as supercapacitor electrodes. *Carbon*. **55**(2013): 291-298.
- Gryglewicz, G., Machnikowski, J., Lorenc-Grabowska, E., Lota, G. and Frackowiak, E. (2005). Effect of pore size distribution of coal-based activated carbons on double layer capacitance. *Electrochimica Acta*. **50**(5): 1197-1206.
- Guo, F. and Fang, Z. (2014). Shape-controlled Synthesis of Activated Bio-chars by Surfactant-templated Ionothermal Carbonization in Acidic Ionic Liquid and Activation with Carbon Dioxide. *BioResources*. **9**(2): 3369-3383.
- Halper, M.S. and Ellenbogen, J.C. (2006). Supercapacitors: A brief overview. *The MITRE Corporation, McLean, Virginia, USA*: 1-34.
- Hammersley, A., Svensson, S., Hanfland, M., Fitch, A. and Hausermann, D. (1996). Two-dimensional detector software: from real detector to idealised image or two-theta scan. *International Journal of High Pressure Research*. **14**(4-6): 235-248.
- Han, J., Li, L., Fang, P. and Guo, R. (2012). Ultrathin MnO₂ nanorods on conducting polymer nanofibers as a new class of hierarchical nanostructures for high-performance supercapacitors. *The Journal of Physical Chemistry C*. **116**(30): 15900-15907.
- Hao, P., Zhao, Z., Tian, J., Li, H., Sang, Y., Yu, G., Cai, H., Liu, H., Wong, C. and Umar, A. (2014). Hierarchical porous carbon aerogel derived from bagasse for high performance supercapacitor electrode. *Nanoscale*. **6**(20): 12120-12129.
- He, S. and Chen, W. (2015). Application of biomass-derived flexible carbon cloth coated with MnO₂ nanosheets in supercapacitors. *Journal of Power Sources*. **294**(2015): 150-158.
- He, X., Ling, P., Qiu, J., Yu, M., Zhang, X., Yu, C. and Zheng, M. (2013a). Efficient preparation of biomass-based mesoporous carbons for supercapacitors with both high energy density and high power density. *Journal of Power Sources*. **240**(109-113).

- He, X., Ling, P., Yu, M., Wang, X., Zhang, X. and Zheng, M. (2013b). Rice husk-derived porous carbons with high capacitance by ZnCl_2 activation for supercapacitors. *Electrochimica Acta*. **105**(635-641).
- Hou, C.-H. and Huang, C.-Y. (2013). A comparative study of electrosorption selectivity of ions by activated carbon electrodes in capacitive deionization. *Desalination*. **314**(2013): 124-129.
- Hu, C.C., Wang, C.C., Wu, F.C. and Tseng, R.L. (2007). Characterization of pistachio shell-derived carbons activated by a combination of KOH and CO_2 for electric double-layer capacitors. *Electrochimica Acta*. **52**(7): 2498-2505.
- Hu, G., Li, C. and Gong, H. (2010). Capacitance decay of nanoporous nickel hydroxide. *Journal of Power Sources*. **195**(19): 6977-6981.
- Huang, J., Sumpter, B.G. and Meunier, V. (2008). A universal model for nanoporous carbon supercapacitors applicable to diverse pore regimes, carbon materials, and electrolytes. *Chemistry—A European Journal*. **14**(22): 6614-6626.
- Huang, W., Zhang, H., Huang, Y., Wang, W. and Wei, S. (2011). Hierarchical porous carbon obtained from animal bone and evaluation in electric double-layer capacitors. *Carbon*. **49**(3): 838-843.
- Huber, G.W., Chheda, J.N., Barrett, C.J. and Dumesic, J.A. (2005). Production of liquid alkanes by aqueous-phase processing of biomass-derived carbohydrates. *Science*. **308**(5727): 1446-1450.
- Hulicova, D., Yamashita, J., Soneda, Y., Hatori, H. and Kodama, M. (2005). Supercapacitors prepared from melamine-based carbon. *Chemistry of Materials*. **17**(5): 1241-1247.
- Hulicova, J.D., Puziy, A.M., Poddubnaya, O.I., Suárez-García, F., Tascón, J.M. and Lu, G.Q. (2009). Highly stable performance of supercapacitors from phosphorus-enriched carbons. *Journal of the American Chemical Society*. **131**(14): 5026-5027.
- Inamdar, A., Kim, Y., Pawar, S., Kim, J., Im, H. and Kim, H. (2011). Chemically grown, porous, nickel oxide thin-film for electrochemical supercapacitors. *Journal of Power Sources*. **196**(4): 2393-2397.
- Ishak, M., Deraman, M., Talib, I., Basri, N., Farma, R., Taer, E., Omar, R., Nor, N. and Dolah, B. (Ed.) (2015). Effect of carbonization temperature on the physical and electrochemical

- properties of supercapacitor electrode from fibers of oil palm empty fruit bunches. *In: The 5th Asian Physics Symposium (APS 2012)*. AIP Publishing, p. 030005, 2015.
- Ismanto, A.E., Wang, S., Soetaredjo, F.E. and Ismadji, S. (2010). Preparation of capacitor's electrode from cassava peel waste. *Bioresource Technology*. **101**(10): 3534-3540.
- Jain, A., Balasubramanian, R. and Srinivasan, M. (Ed.) (2015a). Hydrothermal pre-treatment of biomass waste for high surface area mesoporous activated carbons. *In: Asia Pacific Confederation of Chemical Engineering Congress 2015: APCCChE 2015, incorporating Chemica 2015. Engineers Australia*, p. 981, 2015a.
- Jain, A., Xu, C., Jayaraman, S., Balasubramanian, R., Lee, J. and Srinivasan, M. (2015b). Mesoporous activated carbons with enhanced porosity by optimal hydrothermal pre-treatment of biomass for supercapacitor applications. *Microporous and Mesoporous Materials*. **218**(2015): 55-61.
- Jiang, H., Ma, J. and Li, C. (2012). Mesoporous carbon incorporated metal oxide nanomaterials as supercapacitor electrodes. *Advanced Materials*. **24**(30): 4197-4202.
- Jiang, L., Yan, J., Hao, L., Xue, R., Sun, G. and Yi, B. (2013). High rate performance activated carbons prepared from ginkgo shells for electrochemical supercapacitors. *Carbon*. **56**(2013): 146-154.
- Jisha, M., Hwang, Y.J., Shin, J.S., Nahm, K.S., Kumar, T.P., Karthikeyan, K., Dhanikaivelu, N., Kalpana, D., Renganathan, N. and Stephan, A.M. (2009). Electrochemical characterization of supercapacitors based on carbons derived from coffee shells. *Materials Chemistry and Physics*. **115**(1): 33-39.
- Kalderis, D., Kotti, M., Méndez, A. and Gascó, G. (2014). Characterization of hydrochars produced by hydrothermal carbonization of rice husk. *Solid Earth*. **5**(1): 477.
- Kalpana, D., Cho, S., Lee, S., Lee, Y., Misra, R. and Renganathan, N. (2009). Recycled waste paper—A new source of raw material for electric double-layer capacitors. *Journal of Power Sources*. **190**(2): 587-591.
- Kim, C., Lee, J.W., Kim, J.H. and Yang, K.S. (2006). Feasibility of bamboo-based activated carbons for an electrochemical supercapacitor electrode. *Korean Journal of Chemical Engineering*. **23**(4): 592-594.

- Kim, H. and Popov, B.N. (2002). Characterization of hydrous ruthenium oxide/carbon nanocomposite supercapacitors prepared by a colloidal method. *Journal of Power Sources*. **104**(1): 52-61.
- Kim, M.H., Kim, K.B., Kang, K., Han, J.T. and Roh, K.C. (2013). Ribbon-like activated carbon with a multi-structure for supercapacitors. *Journal of Materials Chemistry A*. **1**(44): 14008-14012.
- Kodama, K., Iikubo, S., Taguchi, T. and Shamoto, S.i. (2006). Finite size effects of nanoparticles on the atomic pair distribution functions. *Acta Crystallographica Section A: Foundations of Crystallography*. **62**(6): 444-453.
- Kötz, R. and Carlen, M. (2000). Principles and applications of electrochemical capacitors. *Electrochimica Acta*. **45**(15): 2483-2498.
- Krishnamoorthy, K., Veerasubramani, G.K., Radhakrishnan, S. and Kim, S.J. (2014). Supercapacitive properties of hydrothermally synthesized sphere like MoS₂ nanostructures. *Materials Research Bulletin*. **50**(2014): 499-502.
- Kuang, M., Wen, Z.Q., Guo, X.L., Zhang, S.M. and Zhang, Y.X. (2014). Engineering firecracker-like beta-manganese dioxides@ spinel nickel cobaltates nanostructures for high-performance supercapacitors. *Journal of Power Sources*. **270**(2014): 426-433.
- Kurniawan, F., Wongso, M., Ayucitra, A., Soetaredjo, F.E., Angkawijaya, A.E., Ju, Y.-H. and Ismadji, S. (2015). Carbon microsphere from water hyacinth for supercapacitor electrode. *Journal of the Taiwan Institute of Chemical Engineers*. **47**(2015): 197-201.
- Laine, J. and Calafat, A. (1989). Preparation and characterization of activated carbons from coconut shell impregnated with phosphoric acid. *Carbon*. **27**(2): 191-195.
- Lanlan, J., Xianyou, W., Hao, W., Chun, W., Qinglan, Z. and Yunfeng, S. (2013). Effect of carbonization temperature on structure and electrochemical performance of porous carbon from metal framework. *Journal of Central South University (Science and Technology)*. **44**(10): 4012-4018 . .
- Largeot, C., Portet, C., Chmiola, J., Taberna, P.L., Gogotsi, Y. and Simon, P. (2008). Relation between the ion size and pore size for an electric double-layer capacitor. *Journal of the American Chemical Society*. **130**(9): 2730-2731.

- Le Van, K. and Thi, T.T.L. (2014). Activated carbon derived from rice husk by NaOH activation and its application in supercapacitor. *Progress in Natural Science: Materials International*. **24**(3): 191-198.
- Lebedeva, M.V., Yeletsky, P.M., Ayupov, A.B., Kuznetsov, A.N., Yakovlev, V.A. and Parmon, V.N. (2015). Micro–mesoporous carbons from rice husk as active materials for supercapacitors. *Materials for Renewable and Sustainable Energy*. **4**(4): 1-9.
- Lee, H.M., An, K.H. and Kim, B.J. (2014). Effects of carbonization temperature on pore development in polyacrylonitrile-based activated carbon nanofibers. *Carbon letters*. **15**(2): 146-150.
- Lei, Y., Fournier, C., Pascal, J.-L. and Favier, F. (2008). Mesoporous carbon–manganese oxide composite as negative electrode material for supercapacitors. *Microporous and Mesoporous Materials*. **110**(1): 167-176.
- Li, J., Ma, S., Cheng, L. and Wu, Q. (2015). Egg yolk-derived three-dimensional porous carbon for stable electrochemical supercapacitors. *Materials Letters*. **139**(2015): 429-432.
- Li, J., Zan, G. and Wu, Q. (2016). Nitrogen and sulfur self-doped porous carbon from brussel sprouts as electrode materials for high stable supercapacitors. *Royal Society of Chemistry Advances*. **6**(2016): 57464-57472.
- Li, L., Dong, S., Chen, X., Han, P., Xu, H., Yao, J., Shang, C., Liu, Z. and Cui, G. (2012a). A renewable bamboo carbon/polyaniline composite for a high-performance supercapacitor electrode material. *Journal of Solid State Electrochemistry*. **16**(3): 877-882.
- Li, L., Hu, Z.A., An, N., Yang, Y.Y., Li, Z.M. and Wu, H.Y. (2014a). Facile synthesis of MnO₂/CNTs composite for supercapacitor electrodes with long cycle stability. *The Journal of Physical Chemistry C*. **118**(40): 22865-22872.
- Li, P., Yang, Y., Shi, E., Shen, Q., Shang, Y., Wu, S., Wei, J., Wang, K., Zhu, H. and Yuan, Q. (2014b). Core-double-shell, carbon nanotube@ polypyrrole@ MnO₂ sponge as freestanding, compressible supercapacitor electrode. *American Chemical Society Applied Materials and Interfaces*. **6**(7): 5228-5234.
- Li, W., Zhang, F., Dou, Y., Wu, Z., Liu, H., Qian, X., Gu, D., Xia, Y., Tu, B. and Zhao, D. (2011a). A Self-Template Strategy for the Synthesis of Mesoporous Carbon Nanofibers as Advanced Supercapacitor Electrodes. *Advanced Energy Materials*. **1**(3): 382-386.

- Li, X., Han, C., Chen, X. and Shi, C. (2010). Preparation and performance of straw based activated carbon for supercapacitor in non-aqueous electrolytes. *Microporous and Mesoporous Materials*. **131**(1): 303-309.
- Li, X., Xing, W., Zhuo, S., Zhou, J., Li, F., Qiao, S.Z. and Lu, G.Q. (2011b). Preparation of capacitor's electrode from sunflower seed shell. *Bioresource Technology*. **102**(2): 1118-1123.
- Li, Z., Wang, J., Liu, S., Liu, X. and Yang, S. (2011c). Synthesis of hydrothermally reduced graphene/MnO₂ composites and their electrochemical properties as supercapacitors. *Journal of Power Sources*. **196**(19): 8160-8165.
- Li, Z., Xu, Z., Tan, X., Wang, H., Holt, C.M., Stephenson, T., Olsen, B.C. and Mitlin, D. (2013). Mesoporous nitrogen-rich carbons derived from protein for ultra-high capacity battery anodes and supercapacitors. *Energy and Environmental Science*. **6**(3): 871-878.
- Li, Z., Zhang, L., Amirkhiz, B.S., Tan, X., Xu, Z., Wang, H., Olsen, B.C., Holt, C. and Mitlin, D. (2012b). Carbonized Chicken Eggshell Membranes with 3D Architectures as High-Performance Electrode Materials for Supercapacitors. *Advanced Energy Materials*. **2**(4): 431-437.
- Liang, C., Li, Z. and Dai, S. (2008). Mesoporous carbon materials: synthesis and modification. *Angewandte Chemie International Edition*. **47**(20): 3696-3717.
- Lin, C., Ritter, J.A. and Popov, B.N. (1999). Development of Carbon-Metal Oxide Supercapacitors from Sol-Gel Derived Carbon-Ruthenium Xerogels. *Journal of the Electrochemical Society*. **146**(9): 3155-3160.
- Lin, X.X., Tan, B., Peng, L., Wu, Z.F. and Xie, Z.L. (2016). Ionothermal synthesis of microporous and mesoporous carbon aerogels from fructose as electrode materials for supercapacitors. *Journal of Materials Chemistry A*. **4**(12): 4497-4505.
- Lin, Y.-R. and Teng, H. (2003). A novel method for carbon modification with minute polyaniline deposition to enhance the capacitance of porous carbon electrodes. *Carbon*. **41**(14): 2865-2871.
- Liu, C., Li, F., Ma, L.P. and Cheng, H.M. (2010a). Advanced materials for energy storage. *Advanced Materials*. **22**(8): E28-E62.

- Liu, M., Gan, L., Xiong, W., Xu, Z., Zhu, D. and Chen, L. (2014a). Development of MnO₂/porous carbon microspheres with a partially graphitic structure for high performance supercapacitor electrodes. *Journal of Materials Chemistry A*. **2**(8): 2555-2562.
- Liu, M., Gan, L., Xiong, W., Zhao, F., Fan, X., Zhu, D., Xu, Z., Hao, Z. and Chen, L. (2013). Nickel-doped activated mesoporous carbon microspheres with partially graphitic structure for supercapacitors. *Energy and Fuels*. **27**(2): 1168-1173.
- Liu, Q.S., Zheng, T., Wang, P. and Guo, L. (2010b). Preparation and characterization of activated carbon from bamboo by microwave-induced phosphoric acid activation. *Industrial Crops and Products*. **31**(2): 233-238.
- Liu, X., Giordano, C. and Antonietti, M. (2014b). A Facile Molten-Salt Route to Graphene Synthesis. *Small*. **10**(1): 193-200.
- Long, C., Chen, X., Jiang, L., Zhi, L. and Fan, Z. (2015a). Porous layer-stacking carbon derived from in-built template in biomass for high volumetric performance supercapacitors. *Nano Energy*. **12**(2015): 141-151.
- Long, C., Jiang, L., Wu, X., Jiang, Y., Yang, D., Wang, C., Wei, T. and Fan, Z. (2015b). Facile synthesis of functionalized porous carbon with three-dimensional interconnected pore structure for high volumetric performance supercapacitors. *Carbon*. **93**(2015): 412-420.
- Lota, G., Fic, K. and Frackowiak, E. (2011). Carbon nanotubes and their composites in electrochemical applications. *Energy and Environmental Science*. **4**(5): 1592-1605.
- Lota, K., Sierczynska, A. and Lota, G. (2010). Supercapacitors based on nickel oxide/carbon materials composites. *International Journal of Electrochemistry*. **2011**(2011): 1-6.
- Lu, B., Hu, L., Yin, H., Mao, X., Xiao, W. and Wang, D. (2016a). Preparation and application of capacitive carbon from bamboo shells by one step molten carbonates carbonization. *International Journal of Hydrogen Energy*. **41**(41): 18713-18720.
- Lu, B., Zhou, J., Song, Y., Wang, H., Xiao, W. and Wang, D. (2016b). Molten-salt treatment of waste biomass for preparation of carbon with enhanced capacitive properties and electrocatalytic activity towards oxygen reduction. *Faraday Discussions*. **190**(2016): 147-159.
- Lufrano, F. and Staiti, P. (2010). Influence of the Surface Chemistry of Modified Mesoporous Carbon on the Electrochemical Behavior of Solid-State Supercapacitors. *Energy and Fuels*. **24**(6): 3313-3320.

- Ma, C., Song, Y., Shi, J., Zhang, D., Zhai, X., Zhong, M., Guo, Q. and Liu, L. (2013). Preparation and one-step activation of microporous carbon nanofibers for use as supercapacitor electrodes. *Carbon*. **51**(2013): 290-300.
- Ma, C., Wang, R., Xie, Z., Zhang, H., Li, Z. and Shi, J. (2017). Preparation and molten salt-assisted KOH activation of porous carbon nanofibers for use as supercapacitor electrodes. *Journal of Porous Materials*. **1**(2017): 1-9.
- Ma, Z., Yu, J. and Dai, S. (2010). Preparation of inorganic materials using ionic liquids. *Advanced Materials*. **22**(2): 261-285.
- Malmberg, H. (2007). Nanoscientific investigations of electrode materials for supercapacitors, Academic Award. Kungliga Tekniska Högskolan.
- Martinot, E., Dienst, C., Weiliang, L. and Qimin, C. (2007). Renewable energy futures: Targets, scenarios, and pathways. *Annual Review of Environmental Resources*. **32**(2007): 205-239.
- Mi, J., Wang, X.R., Fan, R.J., Qu, W.H. and Li, W.-C. (2012a). Coconut-shell-based porous carbons with a tunable micro/mesopore ratio for high-performance supercapacitors. *Energy and Fuels*. **26**(8): 5321-5329.
- Mi, J., Wang, X.R., Fan, R.J., Qu, W.H. and Li, W.C. (2012b). Coconut-shell-based porous carbons with a tunable micro/mesopore ratio for high-performance supercapacitors. *Energy and Fuels*. **26**(8): 5321-5329.
- Miller, J.R. and Burke, A.F. (2008). Electrochemical capacitors: challenges and opportunities for real-world applications. *The Electrochemical Society Interface*. **17**(1): 53.
- Molina-Sabio, M., Rodriguez-Reinoso, F., Caturla, F. and Selles, M. (1995). Porosity in granular carbons activated with phosphoric acid. *Carbon*. **33**(8): 1105-1113.
- Nabais, J.V., Carrott, P., Carrott, M.R. and Menéndez, J. (2004). Preparation and modification of activated carbon fibres by microwave heating. *Carbon*. **42**(7): 1315-1320.
- Nabais, J.V., Teixeira, J.G. and Almeida, I. (2011). Development of easy made low cost bindless monolithic electrodes from biomass with controlled properties to be used as electrochemical capacitors. *Bioresource Technology*. **102**(3): 2781-2787.
- Nor, N.S.M., Deraman, M., Omar, R., Farma, R., Basri, N.H., Dolah, B.N.M., Mamat, N.F., Yatim, B. and Daud, M.N.M. (2015). Influence of gamma irradiation exposure on the performance of supercapacitor electrodes made from oil palm empty fruit bunches. *Energy*. **79**(2015): 183-194.

- Obreja, V.V. (2008). On the performance of supercapacitors with electrodes based on carbon nanotubes and carbon activated material—a review. *Physica E: Low-dimensional Systems and Nanostructures*. **40**(7): 2596-2605.
- Oh, Y.J., Yoo, J.J., Kim, Y.I., Yoon, J.K., Yoon, H.N., Kim, J.-H. and Park, S.B. (2014). Oxygen functional groups and electrochemical capacitive behavior of incompletely reduced graphene oxides as a thin-film electrode of supercapacitor. *Electrochimica Acta*. **116**(2014): 118-128.
- Olivares-Marín, M., Fernández-González, C., Macías-García, A. and Gómez-Serrano, V. (2006). Preparation of activated carbons from cherry stones by activation with potassium hydroxide. *Applied Surface Science*. **252**(17): 5980-5983.
- Ong, L., Kurniawan, A., Suwandi, A., Lin, C., Zhao, X. and Ismadji, S. (2012). A facile and green preparation of durian shell-derived carbon electrodes for electrochemical double-layer capacitors. *Progress in Natural Science: Materials International*. **22**(6): 624-630.
- Otowa, T., Tanibata, R. and Itoh, M. (1993). Production and adsorption characteristics of MAXSORB: high-surface-area active carbon. *Gas Separation and Purification*. **7**(4): 241-245.
- Pagketanang, T., Artnaseaw, A., Wongwicha, P. and Thabuot, M. (2015). Microporous Activated Carbon from KOH-Activation of Rubber Seed-Shells for Application in Capacitor Electrode. *Energy Procedia*. **79**(2015): 651-656.
- Pampel, J., Denton, C. and Fellingner, T.-P. (2016). Glucose derived ionothermal carbons with tailor-made porosity. *Carbon*. **107**(2016): 288-296.
- Pandolfo, A. and Hollenkamp, A. (2006). Carbon properties and their role in supercapacitors. *Journal of Power Sources*. **157**(1): 11-27.
- Paraknowitsch, J.P., Zhang, J., Su, D., Thomas, A. and Antonietti, M. (2010). Ionic Liquids as Precursors for Nitrogen-Doped Graphitic Carbon. *Advanced Materials*. **22**(1): 87-92.
- Peng, C., Yan, X.B., Wang, R.T., Lang, J.W., Ou, Y.J. and Xue, Q.J. (2013). Promising activated carbons derived from waste tea-leaves and their application in high performance supercapacitors electrodes. *Electrochimica Acta*. **87**(2013): 401-408.
- Puligundla, P., Oh, S.-E. and Mok, C. (2016). Microwave-assisted pretreatment technologies for the conversion of lignocellulosic biomass to sugars and ethanol: a review. *Carbon letters*. **17**(1): 1-10.

- Qian, W., Sun, F., Xu, Y., Qiu, L., Liu, C., Wang, S. and Yan, F. (2014). Human hair-derived carbon flakes for electrochemical supercapacitors. *Energy and Environmental Science*. **7**(1): 379-386.
- Qin, W., Li, J.L., Fei, G., Li, W.S., Wu, K.Z. and Wang, X.D. (2008). Activated carbon coated with polyaniline as an electrode material in supercapacitors. *New Carbon Materials*. **23**(3): 275-280.
- Randles, J.E.B. (1947). Kinetics of rapid electrode reactions. *Discussions of the faraday society*. **1**(1947): 11-19.
- Raymundo-Piñero, E., Cadek, M. and Béguin, F. (2009). Tuning carbon materials for supercapacitors by direct pyrolysis of seaweeds. *Advanced Functional Materials*. **19**(7): 1032-1039.
- Redondo, E., Carretero, G.J., Goikolea, E., Ségalini, J. and Mysyk, R. (2015). Effect of pore texture on performance of activated carbon supercapacitor electrodes derived from olive pits. *Electrochimica Acta*. **160**(178-184).
- Ren, Y., Zhang, J., Xu, Q., Chen, Z., Yang, D., Wang, B. and Jiang, Z. (2014). Biomass-derived three-dimensional porous N-doped carbonaceous aerogel for efficient supercapacitor electrodes. *Royal Society of Chemistry Advances*. **4**(45): 23412-23419.
- Rouquerol, J., Rouquerol, F., Llewellyn, P., Maurin, G. and Sing, K.S. (2013). Adsorption by powders and porous solids: principles, methodology and applications. Academic presspp. 428-439pp.
- Rufford, T.E., Hulicova-Jurcakova, D., Khosla, K., Zhu, Z. and Lu, G.Q. (2010). Microstructure and electrochemical double-layer capacitance of carbon electrodes prepared by zinc chloride activation of sugar cane bagasse. *Journal of Power Sources*. **195**(3): 912-918.
- Rufford, T.E., Hulicova-Jurcakova, D., Zhu, Z. and Lu, G.Q. (2008). Nanoporous carbon electrode from waste coffee beans for high performance supercapacitors. *Electrochemistry Communications*. **10**(10): 1594-1597.
- Sawangphruk, M., Srimuk, P., Chiochan, P., Krittayavathananon, A., Luanwuthi, S. and Limtrakul, J. (2013). High-performance supercapacitor of manganese oxide/reduced graphene oxide nanocomposite coated on flexible carbon fiber paper. *Carbon*. **60**(2013): 109-116.

- Sekirifa, M.L., Hadj Mahammed, M., Pallier, S., Baameur, L., Richard, D. and Al Dujaili, A.H. (2013). Preparation and characterization of an activated carbon from a date stones variety by physical activation with carbon dioxide. *Journal of Analytical and Applied Pyrolysis*. **99**(2013): 155-160.
- Senthilkumar, S., Selvan, R.K., Lee, Y. and Melo, J. (2013). Electric double layer capacitor and its improved specific capacitance using redox additive electrolyte. *Journal of Materials Chemistry A*. **1**(4): 1086-1095.
- Senthilkumar, S., Senthilkumar, B., Balaji, S., Sanjeeviraja, C. and Selvan, R.K. (2011). Preparation of activated carbon from sorghum pith and its structural and electrochemical properties. *Materials Research Bulletin*. **46**(3): 413-419.
- Seredych, M. and Bandosz, T.J. (2013). S-doped micro/mesoporous carbon-graphene composites as efficient supercapacitors in alkaline media. *Journal of Materials Chemistry A*. **1**(38): 11717-11727.
- Seredych, M., Hulicova Jurcakova, D., Lu, G.Q. and Bandosz, T.J. (2008). Surface functional groups of carbons and the effects of their chemical character, density and accessibility to ions on electrochemical performance. *Carbon*. **46**(11): 1475-1488.
- Sevilla, M. and Fuertes, A.B. (2009). The production of carbon materials by hydrothermal carbonization of cellulose. *Carbon*. **47**(9): 2281-2289.
- Sevilla, M. and Mokaya, R. (2014). Energy storage applications of activated carbons: supercapacitors and hydrogen storage. *Energy and Environmental Science*. **7**(4): 1250-1280.
- Shafizadeh, F. (1982). Introduction to pyrolysis of biomass. *Journal of Analytical and Applied Pyrolysis*. **3**(4): 283-305.
- Shakir, I. (2014). High performance flexible pseudocapacitor based on nano-architected spinel nickel cobaltite anchored multiwall carbon nanotubes. *Electrochimica Acta*. **132**(2014): 490-495.
- Shang, H., Lu, Y., Zhao, F., Chao, C., Zhang, B. and Zhang, H. (2015). Preparing high surface area porous carbon from biomass by carbonization in a molten salt medium. *Royal Society of Chemistry Advances*. **5**(92): 75728-75734.
- Shao, G.N., Jeon, S.-J., Haider, M.S., Abbass, N. and Kim, H.T. (2016). Investigation of the influence of vanadium, iron and nickel dopants on the morphology, and crystal structure

- and photocatalytic properties of titanium dioxide based nanopowders. *Journal of Colloid and Interface Science*. **474**(2016): 179-189.
- Shi, H. (1996). Activated carbons and double layer capacitance. *Electrochimica Acta*. **41**(10): 1633-1639.
- Si, W., Zhou, J., Zhang, S., Li, S., Xing, W. and Zhuo, S. (2013). Tunable N-doped or dual N, S-doped activated hydrothermal carbons derived from human hair and glucose for supercapacitor applications. *Electrochimica Acta*. **107**(2013): 397-405.
- Simon, P. and Gogotsi, Y. (2008). Materials for electrochemical capacitors. *Nature materials*. **7**(11): 845-854.
- Simon, P. and Gogotsi, Y. (2013). Capacitive energy storage in nanostructured carbon-electrolyte systems. *Accounts of Chemical Research*. **46**(5): 1094– 1103.
- Simon, P., Taberna, P.L. and Béguin, F. (2013). Electrical Double-Layer Capacitors and Carbons for EDLCs. *Supercapacitors: Materials, Systems, and Applications*: 131-165.
- Sivakkumar, S., Ko, J.M., Kim, D.Y., Kim, B. and Wallace, G. (2007). Performance evaluation of CNT/polypyrrole/MnO₂ composite electrodes for electrochemical capacitors. *Electrochimica Acta*. **52**(25): 7377-7385.
- Stoller, M.D., Park, S., Zhu, Y., An, J. and Ruoff, R.S. (2008). Graphene-based ultracapacitors. *Nano Letters*. **8**(10): 3498-3502.
- Stoller, M.D. and Ruoff, R.S. (2010). Best practice methods for determining an electrode material's performance for ultracapacitors. *Energy and Environmental Science*. **3**(9): 1294-1301.
- Subramanian, V., Luo, C., Stephan, A., Nahm, K., Thomas, S. and Wei, B. (2007). Supercapacitors from activated carbon derived from banana fibers. *The Journal of Physical Chemistry C*. **111**(20): 7527-7531.
- Subramanian, V., Zhu, H. and Wei, B. (2006). Synthesis and electrochemical characterizations of amorphous manganese oxide and single walled carbon nanotube composites as supercapacitor electrode materials. *Electrochemistry Communications*. **8**(5): 827-832.
- Sudaryanto, Y., Hartono, S., Irawaty, W., Hindarso, H. and Ismadji, S. (2006). High surface area activated carbon prepared from cassava peel by chemical activation. *Bioresource Technology*. **97**(5): 734-739.

- Sun, K. and Chun Jiang, J. (2010). Preparation and characterization of activated carbon from rubber-seed shell by physical activation with steam. *Biomass and Bioenergy*. **34**(4): 539-544.
- Syarif, N. and Pardede, M.C. (2013). Hydrothermal Assisted Microwave Pyrolysis of Water Hyacinth for Electrochemical Capacitors Electrodes. *Concrete Structures in Thailand 087 Hydrothermal Assisted Microwave Pyrolysis of Water Hyacinth for Electrochemical Capacitors Electrodes 095 Group Technology Paves the Road for Automation 105 Effect of Laser Priming on accumulation of Free Proline in Spring: 95*.
- Syarif, N., Tribidasari, A. and Wibowo, W. (2011). Direct synthesis carbon/Metal oxide composites for electrochemical capacitors electrode. *International Transaction Journal of Engineering, Management, and Applied Sciences and Technologies*. **3**(1): 21-34.
- Taberna, P., Simon, P. and Fauvarque, J.-F. (2003). Electrochemical characteristics and impedance spectroscopy studies of carbon-carbon supercapacitors. *Journal of the Electrochemical Society*. **150**(3): A292-A300.
- Taberna, P.L., Chevallier, G., Simon, P., Plée, D. and Aubert, T. (2006). Activated carbon-carbon nanotube composite porous film for supercapacitor applications. *Materials Research Bulletin*. **41**(3): 478-484.
- Taer, E., Sumantre, M., Taslim, R., Dahlan, D. and Deraman, M. (Ed.) (2014). Eggs shell membrane as natural separator for supercapacitor applications. *In: Advanced Materials Research. Transition Technology Publication*, pp. 66-69, 2014.
- Tan, I., Ahmad, A. and Hameed, B. (2008). Preparation of activated carbon from coconut husk: Optimization study on removal of 2, 4, 6-trichlorophenol using response surface methodology. *Journal of Hazardous materials*. **153**(1): 709-717.
- Thambidurai, A., Lourdasamy, J.K., John, J.V. and Ganesan, S. (2014). Preparation and electrochemical behaviour of biomass based porous carbons as electrodes for supercapacitors—a comparative investigation. *Korean Journal of Chemical Engineering*. **31**(2): 268-275.
- Tseng, R.-L. (2006). Mesopore control of high surface area NaOH-activated carbon. *Journal of Colloid and Interface Science*. **303**(2): 494-502.

- Tseng, R.-L. (2007). Physical and chemical properties and adsorption type of activated carbon prepared from plum kernels by NaOH activation. *Journal of Hazardous materials*. **147**(3): 1020-1027.
- Umeshbabu, E., Rajeshkhanna, G. and Rao, G.R. (2014). Urchin and sheaf-like NiCo₂O₄ nanostructures: synthesis and electrochemical energy storage application. *International Journal of Hydrogen Energy*. **39**(28): 15627-15638.
- Venkata, B. (2016). WBA Global Bioenergy Statistics 2016. *World Bioenergy Association (WBA), Stockholm*.
- Wallar, C., Zhang, T., Shi, K. and Zhitomirsky, I. (2016). Synthesis of metal and metal oxide nanoparticles, liquid–liquid extraction and application in supercapacitors. *Colloids and Surfaces A: Physicochemical and Engineering Aspects*. **500**(2016): 195-202.
- Wang, D.-W., Li, F. and Cheng, H.-M. (2008). Hierarchical porous nickel oxide and carbon as electrode materials for asymmetric supercapacitor. *Journal of Power Sources*. **185**(2): 1563-1568.
- Wang, D., Geng, Z., Li, B. and Zhang, C. (2015a). High performance electrode materials for electric double-layer capacitors based on biomass-derived activated carbons. *Electrochimica Acta*. **173**(2015): 377-384.
- Wang, D., Xiao, W., Hu, L., Lu, B. and Yin, H. (2016a). One-step Molten Salt Carbonization (MSC) of Firwood Biomass for Capacitive Carbon. *Royal Society of Chemistry Advances*. **6** (2016): 106485-106490.
- Wang, H., Gao, Q. and Jiang, L. (2011a). Facile approach to prepare nickel cobaltite nanowire materials for supercapacitors. *Small*. **7**(17): 2454-2459.
- Wang, H., Holt, C.M., Li, Z., Tan, X., Amirkhiz, B.S., Xu, Z., Olsen, B.C., Stephenson, T. and Mitlin, D. (2012a). Graphene-nickel cobaltite nanocomposite asymmetrical supercapacitor with commercial level mass loading. *Nano Research*. **5**(9): 605-617.
- Wang, H., Xu, Z., Kohandehghan, A., Li, Z., Cui, K., Tan, X., Stephenson, T.J., King'ondo, C.K., Holt, C.M. and Olsen, B.C. (2013a). Interconnected carbon nanosheets derived from hemp for ultrafast supercapacitors with high energy. *ACS nano*. **7**(6): 5131-5141.
- Wang, J.-W., Chen, Y. and Chen, B.-Z. (2015b). A synthesis method of MnO₂/activated carbon composite for electrochemical supercapacitors. *Journal of the Electrochemical Society*. **162**(8): A1654-A1661.

- Wang, J. and Kaskel, S. (2012). KOH activation of carbon-based materials for energy storage. *Journal of Materials Chemistry*. **22**(45): 23710-23725.
- Wang, J., Xu, Y., Yan, F., Zhu, J. and Wang, J. (2011b). Template-free prepared micro/nanostructured polypyrrole with ultrafast charging/discharging rate and long cycle life. *Journal of Power Sources*. **196**(4): 2373-2379.
- Wang, J.W., Chen, Y. and Chen, B.Z. (2015c). A synthesis method of MnO₂/activated carbon composite for electrochemical supercapacitors. *Journal of the Electrochemical Society*. **162**(8): A1654-A1661.
- Wang, K., Gao, S., Du, Z., Yuan, A., Lu, W. and Chen, L. (2016b). MnO₂-Carbon nanotube composite for high-areal-density supercapacitors with high rate performance. *Journal of Power Sources*. **305**(2016): 30-36.
- Wang, K., Zhao, N., Lei, S., Yan, R., Tian, X., Wang, J., Song, Y., Xu, D., Guo, Q. and Liu, L. (2015d). Promising biomass-based activated carbons derived from willow catkins for high performance supercapacitors. *Electrochimica Acta*. **166**(2015): 1-11.
- Wang, L., Mu, G., Tian, C., Sun, L., Zhou, W., Yu, P., Yin, J. and Fu, H. (2013b). Porous graphitic carbon nanosheets derived from cornstalk biomass for advanced supercapacitors. *ChemSusChem*. **6**(5): 880-889.
- Wang, L., Zheng, Y., Chen, S., Ye, Y., Xu, F., Tan, H., Li, Z., Hou, H. and Song, Y. (2014a). Three-Dimensional Kenaf Stem-Derived Porous Carbon/MnO₂ for High-Performance Supercapacitors. *Electrochimica Acta*. **135**(2014): 380-387.
- Wang, Q., Cao, Q., Wang, X., Jing, B., Kuang, H. and Zhou, L. (2013c). A high-capacity carbon prepared from renewable chicken feather biopolymer for supercapacitors. *Journal of Power Sources*. **225**(2013): 101-107.
- Wang, Q., Yan, J. and Fan, Z. (2016c). Carbon materials for high volumetric performance supercapacitors: design, progress, challenges and opportunities. *Energy and Environmental Science*. **9**(3): 729-762.
- Wang, Q., Yan, J., Wang, Y., Wei, T., Zhang, M., Jing, X. and Fan, Z. (2014b). Three-dimensional flower-like and hierarchical porous carbon materials as high-rate performance electrodes for supercapacitors. *Carbon*. **67**(2014): 119-127.
- Wang, R., P. Wang, X. Yan, J. Lang, C. Peng, a., Xue., Q. and (2012b). Promising Porous Carbon Derived from Celtuce Leaves with Outstanding Supercapacitance and CO₂

- Capture Performance. *American Chemical Society Applied Materials and Interfaces*. **4**(11): 5800–5806.
- Wang, R., Wang, P., Yan, X., Lang, J., Peng, C. and Xue, Q. (2012b). Promising porous carbon derived from celtuce leaves with outstanding supercapacitance and CO₂ capture performance. *American Chemical Society Applied Materials and Interfaces*. **4**(11): 5800-5806.
- Wang, X., Han, X., Lim, M., Singh, N., Gan, C.L., Jan, M. and Lee, P.S. (2012c). Nickel cobalt oxide-single wall carbon nanotube composite material for superior cycling stability and high-performance supercapacitor application. *The Journal of Physical Chemistry C*. **116**(23): 12448-12454.
- Wang, X., Wang, M., Zhang, X., Li, H. and Guo, X. (2016d). Low-cost, green synthesis of highly porous carbons derived from lotus root shell as superior performance electrode materials in supercapacitor. *Journal of Energy Chemistry*. **25**(1): 26-34.
- Wei, L. and Yushin, G. (2012). Nanostructured activated carbons from natural precursors for electrical double layer capacitors. *Nano Energy*. **1**(4): 552-565.
- Wen, Z., Qu, Q., Gao, Q., Zheng, X., Hu, Z., Wu, Y., Liu, Y. and Wang, X. (2009). An activated carbon with high capacitance from carbonization of a resorcinol–formaldehyde resin. *Electrochemistry Communications*. **11**(3): 715-718.
- Winter, M. and Brodd, R.J. (2004). What are batteries, fuel cells, and supercapacitors? *Chemical Reviews*. **104**(10): 4245-4270.
- Wu, F.C., Tseng, R.L., Hu, C.C. and Wang, C.C. (2005). Effects of pore structure and electrolyte on the capacitive characteristics of steam-and KOH-activated carbons for supercapacitors. *Journal of Power Sources*. **144**(1): 302-309.
- Wu, K., Gao, B., Su, J., Peng, X., Zhang, X., Fu, J., Peng, S. and Chu, P.K. (2016). Large and porous carbon sheets derived from water hyacinth for high-performance supercapacitors. *Royal Society of Chemistry Advances*. **6**(36): 29996-30003.
- Wu, M.-S., Huang, Y.-A., Yang, C.-H. and Jow, J.-J. (2007). Electrodeposition of nanoporous nickel oxide film for electrochemical capacitors. *International Journal of Hydrogen Energy*. **32**(17): 4153-4159.

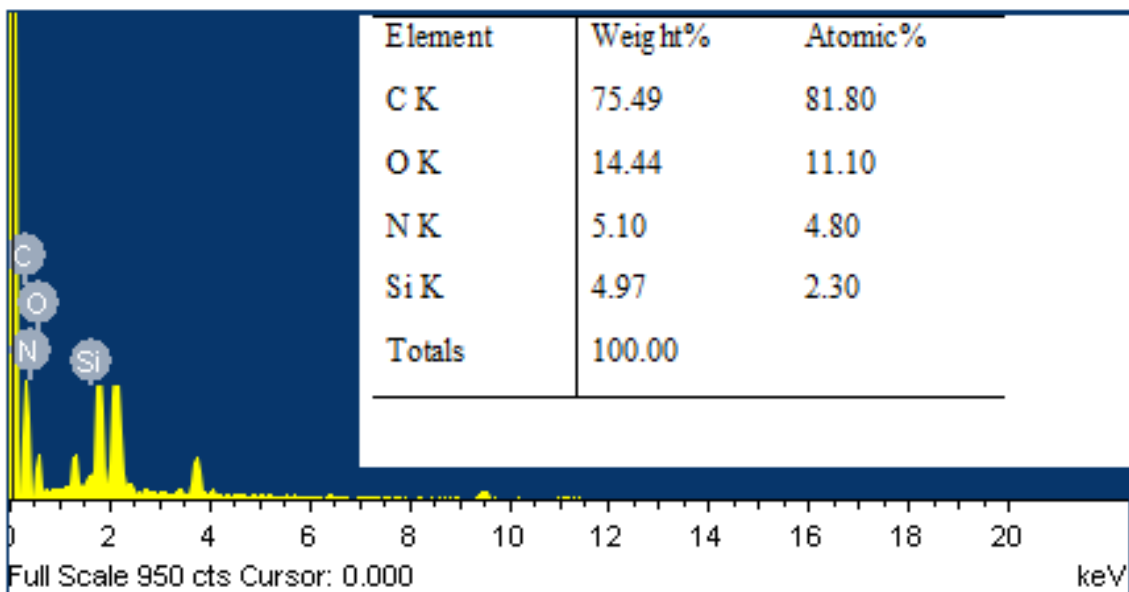
- Wu, X.-L., Wen, T., Guo, H.-L., Yang, S., Wang, X. and Xu, A.-W. (2013). Biomass-derived sponge-like carbonaceous hydrogels and aerogels for supercapacitors. *ACS nano*. **7**(4): 3589-3597.
- Wu, X., Xiong, W., Chen, Y., Lan, D., Pu, X., Zeng, Y., Gao, H., Chen, J., Tong, H. and Zhu, Z. (2015). High-rate supercapacitor utilizing hydrous ruthenium dioxide nanotubes. *Journal of Power Sources*. **294**(2015): 88-93.
- Wu, Z., Zhu, Y. and Ji, X. (2014). NiCo₂O₄-based materials for electrochemical supercapacitors. *Journal of Materials Chemistry A*. **2**(36): 14759-14772.
- Xia, K., Gao, Q., Jiang, J. and Hu, J. (2008). Hierarchical porous carbons with controlled micropores and mesopores for supercapacitor electrode materials. *Carbon*. **46**(13): 1718-1726.
- Xia, X., Liu, H., Shi, L. and He, Y. (2012). Tobacco stem-based activated carbons for high performance supercapacitors. *Journal of Materials Engineering and Performance*. **21**(9): 1956-1961.
- Xie, Q., Bao, R., Zheng, A., Zhang, Y., Wu, S., Xie, C. and Zhao, P. (2016). Sustainable Low-Cost Green Electrodes with High Volumetric Capacitance for Aqueous Symmetric Supercapacitors with High Energy Density. *ACS Sustainable Chemistry and Engineering*. **4**(3): 1422-1430.
- Xie, X. and Gao, L. (2007). Characterization of a manganese dioxide/carbon nanotube composite fabricated using an in situ coating method. *Carbon*. **45**(12): 2365-2373.
- Xie, Z.L., White, R.J., Weber, J., Taubert, A. and Titirici, M.M. (2011). Hierarchical porous carbonaceous materials via ionothermal carbonization of carbohydrates. *Journal of Materials Chemistry*. **21**(20): 7434-7442.
- Xing, B., Huang, G., Chen, L., Guo, H., Zhang, C., Xie, W. and Chen, Z. (2016). Microwave synthesis of hierarchically porous activated carbon from lignite for high performance supercapacitors. *Journal of Porous Materials*. **23**(1): 67-73.
- Xing, W., Li, X., Gao, X.L. and Zhuo, S.P. (Ed.) (2011). Highly porous carbon derived from sunflower seed shell for electrochemical capacitor. *In: Advanced Materials Research. Transition Technology Publication*, pp. 1420-1423, 2011.
- Xiong, W., Gao, Y., Wu, X., Hu, X., Lan, D., Chen, Y., Pu, X., Zeng, Y., Su, J. and Zhu, Z. (2014). Composite of macroporous carbon with honeycomb-like structure from mollusc

- shell and NiCo₂O₄ nanowires for high-performance supercapacitor. *American Chemical Society Applied Materials and Interfaces*. **6**(21): 19416-19423.
- Xu, B., Chen, Y., Wei, G., Cao, G., Zhang, H. and Yang, Y. (2010). Activated carbon with high capacitance prepared by NaOH activation for supercapacitors. *Materials Chemistry and Physics*. **124**(1): 504-509.
- Xu, B., Wu, F., Chen, S., Zhang, C., Cao, G. and Yang, Y. (2007). Activated carbon fiber cloths as electrodes for high performance electric double layer capacitors. *Electrochimica Acta*. **52**(13): 4595-4598.
- Xu, B., Wu, F., Chen, S., Zhou, Z., Cao, G. and Yang, Y. (2009). High-capacitance carbon electrode prepared by PVDC carbonization for aqueous EDLCs. *Electrochimica Acta*. **54**(8): 2185-2189.
- Yan, J., Fan, Z., Wei, T., Qian, W., Zhang, M. and Wei, F. (2010). Fast and reversible surface redox reaction of graphene–MnO₂ composites as supercapacitor electrodes. *Carbon*. **48**(13): 3825-3833.
- Yang, C.-S., Jang, Y.S. and Jeong, H.K. (2014a). Bamboo-based activated carbon for supercapacitor applications. *Current Applied Physics*. **14**(12): 1616-1620.
- Yang, D. (2012). Application of nanocomposites for supercapacitors: characteristics and properties. INTECH Open Access Publisherpp.
- Yang, M., Kim, D.S., Hong, S.B., Sim, J.-W., Kim, J., Kim, S.S. and Choi, B.G. (2017). MnO₂ Nanowire/Biomass-Derived Carbon from Hemp Stem for High-Performance Supercapacitors. *Langmuir*. **33**(21): 5140-5147.
- Yang, X., Juhas, P., Farrow, C.L. and Billinge, S.J. (2014b). xPDFsuite: an end-to-end software solution for high throughput pair distribution function transformation, visualization and analysis. *arXiv preprint arXiv:1402.3163*.
- Yin, H., Lu, B., Xu, Y., Tang, D., Mao, X., Xiao, W., Wang, D. and Alshwabkeh, A.N. (2014). Harvesting capacitive carbon by carbonization of waste biomass in molten salts. *Environmental Science and Technology*. **48**(14): 8101-8108.
- Zhang, D., Yan, H., Lu, Y., Qiu, K., Wang, C., Tang, C., Zhang, Y., Cheng, C. and Luo, Y. (2014a). Hierarchical mesoporous nickel cobaltite nanoneedle/carbon cloth arrays as superior flexible electrodes for supercapacitors. *Nanoscale research letters*. **9**(1): 139.

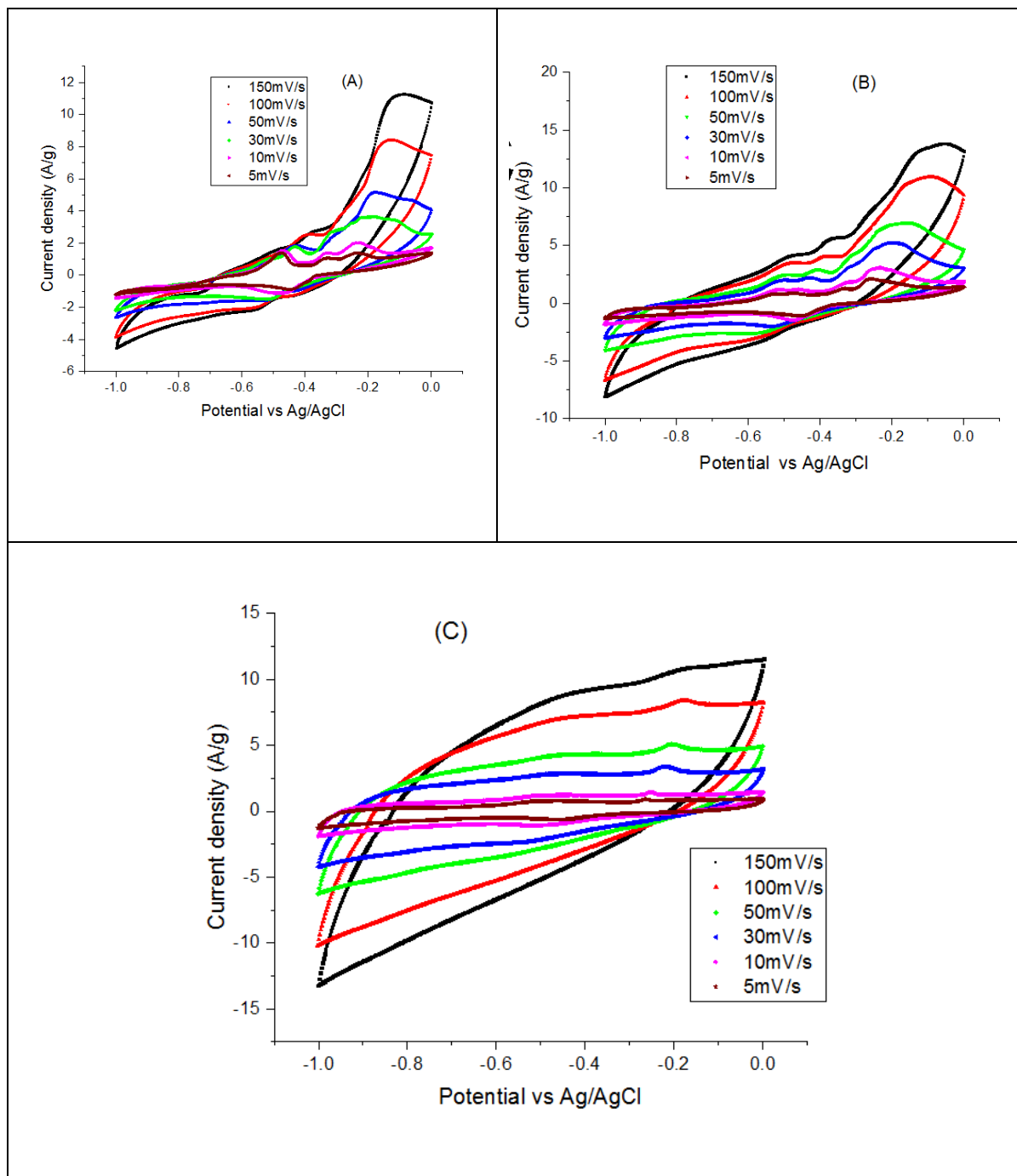
- Zhang, D., Zheng, L., Ma, Y., Lei, L., Li, Q., Li, Y., Luo, H., Feng, H. and Hao, Y. (2014b). Synthesis of nitrogen-and sulfur-codoped 3D cubic-ordered mesoporous carbon with superior performance in supercapacitors. *American Chemical Society Applied Materials and Interfaces*. **6**(4): 2657-2665.
- Zhang, G. and Lou, X.W.D. (2013). Controlled growth of NiCo₂O₄ nanorods and ultrathin nanosheets on carbon nanofibers for high-performance supercapacitors. *Scientific reports*. **3**(1470).
- Zhang, L., Liu, S., Wang, B., Wang, Q., Yang, G. and Chen, J. (2015a). Effect of residence time on hydrothermal carbonization of corn cob residual. *BioResources*. **10**(3): 3979-3986.
- Zhang, L., Wang, Q., Wang, B., Yang, G., Lucia, L.A. and Chen, J. (2015b). Hydrothermal carbonization of corncob residues for hydrochar production. *Energy and Fuels*. **29**(2): 872-876.
- Zhang, L.L., and Zhao, X.S. (2009). Carbon-based materials as supercapacitor electrodes. *The Royal Society of Chemistry*. **38**(9): 2520–2531.
- Zhang, P., Gong, Y., Wei, Z., Wang, J., Zhang, Z., Li, H., Dai, S. and Wang, Y. (2014c). Updating biomass into functional carbon material in ionothermal manner. *American Chemical Society Applied Materials and Interfaces*. **6**(15): 12515-12522.
- Zhang, X., Sun, X., Zhang, H., Zhang, D. and Ma, Y. (2013a). Microwave-assisted reflux rapid synthesis of MnO₂ nanostructures and their application in supercapacitors. *Electrochimica Acta*. **87**(2013): 637-644.
- Zhang, X., Sun, X., Zhang H., Zhang D. and Y., M. (2013b). Microwave-assisted reflux rapid synthesis of MnO₂ nanostructures and their application in supercapacitors. *Electrochimica Acta*. **87**(2013): 637-644.
- Zhang, Y., Zhang, Y., Huang, J., Du, D., Xing, W. and Yan, Z. (2016). Enhanced Capacitive Performance of N-Doped Activated Carbon from Petroleum Coke by Combining Ammoxidation with KOH Activation. *Nanoscale research letters*. **11**(1): 1-7.
- Zhao, Y., Liu, M., Deng, X., Miao, L., Tripathi, P.K., Ma, X., Zhu, D., Xu, Z., Hao, Z. and Gan, L. (2015). Nitrogen-functionalized microporous carbon nanoparticles for high performance supercapacitor electrode. *Electrochimica Acta*. **153**(2015): 448-455.

- Zhao, Y.Q., Lu, M., Tao, P.Y., Zhang, Y.J., Gong, X.T., Yang, Z., Zhang, G.Q. and Li, H.L. (2016). Hierarchically porous and heteroatom doped carbon derived from tobacco rods for supercapacitors. *Journal of Power Sources*. **307**(2016): 391-400.
- Zhi, M., Xiang, C., Li, J., Li, M. and Wu, N. (2013). Nanostructured carbon–metal oxide composite electrodes for supercapacitors: a review. *Nanoscale*. **5**(1): 72-88.
- Zhou, X., Li, H. and Yang, J. (2016). Biomass-derived activated carbon materials with plentiful heteroatoms for high-performance electrochemical capacitor electrodes. *Journal of Energy Chemistry*. **25**(1): 35-40.

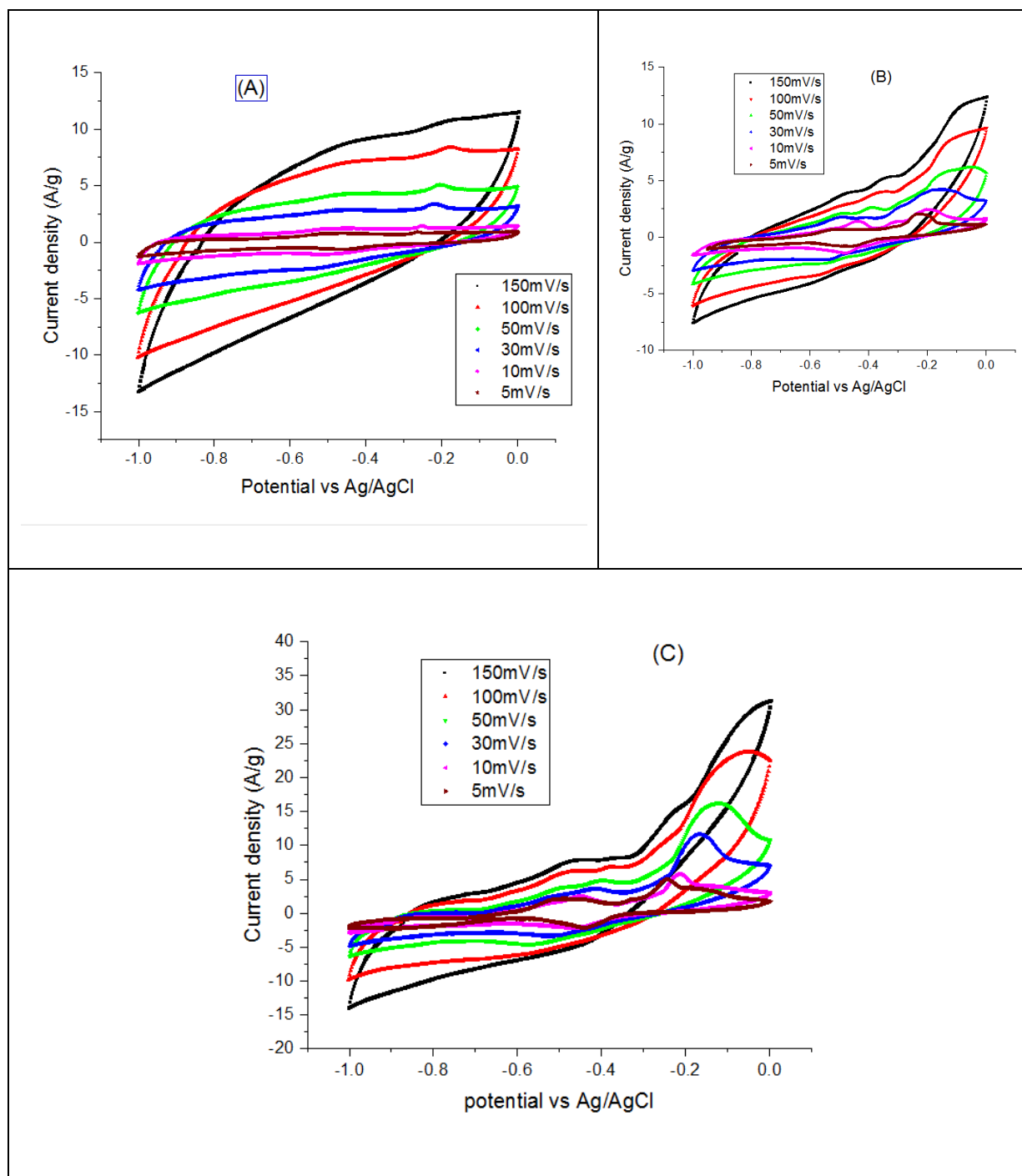
APPENDICES



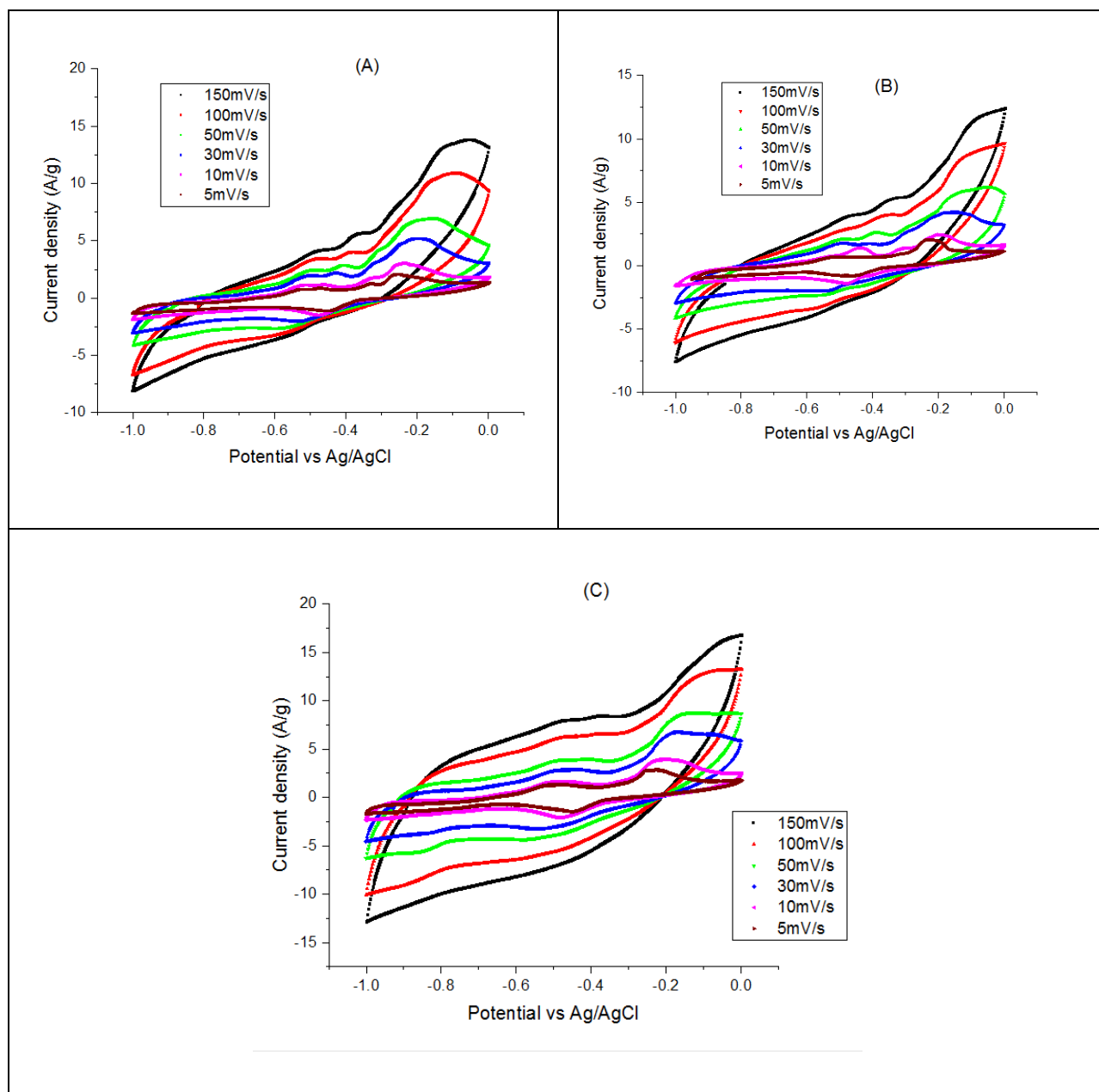
Appendix 1: EDX spectrum for BC-3-700-30



Appendix 2: Cyclic voltammograms of biogas slurry derived carbons in three-electrode system in 6 M KOH at sweep rates of 5, 10, 30, 50, 100 and 150 mV s^{-1} (A) BC-1-700-30 (B) BC-2-700-30, and (C) BC-3-700-30.



Appendix 3: Cyclic voltammograms of biogas slurry derived carbons in three-electrode system in 6 M KOH at sweep rates of 5, 10, 30, 50, 100 and 150 mV s^{-1} (A) BC-3-700-30 (B) BC-3-700-60, and (C) BC-3-700-120.



Appendix 4: Cyclic voltammograms of biogas slurry derived carbons in three-electrode system in 6 M KOH at sweep rates of 5, 10, 30, 50, 100 and 150 mV s^{-1} (A) BC-3-600-60 (B) BC-3-700-60, and (C) BC-3-800-60.